Microwave Characterization and Microwave Non-Destructive Testing Applied to Carbon Fibre Reinforced Polymers

by Daniela Munalli, BSc, MSc

Thesis submitted to The University of Nottingham for the degree of Doctor of Philosophy, March 2022



Abstract

The instrumentations and the developments presented in this thesis aim to address the challenges of the applicability of microwave characterization and microwave non-destructive testing (MNDT) methods to carbon fibre reinforced polymers (CFRP).

Microwave characterization of carbon fibre composites has become an issue particularly relevant in recent years, as the prevalence of using CFRP based materials has significantly increased in many electromagnetic applications, including radio frequency (RF) absorption or electromagnetic interference (EMI) shielding. In addition, MNDT methods represent an effective solution in detecting defects and flaws within material structures, as they offer the advantage to overcome the problems of traditional NDT techniques such as coupling and danger coming from ionizing radiation.

However, when it comes to the analysis of CFRP, the use of these techniques is limited by the composite relatively high conductivity of $\simeq 10^4$ S/m. The electromagnetic signal is unable to penetrate the material, making the electromagnetic characterization difficult and restricting the MNDT applicability to surface defects (e.g., impact damage, indentation).

In regards to these observations, the shielding effectiveness of woven and unidirectional carbon fibre composites is studied at low-band frequencies, to achieve a more detailed definition of the electromagnetic behaviour of woven and unidirectional carbon fibre composites. The percentages of power reflected and transmitted are reported and the electrical behaviour of the samples suggests that a single layer of carbon fibre fabric is able to shield more than 99 % of the electromagnetic radiation.

Consequently, a waveguide-based measurement configuration is proposed, as a modification to the traditional completely-filled waveguide technique, for microwave characterization of relatively thin and high-loss materials. This method is aimed to overcome the large measurement errors caused by gaps and cross-sectional distortions, which are of great concern when measuring high-loss samples, such as CFRP. The influence of critical parameters, namely; dielectric constant, loss factor, material thickness and waveguide misalignment, on measured complex permittivity of several diverse samples, is fully investigated through numerical electromagnetic simulations and measurements at X-band (8.2-12.4 GHz). By the virtue of the electromagnetic properties associated with high-loss dielectric materials, it was found that this technique coupled with the NRW/Backer-Jarvis conversion procedure is a capable method for measuring high-loss dielectric materials.

After having established a reliable method of electromagnetic characterization, the complex permittivities of thin and high-loss unidirectional composites are measured at X-band and Ku-band. The use of unidirectional CFRP coupled with appropriate polarization of the electric field is the key to allow transmission of the signal through the CFRP composite. In addition, a mesoscale model for numerical electromagnetic simulations of unidirectional composites is adopted.

Extensive simulation results and free-space measurements are also presented at Ka-band, to further determine the permittivity of unidirectional CFRP and to assess damage detection in case of delamination of a unidirectional composite laminate.

Finally, synthetic aperture radar (SAR) imaging method is applied at Ka-band frequencies, to detect and characterize manufacturing defects such as gaps, overlays, missing tow, fibre misalignment and fibre waviness in carbon fabric and CFRP laminates. This approach makes particular use of the changes in the scattered signal with the orientation of a polarizing target (i.e., conducting fibres).

Acknowledgements

With the conclusion of my work come a sense of accomplishment and relief, as well as gratitude towards those who accompanied me on this journey.

First and foremost, I would like to thank my supervisors Dr Dimitrios Chronopoulos, Dr Georgios Dimitrakis, Dr Steve Greedy and Professor Andrew Long, who were instrumental in getting the project started, providing key advice in the direction of the research and helping me understand the topic more fully. I appreciate all their support.

My research would not have been possible without the help and guidance of Professor Reza Zoughi and Dr Tayeb Al Qaseer, I owe them and all the research group of the Applied Microwave Nondestructive Testing Laboratory my deepest gratitude for giving me the opportunity to join their laboratory at Iowa State University. Thank you Anna, Katie, Matt and Chao.

I would like to thank my fellow colleagues and friends of the ATC. You made this PhD fun. A particular thanks goes to Cohort 1, which helped us to adjust quickly to the new workplace, thank you Cosimo and Vincenzo, you were always there when we needed help and explanations. Thank you Helen for having helped us throughout the PhD. Thanks to my fellow Cohort member Milos, as we continued this journey together until the end. I cannot name all of you Cohorts colleagues because we are more than 20, but I enjoyed our time working together.

Finally, my sincere thanks goes to my family who have been extremely loving and supporting. I would like to thank them for encouraging my life in the science and engineering fields.

Contents

Abstract **2**

Acknowledgements **4**

List of Tables **8**

List of Figures **10**

Chapter 1 Introduction **19**

1.1 CFRP materials 19
1.1.1 Carbon fibres 20
1.1.2 Matrix 21
1.1.3 Manufacture 21
1.2 Defects types and damage in composite materials 22
1.2.1 Porosity 23
1.2.2 Foreign bodies 24
1.2.3 Fibre or ply misalignment. 24
1.2.4 Fibre waviness 26
1.3 Non-destructive testing for composite materials 26
1.4 The drive to use microwave NDT 29
1.5 Thesis objectives and layout 31

Chapter 2 Literature survey **33**

2.1 Electromagnetic radiation 33
2.1.1 Electromagnetic waves 33
2.1.2 Electromagnetic classification of materials 38
2.1.3 Plane wave approach 39
2.2 Electromagnetic properties of CFRP 41
2.2.1 Electromagnetic parameters of thermoset matrices 42
2.2.2 Electromagnetic parameters of carbon fibres 43
2.2.3 Conductivity of CFRP 44
2.3 Microwave methods 45
2.3.1 Field regions 45
2.3.2 Measurement methods 46
2.3.3 Microwave characterization and MNDT applied to CFRP 53
2.3.4 Summary 59
2.4 Measurements procedures 60
2.4.1 Vector Network Analyzer 60
2.4.2 Sensing architecture 62
2.4.3 Test locations 66

2.5 Computational tool 68

Chapter 3 Low-band Electromagnetic Interference (EMI) shielding of CFRP . 71

3.1 EMI shielding and CFRP 71
3.2 EMI shielding theory 73
3.2.1 The shielding mechanism 73
3.2.2 EMI SE of a conductive plate 74
3.2.3 EMI SE measurement of non-metallic materials 77
3.2.4 SE as function of resistivity 78
3.3 Experimental evaluation of SE of CFRP 79
3.3.1 Materials preparation 79
3.3.2 ASTM D4935 method 83
3.3.3 Experimental results 84
3.4 Numerical simulations 90
3.4.1 Coaxial line simulation 90
3.4.2 Textile fabric simulation 95
3.5 Summary 98

Chapter 4 Modified waveguide-based method for microwave characterization of high-loss materials 100

4.1 Limitations to traditional characterization methods for high-loss materials .. 100
4.2 Clamped waveguide measurement approach 103
4.3 NRW/Backer-Jarvis method applied to plug-loaded transmission line 106
4.4 Simulation results 108
4.4.1 Error due to material dielectric properties and thickness 108
4.4.2 Error in dielectric constant for fixed loss factor 112
4.4.3 Error in loss factor for fixed dielectric constant 112
4.4.4 Error due to thickness 113
4.4.5 Error due to waveguide misalignment 114
4.5 Measurements results 116
4.5.1 Error due to dielectric properties 116
4.5.2 Error due to material thickness 119
4.5.3 Error due to misalignment 120
4.6 Accuracy between simulations and measurements 121
4.7 Summary and conclusion 122

Chapter 5 Wide-band microwave characterization of unidirectional CFRP sheets 124

5.1 Materials 125
5.2 Mesoscale simulations of unidirectional CFRP sheets 125
5.2.1 Parallel polarization 127
5.2.2 Perpendicular polarization 138
5.3 Measurement methods 148
5.3.1 Method 1: Two-port plug-loaded transmission line 149

5.3.2 Method 2: Clamped waveguide method 152
5.3.3 Complex permittivity 155
5.3.4 Conductivity 157
5.4 Simulations results and discussion 158
5.4.1 Homogeneous model 158
5.4.2 Mesoscale model 162

Chapter 6 Free-space characterization and damage detection in unidirectional CFRP 167

6.1 Free-space measurement system 167
6.2 Materials 169
6.3 TRL Calibration 172
6.4 Permittivity extraction 174
6.5 Measurements results 176
6.5.1 Permittivity characterization 182
6.6 Damage identification, numerical simulation 183
6.7 Damage identification, experimental 188
6.7.1 Reducing the frequency range 190
6.7.2 Energy of the scattered signal 190

Chapter 7 Characterization of defects in carbon fabric and CFRP sheets using Synthetic Aperture Radar (SAR) 192

7.1 Electromagnetic waves polarization 193
7.2 Microwave SAR imaging 194
7.2.1 Dual polarized antenna 194
7.2.2 SAR polarimetry 197
7.2.3 3D SAR algorithm 198
7.3 Measurements 200
7.3.1 Detection of fibre misalignment and in-plane waviness 200
7.3.2 In-plane waviness 205
7.3.3 Fibre orientation 207
7.3.4 Gaps, overlaps, missing tow 208
7.3.5 Inclusion 214
7.3.6 Out-of-plane fibre waviness 218

Conclusion and suggestions for further work 220

Bibliography 225

Appendix I 240

List of Tables

Table 1.1: Conventional carbon fibre reinforcements for aerospace applications [2], [10]... 20

Table 1.2: Properties of commonly used matrices in aerospace [2], [10]. 21

Table 2.1:Dielectric constant, tangent loss and resistivity of commonly used thermoset polymers [48], [49]. 43

Table 2.2: Resistivity of commonly used carbon fibres [49]. 43

Table 2.3: Comparison between microwave measurement methods [76]. 47

Table 3.1: Geometrical properties of CFRP samples. 79

Table 3.2: Geometrical properties of dry carbon fibre samples. 80

Table 3.3: Comparison between CFRP and carbon fibre samples. Volume resistivity and SE of specimen A, B, D, E. 86

Table 3.4: Percentage of power reflected with load specimen and reference samples in place; power transmitted through the load sample. 89

Table 3.5: Properties of the assembly components. 91

Table 3.6: Calculated average value over frequency of conductivity with Simon formalism for different values of thicknesses for specimen A and B. 92

Table 3.7: Pyrofil TR30S properties. 95

Table 4.1: Dielectric properties of materials chosen. Simulated results for ideal model (L) and clamped waveguide method (C). 110

Table 4.2: Complex dielectric permittivities calculated with loaded method (L) and clamped method (C) and relevant errors. 117

Table 5.1: Unidirectional CFRP sheets specifications. 125

Table 5.2: CFRP properties of filler and polymer..... 125

Table 5.3: CFRP1 model, geometric and electromagnetic parameters. 126

Table 5.4: $S11$ and $S21$ for plug-loaded (L) and clamped (C) waveguide method measured at fixed frequencies– polarization perpendicular to fibres. 153

Table 5.5: Measured complex permittivities over X-band and Ku-band and errors between two models, for electric field polarized perpendicularly to fibres. 156

Table 5.6: Average values of conductivity over X-band and Ku-band for CFRP1, CFRP2 and CFRP3 with electric field polarized along the fibre axis. 157

Table 5.7: Mean squared errors between estimated values and measured values..... 159

Table 5.8: Power balance over 8.2 – 18 GHz for CFRP1, CFRP2 and CFRP3 in case of electric field polarized perpendicularly to fibre axis. 161

Table 5.9: MAPE between estimated values and measured values of $S21$ for Method 2. .. 161

Table 5.10: CFRP1 model, geometric and electromagnetic parameters. 164

Table 6.1: LB-28-20-C horn technical specification..... 185

Table 6.2: Damage types considered for simulation. 185

List of Figures

Figure 1.1: CFRP parts of Airbus A350 (a) and Dreamliner Boeing 787 (b). 20

Figure 1.2: Examples of ply sequence for a laminated composite [13]. 22

Figure 1.3: Spherical porosity in a CFRP sample. 24

Figure 1.4: From left to right, schematic of overlap, gap, missing tow, twisted tow, wrinkled and an upfolded tow within a ply [22]. 25

Figure 1.5: Project layout. 32

Figure 2.1: Dielectric constant and loss factor as function of frequency [41], [42]. 38

Figure 2.2: Reflection and transmission of an electromagnetic wave at the surface between air $\eta 0$ and medium ηS with normal incidence. 40

Figure 2.3: Schematic diagram of electromagnetic wave reflection and transmission pathways at two boundaries with different impedance [44], [45]. 40

Figure 2.4: Percolation state in carbon fibre composite [52]. 44

Figure 2.5: Antenna field regions, D is the antenna length or diameter and $\lambda 0$ the free space wavelength [54]. 45

Figure 2.6: Example of transmission-line experimental setup. 48

Figure 2.7: Cross-section of an open-ended rectangular waveguide radiating into a material with permittivity $\varepsilon r 1$ terminated by a conducting sheet. 49

Figure 2.8: Diagram of a free-space microwave method, using two horn antennas. 50

Figure 2.9: Schematic of an antenna imaging system. 52

Figure 2.10: 2D wideband SAR image of cracks artificially made on a metal plate [123]. .. 53

Figure 2.11: Millimeter wave images of carbon fibre strip: (a) without breakage, (b) with breakage and field polarized in the direction of the fibres [140]. 55

Figure 2.12: Microwave image of square shaped disbond at 10 GHz and standoff distance of 1.5 mm using orthogonal polarization (dimensions in millimeters) [64]. 56

Figure 2.13: (a) Experiment setup; (b) image of specimen damaged at 13.21 J; (c) image of specimen damaged at 3.63 J [141]. 57

Figure 2.14: (1) Schematic a microwave resonator setup; (2) delaminated (a) and intact (b) composites imaged side by side [142]. 58

Figure 2.15: Schematic two-port S-parameter VNA measurement setup. 60

Figure 2.16: 12 terms error model for full two-port calibration [148]. 62

Figure 2.17: Schematic diagram of a rectangular waveguide of aperture $a \times b$. 63

Figure 2.18: Schematic diagram of a rectangular waveguide of aperture $a \times b$ [149]. 64

Figure 2.19: Simulated radiation pattern of LB-28-20. 65

Figure 2.20: Example of a radiated emission test in semi anechoic chamber. 67

Figure 2.21: Example of reverberation chamber with a stirrer on the ceiling [153]. 68

Figure 2.22: Electric voltage **e** and magnetic flux **b** on the face of a mesh grid hexahedral element. 69

Figure 3.1: Concept of shielding effectiveness (SE) for a slab of conductive material, wave absorption, reflection, re-reflection and transmission mechanisms. 74

Figure 3.2: Incident wave transmitted at two boundaries with different impedance. ES and $Er1$ are respectively the intensity of the transmitted and reflected wave at the first interface and Et is the transmitted wave through the second boundary. 75

Figure 3.3: (a) Composite panel of Specimen A, B and C; (b) 2/2 twill carbon fibres. 80

Figure 3.4: ASTM D4935: Dimension of (a) Reference specimen; (b) Load specimen. 81

Figure 3.5: Specimen A-B: CFRP laminate; Specimen C: Carbon sandwich panel; Specimen D: 1 layer of dry 2/2 twill fibres; Specimen E: 4 layers of dry 2/2 twill fibres; Specimen F: 1 layer of dry UD fibres. 81

Figure 3.6: (a) Diagram of the ASTM D4935 measurement setup for electromagnetic SE measurement; (b) coaxial unit holder manufactured according to ASTM D4935-99; (c) Load specimen B in place. 82

Figure 3.7: $S21$ measured for both reference and load samples made of fiberglass. 84

Figure 3.8: $S21$ measured for reference and load samples of materials listed in Table. 3.1, Table 3.2 and Figure 3.4. 85

Figure 3.9: SE measured for specimen A, B, D and F. 87

Figure 3.10: Incident, reflected and transmitted power for Specimen A, B and D. The first column refers to reference specimens in place. The second column refers to Load specimens in place for each material. 88

Figure 3.11: ASTM D4935 equipment model. 90

Figure 3.12: Detail of ASTM D4935 simulation equipment with its components 91

Figure 3.13: Electric field propagation in presence of the reference specimen. 92

Figure 3.14: Electric field propagation in presence of the load specimen with a thickness of 3 mm and conductivity of 3161.45 S/m. 92

Figure 3.15: Shielding effectiveness of specimen A, measured data [M] and simulated data [S]..... 93

Figure 3.16: Shielding effectiveness of specimen B, measured data [M] and simulated data [S]..... 93

Figure 3.17: 2/2 twill woven fabric made of TR30S 3k. 95

Figure 3.18: Unit cell of 2/2 twill weave pattern. 96

Figure 3.19: Simulation methodology for the mesoscale fabric layer. 97

Figure 3.20: Effect of fabric thickness, yarn width and UC side length on simulated microwave transmission coefficient..... 98

Figure 3.21: Measured [M] and simulated [S] transmission coefficient of TR30S fabric over 0.03-1.5 GHz..... 98

Figure 4.1: Clamped waveguide method measurement setup..... 102

Figure 4.2: Diagram of the clamped method simulation setup, showing two open-ended waveguides with standard flanges. The field wave propagation is recorded at 10.3 GHz on the x-y plane for samples with thickness = 1.5 mm and $tan\delta = 0.01$ (b), $tan\delta = 0.4$ (c) and $tan\delta = 0.8$ (d). White dashed lines indicate waveguide flange perimeters; (e) Simulated dielectric constant and loss factor as function of $tan\delta$ with clamped method and NRW/BJ compared to reference values..... 104

Figure 4.3: Schematic of the two-port completely-filled waveguide method, showing a rectangular waveguide filled with a homogeneous dielectric sheet with planar dimensions equal to the waveguide cross-section..... 105

Figure 4.4: Diagram of the two-port plug-loaded completely-filled waveguide technique. 107

Figure 4.5: (a) Simulated dielectric constant and loss factor of ideal case model and clamped method; (b) error (%) in dielectric constant and loss factor of ideal case model and clamped method; (c) error (%) in dielectric constant and loss factor as function of sample thickness (materials are indicated with numbers reported in Table 4.1). 109

Figure 4.6: Error in $\varepsilon r'$ with fixed loss factor and thickness ($\varepsilon r'' = 0.5$, 5 and 40, t = 2 mm). 112

Figure 4.7: Error in loss factor with fixed dielectric constant and thickness ($\varepsilon r' = 2$, 10, 20 and 30, t = 2 mm). 113

Figure 4.8: Error in dielectric constant and loss factor as function of thickness for fixed $\varepsilon r = 12.9$..... 114

Figure 4.9: Error in dielectric constant and loss factor as function of horizontal and vertical misalignment of waveguides..... 115

Figure 4.10: Horizontal (dx) and vertical (dy) misalignment of waveguides and their flanges..... 115

Figure 4.11: Measured dielectric constant (a) and loss factor, (b) with loaded and clamped transmission line, (c) and error in loss factor for clamped waveguide method. 117

Figure 4.12: Simulated [S] and measured [M] permittivities for completely-filled and clamped waveguide method for CFRP sample with $t = 0.35$ mm..... 119

Figure 4.13: Error as function of sample thickness. 120

Figure 4.14: Error in dielectric constant and loss factor calculations as function of waveguide horizontal (d_x), and vertical misalignment (d_y). 121

Figure 4.15: Dielectric constant and loss factor for simulations [S] and measured data [M] as function of $tan\delta$. 122

Figure 5.1: Simulation methodology for the mesoscale CFRP1 composite, inserted inside a WR90 waveguide: a) T800 carbon fibres, b) Simulated CFRP1 model inside a rectangular waveguide and c) particular of CFRP1 model with elliptical yarns (blue) and epoxy region (light green)..... 126

Figure 5.2: Propagation of $TE10$ in an empty WR-90 waveguide at 10.3 GHz: a) electric field pattern; b) **E** plotted on y-z cross-section; c) magnetic field pattern; d) **H** plotted on x-z cross-section..... 127

Figure 5.3: Parallel polarization models. WR-90 used for X-band simulations and WR-62 used for Ku-band simulations. **E** on port 1 is polarized along y and yarns are oriented along y. Material simulated: CFRP1..... 128

Figure 5.4: $S11$ and $S21$ calculated for CFRP1 over frequency range (8.2 to 18 GHz)..... 129

Figure 5.5: a) Electric field pattern; b) Electric field vector plotted on y-z cross-section; c) Magnetic field pattern; d) Magnetic field vector plotted on x-z cross-section. The fields are calculated at 10.3 GHz. 129

Figure 5.6: Reflection and transmission coefficient over frequency for $\sigma = 60000$, 70000, 100000 and 1200000 S/m. 130

Figure 5.7: Reflection and transmission coefficient over frequency for yarn width = 2.2, 2.4, 2.6 and 2.8 mm..... 131

Figure 5.8: Fibre volume fraction as function of yarn spacing [208]. 132

Figure 5.9: Reflection and transmission coefficient over frequency for p = 0.15, 0.25, 0.3, 0.35 and 0.5 mm..... 133

Figure 5.10: Reflection and transmission coefficient over frequency for $tyarn = 0.10$, 0.15 and 0.20 mm..... 134

Figure 5.11: Power elliptical shapes for different exponents n: a) lenticular shape with n = 2, 3 and 6, b) n = 0.3, 0.6 and 0.9. 135

Figure 5.12: Reflection and transmission coefficient over frequency for n = 1, 2, 3 and 6. 136

Figure 5.13: Reflection and transmission coefficient over frequency for n = 0.3, 0.6, 0.9 and 1. 137

Figure 5.14: Magnetic field distribution at X-band between two consecutive yarns plotted on x-z plane for n = 1, 2, 3 and 6. 138

Figure 5.15: Perpendicular polarization models for WR-90 and WR-62. **E** on Port 1 is polarized along y and yarns are oriented along x. Material simulated: CFRP1. 138

Figure 5.16: $S11$ and $S21$ calculated for CFRP1 with perpendicular polarization. 139

Figure 5.17: a) Electric field pattern; b) Electric field vector plotted on y-z cross-section; c) Magnetic field pattern; d) Magnetic field vector plotted on x-z cross-section. The fields are calculated at 10.3 GHz. 140

Figure 5.18: Electric field vector plotted on y-z plane at 10.3 GHz. 140

Figure 5.19: Reflection and transmission coefficient over frequency for $\sigma =$ 60000, 70000, 100000 and 1200000 S/m. 141

Figure 5.20: Reflection and transmission coefficient over frequency for yarn width = 2.2, 2.4, 2.6 and 2.8 mm. 142

Figure 5.21: Reflection and transmission coefficient over frequency for p = 0.15, 0.25, 0.3, 0.35 and 0.5 mm. 144

Figure 5.22: Reflection and transmission coefficient over frequency for $tyarn =$ 0.10, 0.15 and 0.20 mm. 145

Figure 5.23: Reflection and transmission coefficient over frequency for n = 0.3, 0.6, 0.9 and 1. 146

Figure 5.24: Reflection and transmission coefficient over frequency for n = 1, 2, 3 and 6. 147

Figure 5.25: Electric field vector plotted on y-z plane at 10.3 GHz for lenticular yarn cross-section with for n = 3. 148

Figure 5.26: (a) MUT cross section with fibres parallel to the electric field, and (b) MUT cross section with fibres perpendicular to the electric field. 149

Figure 5.27: Geometry of the measurement setup for: (a) the two-port plug loaded transmission line method, and (b) clamped waveguide method. 149

Figure 5.28: (a) Waterjet cutting process with composites in place, (b) example of plug-loaded line setup for WR62, (c) picture of shifts used for measurement at Ku-band on the left and X-band on the right, particular of red plug inserted in Ku-band shift; (d) CFRP1 samples for X-band waveguide (WR90) with fibres aligned along x-axis. 150

Figure 5.29: Average values of $S11$ and $S21$ over 8.2-18 GHz for perpendicular polarization measured with Method 1. 151

Figure 5.30: $S11$ and $S21$ measured for each sample in red and their average values over 8.2-12.4 GHz for parallel polarization with Method 1..... 151

Figure 5.31: Average values of $S11$ and $S21$ over 8.2-18 GHz for perpendicular polarization measured with Method 2..... 153

Figure 5.32: Average values of $S11$ and $S21$ over 8.2-18 GHz for parallel polarization measured with Method 2..... 154

Figure 5.33: Dielectric constant and loss factor as function of thickness for Method 1 and Method 2. *M1 = Method 1 and M2 = Method 2..... 155

Figure 5.34: Dielectric constant and loss factor as function of frequency for Method 2. The loss factor is plotted with the negative sign. 156

Figure 5.35: Simulated [S] and measured [M2] scattering parameters in perpendicular polarization for Method 2: (a) CFRP1, (b) CFRP2 and (c) CFRP3. *M2 = Method 2..... 160

Figure 5.36: Simulated [S] and measured [M2] $S21$ in parallel polarization for Method 2 at X-band and Ku-band..... 162

Figure 5.37: Simulated [S] and measured [M2] scattering parameters with electric field parallel to fibre axis for CFRP1. 163

Figure 5.38: Simulated yarns in epoxy resin for CFRP2 model. 164

Figure 5.39: Simulated [S] and measured [M2] scattering parameters with electric field parallel to fibre axis for CFRP2. 165

Figure 5.40: Simulated [S] and measured [M2] scattering parameters with electric field perpendicular to fibre axis for CFRP1. 165

Figure 5.41: Simulated [S] and measured [M2] scattering parameters with electric field perpendicular to fibre axis for CFRP2. 166

Figure 6.1: Free-space measurement system. 168

Figure 6.2: LB-28-20-C horn antenna with 2.4 mm female output and L type mounting bracket..... 168

Figure 6.3: CAD for: (a) antenna base support; (b) specimen holder support. 169

Figure 6.4: 50 mm travel linear translation stage with side mounted micrometer..... 169

Figure 6.5: CAD for specimen support holder and junction to rotation stage. 170

Figure 6.6: CFRP samples. C3 unidirectional fibres are directed long y-axis. 170

Figure 6.7: Measured S-parameters at X-band for C1 and C2..... 171

Figure 6.8: Measured S-parameters at X-band for C3 with different polarizations..... 172

Figure 6.9: TRL error model [148]. 173

Figure 6.10: Schematic of experimental setup. 176

Figure 6.11: Reflection and transmission coefficient after TRL calibration and unloaded line. 177

Figure 6.12: Reflection and transmission coefficients for C1 and C2 samples in vertical and horizontal polarization. 177

Figure 6.13: Reflection and transmission coefficient for C3 samples in vertical and polarization. 178

Figure 6.14: Reflection and transmission coefficients for healthy area of C3 sample in horizontal polarization. 179

Figure 6.15: Reflection coefficients for healthy and damaged area of C3 sample in horizontal polarization. 180

Figure 6.16: Transmission coefficients for healthy and damaged area of C3 sample in horizontal polarization. 181

Figure 6.17: C3 permittivity estimation with free-space method. 183

Figure 6.18: Carbon fibre fabric with in-plane waviness. 184

Figure 6.19: Free-space model used to calculate the S- parameter S21. 184

Figure 6.20: Comparison of the simulated transmission coefficient of damaged models with undamaged case, over 27-32 GHz. 186

Figure 6.21: Comparison of measured [M] and simulated [S] transmission coefficient. 186

Figure 6.22: Comparison of the simulated three damage case (indentation, delamination and surface defect) with undamaged case, in presence of systematic errors. 187

Figure 6.23: Comparison of healthy structure and free-edge delamination damage (27-32 GHz). 188

Figure 6.24: Comparison of average measured data of healthy structure and free-edge delamination damage (27-32 GHz). 188

Figure 6.25: Pre and post processed data with k-means (28.7-29.2 GHz). 189

Figure 6.26: Comparison of healthy structure and free-edge delamination damage (28.7-29.2 GHz). 190

Figure 6.27: Comparison of healthy structure and free-edge delamination damage in terms of signal energy. 191

Figure 7.1: Schematic of a four-port dual polarized probe. 194

Figure 7.2: Dual linearly polarized probe illuminating a 2D target of interest. The blue arrows show the direction of the irradiating electric field Ei in case of vertical polarization, the red arrows in case of horizontal polarization. 195

Figure 7.3: Dual polarized probe scanning the sample under test at stand-off distance $z0$. 197

Figure 7.4: SAR ω–k algorithm used. 199

Figure 7.5: Carbon fibre ribbon with in-plane waviness ($20°$ rotation), fixed on an aluminium plate. 200

Figure 7.6: Raw measurement of SVH for carbon unidirectional ribbon with in-plane waviness. 201

Figure 7.7: Normalized S-parameters magnitude SAR images of the carbon unidirectional ribbon with waviness. 202

Figure 7.8: Phase (degrees), real part and imaginary part of SVH SAR images. 203

Figure 7.9: Normalized magnitude, phase in degrees, real part and imaginary part of SVH as function of x at y = 46 mm. 203

Figure 7.10: Polarimetric SAR image. The orientation of the fibres (in degrees) is represented in the form of a colored image and indicates the angle between the fibres direction and y-axis. 204

Figure 7.11: Carbon fibre fabric with in-plane waviness, ($\pm 25°$ rotation). 205

Figure 7.12: (a) Normalized magnitude and (b) imaginary part of SVH. 206

Figure 7.13: SAR image depicting the orientation of the fibres (in degrees) relative to y-axis. 206

Figure 7.14: Carbon fibre fabric with wrong fibre orientation in the area highlighted in red for: (a) 1 layer of fabric, (b) 2 layers of fabric. 207

Figure 7.15: : Normalized magnitude of SVH for: (a) 1 layer of fabric, (b) 2 layers of fabric. 208

Figure 7.16: SAR images depicting the orientation of the fibres (in degrees) relative to y-axis. 208

Figure 7.17: (a) sample with overlap, (b) SVH SAR image and (c) SAR image depicting the orientation of the fibres (in degrees) relative to y-axis. 209

Figure 7.18: Samples with implemented common manufacturing defects that occur during AFP/ATL, such as gaps, overlaps, missing tow, fibre misalignment. 209

Figure 7.19: Normalized magnitude SAR images of $SLin$ coefficients. 210

Figure 7.20: Normalized magnitude SAR images of $SCirc$ coefficients. 211

Figure 7.21: Carbon fabric sample with implemented missing tow, inclusion and gap. 212

Figure 7.22: Carbon fabric sample with implemented in-plane fibre waviness on the 1st layer oriented along $0°$, and covered by 2nd layer stacked at $90°$. 212

Figure 7.23: S-parameters of interest for the characterization of gaps and missing tow. 213

Figure 7.24: Normalized SVH and SHV magnitude SAR image. 214

Figure 7.25: SAR image of interest for the characterization of embedded in-plane waviness. 214

Figure 7.26: SAR images of interest for the characterization of embedded PTFE patch inside a CFRP with discontinuous fibres. 215

Figure 7.27: Normalized magnitude and phase of SHH and SRR for CFRP with discontinuous fibres. 216

Figure 7.28: Normalized magnitude and real part of SVV and SRL for CFRP with unidirectional continuous fibres. 217

Figure 7.29: Phase of SVV and SRL for CFRP with unidirectional continuous fibres. 217

Figure 7.30: CFRP unidirectional fabric sample with out-of-plane fibre waviness. 218

Figure 7.31: SAR images of out-of-plane fibre waviness. 219

Chapter 1

Introduction

1.1 CFRP materials

The union of several components leads to a new material that can enhance the properties of its individual constituents, mitigating at the same time less desirable effects. Here lies the idea behind the production of composite materials, a relatively new family of materials, characterized by lighter weight and greater strength and defined by a combination of a matrix (polymer) and a reinforcement (fibres).

When the reinforcement is made of carbon fibres, the composite material is commonly defined as Carbon-fibre-reinforced polymer (CFRP). Unlike isotropic materials like steel and aluminium, CFRP has directional physical and chemical properties, which depend on the layouts of the carbon fibre and the proportion of the carbon fibres relative to the polymer [1]. Among their distinguishing features, CFRPs are able to provide high specific stiffness, fatigue resistance, corrosion resistance, dimensional and alignment stability, and capability to be formed into large complex shapes [2]. Therefore, CFRP has become a notable material in all those applications that require high strength-to-weight ratio and stiffness, such as structural engineering applications, automotive (e.g., high-end automobile racing), superstructures of ships and aerospace [3]–[5].

Particularly in the aerospace domain, the use of CFRP composites has progressed even more in recent years. Leading commercial aircraft, such as the Boeing 787 Dreamliner and the Airbus A350 XWB, make greater use of carbon fibre composites to build their aircraft bodies, as they increase fuel efficiency, improve aerodynamic performance and reduce the costs in the number of parts needed to build the plane (see

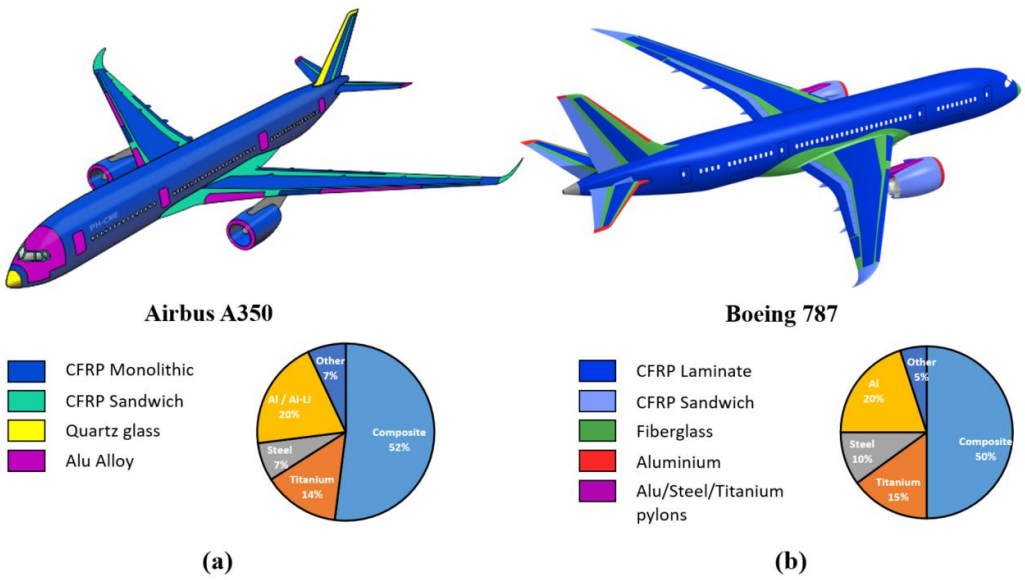


Figure 1.1: CFRP parts of Airbus A350 (a) and Dreamliner Boeing 787 (b).

Figure 1.1). Therefore, structural components of aircraft and helicopters such as frames, fuselage, rotor blades, cowling, control surfaces, wing skins, leading edge and trailing edge panels are made of carbon fibre composites [6]. In space applications, CFRP composites are used for bus structures, solar panels, booms, tube, trusses and antenna struts, which use a combination of metal matrix composites and polymeric matrix composites [7]–[9].

1.1.1 Carbon fibres

Table 1.1: Conventional carbon fibre reinforcements for aerospace applications [2], [10].

Carbon Fibre	**Diameter [µm]**	**Density [g/cm^3]**	**Modulus [GPa]**	**Strength [GPa]**	**T_{max} [°C]**
Standard Modulus (high strength)	7	1.77-1.80	220-240	3.0-3.5	> 1500
Intermediate modulus	7	1.77-1.81	270-300	5.4-5.7	> 1500
High modulus	6.5	1.77-1.80	390-450	2.8-4.5	> 1500
Ultra high strength	-	1.80-1.82	290-310	7.0-7.5	-

The primary element of CFRP is the carbon filament. This is obtained from a polymer precursor such as polyacrylonitrile (PAN), rayon, or petroleum pitch. The precursor is first spun into filament yarns, using chemical and mechanical processes. After drawing or spinning, the polymer filament yarns are then heated to drive off non-carbon atoms (carbonization), producing the final carbon fibre [10]. Carbon filaments have diameter of about 5 to 10 micrometres and are bundled together to form a tow made of several thousand carbon fibres. The yarns may be further treated to improve handling qualities and then wound onto bobbins. From these yarns, unidirectional (UD) sheets are

created. However, they can also be woven into fabric sheets according to different textile patterns (i.e., twill weave, satin weave, basket weave), for applications where more than one fibre orientation is required [11]. The most common carbon reinforcing fibres used in aerospace applications are listed in Table 1.

1.1.2 Matrix

To provide support and stability to the reinforcements, organic matrices are commonly employed. The binding polymers can be classified into two main groups, thermoset and thermoplastic (i.e., according to their curing process), and include resins such as epoxy, polyester, vinyl ester, polycarbonate and nylon as shown in Table 1.2. Nonetheless, the preferred choice is often a thermoset resin such as epoxy. Epoxy resin can be used at moderately high temperatures until $\simeq 170℃$, can be polymerized in several formulations and offer good storage stability in prepregs, low shrinkage (2-3%), high adhesion, heat and corrosion resistance, and good mechanical strength [12].

Table 1.2: Properties of commonly used matrices in aerospace [2], [10].

Matrix	**Density [g/cm^3]**	**Elastic Modulus [GPa]**	**Tensile Strength [MPa]**	**T_{max} [°C]**
Thermosets				
Epoxy	1.1-1.4	2.7-5.5	40-85	90 to 200
Phenolic	1.2-1.4	2.7-4.1	35-60	120 to 200
Polyester	1.1-1.4	1.3-4.1	40-85	60 to 200
Polyimide	1.4	4.0-19.0	70	250 to 300
Thermoplastics				
Polyphenylene sulfide (PPS)	1.3-1.7	4.0	75-190	130 to 250
Polyether-etherketone (PEEK)	1.3-1.5	4.0	97-200	140 to 250
Polycarbonate	1.1-1.2	2.0	28-51	130 to 221
Nylon	1-1.2	3.7	39-93	80 to 200

1.1.3 Manufacture

One of the most common forms of CFRP used in aerospace is the laminate, made of layered sheets according to a quasi-isotropic layup. The carbon fibre sheets, unidirectional or woven, are pre-impregnated with an uncured epoxy or other thermosetting polymer (i.e., prepregs), and the layup sequence is tailored to achieve the desired strength and stiffness properties. The layup can be unidirectional, symmetric respect to the mid-plane of the laminate, or balanced when for each lamina stacked at $+x$ there is a lamina at $-x$, as shown in Figure 1.2 [13].

To manufacture a specific CFRP part, the prepreg sheets can be layered into a mold in the shape of the final product (Molding). This process can also be realized using preformed carbon fibre cloth placed in the mold. The mold is then closed and a liquid thermoset resin is injected (Liquid Composite Molding - LCM) [14], [15]. To enhance

the resin flow speed and the fiber volume fraction, as well as reducing the mold filling time, compression can be incorporated into the process (Resin Transfer/Compression Molding-RT/CM) [16]. This process consists of heating the thermoset resin, under severe pressure, within the closed mold cavity until the resin cures. The resin liquefies and flows, taking the shape of the mold cavity, and then hardens into the desired product [16].

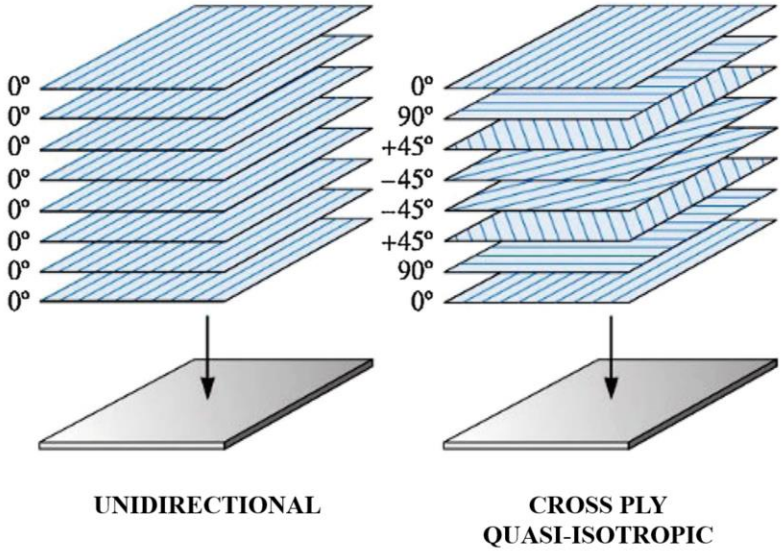


Figure 1.2: Examples of ply sequence for a laminated composite [13].

The layup placement process can be performed manually, which is time consuming and labour intensive and leads to a low production volume of composite structures. To overcome these problems, robust and fast automated placement techniques have been implemented, such as automated fibre placement (AFP) and automated tape laying (ATL). The automated process provides accuracy, repeatability and on site consolidation of thermoplastic composites with high throughputs. Unidirectional pre-impregnated tows or tapes are fed down to the top surface of the previously placed layers (substrate). After the deposition, the resulting product of tape/tow and substrate is then heated and pressed by a compaction device (e.g., roller), to create a bonded composite laminate of the desired shape. Automated placement machines are capable of producing flat laminates, panels with mild curvatures, and three-dimensional surfaces (e.g., wing skins, fuselage structures, frames) [17]. For more complex and particularly convoluted shapes, a filament or tape winding method can be used instead, which involves winding filaments under tension over a rotating mandrel [18].

1.2 Defects types and damage in composite materials

Unlike metals, composite materials present non-homogeneity and anisotropy or eventually orthotropic behaviour. The damage propagation is diffused and progressive

instead of being confined to a single macrofracture and involves different modes of failures such as fibre breakages and matrix transverse cracking (i.e., intralaminar damage) or delamination of two consecutive layers (i.e., interlaminar damage) [19]. The failure process is often triggered by the presence of small defects and flaws embedded in the composite structure, whose formation can arise either during in life service of the structures/components or even during the above-mentioned manufacturing processes.

Defects that occur during service life can be caused by non-intentional overloads, impact damage, fatigue damage etc. Environmental factors such as, high temperatures, chemicals, electrochemical problems increase the development of damage inside composite structures. Most important defects or damage causes are:

- Impact damage of foreign objects;
- Low-velocity impact damage;
- Holes;
- Ply delamination;
- Fatigue;
- Surface and internal cuts;
- Skin/core debond.

On the other hand, manufacturing induced defects depend on the particular manufacturing method used and commonly originate from lack in the process control, specifically on control parameters as pressure, temperature, etc., or from machine tools inadequate handling, erroneous understanding of the current legislation, incorrect design of the manufacturing equipment and human factor. The frequency and the size of defects may change with the particular process cycle. As topic of interest for the work presented in this thesis, a brief description of the most common manufacturing induced defects is presented here below. Their detailed description can be found in [20], [21].

1.2.1 Porosity

When using Liquid Composite Molding, one of the main difficulties is to avoid the formation of voids in the matrix post-cure. This phenomenon is called porosity, and is caused by the trapped air or volatile gas that is released during an incorrect curing process, as shown in Figure 1.3. Contributing factors are represented by non-optimal choice of curing parameters such as duration, temperature, pressure or resin flow speed. If porosity levels are critical, the mechanical performances of the structure can be affected (e.g., interlaminar shear stress).

1.2.2 Foreign bodies

One of the major concerns during layup process of prepregs is the accidental occurrence of inclusion of foreign bodies such as release film, backup film, greasy marks from fingers or fuzzballs (i.e., frayed fibre material, usually at the edges of a narrow tow). These inclusions may go unnoticed, as they can be very thin and difficult to differentiate from the substrate material. Therefore, foreign bodies can affect the quality of both prepreg and laminate and lead to delamination or disbonds during the service life of the component.

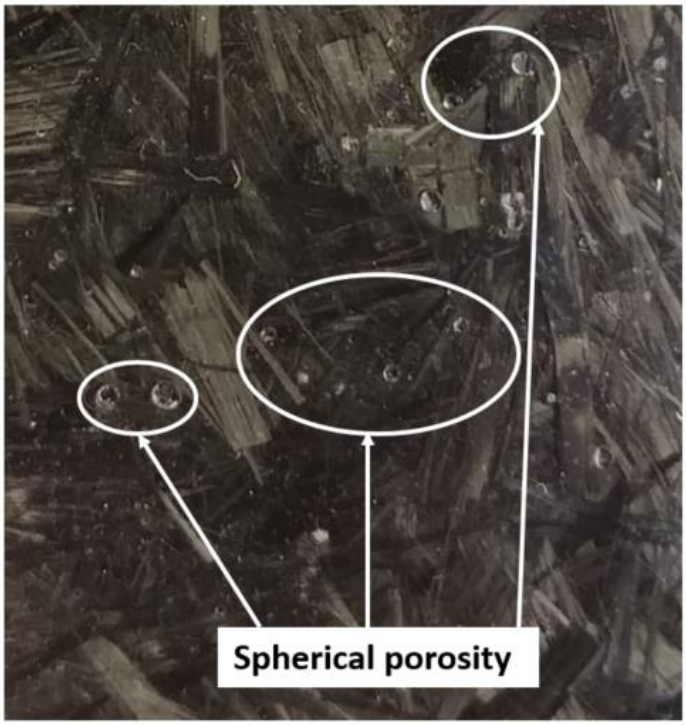


Figure 1.3: Spherical porosity in a CFRP sample.

1.2.3 Fibre or ply misalignment.

Automated fibre/tape deposition may cause manufacturing imperfections induced by incorrect alignment of fibre/ply. This phenomenon is referred as fibre or ply misalignment and is mainly induced by speed and inertia effects of the ATL/AFP robot under load. These kinematic effects reduce the positioning accuracy of the layup, and consequently, the fibres deviate from the original path and can no longer be precisely positioned. Additionally, the process of setting them again to the right path leads to fibre straightening. Secondary phenomena of fibre/ply misalignments are gaps and overlaps between adjacent tows, missing tow, twists and fibre wrinkling (see Figure 1.4).

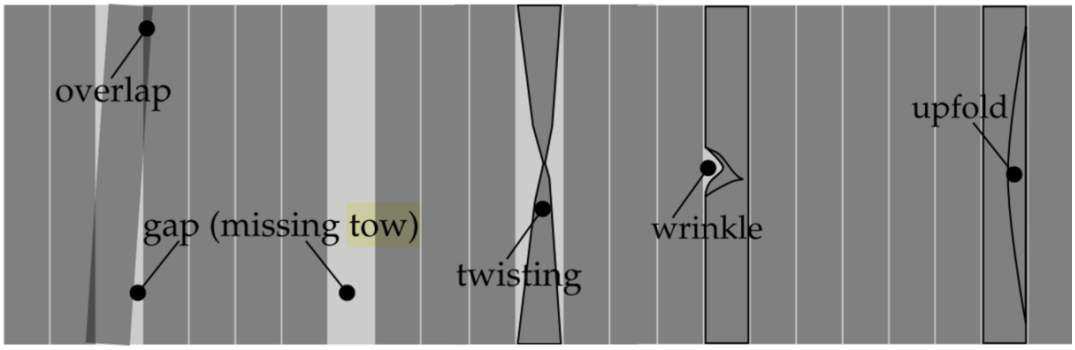


Figure 1.4: From left to right, schematic of overlap, gap, missing tow, twisted tow, wrinkled and an upfolded tow within a ply [22].

Gaps, overlaps and missing tow

These imperfections occur frequently during ATL/AFP process and are influenced by the quality of the material, the machine parameters and the geometry of the manufactured part. More the geometry is complex more the fibre course will vary from the original path, leading to the formation of transition zones of gaps and overlaps. These transitions in turn can promote fibre angle deviations and fibre waviness. According to the dimension of a gap or overlap, out-of-plane fibre waviness may occur in adjacent plies. In addition, resin can accumulate within a gap creating resin pockets and resin rich areas. Therefore, the laminate mechanical properties may be negatively affected, such as reduction in strength under compression [23], [24].

Twisted tow

The movement of the AFP machine along the fibre placement path is the main cause for twisting of tows. Specifically, changes in width of the tow produce sideways movements in the guiding system resulting in a flip over of individual tows. Gaps arise in proximity of the twisted tow with all the consequences previously descripted (i.e., fibre waviness, resin rich areas, altered strength properties).

Fibre wrinkling

Failed adhesion to the substrate during the layup process can result in fibre wrinkling or fold up. Also in this case, a wrinkle or fold up can cause out-of-plane fibre waviness with consequent effects on the material strength and stiffness.

1.2.4 Fibre waviness

Often a consequence of other primary imperfections incorporated in the laminate such as foreign bodies and misalignment, this defect can be also inherent to textile composites (i.e., woven architecture) and generally occurs in two main forms, in-plane and out-of-plane waviness. As indicated by their definition, in-plane fibre waviness refers to the deviation of the fibres from the normal fibre direction in the lamina plane (i.e., in the ply), while, bending of a single or multiple fibre separated from the lamina plane is known as out-of-plane waviness.

In-plane waviness is mostly caused by the temperature gradient and the compression during the manufacturing process. In the first case, the different thermal expansion coefficient in the lamina plane produces thermoelastic distortions (i.e., residual thermal stresses) which lead to fibre waviness. In the second case, for components manufactured by Resin Transfer/Compression Molding, the fibre waviness is produced by the dry fibres sliding because of an excess of resin under pressure [25].

Out-of-plane waviness can also be due to thermoelastic distortions through the thickness of the laminate and external compression (i.e., rise in compaction increases friction, which creates out-of-plane waviness). However, as previously mentioned, misalignment of prepreg and wrinkling can also be listed among the main causes of fibre waviness out of the lamina plane [21], [26].

1.3 Non-destructive testing for composite materials

As mentioned in Section 1.2, failure in composite materials is often triggered by the presence of defects and flaws and evolves progressively according to the type of damage propagation that can be classified in two main categories:

- Intra-laminar damage (i.e., matrix transverse cracking, fibre-matrix debonding or fibre fracture under tension or compression);
- Inter-laminar damage (i.e., delamination of two consecutive layers).

Therefore, describing the behaviour of composites and predicting the damage evolution can be difficult due to their complexities. Consequently, the increasing use of composites for aerospace applications requires a parallel use of Non Destructive Testing (NDT) methods to ensure a high degree of reliability and safety, both during the manufacture and in service life of the components. The purpose of non-destructive controls is to verify the quality state of a structure without producing damages or fractures or any significant change in the structure itself. These examinations can be performed at the end of the manufacturing process to verify the compliance of the final products, or during in line and base maintenance for preventive damage detection [27],

[28]. A brief description of the most common techniques employed in aerospace NDT is presented below, their detailed description can be found in [29]–[32].

Visual inspection

Visual inspection consists of the direct observation of the inspected area in bright light with the naked eye or by using a magnifying glass or a mirror. Although it is the cheapest method, which constitutes around 80% of performed inspections, the detection capability is limited to surface defects, which are big enough to be visually identified. In addition, albeit qualified personnel is required, this method is subjected to possible misinterpretation of flaws due to human factor errors.

Liquid penetrant inspection

The penetrant inspection method is based on the application of a liquid penetrant (paint, fluorescent dye) to a thoroughly cleaned surface of the sample where it enters and fills any defects open to the surface. After the excess penetrant is removed and the surface is dried, the application of the developer draws out the dye to reveal the presence of the flaws.

Magnetic particle inspection

Magnetic particle inspection requires ferromagnetic materials and magnetisation of the test part. The ferromagnetic particles applied to the surface of the magnetised test component become trapped in the areas of the magnetic flux leakage produced by the flaw. The shape and location of the near-surface defects is indicated with this method, including detection of flaws not open to the surface. Surface cleaning and visual observations are required as well as the demagnetisation of the inspected component after the test.

Eddy currents

This method requires electrically-conducting samples and can be used to detect surface and sub-surface defects, and can operate through coatings. The alternating current in the coil of the probe produces a changing magnetic field that, when placed in close proximity to the sample, induces the circular flow of eddy currents on and below the surface. The interaction of the secondary magnetic field produced by the eddy currents with the field of the probe changes the impedance of the coil and can be measured as a change of voltage. The presence of the defects interrupts the flow of eddy currents

affecting the measured output. This method does not require surface preparation and can be non-contact. An advantage is represented by their fast application, useful for inspecting in line and semi-finished products. The inspection results can be real time, making it a method of interesting application for example in the chain of production of conductive composites materials. The challenge represented by composites materials for this type on technique is due to their conductivity, inferior to the one of metals. For instance, their conductivity is lower than that of brass by a factor of about 10^4 to 10^5. In addition, their conductivity is anisotropic, and using of eddy currents for CFRP materials requires specific probes which are suitable for detection of defects in CFRP and signal processing [33].

Radiography

The radiographic techniques are based on the differential absorption of penetrating γ- or X-ray radiation in the sample or their assembly. The differences in thickness, density, shapes and absorption characteristics are displayed as a variation of contrast in the image created by the unabsorbed radiation that passes through the part. It is an expensive method with associated health hazards. It is used predominantly to detect cracks but not planar defects. The use of computed tomography produces cross-sectional sample views, which allows the location and measurement of flaws within the structure independent of their orientation.

Ultrasonic techniques

Ultrasonic testing consists of observation and analysis of the transmitted or reflected high-frequency sound waves originated in or sent through a structure. The changes experienced by the propagating wave and observed in the detected signal are indicative of the material condition and discontinuities present in the propagation medium. This is a very versatile method without specific requirements to the material properties or surface condition. It can be used for the inspection of surface and bulk material, including detection of flaws, dimensional measurements and material characterisation. The conventional techniques require a good contact with the sample and the use of couplants such as oil or gel to introduce the wave into the structure.

Thermography

The thermal and infrared methods are based on obtaining an image of the temperature distribution on the surface of the test part (in a steady state) or the measurement of the infrared emission from the surface when a temperature gradient is created by the

application of a pulsed heat source. The presence of the defects is indicated by the non-uniformities in the detected distributions.

Shearography

Also known as speckle pattern shearing interferometry, this laser optical technique works through the application of a load (e.g., thermal, vacuum-ambient, vibration-mechanical excitation) to the structure, and then a laser shearography sensor to observe minimal surface bending in the form of an out-of-plane strain field, and subsequently image the measurement as a phase map.

Acoustic emission (AE)

This method is based on the mechanical vibration arising from damage events, the circular stress waves generated by these defects are detected by an array of piezoelectric sensors at ultrasonic frequencies. Acousto-ultrasonics, a combination of ultrasounds and AE and advanced form of AE, utilises active transducers to stress the structure, in this way the energy of the signal and the excited wave modes allow to analyse internal imperfections and inhomogeneity.

1.4 The drive to use microwave NDT

Among the NDT techniques just mentioned in Section 1.3, the most suitable for carbon fibre composites are ultrasonic inspections, acoustic emission, thermography, radiography and shearography, as they allow analysts to detect internal cracking and other flaws indication on a volumetric level. These methods have been widely applied to detect state of cure, porosity, presence of moisture, voids, inclusions, fibre waviness, debonding, delamination and cracking [34], to name a few. Ultrasonic testing is widely used, due to its capability to obtain good results. However, the necessity of a coupling agent between probe and structure prevents the investigation of big areas and introduces the need for a contact between probe and structure [35]. Acoustic emission and acousto-ultrasonics techniques require attached or embedded transducers and mandatory pre-calculations. Nonetheless, they have been proved not useful to detect individual large flaws such as delamination or voids [36]. Thermography testing requires expensive instrumentation and qualified inspectors. However, when the defect is internal to the structure, the capability to detect heat fluctuation is reduced [36]. Classic radiography techniques allow to inspect mostly thin laminates from 1 mm to 5 mm of thicknesses, precluding volumetric inspections, while, for tomography and more advanced radiography methods, the necessity to disassemble the components for

testing purposes makes them non-practical [36], [37]. Shearography is less susceptible to noise compared with other methods, however while it can be applied to thin skinned composites, the same is not true for detection of buried defects and for the characterization of defect types other than delamination [36], [37]. Thus, it seems clear there is a need to use more than one of these inspection methods together to obtain a comprehensive analysis of the overall structure. As each one of them has their own strength and shortcoming.

A new group of inspection techniques that is still under development is represented by methods that exploit the electrical properties of the materials (i.e., electrical conductivity, relative permittivity). These methods are commonly defined as microwave non-destructive testing (MNDT) techniques and use electromagnetic waves, which are sent from a transmitting antenna to the tested material in microwave and millimetre wave regime (300 MHz to 300 GHz). The portion of the signal reflected and/or transmitted to a receiver is analysed in order to evaluate structural flaws [38]. These methods may be the answer to the aforementioned limitations of conventional NDT.

As a matter of fact, there are conditions in which conventional NDT are weak compared to this new family of inspection techniques. For example, during the automated deposition of fibre/tape, there is a need of real-time parameters acquisition. If manufacturing errors like fibre misalignment, waviness and inclusions can be detected to an early stage, it would be possible to correct the process or repair the incoming product, resulting in less rejects and material waste. However, conventional NDT methods such as ultrasound, AE, thermography or shearography requires not only solid-state material (i.e., for mechanical or thermal wave propagation and for deformation analyses), but also a coupling agent or transducers directly applied to the material. Thus, they become of difficult application in all those cases where a direct contact cannot be performed. Eddy currents can be non-contact and useful for in-line applications; however, they are restricted to conductive materials, while composites generally displays conductivity lower than metals and anisotropy. Conversely, Radio Frequency (RF) based solution offer a potential way to detect in-line structural integrity of dry multi-layered carbon textiles and wet and consolidated materials without coupling and high sensitivity.

Other advantages of microwave methods are the applicability to dielectric materials, which follows the trend in industry towards the replacements of metallic structures with non-metallic and lighter materials. As stated before, there is no need for contact between probe and tested object, thus useful for the analysis of high temperatures and moving components. They work easily in reflection and transmission configuration, the microwave testing systems are safe to use due to their low power

needs and it is possible to achieve real time applications and repetitiveness of measurements [39]. Typical application of radio frequency techniques connects changing of structures integrity with its complex permittivity. Through changing in permittivity, is it possible to assess fibre texture like orientations, gaps or undulations, fatigue, impact damage, corrosion in composites with metal reinforcements [39]. Dielectric properties of the material can be linked to density, porosity, state of cure, ageing, orientation, homogeneity and moisture content in dielectrics [34]. For all these reasons, MNDT and microwave characterization are a becoming competitive among the non-destructive evaluation techniques and may be the only viable solution or can be used in combination with other methods to obtain a more comprehensive picture of an inspection problem [39]. A more extensive review of MNDT and microwave characterization will be provided in the next chapter.

1.5 Thesis objectives and layout

The purpose of this work is to explore microwave characterization and the applicability of MNDT methods for carbon fibre composites. Little has been written in literature about these techniques in regards to this particular group of materials. Issues arise from the difficulty to describe the electrical behaviour of CFRP, unlike for other composites (i.e., fiberglass) and dielectric materials. The cause lies of the absence of electromagnetic mixing formula models and reliable electromagnetic testing methods.

Hence, the thesis contains four main subjects:

- Measurement of shielding effectiveness of carbon fibre composites;
- Validation of a reliable measurement method for characterization of the complex permittivity in high-loss materials;
- Complex permittivity characterization;
- Damage identification.

The thesis structure is organised as follows. Chapter 2 provides a general background about the electromagnetic wave propagation theory, literature review on the electromagnetic characteristics of CFRP materials and microwave methods used for permittivity testing and damage testing.

The measurement of shielding effectiveness for CFRP sheets and carbon fabric is presented in Chapter 3.

Consequently, a waveguide-based measurement configuration is proposed, as a modification to the traditional completely-filled waveguide technique, for microwave characterization of relatively thin and high-loss materials in Chapter 4, followed by wideband permittivity measurements performed on unidirectional carbon fibre composite sheets in Chapter 5.

A free space method was adopted for high frequency and non-destructive measurements in Chapter 6.

Finally, defects in carbon fabric and carbon fibre laminates were identified using Synthetic Aperture Radar (SAR) imaging.

A quick visual layout of the project work can be found in Figure 1.5.

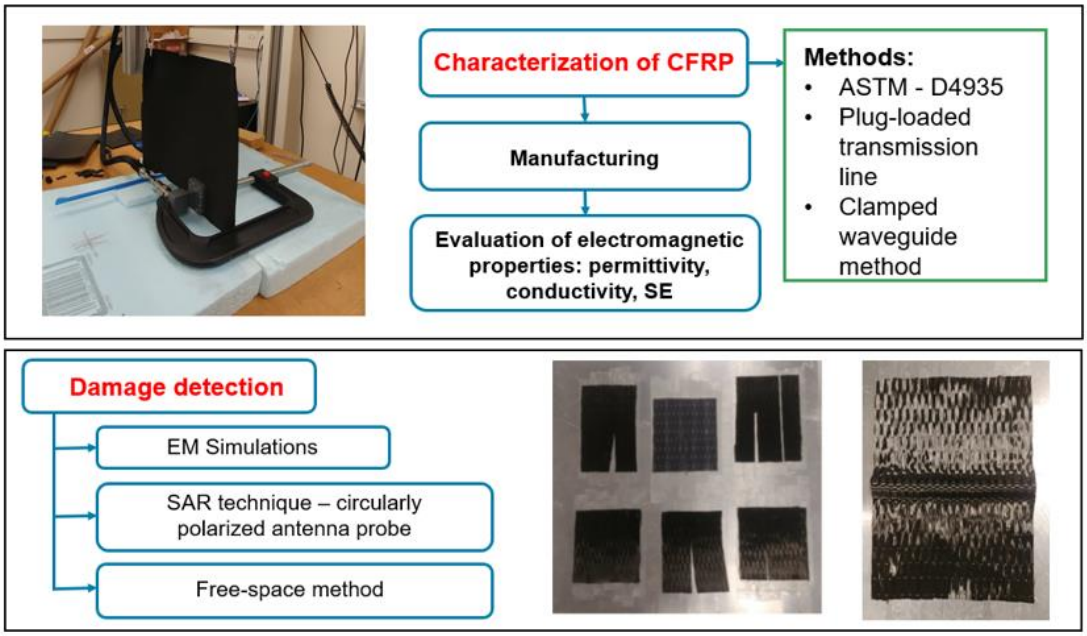


Figure 1.5: Project layout.

Chapter 2

Literature survey

2.1 Electromagnetic radiation

The radiation produced by an illuminating device, typically an antenna, can be sent towards a medium and the analysis of differences in phase, frequency and amplitude between transmitted and received signals provides an electromagnetic characterization of the medium through which the signal is transmitted, reflected or scattered [40]. In the following section, microwave and millimetre wave characterization methods and their application to non-destructive evaluation will be described, focusing on their use with CFRPs materials. First, a description of the electromagnetic wave theory is given to better understand the basic definitions and relationships between electromagnetic waves and materials. While a full derivation of the appropriate equations and their consequences is not required as part of this thesis, it is nonetheless useful to introduce a brief overview of the relevant theory and how it relates to the problem at hand.

2.1.1 Electromagnetic waves

When an electromagnetic field with waves propagates towards the surface of an object, the electronic state of the material is perturbed. The field causes movement in each individual electric charge, slightly changing its initial configuration. This movement causes polarisation of the entire region and generates an electric and sometimes a magnetic field in opposition to the applied field. This internal field can either repel the applied field from penetrating the material (e.g., conductors), partially allow a portion of the field to pass through the material, or it can allow the radiation to pass through with almost no loss (e.g., dielectrics). This behaviour is dependent upon the

electromagnetic properties of the materials and material-specific parameters have been designed to give an indication of how the material will respond to an applied radiation (i.e., electrical permittivity, electrical conductivity).

Considering the electromagnetic field time harmonic with the variation represented by $e^{i\omega t}$, the Maxwell's equations [41], [42] can be written in the frequency domain as:

$$\nabla \cdot \mathbf{D} = q_{ev} \tag{2.1}$$

$$\nabla \cdot \mathbf{B} = q_{mv} \tag{2.2}$$

$$\nabla \times \mathbf{E} = -\mathbf{K}_{\mathrm{i}} - i\omega\mathbf{B} \tag{2.3}$$

$$\nabla \times \mathbf{H} = \mathbf{J}_{\mathrm{i}} + \mathbf{J}_{\mathrm{c}} + i\omega\mathbf{D} \tag{2.4}$$

where **E** is the electric field intensity [V/m], **D** is the electric flux density [C/m^2], **H** is the magnetic field intensity [A/m], **B** is the magnetic flux density [Wb/m^2] or [T], $\mathbf{J}_{\mathrm{i}}$ is the impressed (source) electric current density [A/m^2], $\mathbf{J}_{\mathrm{c}}$ is the conduction electric current density [A/m^2], $\mathbf{K}_{\mathrm{i}}$ is the impressed magnetic current density [V/m^2], q_{ev} is the electric charge density [C/m^3], q_{mv} is the magnetic charge density [Wb/m^3], and ω is the angular frequency [rad/s]. The complex vectors are indicated in bold and are function of space and frequency.

D and **H** are respectively the electric and magnetic field when the radiation propagates through a material. A material subjected to the electromagnetic field is characterised by its complex constitutive parameters: permittivity ε [Farads/m], conductivity σ [Siemens/m], and permeability μ [Henries/m]. The constitutive parameters are a function of the field strength and direction, position and frequency of the applied field. Materials whose parameters are not functions of the applied field are called linear. If the response of a material is independent of the direction of the applied field, the material is known as isotropic. The properties of nearly all materials are frequency dependent. For linear isotropic materials the constitutive parameters can be expressed as a single complex number at a given frequency, and relate the electric and magnetic fields by the equations:

$$\mathbf{D} = \varepsilon\mathbf{E} \tag{2.5}$$

$$\mathbf{B} = \mu\mathbf{H} \tag{2.6}$$

$$\mathbf{J}_{\mathrm{c}} = \sigma\mathbf{E} \tag{2.7}$$

Substituting equation 2.5 in equation 2.6, the Ampère's circuital law can be rewritten as:

$$\begin{aligned}\nabla \times \mathbf{H} &= \mathbf{J}_\mathrm{i} + \sigma\mathbf{E} + i\omega\varepsilon\mathbf{E} \\ &= \mathbf{J}_\mathrm{i} + (\sigma + i\omega\varepsilon' + \omega\varepsilon'')\mathbf{E} \\ &= \mathbf{J}_\mathrm{i} + i\omega\varepsilon_e\mathbf{E}\end{aligned} \tag{2.8}$$

where the effective complex permittivity ε_e can be expressed by its real and imaginary components as:

$$\varepsilon_e = \varepsilon' - i\left(\varepsilon'' + \frac{\sigma}{\omega}\right) = \varepsilon_e' - i\varepsilon_e'' \tag{2.9}$$

with $\varepsilon_e' = \varepsilon'$ and $\varepsilon_e'' = \varepsilon'' + \frac{\sigma}{\omega}$.

The real part ε_e' or dielectric constant is related to the efficiency of the material to store the electrical energy, while the imaginary part ε_e'' or loss factor is linked to the energy losses within it. In particular, the imaginary part of the permittivity is related to the Joule effect losses through the electrical conductivity σ and to the losses due to dipoles orientation in the medium (i.e., relaxation time that dipoles employ to answer to the excitation of a driving force) through ε''.

The solutions to Maxwell's equations for any given field are in the form of a second order partial differential equation, usually referred to as the reduced wave equation. Considering an electromagnetic source free region ($\mathbf{J}_\mathrm{i} = q_{ev} = 0$ and $\mathbf{K}_\mathrm{i} = q_{mv} = 0$) and no currents ($\mathbf{J}_\mathrm{c} = 0$), Maxwell's equations for linear materials become:

$$\nabla \cdot \mathbf{D} = 0 \tag{2.10}$$

$$\nabla \cdot \mathbf{B} = 0 \tag{2.11}$$

$$\nabla \times \mathbf{E} = -i\omega\mathbf{B} \tag{2.12}$$

$$\nabla \times \mathbf{H} = i\omega\mathbf{D} \tag{2.13}$$

Considering the curl of equation 2.12 (i.e., Faraday's law of induction) and using equations 2.6 and 2.8, an equation with only **E** as variable can be obtained, which controls the space-time evolution of the electric field:

$$\begin{aligned}\nabla \times (\nabla \times \mathbf{E}) &= -i\omega\nabla \times \mathbf{B} \\ \nabla(\nabla \cdot \mathbf{E}) - \nabla^2\mathbf{E} &= -i\omega\mu\nabla \times \mathbf{H} \\ \nabla\left(\nabla \cdot \frac{\mathbf{D}}{\varepsilon}\right) - \nabla^2\mathbf{E} &= -i\omega\mu(i\omega\varepsilon_e\mathbf{E}) \\ \nabla^2\mathbf{E} &= -\omega^2\mu\varepsilon_e\mathbf{E} = \gamma^2\mathbf{E}\end{aligned} \tag{2.14}$$

The equation above has the form of a standard plane wave equation. A similar expression can be derived for the magnetic field, using the curl of equation 2.13:

$$\nabla^2\mathbf{H} = -\omega^2\mu\varepsilon_e\mathbf{H} = \gamma^2\mathbf{H} \tag{2.15}$$

where γ is the propagation constant and can be usually defined by its real and imaginary components α and β:

$$\begin{aligned} \gamma^2 &= -\omega^2\mu\varepsilon_e \\ &= -\omega^2(\mu' - i\mu'')(\varepsilon_e' - i\varepsilon_e'') \\ \gamma &= \sqrt{-\omega^2(\mu'\varepsilon_e' - \mu''\varepsilon_e'') + i\omega^2(\mu'\varepsilon_e'' + \mu''\varepsilon_e')} \\ &= \alpha + i\beta \end{aligned} \tag{2.16}$$

where α is known as the attenuation constant [Np/m] and β is the phase constant [rad/m]. For a material with both electric and magnetic losses, these constants can be defined as:

$$\alpha = \frac{\omega\sqrt{\mu'\varepsilon_e'}}{\sqrt{2}}\sqrt{\sqrt{\left(1+\left(\frac{\varepsilon_e''}{\varepsilon_e'}\right)^2\right)\left(1+\left(\frac{\mu''}{\mu'}\right)^2\right)} - \left(1-\frac{\varepsilon_e''}{\varepsilon_e'}\frac{\mu''}{\mu'}\right)} \tag{2.17}$$

$$\beta = \frac{\omega\sqrt{\mu'\varepsilon_e'}}{\sqrt{2}}\sqrt{\sqrt{\left(1+\left(\frac{\varepsilon_e''}{\varepsilon_e'}\right)^2\right)\left(1+\left(\frac{\mu''}{\mu'}\right)^2\right)} + \left(1-\frac{\varepsilon_e''}{\varepsilon_e'}\frac{\mu''}{\mu'}\right)} \tag{2.18}$$

The general solution of the wave equations 2.14 and 2.15 is given by functions that move with time through a medium, with velocity v_m and wavelength λ_m:

$$v_m = \frac{\omega}{\beta} \simeq \frac{\sqrt{2}}{\sqrt{\mu'\varepsilon_e'}\sqrt{\sqrt{1+\left(\frac{\varepsilon_e''}{\varepsilon_e'}\right)^2}+1}} \tag{2.19}$$

$$\lambda_m = \frac{2\pi}{\beta} \simeq \frac{2\sqrt{2}\pi}{\omega\sqrt{\mu'\varepsilon_e'}\sqrt{\sqrt{1+\left(\frac{\varepsilon_e''}{\varepsilon_e'}\right)^2}+1}} \tag{2.20}$$

where equations 2.19 and 2.20 have been considered for a medium with no magnetic losses ($\mu'' = 0$). The time dependence of the harmonic functions is sinusoidal. The sinusoidal functions are represented in the frequency domain with complex exponentials. The imaginary part of the exponential (i.e., argument of the function) is the phase, while the real part is the amplitude. In the case of wave transmission in free space, the velocity of the wave becomes:

$$v = c = \frac{\omega\sqrt{2}}{\omega\sqrt{\mu_0\varepsilon_0}\sqrt{2}} = \frac{1}{\sqrt{\mu_0\varepsilon_0}} \tag{2.21}$$

where the permeability and permittivity are equal to that of free space, and they are defines as:

$$\mu_0 = 4\pi \times 10^{-7} \text{ H/m} \tag{2.22}$$

$$\varepsilon_0 = 8.854188 \times 10^{-12} \text{ F/m} \tag{2.23}$$

If the wave transmission occurs through a low-loss or good dielectrics material (i.e., $\varepsilon''/\varepsilon' \ll 1$ and $\sigma/(\omega\varepsilon') \ll 1$), where dissipative phenomena related to the dipoles orientation and Joule effect due to the external electromagnetic field are absent, the velocity of the wave is:

$$\mathrm{v}_m = \frac{1}{\sqrt{\mu'\varepsilon'_e}} \tag{2.24}$$

with wavelength equal to:

$$\lambda_m = \frac{2\pi}{\omega\sqrt{\mu'\varepsilon'_e}} = \frac{\mathrm{v}_m}{f} \tag{2.25}$$

being the phase constant equal to the one for a lossless material $\beta = \omega\sqrt{\mu'\varepsilon'_e}$.

When σ is non-negligible the material is a conductor and $\left(\frac{\varepsilon''_e}{\varepsilon'_e}\right)^2 + 1 \simeq \left(\frac{\varepsilon''_e}{\varepsilon'_e}\right)^2$. The phase constant can be expressed as:

$$\beta = \frac{\omega\sqrt{\mu'\varepsilon'_e}}{\sqrt{2}}\sqrt{\frac{\sigma}{\omega\varepsilon'_e}} = \sqrt{\frac{\mu'\sigma\omega}{2}} \tag{2.26}$$

and therefore, the velocity and wavelength in a conductor can be approximated as:

$$\mathrm{v}_m = \sqrt{\frac{2\omega}{\mu'\sigma}} \tag{2.27}$$

$$\lambda_m = \frac{2\pi\sqrt{2}}{\sqrt{\mu'\sigma\omega}} = 2\pi\eth \tag{2.28}$$

where ð is a distance and is called skin depth and gives an idea of the depth of penetration that the electromagnetic field can reach in a good conductor. More precisely ð is the depth of the material at which the electromagnetic field drops exponentially to $1/e$ of the incident value and is defined by the equation:

$$\eth = \sqrt{\frac{2}{\mu'\sigma\omega}} \tag{2.29}$$

2.1.2 Electromagnetic classification of materials

As previously seen, the reaction of a medium to an external electromagnetic field is dependent upon its electromagnetic properties. In particular, materials can be identified according to their relative to free-space complex permittivity $\varepsilon_r(\omega)$, which describes macroscopically the ability of a material to be polarized once irradiated by an electromagnetic wave and is defined as:

$$\varepsilon_r(\omega) = \frac{\varepsilon_e}{\varepsilon_0} = \varepsilon_r'(\omega) - i\varepsilon_r''(\omega) \tag{2.30}$$

where:

$$\varepsilon_r' = \frac{\varepsilon_e'}{\varepsilon_0} \text{ and } \varepsilon_r'' = \frac{\varepsilon_e''}{\varepsilon_0} \tag{2.31}$$

The complex permittivity is a function of the frequency of the external electromagnetic field. This dependence suggests that the material's polarization due to the applied field is not instantaneous and the response arise after the excitation (i.e., phase difference). Figure 2.1 shows how the real and imaginary components of permittivity typically vary with the frequency of the external electromagnetic field. Low frequency behaviour is attributed to free ionic motion in the material, which can occur only if some solvent is present. At microwave frequencies spinning polar molecules cause the Debye relaxation shown in Figure 2.1 [42], [43].

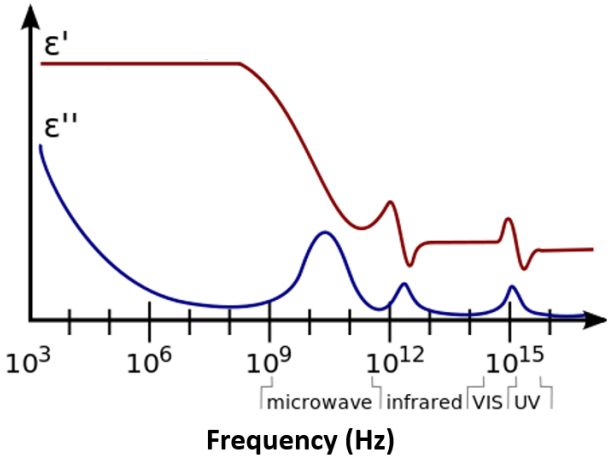


Figure 2.1: Dielectric constant and loss factor as function of frequency [42], [43].

Each dielectric mechanism has a characteristic resonant frequency. As the frequency becomes larger (i.e., infrared and visible regions), the slower mechanisms leaves place to the faster mechanisms to contribute to the dielectric constant. The loss factor will correspondingly peak at each critical frequency (i.e., resonances related to electronic and atomic polarisations give rise to sharp peaks) [42], [43].

Another index can be defined as the ratio of the imaginary and the real part of the relative complex permittivity, the loss tangent or dissipation factor ($tan\delta$), i.e. the ratio (or angle in a complex plane) of the lossy reaction to the electric field **E** in the curl equation to the lossless reaction:

$$tan\delta(\omega) = \frac{\varepsilon_r''(\omega)}{\varepsilon_r'(\omega)} \tag{2.32}$$

Hence, materials can be classified as perfect dielectric or lossless when $tan\delta = 0$ (or $\sigma = 0$), low-loss or good dielectrics or poor conductors when $tan\delta \ll 1$ (or $\sigma/\varepsilon_0\omega \ll 1$), and good conductors or high-loss when $tan\delta \gg 1$ (or $\sigma/\varepsilon_0\omega \gg 1$) and perfect conductors if $tan\delta = \infty$ (or $\sigma = \infty$) [44]. Most materials fall somewhere between the two extremes (e.g., plastic for dielectrics, metal for conductors).

In addition, in case of magnetic material, a relative to free-space complex permeability can be expressed as:

$$\mu_r = \frac{\mu}{\mu_0} \tag{2.33}$$

Hence, material properties are sometimes also addressed in terms of the wave impedance (η):

$$\eta = \sqrt{\frac{\mu}{\varepsilon}} \tag{2.34}$$

where, using the values of equations 2.22 and 2.23, it is possible to calculate the impedance of free-space η_0, which is approximatively equal to 376.7 ohms.

2.1.3 Plane wave approach

The permittivity and permeability completely define how an electromagnetic field behaves when encounters a material. An example is given by a plane wave propagating in the free-space, which encounters at normal incidence a semi-infinite dielectric media with impedance η_S. At the interface between two media, part of the radiation will be reflected and part transmitted through the medium, as shown in Figure 2.2. Having defined magnitude and phase of an incident electric field through the complex number E_i, the magnitude and phase of the reflected and transmitted wave, i.e., E_r and E_t respectively, can be obtained by the following expressions:

$$E_r = \Gamma E_i \tag{2.35}$$

$$E_t = \mathrm{T} E_i \tag{2.36}$$

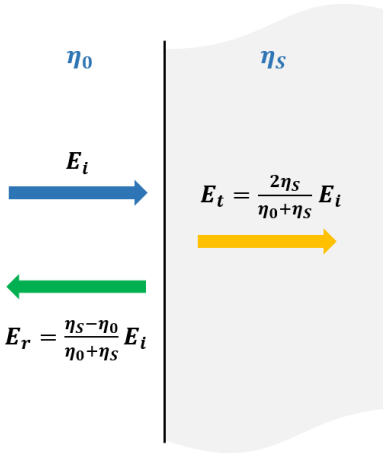


Figure 2.2: Reflection and transmission of an electromagnetic wave at the surface between air η_0 and medium η_S with normal incidence.

where Γ and T are respectively the reflection and transmission coefficient. Their values are obtained from the impedances of the two media:

$$\Gamma = \frac{\eta_S - \eta_0}{\eta_0 + \eta_S} = \frac{\sqrt{\frac{\mu_r}{\varepsilon_r}} - 1}{\sqrt{\frac{\mu_r}{\varepsilon_r}} + 1} \tag{2.37}$$

$$\mathrm{T} = \frac{2\eta_S}{\eta_0 + \eta_S} \tag{2.38}$$

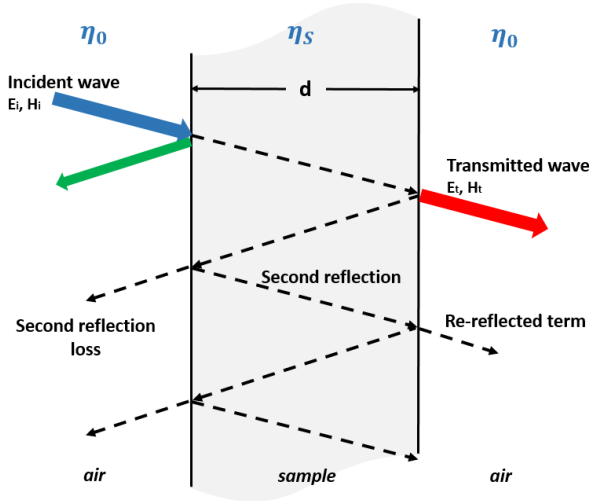


Figure 2.3: Schematic diagram of electromagnetic wave reflection and transmission pathways at two boundaries with different impedance [45], [46].

Considering that the first medium is air, equation 2.37 holds true in this specific case. In case of a finite sample, the radiation can be reflected at the first boundary between air and sample and transmitted through the second boundary between sample and air,

as depicted in Figure 2.3. A third part of the electromagnetic radiation is then attenuated by multiple reflections, which take place at the interfaces between air-sample and sample-air. The amount of electric field transmitted through the material is dependent upon the thickness of the sample. This is due to any lossy behaviour that may occur in the sample (i.e., wave absorption) and to the re-reflection phenomenon, which occur within the material from each boundary.

Each constituent reflection is taken into account by equation 2.40. The effects of the multiple reflections cause constructive and destructive interferences if the thickness of the material (d) is close to a multiple of a quarter of the wavelength of the field inside that material. Odd quarter wavelengths give rise to destructive interference conditions whereas even multiples cause constructive interference. This affects both the total reflection and transmission. The overall effective reflection and transmission coefficients are equal to [42]:

$$\Gamma = \frac{(1-\eta_{0S})(1+\eta_{S0}) + (1+\eta_{0S})(1-\eta_{S0})e^{-2\gamma_S d}}{(1+\eta_{0S})(1+\eta_{S0}) + (1-\eta_{0S})(1-\eta_{S0})e^{-2\gamma d}} \tag{2.39}$$

$$\mathrm{T} = \frac{4e^{-\gamma_S d}}{(1+\eta_{0S})(1+\eta_{S0}) + (1-\eta_{0S})(1-\eta_{S0})e^{-2\gamma_S d}} \tag{2.40}$$

where

$$\eta_{ij} = \frac{\mu_i \gamma_j}{\mu_j \gamma_i} \tag{2.41}$$

Finally, the amount of electric radiation that is shielded by the material is defined as Shielding Effectiveness (SE), and is equal to the sum of the reflected, absorbed and re-reflected radiation.

2.2 Electromagnetic properties of CFRP

As seen in the previous paragraph, materials can be classified according to their constitutive parameters into perfect dielectrics, low lossy materials, high lossy materials and perfect conductors. In this section, before introducing microwave characterization and microwave NDT and their application to CFRP, a classification and description of the electromagnetic properties of general interest for carbon fibre composites is provided. In fact, it is important to understand first the electromagnetic properties of the material to inspect (i.e., complex permittivity, electrical conductivity or resistivity), in order to establish the effectiveness of MNDT upon the CFRP being analysed.

The use of CFRP in the aerospace sector is to a great extent driven by their mechanical characteristics. However, the need for structural components able to display more than one physical feature is recently increasing. CFRP materials for their definition contain diverse components (i.e., matrix and reinforcements), which have different electrical properties. Their effective permittivity is influenced by many factors, such as fibre volume fraction, architecture of laminae, and disposition of laminae. In general, rules of mixtures for continuous and unidirectional fibres can be used to predict upper and lower limits for a composite's effective permittivity. Jylhä and Sihvola summarized diverse mixing formulae reported in literature based on the volume fraction of fibres and resin [47]. However, unlike for dielectric composites such as fiberglass, they cannot be easily applied to carbon-based composites due to the extreme anisotropy between matrix permittivity and fibres permittivity and, so far, there is no empirical model available for permittivity prediction of continuous carbon fibre composites [48]. Therefore, to get quantitative knowledge of their electromagnetic properties still experimental measurements need to be carried out. In the first place, to have a better understanding of the electric properties of CFRP, the electrical parameters of matrix and carbon fibres will be reported in the following paragraph.

2.2.1 Electromagnetic parameters of thermoset matrices

Thermoset polymers and in particular epoxies are known for their excellent adhesion, chemical and heat resistance, good mechanical properties and excellent electrical insulating properties. In fact, thermoset polymers are commonly considered low-loss or good dielectrics (i.e., materials where conduction of electric current is absent), due to their low loss factor, low tangent loss and high electrical resistivity as shown in Table 2.1, where dielectric constant, loss tangent and resistivity values have been collected for the most common thermoset matrices used in aerospace.

As previously mentioned, epoxy is the most employed structural matrix. For its insulating properties, epoxy resin formulations are also appreciated in the electronics industry, where they are used in microelectronics as interconnections, printed circuit boards, substrates, encapsulations, interlayer dielectrics, die attach, electrical contacts, connectors, thermal interface materials, heat sinks, lids and housing.

For the same reasons, epoxy resin is perfectly suited for microwave inspection, as it allows penetration of electromagnetic waves. On the other hand, electromagnetic applications such as shielding, reflection and absorption of the electromagnetic radiation (i.e. the capability of a material to act as a shield against the penetration of electromagnetic waves) require instead a conductive material. Therefore, the ability of

a composite made with epoxy resin to be electrically conductive depends solely upon the reinforcement used.

Table 2.1:Dielectric constant, tangent loss and resistivity of commonly used thermoset polymers [49], [50].

Thermosets	ε_r'	$tan\delta$	**Electrical Resistivity [Ωcm]**
Epoxy	**2.58 - 8.00**	**0.0007 - 0.310**	**0.001 - 8.10e+15**
Abatron 8109-6 (1 MHz)	3.30 - 3.50	0.010 - 0.015	1.50e+16
ERL-4221[a] (1 MHz, 22.78˚C)	3.33	0.017	
ERL-4221/ERRA-4090[h] (1 MHz, 22.78˚C)	4.42	0.027	
Phenolic Resin	**5.00 - 6.50**	**0.019 - 0.080**	**1.00e+11 - 1.00e+13**
Polyester Resin	**4.20 - 6.00**	**0.014 - 0.050**	**2.50e+14 - 6.60e+15**
EKONOL (1 MHz, 25˚F)	3.16	0.00325	
Hexion Bakelite^R UP 802 (100 Hz)	5.50	0.020	1.00e+13
Polyimide	**2.40 - 4.00**	**0.0013 - 0.010**	**1.00e+9 - 2.30e+17**
Arlon 33N (1 MHz)	4.00	0.010	7.20e+13 - 4.50e+14
Arlon 38N (1 MHz)	4.25	0.010	8.20e+13 - 4.70e+15

2.2.2 Electromagnetic parameters of carbon fibres

Unlike for composites made with glass or aramid fibres, composites reinforced with carbon fibres have high electrical and thermal conductivity. Contrary to epoxy resin, carbon fibres cannot be very well described by their complex permittivity as they are conductive rather than dielectric. As mentioned before, carbon fibres are based on Polyacrylonitrile (PAN) precursor or pitch precursor. However, PAN carbon fibres have superior mechanical strength and are widely used compared to pitch carbon fibres, which are, nonetheless, more conductive. PAN based carbon fibres have electrical conductivity of about 60000-70000 S/m [51]. Common values of conductivity of carbon fibres are reported Table 2.2.

Table 2.2: Resistivity of commonly used carbon fibres [52].

Carbon Fibres	**Electrical conductivity [S/m]**
Zoltek Panex 35	65000
SGL Carbon Group SIGRAFIL C^R C25	62500
Cytec Thornel T-300 3K Carbon Fiber, PAN Precursor	56000
Cytec Thornel T-650/35 3K Carbon Fiber, PAN Precursor	67000
Cytec Thornel P-25 4K Carbon Fiber, Pitch Precursor	77000
Cytec ThornelⓍR P-55S 2K Carbon Fiber, Pitch Precursor	118000
Toho Tenax Besfight G30-500 12K Continuous Filament Carbon Fiber	66700
Hexcel HexTow^T M AS4 Carbon Fiber	59000

2.2.3 Conductivity of CFRP

Because of the high conductivity of carbon fibres, CFRP are as well considered medium to high-loss materials [53]. The conductivity of the whole CFRP can vary according to the disposition of the fibres and to the fibre volume ratio (i.e., percentage of fibre volume in the entire volume of the composite) compared to the amount of resin. The conductivity of the CFRP will increase with the fibre volume ratio.

Considering a CFRP with continuous fibres, if the fibres were to be perfectly straight and aligned and did not touch adjacent fibres in the lamina plane, or in the transversal direction (i.e., out of lamina plane), even composites filled with high conductive reinforcements would be highly insulating. In reality, fibres are in contact with each other in the lamina plane even in the case of a unidirectional CFRP, and unavoidably in the case of a fabric cloth. Fibres are also in contact in the direction transversal to the lamina plane. Thus, in literature the mean conductivity of CFRPs is reported to be of about 10^4 S/m [53], while the electrical conductivity in the direction transversal to the fibres is of four orders lower than the in-plane conductivity [51]. Overall, the conductivity of the whole CFRP depends upon the numbers of contact points between reinforcements in the transversal direction and increases with their number [51].

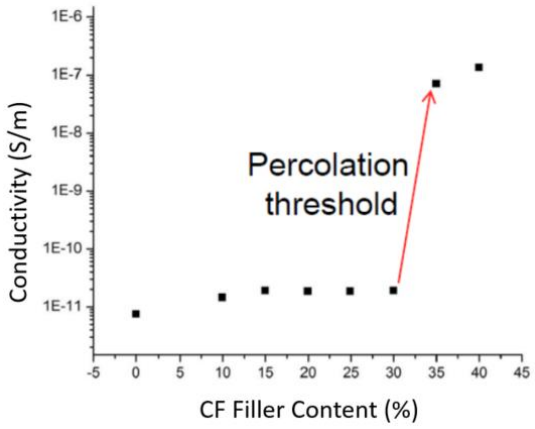


Figure 2.4: Percolation state in carbon fibre composite [54].

This can be explained in terms of percolation theory. In fact, inside a composite a percolation threshold can be reached when the bulk conductivity of the material rapidly increases at a given fibre volume ratio, where continuous macroscopic conducting fibre chains form, exhibiting graphitic conduction [55]. Before reaching the percolation threshold, the composite behaviour is similar to that one of an insulator or a semiconductor, as shown in Figure 2.4 [54].

Summing up the electrical conductivity is higher in the direction parallel to the fibre axis than in the direction perpendicular to the lamina plane. The conductivity is anisotropic: the longitudinal conductivity σ_L (i.e., in the lamina plane) can be

approximatively defined as a function of the conductivity of the carbon fibres σ_f: $\sigma_L \approx \nu_f \sigma_f$, given the fibre volume fraction ν_f. The transverse conductivity σ_T depends upon the out-of-plane waviness of the fibres and number of contact among those in the direction perpendicular to the lamina plane.

2.3 Microwave methods

2.3.1 Field regions

An electronic oscillator can generate electromagnetic waves with propagation coherent with plane polarization. Around a microwave source (e.g., antenna, scattering object), three regions of the electromagnetic field can be recognized: non-radiative near-field, radiative near-field or Fresnel region and far-field region, as depicted in Figure 2.5 [56].

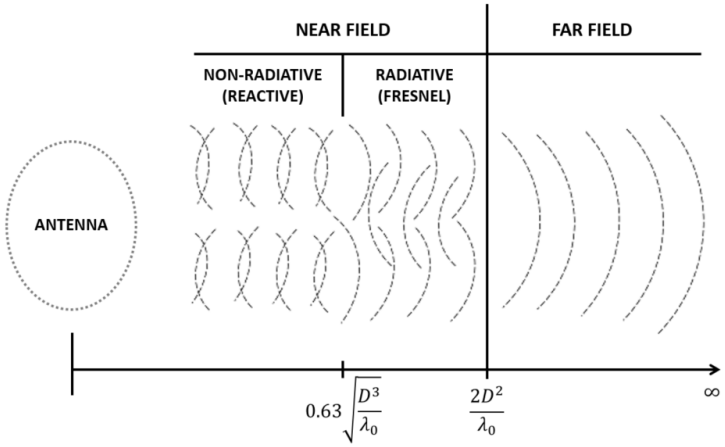


Figure 2.5: Antenna field regions, D is the antenna length or diameter and λ_0 the free space wavelength [56].

Non-radiative near-field dominates the area close to the antenna or sensor, from which originates the electromagnetic field. In this region, reactive (stored) fields are widespread and quasi-static fields exist. For near field applications open ended coaxial cable are generally used. In the radiative near-field zone, the reactive fields are not dominant; the radiating fields begin to emerge. However, unlike for the far-field region, here the shape of the radiation pattern may vary appreciably with distance. Antenna devices, such as open-ended coaxial probe or rectangular waveguides can operate in this region. In the far-field region, the radiation pattern does not change shape with distance and radiating fields exist, with the electric and magnetic fields orthogonal to each other. Plane waves or TEM (transverse electromagnetic) waves are assumed to exist in this region. Usually a microwave antenna (e.g., horn antenna) is employed for far field techniques.

The theoretical model of far-field plane waves is simpler to obtain than the modelling of near-field approaches. However, for what concerns microwave characterization and MNDT, the results obtained with the application of far-field plane waves are not very accurate and do not offer a fine resolution for defects characterization as it happens when using near-field methods. Near-field techniques are generally more suitable for NDT applications as they offer finer spatial resolution and access to areas of structures with complex geometry. In addition, the distance between probe and specimen can be manipulated (e.g., liftoff or standoff distance) as a parameter for detection sensitivity and the required microwave power is in the low milliwatt range [57]. However, complex analytical and numerical solution are required for the theoretical simulation of the interaction between near fields and materials media such as complex dielectric composites or sandwich structured composites.

In the following paragraphs, microwave techniques adopted for the determinations of permittivity and permeability of materials and their application to non-destructive testing will be described. The vast majority of techniques used in literature operates in the near-field zone. However, far-field techniques are also widely used, such as free-space technique and microwave imaging.

2.3.2 Measurement methods

The electromagnetic properties of a material are linked to their physical, chemical and molecular characteristics [40]. A change in dielectric properties can be correlated to the constituents of a mixture [58], [59], degree of in-service induced aging [60], moisture and chemical permeation in materials [61], [62], state of cure [63], composite fibre orientation assessment [64], and presence of disbonds and corrosion in composite laminates [65], [66], to name a few applications. Consequently, microwave materials characterization has been recognized as an important non-destructive evaluation (NDE) method for assessment of materials properties and mixture constituents [57].

When a material is irradiated by an electromagnetic wave, dielectric polarization takes place. The ability of a material to be polarized is macroscopically described by the material's complex permittivity $\varepsilon_r(\omega)$, as previously seen in Section 2.1.2. Therefore, to determine complex dielectric properties, which are intrinsic to the material, different measurement techniques can be adopted experimentally. These techniques can be divided into two main categories, resonant methods and non-resonant methods. Resonant methods, i.e. cavity resonators, open-ended and planar resonant transmission line [67], [68], are generally used for characterization of low-loss materials. These methods are limited to narrow band of frequencies only and on the loss characteristics of the materials that can be measured. In addition, precise

sample preparation and positioning is required [69], [70]. Non-resonant methods include the transmission/reflection (TR) line method [71], open-ended transmission lines (i.e., rectangular and coaxial probes) [72], [73], and the free-space transmission/reflection method [74]–[76]. These methods are used for broadband measurements, and each of them has their own advantages and disadvantages in terms of sample preparation, type of material to be tested, electromagnetic properties acquired and conversion method used. A quick summary of non-resonant method with corresponding sensing architecture, type of configuration (i.e., Reflection S_{11} or Reflection-Transmission S_{11} and S_{21}), conversion method and electromagnetic properties acquired is presented in Table 2.3. An overview of the microwave non-resonant methods, which were chosen for this thesis project because of their broadband application, is presented here below. Their detailed description can be found in [77], [78].

Table 2.3: Comparison between microwave measurement methods [78].

Measurement technique	Sensing architecture	Operating configuration	Conversion method	EM properties
Transmission/reflection Line (TR)	Coaxial/rectangular/cylindrical waveguides	S_{11}, S_{21}	NRW / NIST iterative / New non-iterative	ε_r, μ_r
Open-ended probe	Coaxial/rectangular waveguides	S_{11}	RFM / N-layer	ε_r
Free-space	Horn antenna/Open resonator	S_{11}, S_{21}	NRW / NIST iterative / New non-iterative	ε_r, μ_r
SAR	Horn antenna, dual polarized antenna, circular antenna, antennas' array	S_{11}	Amplitude-phase method / Backprojection algorithm	ε_r

Transmission/reflection (TR) line techniques

TR methods involve placing the sample under test in the section of a rectangular or cylindrical waveguide or coaxial line and measuring the scattered reflected and transmitted signal using a two-port vector network analyser (VNA), as shown in Figure 2.6. In particular, the reflected and transmitted signal are obtained through the VNA in the form of scattering parameters or S-parameters S_{ij}. For instance, considering the signal emitted from Port 1 and transmitted to Port 2, the portion of electromagnetic signal reflected from the sample will be measured at Port 1 (S_{11}) and the portion of signal transmitted through the sample will be obtained at Port 2 (S_{21}). Consequently, a numerical conversion method will be used to calculate the complex permittivity and

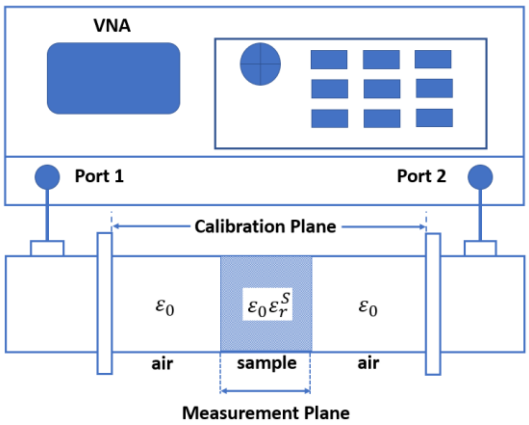


Figure 2.6: Example of transmission-line experimental setup.

permeability from these scattering parameters. The most commonly applied is the Nicholson-Ross-Weir (NRW), further improved by Backer-Jarvis as the NRW/ Backer-Jarvis conversion procedure given in [71], [79], [80]. The method utilizes all four of S-parameters (S_{11}, S_{12}, S_{21}, S_{22}) or a pair (S_{11}, S_{21}) to calculate the reflection and transmission coefficient. Attention must be paid to the sample length, as the method has poor accuracy when the sample length is a multiple of one-half wavelength ($\lambda_m/2$).

Calibration of cables and probes is required as for permittivity measurements it is advantageous to have a maximal electric field. A standard full two-port SSLT (short, shifted short, load, and thru) calibration technique is generally adopted for transmission-line measurements. The sample must fit tightly in the sample holder in order to reduce the measurement uncertainty caused by air gaps. The presence of air gaps leads to the formation of high order modes. Therefore, precise machining of the sample is required.

Transmission-line methods have mostly been applied for accurate complex permittivity characterization and shielding effectiveness (SE) evaluation [71], [80]–[83].

Open-ended techniques

Open-ended methods have been used widely as a non-destructive testing method. In the open-ended coaxial or waveguide measurement, the probe is pressed against a specimen or at a certain distance from the specimen (stand-off or lift-off) or immersed into a liquid and the reflection coefficient or scattering parameters S_{11} is measured and used to determine the permittivity. The reflection coefficient is measured using a vector network analyser (VNA). The VNA with a probe system is first calibrated so that the reflection coefficient measurements are referenced to the probe aperture plane.

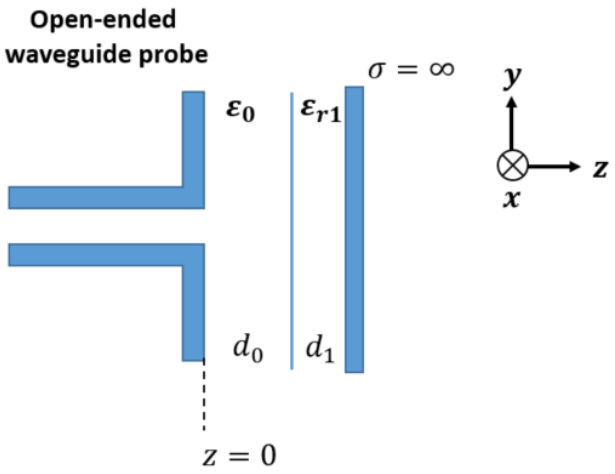


Figure 2.7: Cross-section of an open-ended rectangular waveguide radiating into a material with permittivity ε_{r1} terminated by a conducting sheet.

The calibration process requires to calibrate the VNA at the connector plane using a standard 1-port calibration (open, short and load). The probe is then connected at the connector plane [77], [78].

Open-ended probes can be used for both permittivity and thickness testing, then, it is important to have a model of the probe, which include the lift-off or air gaps between sample and probe. Uncertainty in open-ended measurements include calibration and measurement errors (e.g., phase, magnitude, and lift-off). The method is sensitive to air gaps since the probe has components of the electric field in its aperture plane ***y*** and in the direction transversal to the aperture plane ***z***.

Figure 2.7 shows the diagram of a an open-ended rectangular waveguide radiating on a structure with a lift-off distance d_0, backed by a conducting sheet. This is a standard method adopted by Zoughi for measure of permittivity and thickness in layered structures [84], demonstrates that the application of this type of sensors comes with the advantage of having a dominant TE_{10} mode of propagation and the field can be monitored with minimum perturbation.

Advantages of this method lie in its easy application and sample preparation, which make the open-ended waveguide particularly suited for non-destructive application. However, only the reflection signal can be employed for electromagnetic characterization. Hence, open-ended methods operate well for complex permittivity estimation of dielectric materials, while high lossy and reflective materials/surfaces cannot be easily characterized [57].

A rational function model (RFM) is applied to the reflection coefficient to calculate the permittivity [78]. Formulations, as the one used by Bakhtiari in [73], have been widely employed for the characterization of stratified structures, such as layered dielectric composites.

Among NDT applications, they are mostly used for moisture detection [85]–[87], minute thickness variation detection of each layer in dielectric media [88], [89], mixture constituent [63], [90], [91], disbonds, delamination and void detection [92]–[94], evaluation of rust and corrosion under paint [95]–[97], cracks in metal plates [98]–[100], detection of stress and strain due to correlation with electromagnetic properties [101], [102].

Free-space techniques

Free space methods allow high frequency and non-destructive measurements. The sample can be measured in hostile environment (e.g., high temperature), and both permeability and permittivity can be evaluated through reflection and transmission coefficients. However, a large and flat sample is required, and multiple reflections phenomena can occur between the antenna and the surface of sample, as well as diffraction effects at the sample edges.

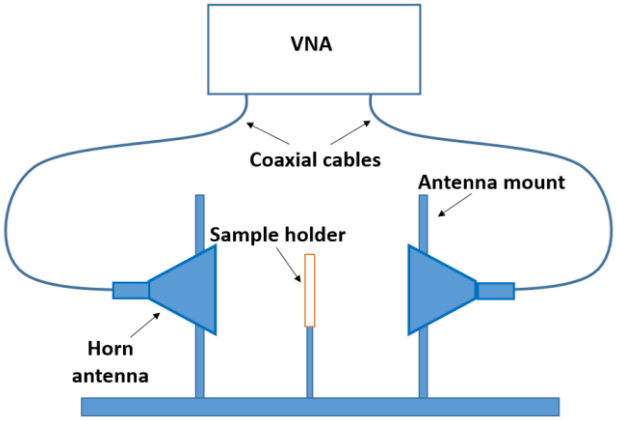


Figure 2.8: Diagram of a free-space microwave method, using two horn antennas.

As shown in Figure 2.8, a free-space measurement system usually requires two antennas facing each other (e.g. horn antennas) and a two-port VNA to collect the reflection and transmission scattering parameters S_{11} and S_{12}. Special calibration is required and several methods can be adopted: the through-reflect-line (TRL), the through-reflect-match (TRM) and the line-reflect-line (LRL). The line standard is usually obtained by separating the focal plane of the two antennas to approximately a quarter of wavelength. The reflect standard for both ports can be achieved by placing a metal plate on the sample holder in place of the specimen. Once calibrated, the specimen is then placed back between the antennas and the s-parameter measurement is performed again.

As for TR methods, free-space techniques are mostly used for material electromagnetic characterization. Examples of the use of free-space technique for can

be found in [74], [75], [103]–[105]. Conversion procedures adopted derives from extension of the NRW formulation, such as the NIST iterative method and the New non-iterative [78], [106]. The NIST iterative method performs the calculation using a Newton-Raphson's root finding method and is suitable for permittivity calculation only. It works well if a good initial guess is available. The method bypasses the inaccuracy peaks that exist in NRW method when the sample thickness is an integer multiple of $\lambda_m/2$. It is suitable for long samples and characterizing low loss materials. The New non-iterative is a simplified version of the NRW method and it is suitable for permittivity calculation for the case permeability equal to the one of free-space.

Free-space method application to non-destructive testing has been studied in the same fashion as per open-ended waveguides [19], [107]–[110].

Microwave imaging

Microwave imaging is a form of MNDT. 2D or 3D visual representation of a sample under test are generated by irradiating the specimen with a microwave signal and reading the reflected energy at prescribed locations on a 2D plane. The method can use monostatic or bistatic detection. In monostatic configuration, the signal is transmitted and received by the same probe. In bistatic configuration, the transmitting probe and the receiving probe are two separate entities and are often located on opposite sides of the sample. In both cases, the reflected signal is recorded, processed and organized as an image, which relates the image intensity to the intensity of the reflected signal [111].

Among the microwave imaging techniques, the most used are near-field techniques, lens-focused techniques and synthetic aperture radar (SAR). Near-field imaging is the simplest microwave imaging technique that allows 2D images. Commonly, it makes use of a single antenna operating in near-field and monostatic configuration to scan a 2D plane where the sample is situated. This method can be employed to inspect cracks, corrosion and corrosion precursor pitting in metal surfaces [104], [105], or thickness variation, disbonds and delaminations between composite laminates and the concrete substrate [66], [114].

Lens-focused techniques consists in applying a dielectric lens between antenna and sample to focus the transmitted signal to a smaller area of the specimen analysed. 2D images can then be created with higher spatial resolution and in the far-field region of a microwave antenna. However, this method is a single frequency approach and only the amplitude of the reflected signal can be registered, without phase information [115], [116]. Lens-focused imaging has been used for detection of defects and flaws; an example is given by its application to inspect the insulating foam of the Space

Shuttle external fuel tank after Columbia's accident, where voids and debonds were found to be the primary cause [117]–[119].

Synthetic aperture radar (SAR) imaging can overcome most of the limitations associated with near-field and lens-focused imaging and enables the creation of two-dimensional images or three-dimensional reconstruction of objects [111]. The imaging method involves the motion of a broad beam antenna or antenna array over a target region (e.g., 2D plane) to provide higher spatial resolution, see Figure 2.9. As a matter of fact, the larger the aperture, the higher the image resolution, regardless of whether the aperture is physical (i.e., large antenna diameter) or synthetic (i.e., moving antenna). Hence, the antenna is generally mounted on a moving platform, operating in either monostatic or bistatic modes. The recorded data can be either complex or real depending on the method used for SAR imaging. The measurements are then back-propagated or focused back to the target region through post processing transformations. The spatial resolution depends from the frequency of operation, the step size of the scan on the analysed plane and the distance between the antenna and the target [120]–[122]. High-resolution 2D images can be obtained at a single frequency or in wideband, but high-resolution 3D images require wideband measurements. The latter method allows the image to be focused at several depth locations, since the reflected signal at particular frequencies within the band add constructively in some locations while adding destructively in others. Thus, a transmitted signal possessing a relatively wide signal bandwidth will produce images that can delineate depth information.

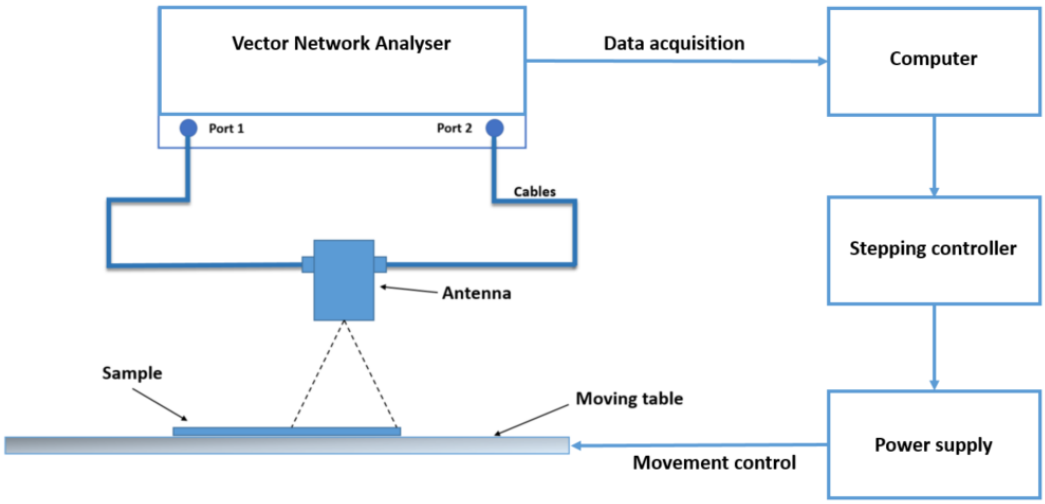


Figure 2.9: Schematic of an antenna imaging system.

SAR methods have been extensively applied for geological sciences, earth mapping and astronomy [122]–[124]. On a smaller scale, this technique can be successfully used for non-destructive evaluation. Applications include detection of

cracks on metal plates as depicted in Figure 2.10 [125], [126], thickness surface variation [127], holes in fiberglass composites [128] and disbonds between composite and concrete [66], [129], to name a few.

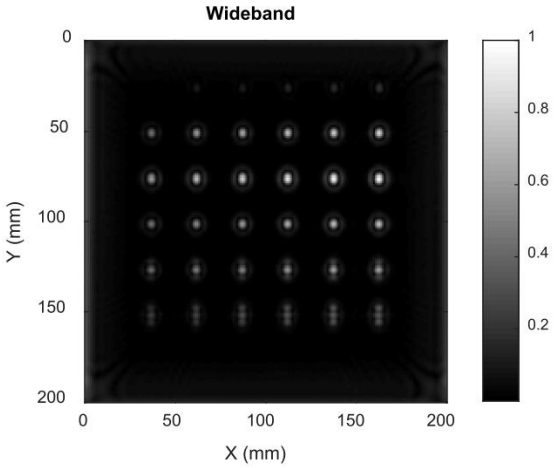


Figure 2.10: 2D wideband SAR image of cracks artificially made on a metal plate [125].

2.3.3 Microwave characterization and MNDT applied to CFRP

Carbon fibre composites represents a challenge when it comes to microwave characterization and microwave non-destructive testing. Due to the carbon fibres conductivity, the electromagnetic signal cannot penetrate deeply through the material, and the degree of penetration is related to the CFRP architecture and polarization of the electric field. Therefore, few studies in literature address the problem of measuring the complex permittivity of CFRP. For the same reasons, unlike for dielectric materials, all those investigations related to damage types hidden in depths, such as inclusions embedded inside the structure, delamination, debond of a substrate, porosity and fibre waviness, are hardly carried out via microwave methods. On the other hand, it is still possible to use microwave methods to assess superficial damage, e.g., impact damage and surface defects. In this section, several developments on microwave characterization and MNDT of carbon fibre composites that are fundamentally pertinent to the work presented in this thesis are outlined.

Microwave characterization of CFRP

Due to the high conductivity of carbon fibres, CFRPs are considered high-loss materials. On this assumption, the measure of the reflection coefficient only would lead to incorrect prediction of the permittivity, as a result of the high reflection of the electromagnetic field which occurs at the interface between air and the first surface of

the material under test. Hence, all four (S_{11}, S_{12}, S_{21}, S_{22}) or a pair (S_{11}, S_{21}) of the scattering parameters of the sample are needed to obtain a good estimation of the complex permittivities. This condition makes transmission/reflection line and free-space methods the most suitable for electromagnetic characterization of high-loss materials, as it can be found in literature [59].

Nonetheless, limited literature is still available regarding the characterization of the complex permittivity of unidirectional CFRP. As a matter of fact, in recent years the focus of the research has moved towards polymeric materials filled with carbon-based nanotubes [59], [130], [131], due to their outstanding ability of microwave absorption, leaving the evaluation of dielectric properties of continuous carbon fiber composites limited to very few studies.

Kim and See employed a two-port TR method and rectangular waveguides with samples cut to appropriate dimensions of the inner waveguide section, to measure the dielectric constant and conductivity of unidirectional CFRP samples [132], the complex permittivities of unidirectional CFRP were obtained applying the method of transformation into an equivalent plane wave (TEPW) proposed by Delecki and Hamid [133]. More recently, a similar study on UD CFRPs was carried out by Li at al. with polarization of the electric field parallel and orthogonal to the direction of the fibres and using the Nicholson-Ross-Weir conversion method in the X-band; the authors conclude that the real part of the permittivity is not significantly anisotropic [48]. Yoon et al. investigated the effective permittivity and conductivity of UD CFRP in the X-band with polarization parallel to the fibres, by applying the TR method and NRW theory and/or the formula of the effective conductivity obtained from the reflected wave information. The significant difference compared to other studies is that the composite panel was clamped between two waveguide sections [64]. Finally, free space methods were also applied for the analysis of electromagnetic properties. A detailed study was presented by Riley et al. on the complex permittivity of CFRP samples at angles of 30°, 60° and 90° to the fibre direction, employing two spot-focusing antennas [134]. A free-space experimental setup in the X-band was considered by Galehdar et al. to measure the conductivity of UD CFRP, directing the electric field of the TE_{10} mode at 90° and 45° in respect to the direction of the fibres [135].

A comparison of the results collected from the different studies found in literature can be challenging. This is caused by many variables: the measurement system adopted, the conversion approach and the manufacturing of the materials. However, considering those studies focused on the transmission/reflection line method [48], [132], it can be observed that the majority does not take into account the effect of gaps modes in the waveguide, which can be dominant for high lossy materials [136].

Particularly in [48], it is possible to observe that the difference in transmission coefficient S_{21} measured for electric field parallel and perpendicular to the fibre direction is not significant, which is unlikely true due to the high electrical anisotropy of unidirectional CFRP. The majority of the research work characterize only electric field polarization angles at which the material can be considered a lossy dielectric [134], [135], [137]. Furthermore, in case of characterization of high lossy CFRP, the conductivity is calculated through theoretical model based on the surface resistance theory [64], [138], [139], were only the reflection coefficient is taken into account, leading to significant errors on the conductivity evaluation.

MNDT applied to CFRP

When it comes to the analysis of carbon fibre reinforced polymers, the use of microwave non-destructive techniques is restricted by the composite relatively high conductivity of about 10^4 S/m, as stated in Section 2.2.3. In this case (as for metals), their applicability is considered limited to surface defects (e.g., impact damage, surface irregularity, indentation), and to defects contained in the first layers of the laminate, due to the electromagnetic field scarce penetrability [140]. Here below are presented few applications of MNDT to CFRP using predominantly non-resonant methods. A detailed review of the work done so far can be found in [141].

Among the first applications of MNDT presented for conductive polymers, it is possible to list the detection of fibre breakage and fibre orientation in unidirectional carbon fibre composites. An early stage study was presented by Kharkovsky and Zoughi, where the method was proved valid [142]. Measurements were performed on several samples consisted of a CFRP strip or patch with artificial fibre breakage on the surface of a lossy rubber substrate using 2D scanning probe.

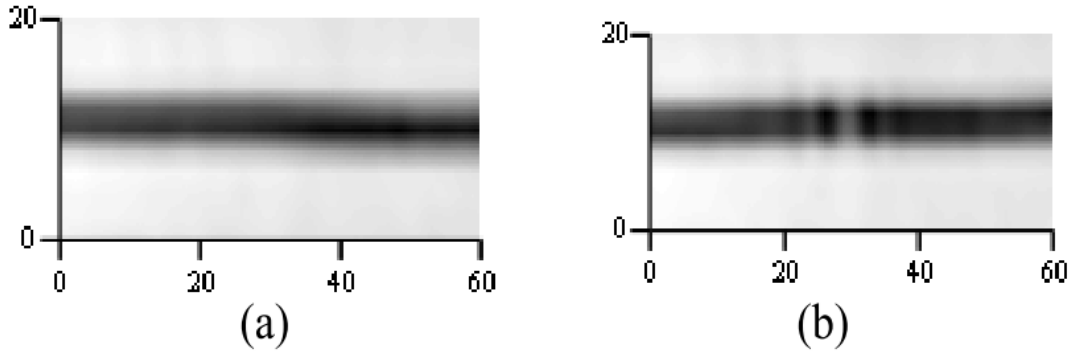


Figure 2.11: Millimeter wave images of carbon fibre strip: (a) without breakage, (b) with breakage and field polarized in the direction of the fibres [142].

It was demonstrated that that very small fibre breakages in CFRP strips may be detected and evaluated using linearly polarized microwave and millimeter wave signals for specific field polarization as shown in Figure 2.11.

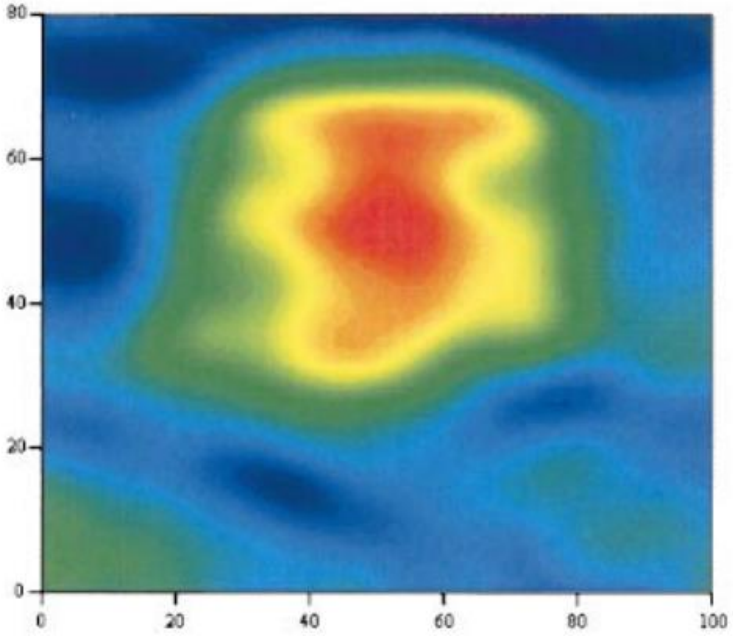


Figure 2.12: Microwave image of square shaped disbond at 10 GHz and standoff distance of 1.5 mm using orthogonal polarization (dimensions in millimeters) [66].

Again, Kharkovsky and Zoughi were able to detect disbonds between CFRP patches and concrete structures using a dual-polarized microwave reflectometer at X-band. The signal reflected by parallel and perpendicular polarization of the electric field with respect to the conductive carbon fibres was used to create 2D raster images of the targeted area: two at orthogonal polarization and one after the influence of standoff distance variation is removed, using the information provided by the parallel polarization [39]. The study was improved by Akuthota et al. as shown in Figure 2.12 [66]. The debond is visible because of minute thickness variation on the surface of the sample analysed.

Near-field millimeter wave reflection was employed using a horn antenna to detect impact damage at V-band, as illustrated in Figure 13(a) [143]. It was found that damage detection was possible when the electric field vector was polarized along the carbon fibre direction. An image of the impact damage was registered over a 2×2 mm^2 area for impact energy equal to 13.21 J, as shown in Figure 13(b). However, for a lower value of impact energy of 3.63 J, no impact was recorded, as shown in Figure 13 (c).

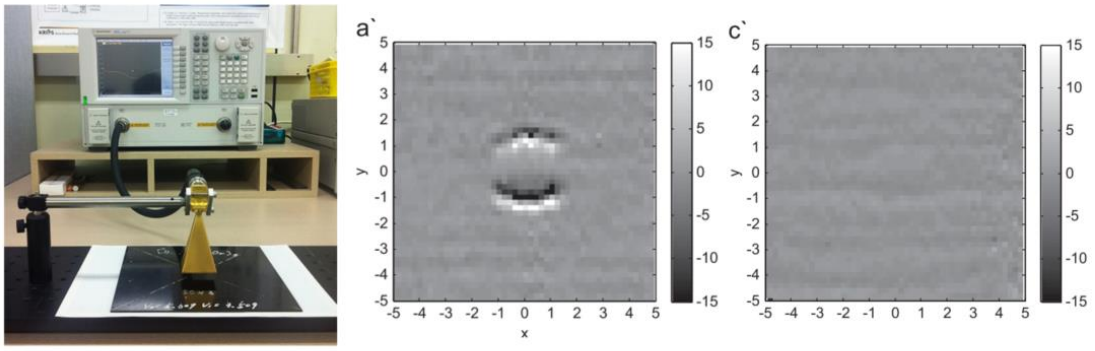


Figure 2.13: (a) Experiment setup; (b) image of specimen damaged at 13.21 J; (c) image of specimen damaged at 3.63 J [144].

Tabib-Azar et al. performed scans of composite materials and other type of test subjects using microwaves generated at the end of a microstripline resonator with 0.4 mm lateral spatial resolution at 1 GHz, in order to detect non-uniformities and defects [145]. The equipment used, consists of a microwave resonator coupled to a feedline, which is connected to a circulator. The circulator is also connected to a 0.01-1.05 GHz signal generator and to a crystal microwave detector. The detector output is a DC voltage proportional to the magnitude of the reflected wave. A schematic representation of the equipment realized by Tabib-Azar et al. is given in Figure 2.14(1). The experimental data presented were obtained from two-dimensional scans over the samples. In the images obtained for delaminated carbon composites, the image pattern was more fragmented (changing in microwave properties) compared to the undamaged specimens. Darker regions corresponded to lower effective density, and hence lower permittivity regions, while lighter region to denser and higher permittivity regions in the composite, as illustrated in Figure 2.14(2).

So far, near-field techniques were considered. However, for non-destructive purposes, far-field techniques are also very attractive, as increasing the distance between the sample and the antenna facilitates the non-destructive inspection and allows testing of complex structural parts or high temperature areas, which would otherwise be difficult to reach for the operators or even dangerous. Although it seems easier to perform measurements with the far field approach, there may be difficulties in the interpretation of the signal reflected. Ghodgaonkar et al. attribute these inaccuracies in free-space measurements to diffraction effects at the edges of the material specimen and to multiple reflection between horn lens antennas and mode transitions via the surface of the sample [74], [76], [110]. Gubinelli et al. demonstrated that a UWB radar could be successfully used to detect defects in CFRP with the size comparable with its resolution. The radar was constituted by a transmitting and receiving antenna, generating UWB nanosecond pulses with a bandwidth from 6 to 8.5

GHz. The radar was able to detect a 3 mm hole in CFRP at 40 cm of distance, by means of the difference in the reflected waveforms of a damaged and a healthy sheet [146].

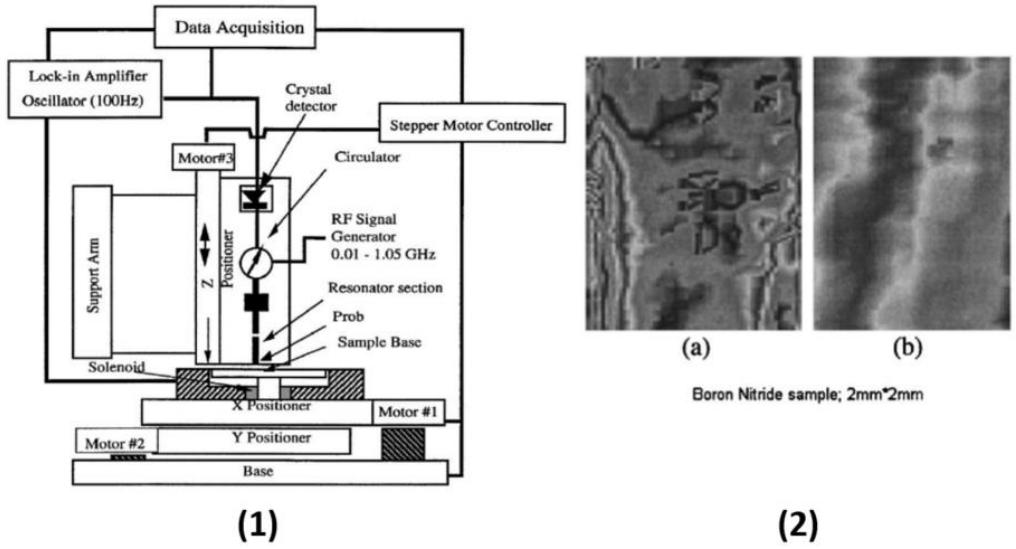


Figure 2.14: (1) Schematic a microwave resonator setup; (2) delaminated (a) and intact (b) composites imaged side by side [145].

Finally, The microwave techniques can also be combined with other NDT methods for better detection performance. Contact-free microwave-based thermography is commonly found in the literature, in which microwaves are used as a heat source [140]. Non-destructive active microwave thermography testing of rehabilitated cement-based materials with 2 mm surface bonded CFRP was studied by Foudazi [147]. Microwave energy was used to heat the target of interest and subsequently the surface thermal profile is measured using a thermal camera. It was demonstrated that CFRP is conductive when illuminated with microwave energy polarized parallel to the fibre direction but behaves as a lossy dielectric when illuminated by energy polarized perpendicularly to the fibre direction, the temperature contrast between healthy and defective areas is much greater for the latter case. Additionally, Keo et al. used a commercial 2.45 GHz magnetron and an IR camera to detect a defect (absence of adhesive) in a CFRP plate. A 360 W microwave signal was applied to heat the sample for 150 s. It was found that the defect area was hotter than the non-defect area [148]. Palumbo studied impact damage in sandwich specimens, which were put into a microwave chamber (power 750 W, frequency 2.45 GHz) for 2 s. The heating and cooling phases were both used for damage evaluation. Good agreement was achieved comparing X-ray imaging and lock-in thermography using two halogen lamps with 500 W power [148].

2.3.4 Summary

Microwave non-destructive testing methods represent an effective solution in detecting defects within material structures with relatively low electrical conductivity. They offer the advantage to overcome the problems of traditional NDT techniques such as coupling, danger coming from ionizing radiation, limited depth of operation, large wavelengths, time consuming post processing.

The microwave method is mainly used for testing dielectric materials in bulk and the surface and subsurface regions of metals. Therefore, in dielectric materials, they can be used for dielectric properties characterization, degree of porosity evaluation, degree of ageing, anisotropy, dielectric mixture constituents' determination, state of cure, determination of thickness, metallic inclusions detection. In complex structures, near-field microwave and millimetre non-invasive inspections have been successfully used for detecting defects such as disbond and delamination.

When it comes to the analysis of carbon fibre reinforced polymers, the use of these non-destructive techniques is restricted by the composite relatively high conductivity. In this case, as well as for metals, their applicability is considered limited to surface and sub-surface defects, due to the small skin depth of CFRP.

As a matter of fact, MNDTs have been proved valid for the detection of fibre breakage and fibre orientation in unidirectional CFRP, disbonds between CF patches and concrete structures, detection of impact damage, indentation.

In UD composites, the carbon fibres (highly conductive) are distributed in the resin matrix (dielectric material) in one direction only. Therefore, they possess electrical anisotropy, and the ability of the electromagnetic radiation to penetrate through the layers of the material if the electric field vector is directed orthogonally to the direction of the fibres (i.e. perpendicular polarization to the fibres). Hence, the UD composite is more affected by the radiation compared to a textile CFRP. The transmission of the electric signal through the material is possible, and therefore, also the investigation of embedded defects, as per a dielectric material.

On the other hand, according to the literature carbon fibre woven composites display a greater shielding power against radiation compared to UD composites, because in these materials the propagation of the electromagnetic field is hindered in more than one direction (the fibres direction varies according to the fabric weave and the orientation of each layers in the laminate). Regarding these observations, it is important to know the electromagnetic behaviour of carbon textile composites. The Electromagnetic Interference (EMI) shielding theory is generally applied to describe the electromagnetic behaviour of conductive materials, such as metals. But more recently, other materials than metals are being studied for their electromagnetic shielding characteristics. In particular, several works have been carried out on polymer

based conductive composites and their application to the enclosures of electronic devices. The advantages offered by conductive plastic composites over conventional metals include lighter weight, corrosion resistance, lightning protection, and flexibility in design, which abates the housing seams typical of a metallic sheets shield.

2.4 Measurements procedures

The characterization of complex permittivity at microwave frequencies requires the use of an apparatus able to generate, receive and process the scattered signal from and through the object of interest. The test system generally involves the use of a vector network analyser (VNA), an instrument that measures in terms of network scattering parameters the radio frequency (RF) performance of microwave devices, coupled with a sensing architecture able to allow the electromagnetic field propagation through the space.

2.4.1 Vector Network Analyzer

A VNA injects a known frequency and amplitude source signal into a RF port and, subsequently, measures the relative amplitude and phase of the signal when received back to the same port, if it is working in reflection configuration, or to another port if in transmission configuration. The basic architecture of a network analyzer involves a signal generator, a test set, one or more receivers and display. In some setups, these units are distinct instruments. Network analyzers are available with an arbitrary number of ports. However, the most common architecture used for the complex permittivity characterization involves the use of a two-port test model, enabling the measurements of four S-parameters, as applied in this thesis work. An example of two-port network is given in Figure 2.15.

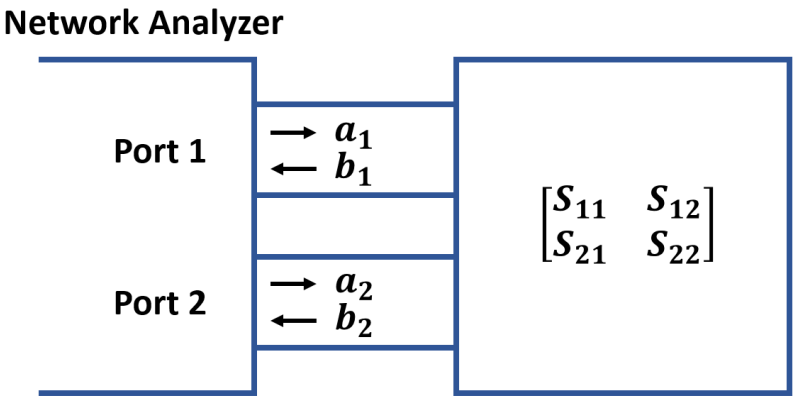


Figure 2.15: Schematic two-port S-parameter VNA measurement setup.

The relationship between the reflected, incident power waves and the S-parameter matrix is given by [149]:

$$\begin{bmatrix} b_1 \\ b_2 \end{bmatrix} = \begin{bmatrix} S_{11} & S_{12} \\ S_{21} & S_{22} \end{bmatrix} \begin{bmatrix} a_1 \\ a_2 \end{bmatrix} \tag{2.42}$$

where a_1 and b_1 are the incident and reflected power waves on Port 1, while a_2 and b_2 are the incident and reflected power waves on Port 2. Therefore:

- $S_{11} = b_1/a_1$ represents the input port voltage reflection coefficient;
- $S_{12} = b_1/a_2$ is the reverse voltage gain or reverse transmission coefficient;
- $S_{21} = b_2/a_1$ is the forward voltage gain or forward transmission coefficient
- $S_{22} = b_2/a_2$ is the output port voltage reflection coefficient.

Nicolson and Ross demonstrated that for a measured planar sample of thickness *d*, reflection coefficient Γ and transmission coefficient *T*, the S-parameters can be expressed as [80]:

$$S_{11} = \frac{(1 - T^2)\Gamma}{1 - T^2\Gamma^2} \tag{2.43}$$

$$S_{21} = \frac{(1 - \Gamma^2)\mathrm{T}}{1 - T^2\Gamma^2} \tag{2.44}$$

where the reflection coefficient is defined as per equation 2.37 and the transmission coefficient is:

$$\mathrm{T} = e^{-\gamma d} \tag{2.45}$$

with γ being the propagation constant defined in 2.16, which relates through the transmission coefficient the S-parameters with effective complex permittivity ε_e.

To achieve highly accurate measurements, it is important to minimize the repeatable measurements errors in the instrument, the characteristics of cables, adapters and test fixtures (i.e., systematic errors), which includes mismatch, directivity, and tracking errors. Calibration allows for the removal of systematic errors from the measurement, by adopting a mathematical error model.

The calibration of a VNA occurs through the measurement of well known standards, and then comparing the measured values with the known responses. The deviation from the standards is incorporated in the mathematical error model, which provides correction factors.

For the case of a two-port network analyzer, the error model must account for cross-talk between all ports, and three known impedance standards and a single transmission standard are required [150]: the Short, Open, Load and Through (SOLT). The Short standard represents a short circuit, with $\Gamma = -1$; the incident wave is reflected completely by the calibration standard, but with a change in phase of 180°.

The Open standard represents an open circuit with $\Gamma = 1$, where the incident wave is reflected completely with no phase change. The Load standard represents a matched load, such that the incident wave is completely absorbed by the load. The Through standard allows for complete transmission of the power wave from port 1 to port 2.

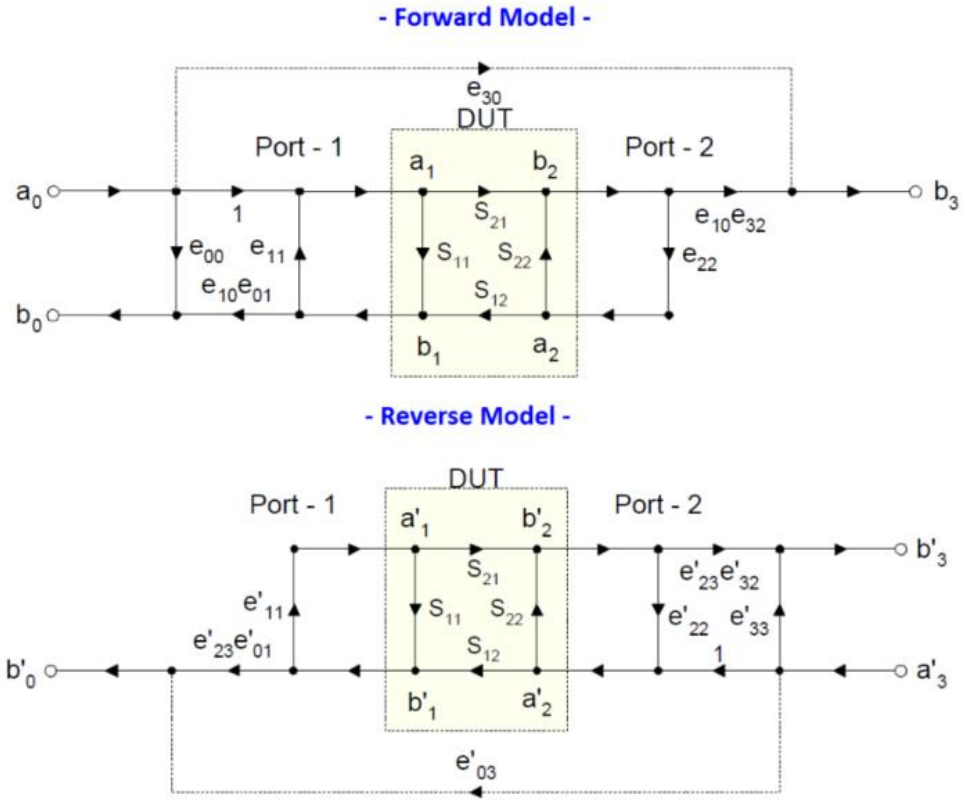


Figure 2.16: 12 terms error model for full two-port calibration [151].

The calibration technique involves an error model with 12 terms (see Figure 2.16), and requires seven measurements of standards [151]:

- Short, Open, Load on port 1;
- Short, Open, Load on port 2;
- Transmission between port 1 and port 2.

2.4.2 Sensing architecture

Different architectures of sensing equipment can be used, based on the type of material under analysis and the desired depth to inspect. The sensing equipment is usually constituted by antenna elements in transmission and in reception, so the variables to choose are their radiation pattern, directivity, efficiency, bandwidth and their arrangement. In this thesis work, the complex permittivity where characterized using rectangular waveguides or horn antennas.

Rectangular waveguide

A rectangular waveguide allows for signal propagation by confining the electromagnetic radiation within a hollow conductive tube (i.e., metallic structure) of rectangular cross-section. The rectangular aperture has dimensions defined as $a \times b$, with $a > b$, as shown in Figure 2.17. A rectangular waveguide supports transverse electric mode (TE) and transverse magnetic mode (TM) of electromagnetic wave propagation, but not transverse electromagnetic mode (TEM).

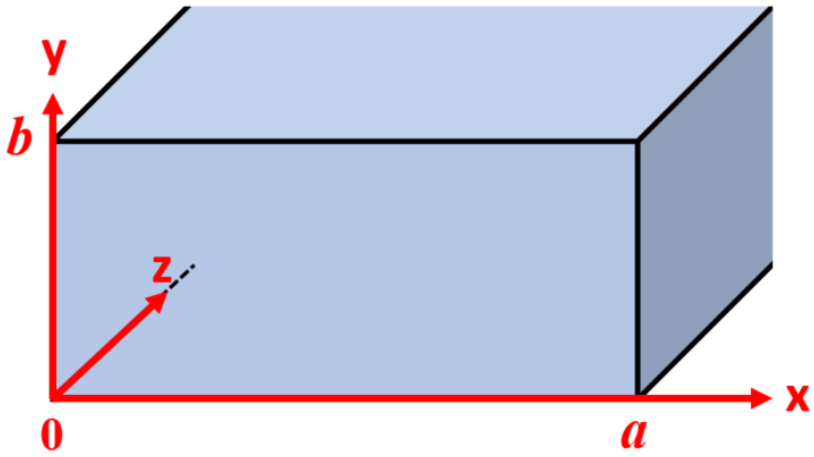


Figure 2.17: Schematic diagram of a rectangular waveguide of aperture $a \times b$.

In the TE mode, the electric field is transverse to the direction of wave propagation (z-axis), while the same is not true for the magnetic field. Therefore, $E_z = 0$ and H_z should be solved from the wave equation 2.15 for TE mode. There is an infinite number of solutions for the magnetic field corresponding to this mode. The solution is given by [152]:

$$H_{z\,mn}(\mathrm{x},\mathrm{y},\mathrm{z}) = h_{mn} \cos\left(\frac{m\pi x}{a}\right) \cos\left(\frac{n\pi y}{b}\right) e^{-jk_z z} \tag{2.46}$$

where k_z is the z component of the wave vector and $m = 0,1, \ldots$ and $n = 0,1, \ldots$, but $m \neq n$. The other fields H_x, H_y, E_x and E_y are determined using this solution and the Maxwell's equations. Thus, the electromagnetic fields corresponding to (m, n) are defined as TE_{mn} modes, being TE_{10} mode the dominant mode in the waveguide. Examples of TE_{mn} modes are given in Figure 2.18, considering that m describes the number of half cycle variations of the electric field along x-axis and n denotes the number of half cycle variations of the electric field along y-axis. If m or n is 0 the field is 0.

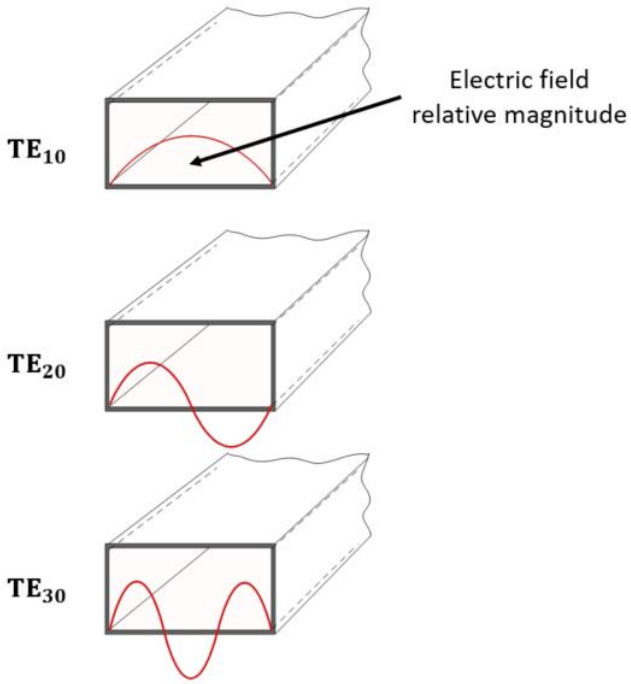


Figure 2.18: Schematic diagram of a rectangular waveguide of aperture $a \times b$ [152].

Conversely, in the TM mode, the magnetic field is transverse to the direction of wave propagation (z-axis), $H_z = 0$ and E_z should be solved from the wave equation 2.14 for TM mode. The solution with infinite roots is given by:

$$E_{z\,mn}(\mathrm{x},\mathrm{y},\mathrm{z}) = e_{mn} \sin\left(\frac{m\pi x}{a}\right) \sin\left(\frac{n\pi y}{b}\right) e^{-jk_z z} \tag{2.47}$$

where the electromagnetic fields corresponding to (m, n) are defined as TM_{mn} modes. Also in this case, m and n indicate the number of half wave of the magnetic fields in both the broader and shorter dimension.

Note that the rectangular waveguide is able to propagate the radiation only above a certain frequency that is called cut-off frequency. The mode of propagation with the lowest cut-off frequency is called dominant mode and TE_{10} corresponds to the lowest cut-off frequency in the rectangular waveguide.

$$E_{z\,mn}(\mathrm{x},\mathrm{y},\mathrm{z}) = e_{mn} \sin\left(\frac{m\pi x}{a}\right) \sin\left(\frac{n\pi y}{b}\right) e^{-jk_z z} \tag{2.48}$$

Horn Antenna

A horn antenna is employed to transmit and receive radio waves from a waveguide out into space. Made by conductive material, the horn antenna is composed by a short a rectangular or cylindrical waveguide closed on one side, while the other side flares

into an open-ended conical or pyramidal shape. The antenna is connected to a coaxial cable attached on one side, with the central conductor projecting into the waveguide to form a quarter-wave monopole antenna. The important parameters of a radiative horn antenna are its bandwidth, directivity, gain, 3dB beamwidth, radiation pattern and polarization.

Horns have very little loss, so the directivity of a horn is roughly equal to its gain, which can be expressed as:

$$G = \frac{4\pi A}{\lambda} e_A \tag{2.49}$$

where A is the aperture area, λ the wavelength and e_A the aperture efficiency. The gain is usually expressed in dBi, i.e., relative to the gain of an isotropic antenna, and is inversely proportional to the antenna coverage, also defined as 3dB beamwidth, i.e., the angle in degrees between the half-power points of an antenna beam over which the relative power is at or above 50% of the peak power. This means that an antenna with high directivity and gain displays a less of a broad field pattern, meaning that the signal strength will go further but in a narrower direction.

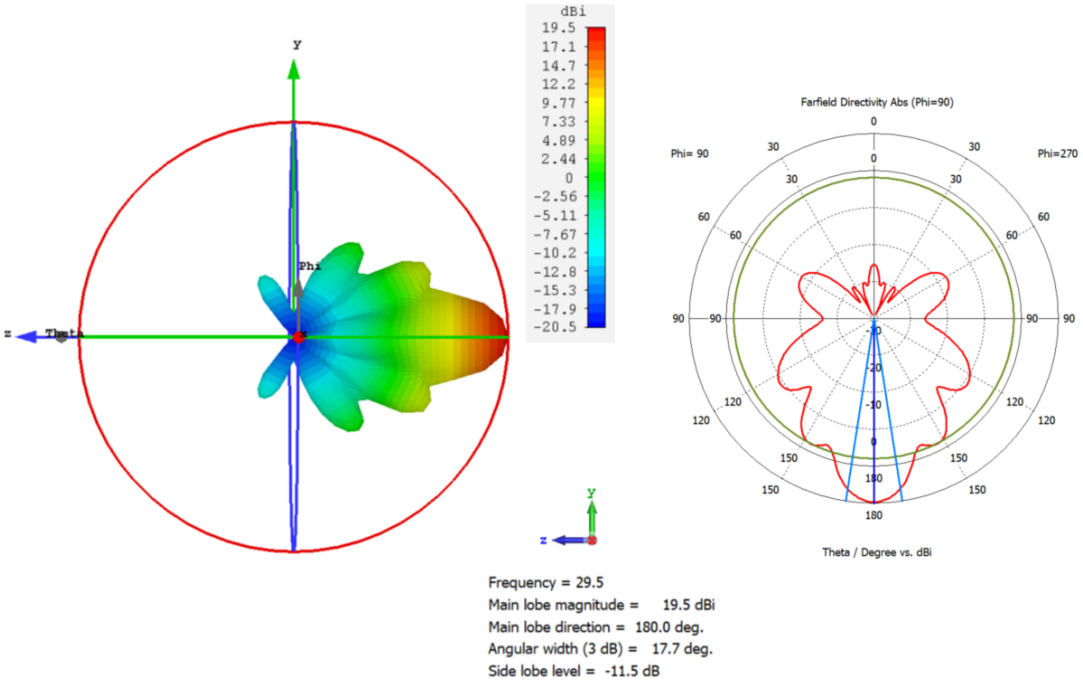


Figure 2.19: Simulated radiation pattern of LB-28-20.

The antenna used for the tests, is a horn antenna LB-28-20 [152], with frequency range in the Ka-band (26.5-40 GHz), waveguide WR28, linear polarization, $G \simeq 20$ dBi, and 3 dB beamwidth of $\simeq 16^\circ - 18^\circ$. Figure 2.19 shows the simulated radiation pattern at 29.5 GHz for LB-28-20.

2.4.3 Test locations

Electromagnetic measurements and Electromagnetic Compatibility (EMC) measures often requires the use of a specifically designed testing room, which has the scope of avoiding electromagnetic interference phenomena coming from external sources (i.e., emissions from electric and electronic devices) and cross-interference in same the test location. EMC measurements of military and civil type (e.g., MIL-STD-461, CE marking) follow standards, which expect the use of test chambers such as anechoic chamber or reverberation chamber. In the following, a brief description of the aforementioned rooms is presented.

RF anechoic chamber

A RF anechoic chamber is a room designed to stop reflections of electromagnetic waves. The chamber is also shielded from energy entering from its surroundings, as to simulate the conditions of free space. Therefore, waves propagating towards the walls, ceiling, and floor of the enclosure must be absorbed using a suitable radiation absorbent material (RAM), generally made in a pyramid shape. The absorber treatment has the aim to render the reflected energy coming from the walls of the range small or negligible respect to any of the features of interest on the radiation pattern of the test equipment. A lossy RF absorber is shaped such that the incoming electromagnetic wave can penetrate the material with minimal reflections, as the energy traveling inside transforms into thermal energy and dissipates into the surrounding air [153].

Uses for RF anechoic chambers include testing of antennas, radars, electromagnetic compatibility measurements, shielding and electromagnetic characterization. It is typically used to house the antennas in transmitting/receiving configuration to perform measurements such as antenna radiation patterns, radiated emission and radiated susceptibility.

Anechoic chambers can be the size of a small room, but also of much larger dimensions, up to those of a hangar; according to their function, there are different types:

- Full anechoic chamber: entirely covered with RF absorbing panels (walls, ceiling, floor);
- Semi-anechoic chamber: when it is not completely shielded, for example the floor may not be covered with a RF absorbing material but, instead, with a reflective one;
- Tapered anechoic chamber: can offer better performance than the standard rectangular chamber for antenna measurements at lower frequencies. One of the wall of the chamber is characterized by a tapered shape, where the

transmitting antenna is allocated. It can be of smaller size than a regular semi or full anechoic chamber, making it useful for small space allocations [154]. In these chambers, the reflectivity is not minimized as it is done on rectangular chambers, but it is used to illuminate the quiet zone of the chamber.

An example of a typical RF test setup of radiated emission is given in Figure 2.20, where the test is held inside a semi anechoic chamber: the radiation coming from the tested electronic device is measured through a biconical antenna and a network analyzer, the signal is then post processed in the control room.

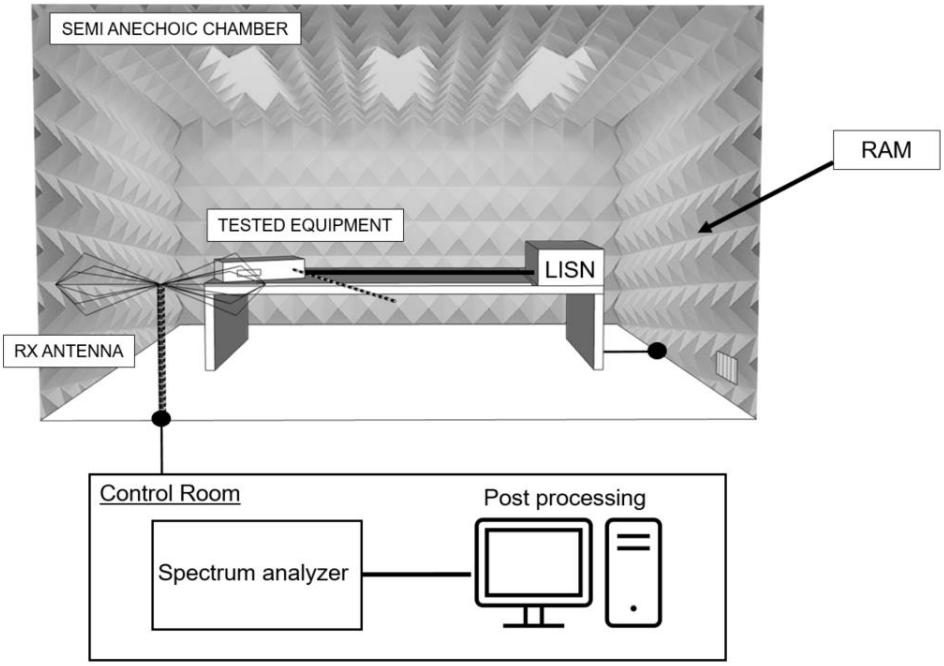


Figure 2.20: Example of a radiated emission test in semi anechoic chamber.

Reverberation chamber

A reverberation chamber generally consists of a rectangular test room with metal walls and one or two mode stirrer(s), usually in the form of a large paddle, near the ceiling of the chamber, as shown in Figure 2.21. Unlike the anechoic chambers, the walls of reverberation chamber do not absorb electromagnetic energy and reflect the incident waves instead. Due to the minimal amount of energy absorbed by the walls, it is possible to obtain high intensity fields by injecting signals of moderate power. A reverberation chamber is a hollow resonator with an extremely high quality factor. The main feature is to provide a statistically homogeneous field to ensure that the device tested inside the chamber is hit at any moment by plane waves having all possible directions of propagation and different polarization. To ensure this field uniformity, a mechanical stirrer is installed inside the reverberation chambers, i.e. a construction

that includes reflective metal shapes oriented at different angles and which, rotating on their own axis, guarantee a continuous change of the surrounding conditions. The average response of the tested equipment to the field is found by integrating the response over the period of one revolution of the stirrer. Hence, the most significant characteristic of a reverberation chambers are [155]:

- Spatially uniform energy density;
- Random polarization of the electric field;
- Isotropy: same energy flow in all directions;
- Longer calibration time compared to anechoic chamber.



Figure 2.21: Example of reverberation chamber with a stirrer on the ceiling [156].

2.5 Computational tool

One popular Computational Electromagnetics software package, which can be used for this purpose is CST Microwave Studio®. The electromagnetic software can be used to simulate the electromagnetic behaviour of a variety of structures, using the Finite Integration Technique (FIT) to numerically solve the Maxwell's equations for the model domain. FIT was proposed in 1977 by Thomas Weiland and has been enhanced continually over the years [157]–[160].

FIT discretizes the integral form of Maxwell's equations, defining a finite calculation domain. The model domain is spatially discretized creating a suitable mesh grid of hexahedral or tetrahedral elements. For simplicity, considering the element cell of a hexahedral mesh, presented in Figure 2.22, the electric voltage $\boldsymbol{e}$ and magnetic

facet flux ***b*** is allocated on the primary grid (a thorough explanation can be found in the CST Studio Suite Help contents).

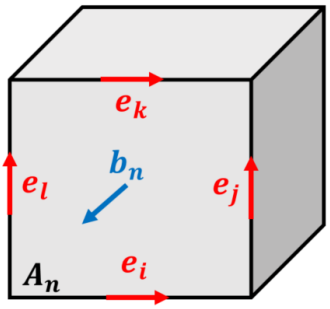


Figure 2.22: Electric voltage **e** and magnetic flux **b** on the face of a mesh grid hexahedral element.

Considering for example the integral form of equation 2.12 written in the time domain, i.e. Faraday's law,

$$\oint \mathbf{E} \cdot \mathrm{d}\mathbf{l} = -\frac{\partial}{\partial t} \iint \mathbf{B} \cdot \mathrm{d}\mathbf{S} \tag{2.50}$$

The closed integral on the contour of A_n can be written as a sum of four grid voltages equal to the time derivative of the magnetic flux on the facet of surface A_n, which is defined following the right-hand rule, as depicted in Figure 2.20. Therefore, the equation 2.46 can be expressed in its discretized form as:

$$e_i + e_j - e_k - e_l = -\frac{\partial}{\partial t} b_n \tag{2.51}$$

Subsequently, equation 2.51 can be rewritten in matrix formulation, once the same procedure is applied to all the cell facets in the finite domain, introducing the matrix $\mathbf{C}$ as the discrete equivalent of the curl operator:

$$\mathbf{Ce} = -\frac{\partial}{\partial t}\mathbf{b} \tag{2.52}$$

Therefore, applying the discretization over the spatial domain to Maxwell's equations, it is possible to obtain the complete discretized set of Maxwell's Grid Equations (MGEs):

$$\check{\mathbf{S}}\mathbf{d} = \mathbf{q} \tag{2.53}$$

$$\mathbf{Sb} = 0 \tag{2.54}$$

$$\mathbf{Ce} = -\frac{d}{dt}\mathbf{b} \tag{2.55}$$

$$\check{\mathbf{C}}\mathbf{h} = -\frac{d}{dt}\mathbf{d} + \mathbf{j} \tag{2.56}$$

where **d** is the dielectric facet flux, **h** is the magnetic grid voltage, $\check{\mathbf{C}}$ is dual discrete curl operator, **S** is the discrete divergence operator, $\check{\mathbf{S}}$ is the dual discrete divergence operator, **q** is the electric charge density and **j** electric current density.

Finally, the necessary constitutive relations can be approximated over the grid edges and cell areas. Consequently, the resulting coefficients depend on the averaged material parameters as well as on the spatial resolution of the grid and are expressed in matrix form as:

$$\mathbf{d} = \mathbf{M}_{\boldsymbol{\varepsilon}}\mathbf{e} \tag{2.57}$$

$$\mathbf{b} = \mathbf{M}_{\boldsymbol{\mu}}\mathbf{h} \tag{2.58}$$

$$\mathbf{j} = \mathbf{M}_{\boldsymbol{\sigma}}\mathbf{e}\mathbf{j}_{\mathbf{S}} \tag{2.59}$$

Chapter 3

Low-band Electromagnetic Interference (EMI) shielding of CFRP

3.1 EMI shielding and CFRP

In order to achieve a more detailed definition of the electromagnetic behaviour of woven and unidirectional carbon fibre composites, a study was conducted at low-band frequencies to assess the transparency of CFRP to electromagnetic radiation. The chosen method involves the Electromagnetic Interference (EMI) shielding theory or Shielding Effectiveness (SE) theory, which is generally applied to describe the electromagnetic behaviour of conductive materials, such as metals. Considering that the CFRP behaves as a high-loss material or at most as a lossy dielectric, a measurement method developed for assessing the SE of metal is a suitable choice for this type of materials. Nonetheless, it is important to remember that EMI shielding measurement methods can be applied to estimate the transmission coefficient S_{21} of both dielectric and high lossy material. At the same time, the estimation of the SE of CFRP and how much this material can be transparent or not to the electromagnetic radiation can be useful to evaluate their utility for Electromagnetic Interference (EMI) shielding applications.

The Electromagnetic Interference is the disturbance generated from an external radiation source [161]. Protecting living organisms and electronic devices from the incoming electromagnetic pollution becomes an important task, to both preserve the wellbeing of living species and integrity and functionality of electromagnetic apparatuses (e.g., mobile phones, television, wireless systems, navigation systems and radar) [162]–[166]. To address this problem, suitable mechanisms of shielding the

radiation are needed. EMI shielding is defined as the act of controlling electromagnetic interference by blocking the field radiation with barriers made of conductive or magnetic materials [167]. Shielding materials present the ability to obstruct and minimize the signal emitted through backwards reflection of the field waves or through absorption and dissipation of the radiation power inside the material [168]. In order to reflect the electromagnetic waves, the shield must be characterized by mobile charge carriers and therefore tends to be electrically conducting; however, high conductivity is not required and a volume resistivity of 1 Ωcm is accepted [169]. Thus, traditional shielding materials consist of sheet metal, metal screen, meshes, metal foam and volume conductive paints with metal powders [169].

To quantify how much these materials exhibit shielding potential, the Shielding Effectiveness (SE) parameter is widely used. For metals the SE can be calculated through the Schelkunoff's equations, knowing the magnetic permeability and electric conductivity [170], [171]. This index is expressed in dB and for most industrial and consumer applications a signal reduction of 30 dB is considered adequate [172], for the making of electronic housing as for electronic appliances at least 40 dB are required, a SE value higher than 100 dB implies that the material is essentially impenetrable [173].

Over recent years, alternatives to traditional metals are being studied for possible EMI shielding applications. In particular, various research has been carried out on polymer based conductive composites and their application to the enclosures of electronic devices. The advantages offered by conductive plastic composites over conventional metals include lighter weight, corrosion resistance, lightning protection, and flexibility in design, which abates the housing seams typical of a metallic sheets shield [174], [175]. Polymer matrix composites with carbon-based filler have therefore been studied as a promising alternative, especially those with carbon nanotubes [176]–[179].

However, as stated in Section 1, CFRPs are extensively used in the aeronautic industry and show also good shielding properties (i.e., due to being high-loss materials), combined with their good mechanical characteristics. Their shielding efficiency depends on the conductive reinforcement used. To obtain a high level of shielding effectiveness the filler/fibres should have small size unit, high conductivity and high aspect ratio, to increase the electrical connectivity [169]. Extensive studies have been made on the shielding effectiveness of carbon materials including carbon fibres, colloidal graphite and flexible graphite by Chung [169], [176], [180]–[183].

For composite materials, theoretical calculation of SE is still developing and can only be realized through experimental work or numerical simulations. SE measurements can be conducted via experimental standard methods, such as the MIL-

STD-285 and ASTM D4935 standard tests [184]–[187]. The equipment required may consist of rectangular or coaxial waveguides, or in some configurations even spot-focusing horn lens antennas [188]. CST Microwave Studio® can be used for the design of the waveguides described by the chosen standard test method, or for the simulation of incident plane waves and consequently can be applied for calculations of SE if the electric properties of the material under test are known [189]–[191].

3.2 EMI shielding theory

3.2.1 The shielding mechanism

The electromagnetic plane wave theory is applied for EMI shielding in the far field region where the shield distance from the radiation source is larger than $\lambda_0/2\pi$, being λ_0 the free space wavelength of the electromagnetic field.

According to Schelkunoff's approach when an electromagnetic plane wave is incident on a shielding material a part of the wave energy is reflected at the interface with the shield, as a result of the difference in impedance between the incident wave and the shield [161], [192], as previously described in Section 2.1.3. This primary mechanism, defined as *reflection loss*, requires the presence of charge carriers in the material, i.e. for the shield to be electrically conducting, and is a function of the ratio between the electrical conductivity and the magnetic permeability of the shield. A second part of the wave energy is then absorbed by the volume of the material, this second mechanism is called *absorption loss* and is inversely proportional to the skin depth of the material. The absorption loss is the result of the heat generated in the shield and is related to the interaction of electric and/or magnetic dipoles with the electromagnetic field. In addition, a third part of the electromagnetic radiation is attenuated by multiple reflections, which take place at various surfaces or interfaces in the shield and is called *multiple reflection loss*. This third mechanism can be disregarded for SE calculations if the shield thickness is much greater than the skin depth, when the absorption loss is ≥15 dB. Finally, the last part of the electromagnetic field is transmitted through the material, so that the effectiveness of the shield can be viewed as the ratio expressed in dB of the electric/magnetic incident field intensity to the intensity of the electric/magnetic field that is transmitted through the shield:

$$\mathrm{SE} = 20\log_{10}\left(\frac{E_i}{E_t}\right) = 20\log_{10}\left(\frac{H_i}{H_t}\right) = 10\log_{10}\left(\frac{P_i}{P_t}\right) \tag{3.1}$$

where the subscripts 'i' and 't' indicate respectively the incident radiation and the transmitted radiation, as per Section 2.1.3. Alternatively, the expression provided by

the ratio of the powers of the incident and transmitted electromagnetic signals can also be used.

3.2.2 EMI SE of a conductive plate

The shielding effectiveness can be expressed as the sum of the three contributions [171], [193], [194]:

$$\mathrm{SE} = SE_R + SE_A + SE_{MR} \tag{3.2}$$

each contribution, reflection loss (SE_R), absorption loss (SE_A) and multiple reflection (SE_{MR}), influence the overall ability of a material to shield from radiation. In order to have a better understanding of these three mechanisms, the case study of a homogeneous conductive slab is presented.

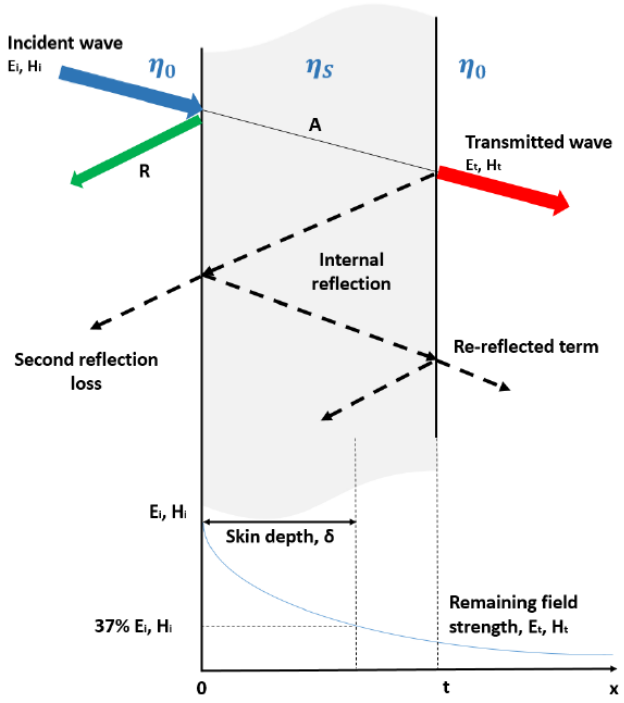


Figure 3.1: Concept of shielding effectiveness (SE) for a slab of conductive material, wave absorption, reflection, re-reflection and transmission mechanisms.

As shown in Figure 3.1 [45], the electromagnetic wave propagates in the free space until it encounters a material with different intrinsic impedance η_S. In the far field region, the intrinsic impedance of the free space is given by the ratio between the incident electric field ($\boldsymbol{E_i}$) amplitude and the incident magnetic field ($\boldsymbol{H_i}$) amplitude and is a constant equal to 377 Ω:

$$\eta_0 = \frac{|\boldsymbol{E_i}|}{|\boldsymbol{H_i}|} = \sqrt{\frac{\mu_0}{\varepsilon_0}} \simeq 377\ \Omega \tag{3.3}$$

while the corresponding intrinsic impedance of a good conductor is given by [171]:

$$\eta_S = \frac{|\boldsymbol{E_i}|}{|\boldsymbol{H_i}|} = \sqrt{\frac{i\omega\mu_r}{\frac{\sigma}{\varepsilon_0} + i\omega\varepsilon_r'}} = \sqrt{\frac{i\omega\mu}{\sigma + i\omega\varepsilon_e'}} \simeq \sqrt{\frac{i\omega\mu}{\sigma}} \tag{3.4}$$

where for high conductivity $\sigma \gg \omega\varepsilon_e'$. The angular frequency ω, the relative ε_r' and absolute ε_e' dielectric constant, the relative μ_r and absolute μ permeability, and the conductivity σ are defined with same notations as Chapter 2.

The reflection loss parameter is related to the difference in characteristic impedances of free space and the conductive medium. As shown in Figure 3.2, the intensity of the transmitted electric field at the first interface between free space and medium is:

$$E_S = \frac{2\eta_S}{\eta_0 + \eta_S} E_i \tag{3.5}$$

At the second boundary of the shielding material, the wave passes from a medium with impedance η_S to the free space again, the intensity of the electric field transmitted through the medium is:

$$E_t = \frac{2\eta_0}{\eta_0 + \eta_S} E_S = \frac{4\eta_0\eta_S}{(\eta_0 + \eta_S)^2} E_i \tag{3.6}$$

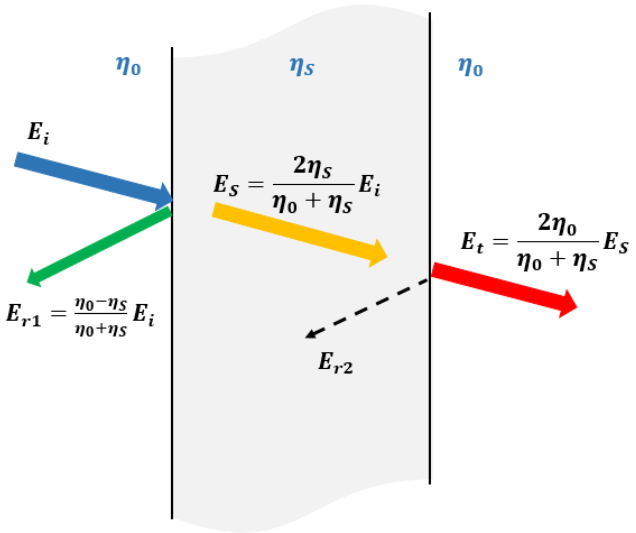


Figure 3.2: Incident wave transmitted at two boundaries with different impedance. E_S and E_{r1} are respectively the intensity of the transmitted and reflected wave at the first interface and E_t is the transmitted wave through the second boundary.

Substituting the wave impedance prior to entering the shield η_w for η_0 and disregarding the effect of the multiple reflections SE_R can be defined as:

$$SE_R = 20\log_{10}\left(\frac{E_i}{E_t}\right) = 20\log_{10}\frac{(\eta_w + \eta_S)^2}{4\eta_w\eta_S} \tag{3.7}$$

If the shield is a homogeneous conductive plate surrounded by an insulator, then the impedance of the shield is much smaller than the impedance of the incident wave and the largest reflection occurs at the first boundary, consequently also a thin sheet of conductive material can provide a good reflection loss. Therefore, if $\eta_w \gg \eta_S$:

$$SE_R = 20\log_{10}\frac{\eta_w}{4\eta_S} \tag{3.8}$$

The absorption loss SE_A is related to the electromagnetic field amplitude. On encountering a shield made of a conductive material, the amplitude of the electromagnetic wave decreases exponentially, according to equation:

$$E_t = E_i e^{-t/\eth} \tag{3.9}$$

where *t* is the thickness of the shield. Therefore, the absorption loss can be written as:

$$SE_A = 20\log_{10}\left(\frac{E_i}{E_t}\right) = 20\log_{10}\left(e^{t/\eth}\right) = 20\left(\frac{t}{\eth}\right)\log_{10}(e) \tag{3.10}$$

Substituting the expression of the skin depth, equation 2.29, written as function of the frequency into equation 3.10, the absorption loss is expressed as:

$$SE_A|_{dB} \simeq 15.4t\sqrt{f\mu\sigma} \tag{3.11}$$

where equation 3.11 shows the absorption loss as function of the permeability, the conductivity and the thickness of the shielding material. Thus, SE_A increases with the frequency and the thickness of the shield.

Finally, the third contribution to the SE for a slab of conductive material surrounded by an insulating medium is linked to the primary reflection of the magnetic field. While for the electric field the primary reflection occurs at the first interface, for the magnetic field the primary reflection occurs at the second boundary of the shield and multiple reflections generates within the shield. If the shield is thin and the absorption loss is not significant, the reflected wave at the second boundary returns to the first boundary where is reflected again and so on until the amplitude of the field gradually decreases because of the multiple passages through the thickness of the

shield. Therefore the correction factor due to the multiple reflections related to the propagation of the magnetic fields is given by:

$$SE_{MR} = 20\log_{10}\left|1 - \frac{(\eta_S - \eta_w)^2}{(\eta_S + \eta_w)^2} e^{-2t/\delta}\right| \tag{3.12}$$

SE_{MR} is a function of the ratio t/δ and is a negative number. This parameter can be neglected if the thickness of the shield is greater than the skin depth, for plane waves the reflection loss is high and the re-reflection loss is small. If the thickness of the material is equal to the skin depth the correction factor is less than 2 dB, when $t = 0.1\delta$ the correction factor is 15 dB [161].

3.2.3 EMI SE measurement of non-metallic materials

A two-port VNA connected across a coaxial or rectangular waveguide sample holder can be used for measuring the power reflected P_r and transmitted P_t at the two ports, when the incident power is known P_i [193], [195]. P_i can be defined as the sum of three terms, power reflected towards port 1 at the first boundary air/sample, power absorbed P_a and power transmitted P_t after the second boundary composite/sample:

$$P_i = P_r + P_a + P_t \tag{3.13}$$

The SE is obtained by means of the phase and magnitude of the scattering parameters S_{11} (or S_{22}) and S_{21} (or S_{12}), where they are related to the reflectance (*R*), the transmittance (*T*) and the absorbance (*A*), according to the following equations:

$$R = |S_{11}|^2 = \frac{P_r}{P_i} \tag{3.14}$$

$$T = |S_{21}|^2 = \frac{P_t}{P_i} \tag{3.15}$$

$$A = \frac{P_a}{P_i} = 1 - R - T \tag{3.16}$$

Considering the power balance, the SE is given by the sum of the shielding by reflection and the shielding by absorption contributions, and in case of negligible SE_{MR}, SE_R and SE_A can be expressed in mathematical terms as follows [179]:

$$\text{SE} = SE_R + SE_A \tag{3.17}$$

$$= 10\log_{10}\left(\frac{P_i}{P_t}\right)$$
$$= 10\log_{10}\frac{P_i}{P_i - P_r} + 10\log_{10}\frac{P_i - P_r}{P_t}$$
$$= 10\log_{10}\frac{1}{1 - |S_{11}|^2} + 10\log_{10}\frac{1 - |S_{11}|^2}{|S_{21}|^2}$$
$$= 10\log_{10}\left|\frac{1}{|S_{21}|^2}\right|$$

Therefore the measure of the transmission coefficient S_{21}, i.e. the forward voltage gain, gives the value of the overall SE along the range of frequencies considered, according to equation 3.17.

3.2.4 SE as function of resistivity

When equations 3.8 and 3.11 are substituted in equation 3.2, having disregarded the multiple reflections mechanism, the SE can be expressed as:

$$SE = 20\log_{10}\frac{\eta_w}{4\eta_S} + 15.4t\sqrt{f\mu\sigma} \tag{3.18}$$

Combining equation 3.4 with equation 3.18 and considering that a polymer composite material is non-magnetic $\mu = \mu_0$, the SE becomes:

$$SE = 20\log_{10}\eta_w - 20\log_{10}\left(4\sqrt{\frac{\omega\mu_0}{\sigma}}\right) + 15.4t\sqrt{f\mu_0\sigma} \tag{3.19}$$

Thus, it is possible to express the EMI shielding of conductive plastics, such as electroconductive composites (e.g., CFRP), as a function of the resistivity (or conductivity), the frequency and the thickness of the composite material used as a shield. This expression is called Simon formalism [196], [197]:

$$SE|_{dB} = 50 + 10\log_{10}(\rho f)^{-1} + 1.7t(f/\rho)^{1/2} \tag{3.20}$$

where f is the frequency in MHz, t the thickness of the material in cm and ρ is the volume resistivity expressed in Ωcm. The reflection loss SE_R is estimated by the first two terms, the third term evaluates the absorption loss SE_A.

3.3 Experimental evaluation of SE of CFRP

3.3.1 Materials preparation

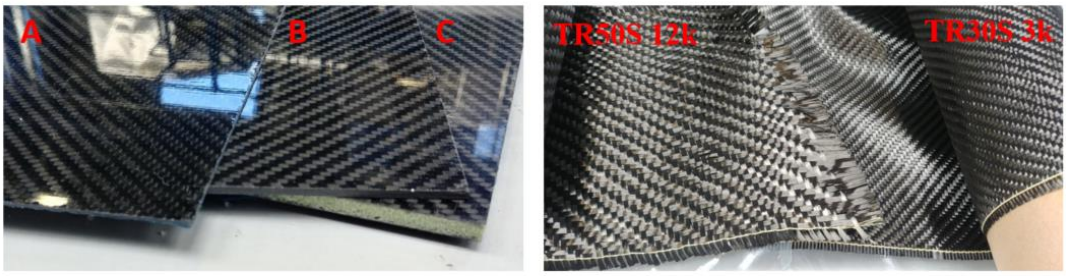
EMI shielding measurements were performed on CFRP samples and on woven and UD dry carbon fibres:

- Two CFRP samples made of pre-impregnated 2/2 twill fabric of two different weights;
- One carbon fibre sandwich panel;
- Two samples made of layers of dry carbon reinforcements in order to verify the impact on the SE parameter of the absence of the epoxy resin medium. To observe meaningful results the dry carbon fibres considered are of the same type and same pattern as in the prepregs;
- One sample made of UD carbon fibres.

Table 3.1: Geometrical properties of CFRP samples.

CFRP Specimen	Thickness [mm]	No of plies	Stacking sequence
A	1 ± 0.15	4	XPREG XC130-210gsm XPREG XC130-450gsm XPREG XC130-450gsm XPREG XC130-210gsm
B	3 ± 0.25	8	XPREG XC130-210gsm XPREG XC130-450gsm XPREG XC130-450gsm XPREG XC130-450gsm XPREG XC130-210gsm XPREG XC130-450gsm XPREG XC130-450gsm XPREG XC130-210gsm
C	6 ± 0.29	5	XPREG XC130-210gsm woven E-glass EasyCell 75 Foam core woven E-glass XPREG XC130-210gsm

The high strength CFRP samples (i.e., specimen A and B) were made of layered prepregs: XPREG XC130 210 g/m^2 and XPREG XC130 450 g/m^2, with standard carbon reinforcements Pyrofil TR30S 210 g/m^2 3k and TR50S 450 g/m^2 12k respectively, intertwined according to a 2/2 twill weave pattern. The stacking sequence and thicknesses are reported in Table 3.1. Each layer is orientated at 0° and 90° orientation. There was no layer rotation during the lay-up procedure. After layering the prepregs as per Table 3.1, both the wet samples underwent a curing cycle in



(a) (b)

Figure 3.3: (a) Composite panel of Specimen A, B and C; (b) 2/2 twill carbon fibres.

autoclave at 100°C and pressure at 8 bar under vacuum for 4 h. Laminates of 1 mm thickness (specimen A) and 3 mm thickness (specimen B) were obtained.

The carbon fibre sandwich panel (i.e., specimen C) was cut out from Easycomposites high strength carbon fibre sandwich panel 6 mm. Specimen C is composed of one layer of XPREG XC130 210 g/m^2 on top of a layer of E-glass on each side (i.e., panels) with a 5 mm of PVC foam core. The carbon composites and carbon fibre used are shown in Figure 3.3.

Consequently, in order to analyse the impact of the carbon reinforcements only, samples with one layer of dry fibres (i.e., specimen D), with four layers of dry fibres (i.e., specimen E) and with one layer of unidirectional carbon fibres (i.e., specimen F) were prepared. The stacking sequence can be found in Table 3.2. Specimen D was made by gluing one layer of dry carbon fibres TR30S, orientated according to 0° and 90° orientation, on a fibreglass panel which displays a good dielectric behaviour and is transparent to radio waves. Specimen D was made with the aim to assess the SE of only one layer of dry fibres. The same procedure was applied to specimen E. Four layers of dry fabric, oriented according to 0° and 90°, were glued to a fiberglass support in order to mimic the stacking sequence of Specimen A and to observe the effect of the absence of the polymer matrix on the overall SE. As epoxy resin is a common electrical insulator with average electrical resistivity of the order of $\simeq 10^{14} - 10^{16}$ Ωm, see Table 1.2.

Table 3.2: Geometrical properties of dry carbon fibre samples.

Carbon fibre specimen	Type	No of plies	Stacking sequence
D	2/2 twill	1	TR30S 3k
E	2/2 twill	4	TR30S 3k TR50S 12k TR50S 12k TR30S 3k
F	UD	1	TR50S 15k

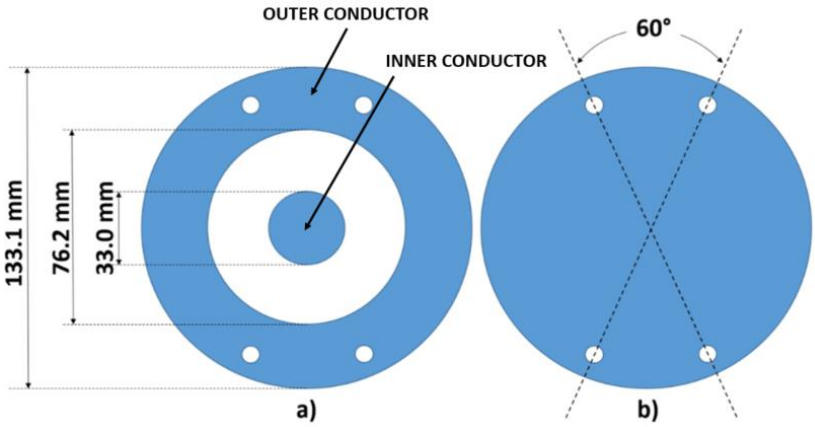


Figure 3.4: ASTM D4935: Dimension of (a) Reference specimen; (b) Load specimen.

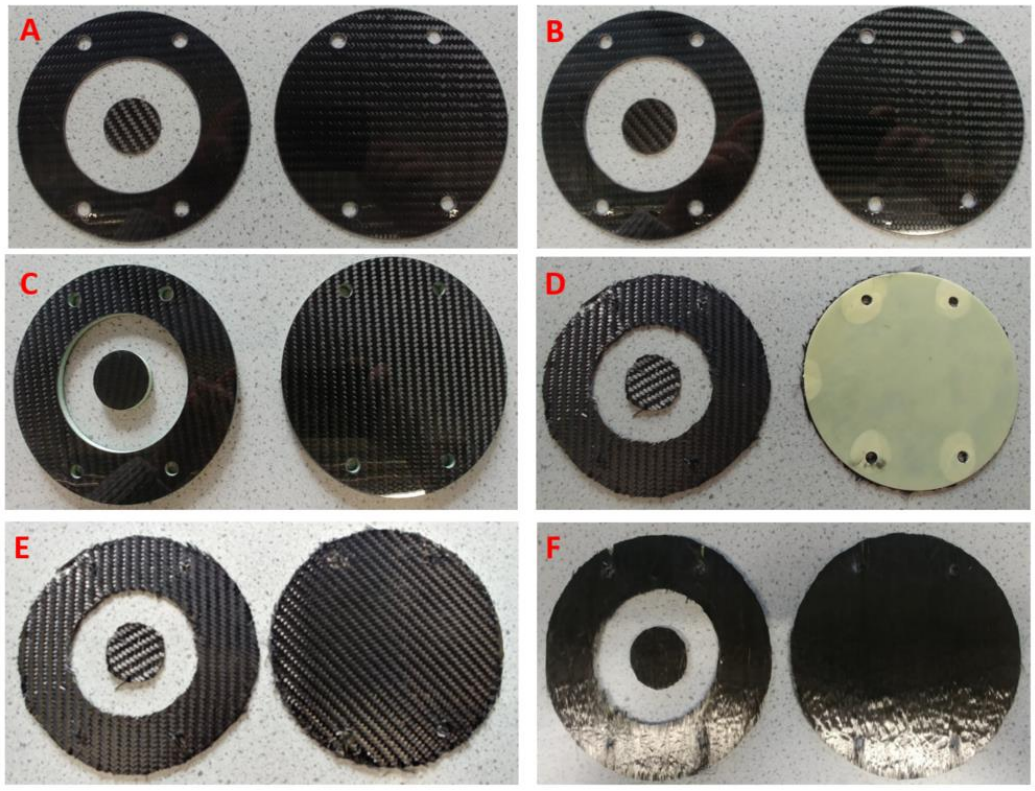


Figure 3.5: Specimen A-B: CFRP laminate; Specimen C: Carbon sandwich panel; Specimen D: 1 layer of dry 2/2 twill fibres; Specimen E: 4 layers of dry 2/2 twill fibres; Specimen F: 1 layer of dry UD fibres.

Therefore, specimen A can be compared to specimen E and an increase in shielding effectiveness is to be expected as a result of the direct contact between the carbon fibres. The experimental tests confirmed this behaviour to the point where specimen E exceeded the dynamic range of the Network Analyser. Hence, the preparation of an additional specimen, which was repeating the stacking sequence of specimen B without resin, was considered not useful for the study purposes, having considered the greater shielding power provided by doubling the number of layers of dry carbon fibres

and the consequent lack of measurable results. Finally, Specimen F was created in a similar fashion as specimen D, but with one layer of Pyrofil TR50S 15k with light weight of 100 g/m^2.

The samples were shaped by waterjet cutting with the dimensions reported in Figure 3.4. For each material to be tested, a reference specimen and a load specimen were prepared. The reference is composed by two parts having dimensions equal to the inner and outer conductors of the coaxial line, while the load has the diameter equal to that of the outer conductor of the coaxial line. A visual depiction of the prepared samples is provided in Figure 3.5.

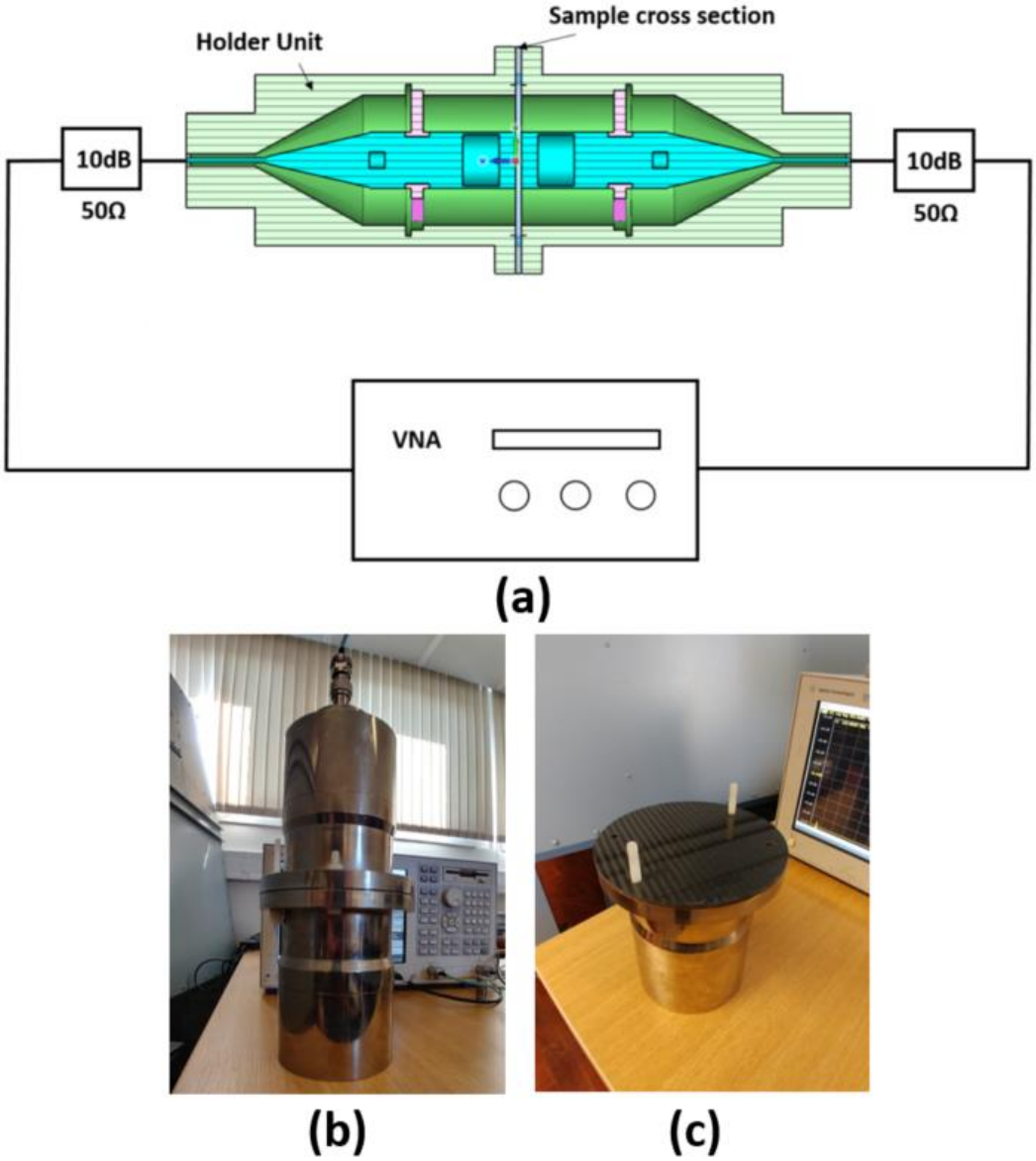


Figure 3.6: (a) Diagram of the ASTM D4935 measurement setup for electromagnetic SE measurement; (b) coaxial unit holder manufactured according to ASTM D4935-99; (c) Load specimen B in place.

3.3.2 ASTM D4935 method

The experimental measurements were realized by means of a coaxial transmission line, according to the ASTM D4935 standard, used to measure the shielding effectiveness of planar specimens [188]. The advantages offered by this technique are repeatability of measurements and the possibility to determine the components of the electromagnetic signal, i.e. which part of the signal is reflected, absorbed or transmitted [184]. The set-up used is shown in Figure 3.6 and consist of a programmable E5062A ENA-L RF network analyser coupled with a coaxial specimen holder unit. The coaxial line is realized with external and internal conductors made of brass, the outer conductor is expanded to maintain throughout the entire length of the holder a 50 Ω impedance and 10 dB attenuators are placed at each end of the specimen holder with the function of insulators from the input and output signal.

The inferior limit of the dynamic measurement range (DR) was ensured using a standard metallic attenuator with a maximum attenuation of DR ≃ 110 dB. Values within 10 dB of the smallest detectable signal were considered beyond the dynamic range according to the ASTM D4935 standard. The frequency was scanned from 30 MHz to 1.5 GHz to ensure transverse electromagnetic (TEM) mode propagation. The values of the incident power (voltage) and the transmitted power (voltage) through the shield were recorded in 401 data points at each frequency. Two rounds of measurements were required for each material. The SE parameter was calculated measuring first the transmitted power while inserting the reference specimen P_t^{Ref}, this allows to repeat the capacitive coupling of the loaded case, when establishing the reference level, leaving the space between the two conductors free (i.e., unloaded). Once replaced the reference with the load, the test was repeated to measure again the transmitted power P_t^{Load}. Therefore, according to equations 3.15 and 3.17 the SE is given by:

$$\begin{aligned} SE|_{dB} &= \left|S_{21}^{Load}\right| - \left|S_{21}^{Ref}\right| = 10\log_{10}\frac{P_t^{Load}}{P_i} - 10\log_{10}\frac{P_t^{Ref}}{P_i} \\ &= 10\log_{10}\frac{P_t^{Load}}{P_t^{Ref}} \end{aligned} \tag{3.21}$$

Furthermore, the power reflected back to the source and the power transmitted from port 1 to port 2, for both reference and load specimens are obtained from the scattering parameters S_{11} and S_{21}:

$$P_r^{Ref/Load} = P_i 10^{\frac{S_{11}^{Ref/Load}}{10}} \tag{3.22}$$

$$P_t^{Ref/Load} = P_i 10^{\frac{S_{21}^{Ref/Load}}{10}} \tag{3.23}$$

3.3.3 Experimental results

The measurements were recorded using a receiver bandwidth of 300 Hz and a signal power of 5 dBm, to lower the minimum range detectable and reduce the signal to noise ratio. The coaxial transmission line was tested with a fiberglass material, as shown in Figure 3.7. The fiberglass is a dielectric material and does not block the electromagnetic radiation. Hence, total transmission of the signal from port 1 to port 2 is expected, i.e., $S_{21} = 0$. The signal measured is of -20 dB, due to the two 10 dB attenuators. Without the attenuators, a value of 0 dB can be observed.

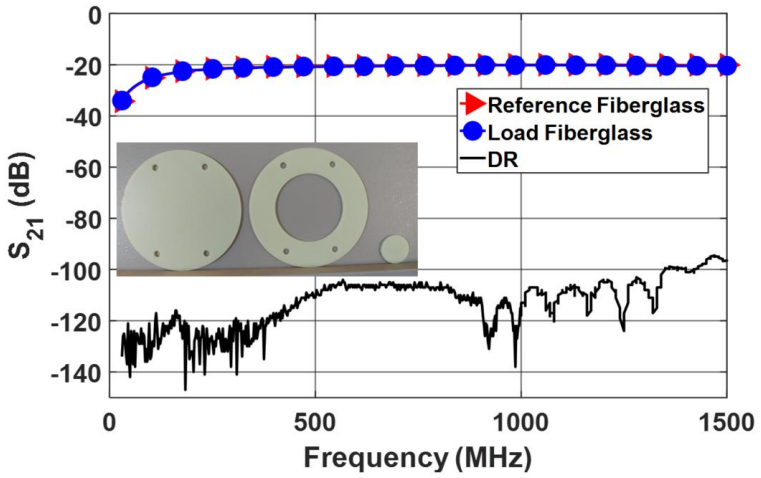


Figure 3.7: S_{21} measured for both reference and load samples made of fiberglass.

Figure 3.8 shows the scattering parameter S_{21} measured for the samples of Figure 3.4. The transmission coefficient were measured for references and loads for each specimen (average over 5 measurements taken, with standard deviation inferior to 3 dB for reference and to 7 dB for load). For the carbon fibres/epoxy laminates (i.e., specimen A and B), it was possible to obtain S_{21} values for a range of frequencies up to 450 MHz, beyond this point the measured values exceed the DR of the system. This behaviour is caused by the high conductivity of carbon fibres that makes the composite high lossy. On the contrary, the S_{21} for one layer of dry carbon fibres (i.e., specimen D) was registered along the entire frequency range from 30 MHz to 1.5 GHz. A single woven fabric of dry fibres is less conductive and consequently less effective as a shield than layered composites as samples A and B. Even a greater value of the transmission coefficient was measured for one layer of UD fibres (i.e., specimen F), as specimen F is more transparent to the TEM radiation in the coaxial transmission line. It is good to

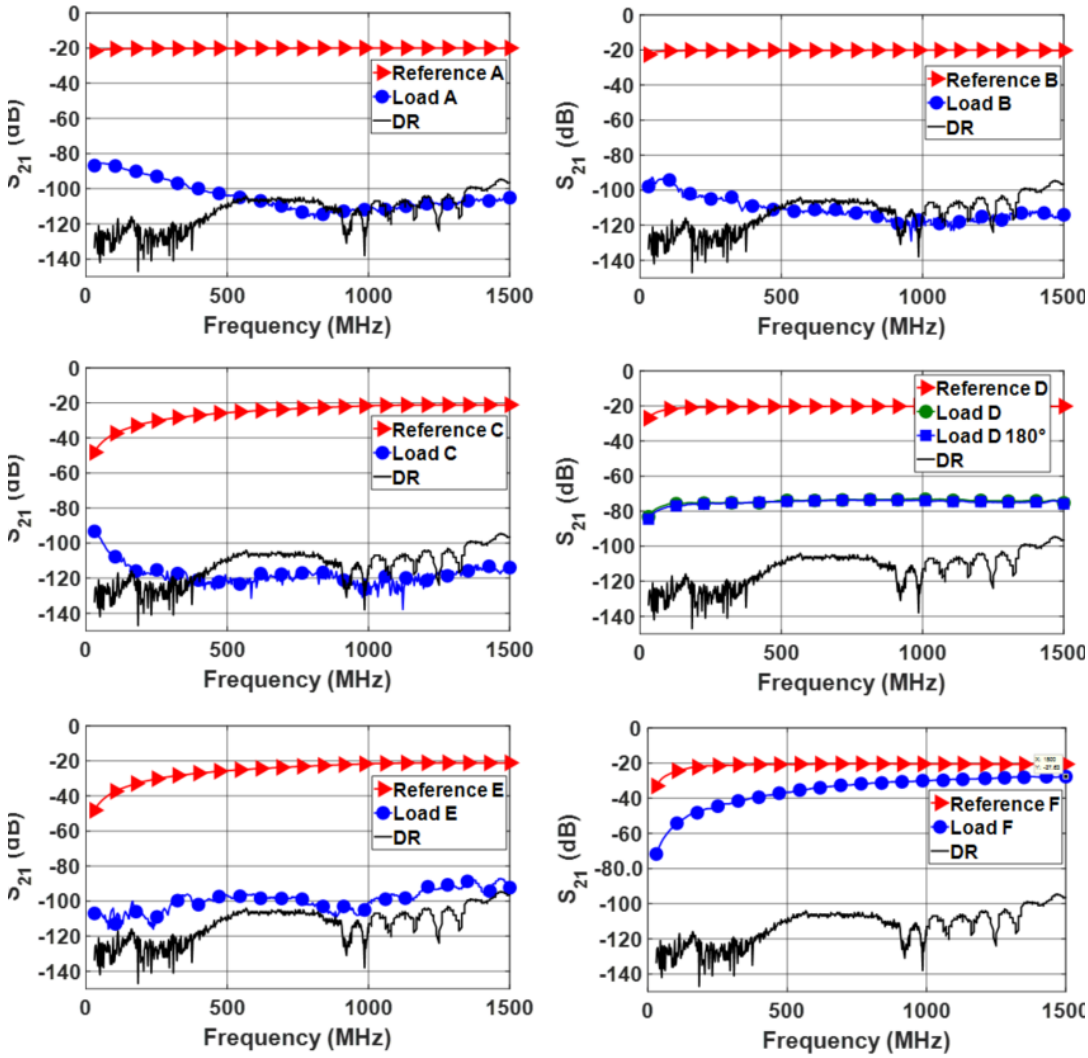


Figure 3.8: S_{21} measured for reference and load samples of materials listed in Table. 3.1, Table 3.2 and Figure 3.4.

remember that the value of the transmission coefficient is reported on the negative ordinate, and that as the value of the transmission coefficient is close to 0, more portion of the signal is actually transmitted through the sample.

However, the situation changes when comparing 4 layers of dry fibres (i.e., specimen E) with specimen A. Both samples have the same stacking sequence of woven fabrics, but specimen E shows greater shielding power than specimen A. As it appears in Figure 3.8, the S_{21} decreases in dB towards the lower measurement limit, exceeding the DR. Therefore, the presence of epoxy resin lessens the contact points between fibres, reducing the overall conductivity of the composite. Specimen C also exceeds the noise floor after 125 MHz. In this case, not only the conductivity of the two CFRP layers on both sides of specimen C is blocking the radiation, but also the

greater thickness of the sample can be a contributing cause to the lower value of the transmission coefficient S_{21}, and therefore to the greater SE displayed by this sample.

Table 3.3 shows the values of the average SE measured for the tested samples, which did not exceed the DR as per ASTM D4935, and the average volume resistivities calculated with Simon formalism (equation 3.20).

Table 3.3: Comparison between CFRP and carbon fibre samples. Volume resistivity and SE of specimen A, B, D, E.

Specimen	Matrix	Filler	Frequency range [MHz]	Average volume resistivity [Ωcm]	Average SE [dB]
A	Epoxy	TR30S 3k TR50S 12k TR50S 12k TR30S 3k	30 to 450	9.8×10^{-3}	72.8 ± 5.5
B	Epoxy	TR30S 3k TR50S 12k TR50S 12k TR50S 12k TR30S 3k TR50S 12k TR50S 12k TR30S 3k	30 to 400	3.3×10^{-2}	81.6 ± 5.3
D	-	TR30S 3k	30 to 1500	-	53.9 ± 0.6
F	-	TR50S 15k	30 to 1500	-	14.4 ± 5.9

Considering the CFRP samples, it can be noticed that specimen B exhibits higher attenuation upon transmission compared to specimen A. As a rule of thumb, the greater the resistivity (i.e., smaller conductivity), the lower the shielding effectiveness, because of the lower reflection loss SE_R [166], [176], [182]. However, the volume resistivities calculated with Simon formalism using the SE measured, prove that specimen B has also a higher resistivity (lower conductivity) than specimen A and that consequently a great contribution to the SE is given by the absorption loss SE_A, which is directly proportional to the thickness of the specimen. In fact, according to equation 3.20, the higher shielding effectiveness of specimen B is caused by a greater SE_A term, due to the greater thickness of the specimen. The volume fraction of polymeric matrix is possibly bigger in specimen B compared to specimen A. In addition, the larger thickness and the different lay up (i.e., the presence of 5 layers of XPREG XC130 450g) may have influenced the spillage of the resin during the curing process in autoclave. A largest amount of resin reduces the overall electrical conductivity of the material because it increases the fraction of insulating material and decreases the contact points between the conductive fibres.

The SE decreases for specimen D and F, as only one layer of 2/2 twill fabric and unidirectional fabric are respectively used for the samples. However, there is a big difference in the two. A woven fabric, having yarns intertwined at 0° and 90° orientation, is able to shield more effectively the TEM radiation, as the electric field is pointing along the radial direction and has radial symmetry. In addition, the number of contact points between fibres increases in the sample plane allowing movement of electric charges in more than one direction. On the other end, a UD cloth allows movement of electric charges primarily along one direction (i.e., along the fibres direction). Resulting in being less polarized than specimen D, for TEM mode.

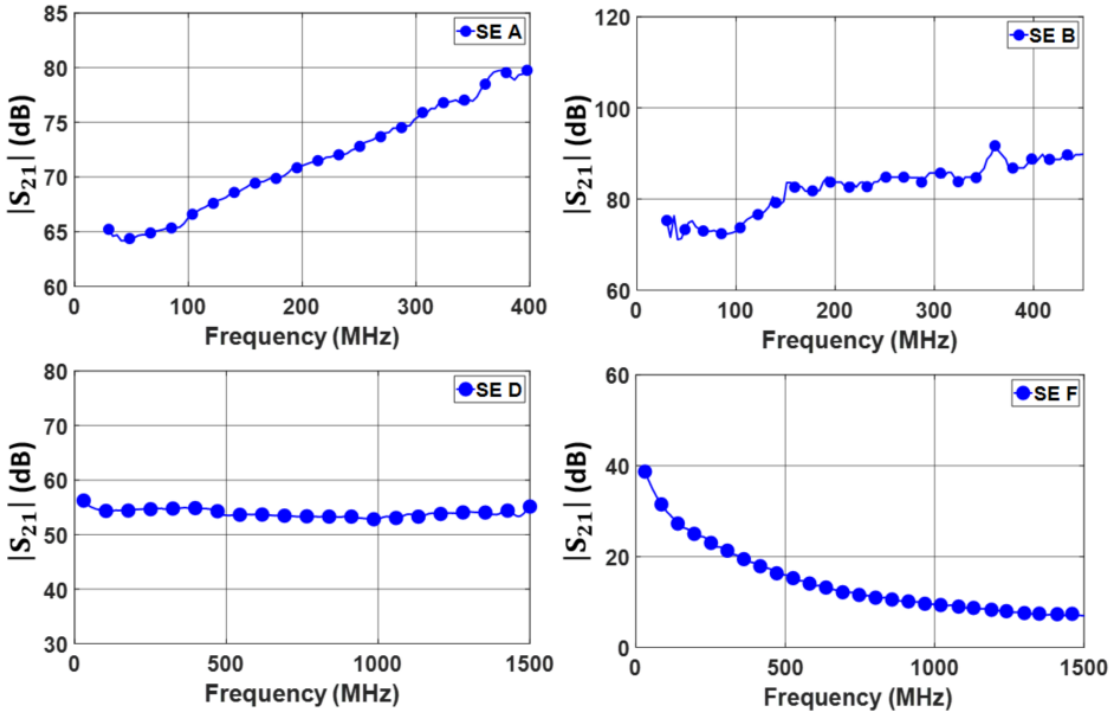


Figure 3.9: SE measured for specimen A, B, D and F.

For sake of completeness, the SE measured for the specimens in Table 3.3 are shown in Figure 3.9.

Figure 3.10 shows the incident, reflected and transmitted power distribution for specimen A, B and D as a function of the frequency in MHz. On the left, the power was measured with the reference in place. On the right, the load is used. When the reference is in place, the power transmitted tends to $P_i = 0.0032$ W, but it does not reach this value, because realistically the contact between flanges and specimen is not perfect. A discontinuity is introduced, which leads to power losses. In addition, a certain amount of power reflected could be measured for specimen A, B and D of the order of $10^{-5} - 10^{-6}$ W, representing the signal reflected from the coaxial holder system. In case of loaded transmission line, the situation is reversed. The power

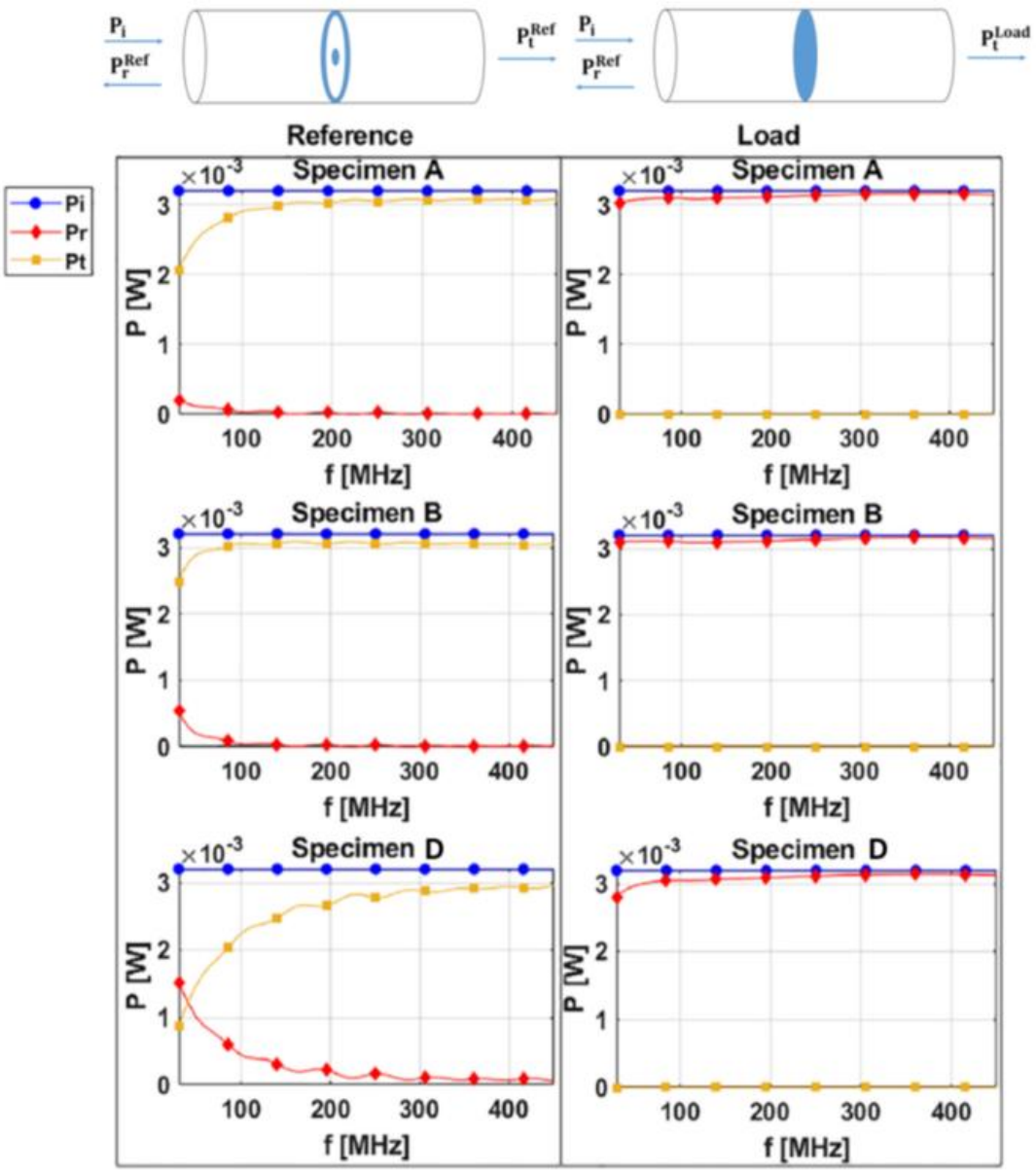


Figure 3.10: Incident, reflected and transmitted power for Specimen A, B and D. The first column refers to reference specimens in place. The second column refers to Load specimens in place for each material.

transmitted to port 2 is extremely low of the order of 10^{-10} W for specimen A, 10^{-12} W for specimen B and 10^{-8} W for specimen D, confirming the high shielding ability of carbon fibres. The power reflected back to port 1 is very high and around 0.0031 W.

Table 3.4 provides the percentages of the incident power that is reflected back to the source and transmitted though the material. Considering specimens A and B, it can be observed that, when the reference is in place, the power reflected from the system increases with the thickness of the sample. With the load in place, the reflected power,

which includes also the contribution of the experimental apparatus, remains almost unchanged. However, at the same time the signal transmitted through the load decreases for specimen B. This behaviour potentially indicates a greater power attenuation due to the absorption loss for specimen B, because of the larger number of layers contained. The primary mechanism of EMI shielding for carbon composites is addressed as reflection loss [182], [183]. However, the decreased absorption loss is also a consequence of the lower power transmitted across the first boundary of the material because of reflection loss.

Table 3.4: Percentage of power reflected with load specimen and reference samples in place; power transmitted through the load sample.

Specimen	**Percentage of power reflected with load in place** $\left(P_r^{Load}/P_i\right)$	**Percentage of power reflected with reference in place** $\left(P_r^{Ref}/P_i\right)$	**Percentage of power transmitted through the load** $\left(P_t^{Load}/P_i\right)$
A	98.8%	8.5%	0.017%
B	98.9%	9.4%	0.004%
D	97.6%	12.7%	0.23%

Considering specimen D, the reflected power with the reference material in place increases, while the signal transmitted through the unloaded coaxial holder decreases (i.e., 96−97% of signal transmitted for specimen A and B against 94% for specimen D). A possible explanation to this behaviour is due to the contact between the sample and the flanges. The specimen presents a non-smooth surface on one side and a dielectric side, which can potentially exacerbate any issues related to the electrical continuity of the transmission line. The single layer of dry fibres in specimen D shows an appreciable reflection loss comparable with specimen A and B, but also a significant transmission of power. The experimental results demonstrate that the prevailing shielding mechanism of specimen D is due to the reflection loss and its value is similar to the one of the CFRP specimen A and B. The reflection mechanism is highly dependent on the first interface encountered by the electromagnetic waves and both specimens A and B have as first layer the same woven fabric as specimen D. On the other hand, as expected, the absorption loss is not predominant, due to a reduced thickness of the dry fibres layer, lack of solidity and compactness provided by the matrix. Consequently, a greater part of the radiation passes through the material. In conclusion, the SE measured for specimen D shows that a layer of 2/2 twill weave dry fabric alone is able to shield more than 99.8% of the electromagnetic radiation. A composite material made of 4 layers of prepregs offers more than 99.97% of attenuation, while a composite with 8 layers more than 99.99%. The higher shielding ability displayed by specimen B can be due to a greater absorption loss. However, an

increase in multiple reflections inside the material can also be considered. A material with an attenuation level between 90 dB and 120 dB is considered to have an excellent shielding performance [187]. In fact, any calculated attenuation higher than 100 dB implies that the material is essentially impenetrable. The composites analysed have a shielding effectiveness between 60 dB and 90 dB. They provide a significant degree of attenuation of the electromagnetic radiation [187].

3.4 Numerical simulations

CST Studio Suite was employed to perform the calculation of the shielding effectiveness. The software is used for designing, simulating and optimizing electromagnetic systems and presents the ability to link multiple simulations with different solvers (e.g., Time domain, Frequency domain) [189]. The experiment was implemented within the suite's CST Microwave Studio® component, a tool for the 3D electromagnetic simulation of high frequency components such as antennas, filters, couplers, planar and multi-layer structures, where the software offers the possibility to build in the same environment circuit elements and 3D components [191].

3.4.1 Coaxial line simulation

The first step of the modelling work was to reproduce the equipment used for the experimental tests, as shown in Figure 3.11. The design was realized following the instructions reported in ASTM D4935.

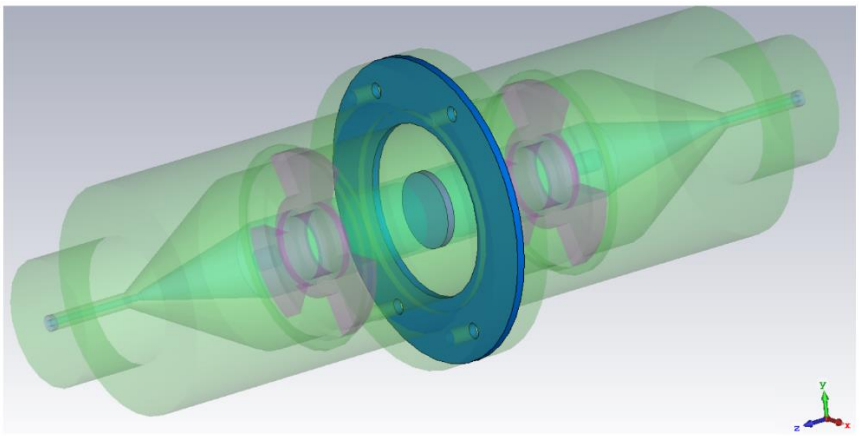


Figure 3.11: ASTM D4935 equipment model.

The coaxial line assembly consists of two mirrored parts and is composed of an external and an inner conductor separated by air, built up from several conic and tapered sections. The sample under test sits in the central part of the system, where it is fixed to an outer flange. An acrylic insert provides support for the centre conductor,

and it is visible in purple in Figures 3.11 and 3.12. The input signal power enters through port 1 and the output power is measured at port 2. In addition, air elements were inserted between inner and outer conductors at the ports location to guarantee the passage of electromagnetic radiation. The properties of the selected materials are described in Table 3.5.

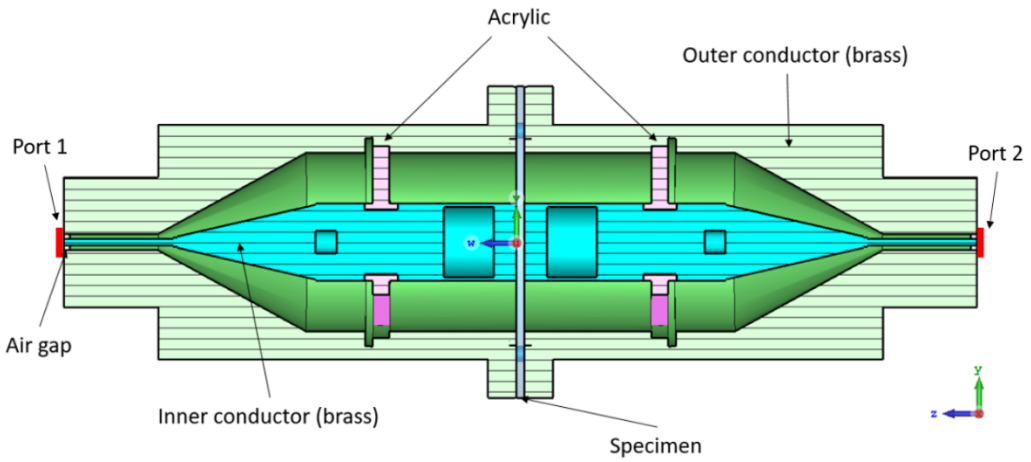


Figure 3.12: Detail of ASTM D4935 simulation equipment with its components

Table 3.5: Properties of the assembly components.

Component	**Type**	$\boldsymbol{\sigma}$ **[S/m]**	$\boldsymbol{\varepsilon_r'}$
Out/In conductor	Lossy metal	2.74×10^7	-
Acrylic	Normal	0.02	3.6
Air gap	Normal	-	1.00059

The internal and external conductors were made of brass with a conductivity of 2.74×10^7 S/m, the acrylic material was simulated by means of a material with dielectric constant of 3.2 and conductivity of 0.02 S/m. The simulations were carried out for specimen A and specimen B. The specimen were simulated considering a single geometry element with homogeneous conductivity, calculated with equation 3.20. Once obtained the values of SE as function of the frequency *f*, the conductivities were calculated as the average of the values registered in a range between 30 MHz and 450 MHz for specimen A, and between 30 MHz and 400 MHz for specimen B, using equations 3.8, 3.11 and 3.19.

Different thicknesses were considered for both specimen A and B. Both reference and load samples were simulated, obtaining 0 dB of SE for references, considering no material is actually acting as a shield. The -20 dB value constantly measured for the reference specimens during the experimental tests is due to the two 10 dB attenuators, which are not present in the simulation.

Table 3.6: Calculated average value over frequency of conductivity with Simon formalism for different values of thicknesses for specimen A and B.

Specimen	Thickness [mm]	Average σ [S/m]
A	1.00	10200.65
	0.85	12954.21
B	3.00	3161.45
	2.75	3636.28

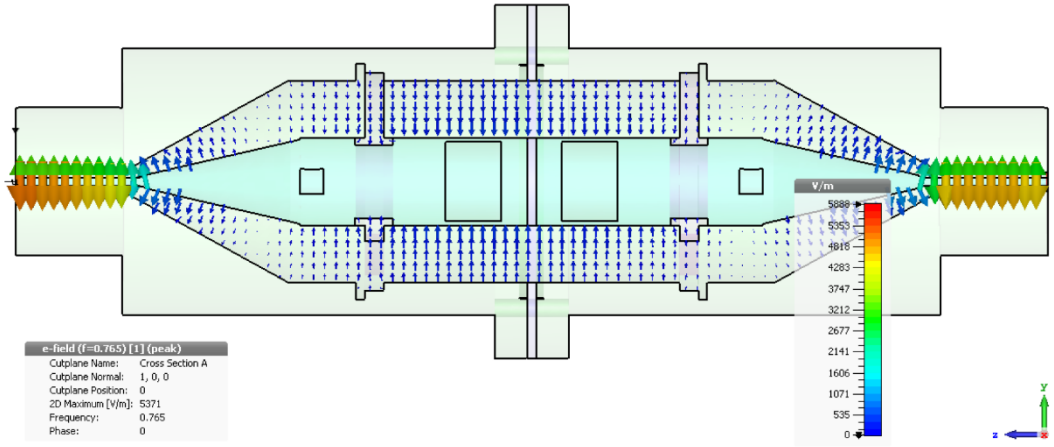


Figure 3.13: Electric field propagation in presence of the reference specimen.

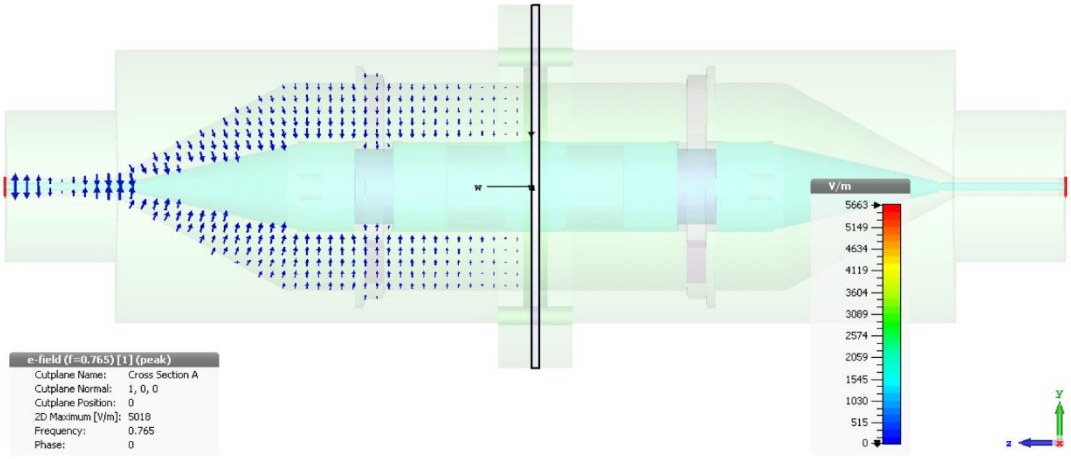


Figure 3.14: Electric field propagation in presence of the load specimen with a thickness of 3 mm and conductivity of 3161.45 S/m.

The electric field lines for the Transverse electromagnetic (TEM) propagation mode are represented in Figure 3.13 when the reference is in place, and in Figure 3.14 if the load specimen is in place. When the reference is inserted, there is no actual shielding material between the two halves of the coaxial line and the electric field is free to propagate throughout the length of the coaxial sample holder. Once the load is inserted, its shielding ability prevents the propagation of the electric field, as shown in Figure 3.14. For instance, Figure 3.14 shows the electric field (V/m), when an

homogeneous element with a thickness of 3 mm and conductivity of 3161.45 S/m is acting as a shield against the electromagnetic waves.

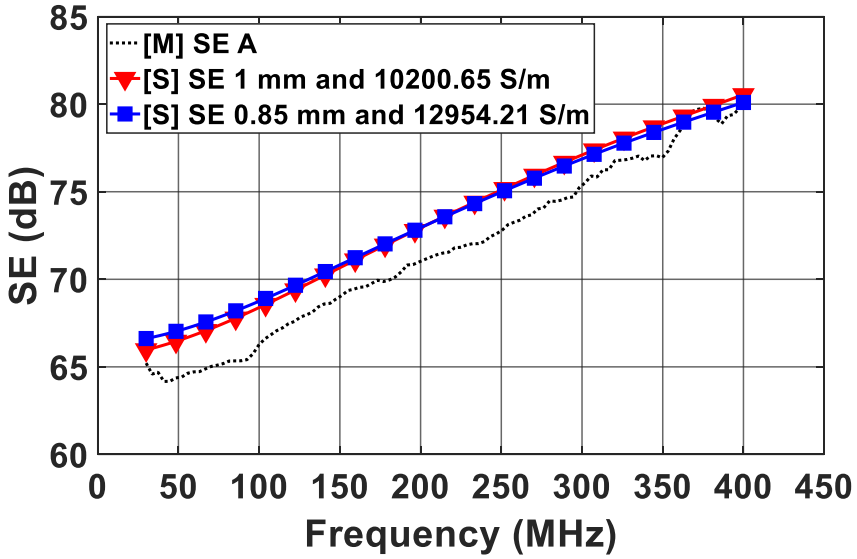


Figure 3.15: Shielding effectiveness of specimen A, measured data [M] and simulated data [S].

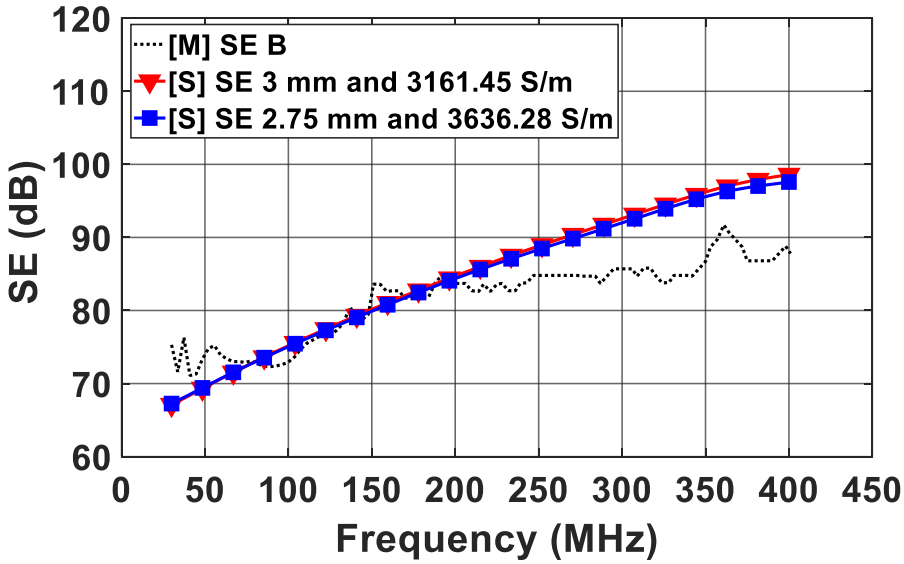


Figure 3.16: Shielding effectiveness of specimen B, measured data [M] and simulated data [S].

The results of the simulations are given in Figures 3.15 and 3.16. To obtain accurate results, a finer mesh was considered for Specimen A. For this sample a mesh of 32 elements with element's length in z direction of $\simeq$ 0.03 mm was used, as a compromise between computational costs and output results. For specimen B, a mesh of 29 elements with element's length in z direction of $\simeq$ 0.10 mm was used. In average,

the simulation results are higher in SE compared to the experimental one. However, in the range considered for the simulations (i.e., 0 to 400 MHz), it was possible to obtain curves comparable to those measured experimentally. For specimen A the simulation with a sample of 0.85 mm in thickness and 12954.21 S/m differs in average from the measured values of $\simeq$ 1.96 dB, while the simulation with a sample of 1 mm and 10200.65 S/m differs in average of $\simeq$ 1.95 dB. The effect of thickness variation is minimal and slightly affects the slope decreasing it. A smaller thickness affects the absorption loss, and in the simulation with 0.85 mm the reflection loss compensates for the decrease in absorption. The more the frequency increases the more the curves obtained seem to converge to the experimental results.

A different trend seems to characterize the case of specimen B. Also in this case, the difference in thickness causes minor variation in the slope of the curve, whereas specimen B has a greater thickness compared to specimen A and, consequently, the impact of a change in this variable may be less significant. However, the simulations obtained have a greater slope compared to the experimental curve. Considering a linear interpolation for both curves, the slope of the simulated curve is m = 0.086, compared to the one of the experimental curve equal to m = 0.045. The differences between the simulations and the experimental data are probably related to the multiple reflection mechanism that takes place because of impedance mismatches at the various interfaces inside the composite, which are not considered. The reflection loss parameter decreases with increasing frequency, while the absorption loss increases at high frequencies and becomes the primary shielding mechanism. Therefore, as the frequency increases, the influence of SE_A becomes important. In the curves obtained from the simulation, the SE becomes greater than the one measured experimentally as the frequency increases. The SE_A may be overestimated because of the lack of a negative correction factor represented by the SE_{MR} parameter. Although the thickness in sample B is greater and a certain absorption loss is expected, the composite material is not homogeneous and contains several boundaries within itself, due to the presence of prepreg layers. Another cause for this behaviour is related to Simon formalism, which assumes the resistivity isotropic. However, both mechanisms of reflection and absorption are related to the in-plane and out-of-plane resistivity, which is not always the same. The assumption of homogeneous resistivity works better with smaller thicknesses. Furthermore, it must be considered that the conductivity was calculated as the average value in the specified range of frequencies.

The overall results of the comparisons between simulations and experimental data suggest that, knowing the conductivity of a thin plate of laminate, the simulations can be used to determine its shielding effectiveness, without resorting to experimental tests. The shielding effectiveness theory of a conductive plate (i.e., equations 3.8, 3.11

and 3.20) can be applied within certain limitations to composite materials with filler content over the percolation threshold, i.e. with conductivities of the order of $10^3 - 10^4$ S/m. The limitations are represented by the number of layers of the laminate. In this study, is shown that with a number of layers between 4 and 8 the simulations are comparable with the experimental measurements.

3.4.2 Textile fabric simulation

In this section, CST Studio Suite was adopted to perform calculations of SE for dry carbon fibres in the frequency range from 30 MHz to 1.5 GHz. The simulation software was applied to numerically analyse the interaction of the textile sample with a far-field electromagnetic radiation in the mentioned frequency band; from the S-parameters calculations, it was possible to assess the shielding effectiveness (SE) value for the material, i.e. the ability of a barrier to block the field radiation. The results were compared with experimental measurements for validation.



Figure 3.17: 2/2 twill woven fabric made of TR30S 3k.

The material under analysis is a layer of dry PAN based carbon fibres fabric (Pyrofil TR30S), intertwined according to a 2/2 twill weave pattern as shown in Figure 3.17. The relevant properties of the carbon fabric are listed Table 3.7. The material is the same as specimen D.

Table 3.7: Pyrofil TR30S properties.

Specimen	**Type**	**Number of Filaments**	**Filament Diameter [µm]**	**Yeld [mg/m]**
D	TR30S	3000	7	200

The first step of the simulation work was to model the geometry of a single unit cell (UC) of the carbon textile at a mesoscale level, using a specialist pre-processor such as Texgen [198]. The in-plane dimensions of the unit cell were obtained from direct measurements of the twill weave. The length of a unit cell is approximately 7.8 mm, while the yarn width is ≃ 1.6 mm as illustrated in Figure 3.18.

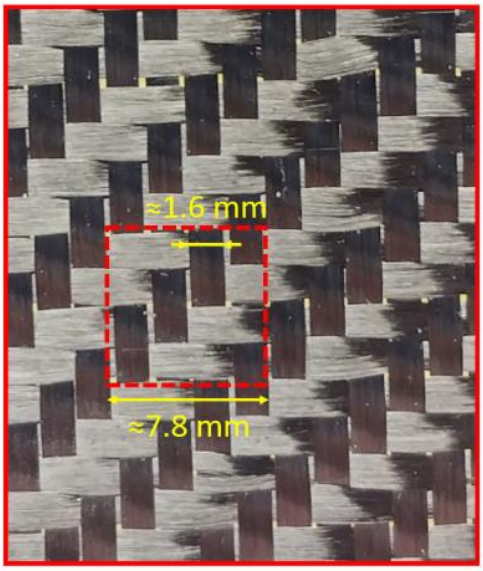


Figure 3.18: Unit cell of 2/2 twill weave pattern.

The thickness of the woven fabric was measured with an electronic micrometre with 0.001 mm resolution and is ≃ 0.23 ± 0.023 mm. The TexGen geometry base model (dimensions are defined in Figure 3.19) was imported in CST Studio Suite, whose frequency solver is based on FIT (Finite Integration Technique). The unit cell boundary condition was adopted, in order to obtain a periodic structure in the *x*-*y* plane, as shown in Figure 3.19.

The excitation used was an incident plane wave polarized according to *y* direction, in the chosen frequency band (30 MHz – 1.5 GHz). For a carbon fibre material with 60000 S/m of conductivity, a refined mesh of 962379 tetrahedron elements (minimum edge length ≃ 2.9e-005 mm) and 24 GB of RAM were required; the simulation time was of 1h 37m 12s, with an Intel XeonW-2123 CPU.

A reflection coefficient of $S_{11} = -0.019$ dB and a transmission coefficient of $S_{21} = -55.9$ dB were obtained. These values indicate a very high level of SE for just a single layer of dry fibres, corresponding to a degree of signal attenuation > 99%. It is worth to observe that this particular structure has also the same geometric configuration along *x*-axis; thus, an eventual polarization of the electromagnetic field along this direction would give the same results in terms of scattering parameters. The

results indicate that a non-isotropic geometry would rather allow greater penetration to electromagnetic waves; this is the case for UD fabric. In Figure 3.20, it can be noticed how conveniently changing the value of the reference parameters can increase or decrease the SE of the fabric. In particular, increased thickness of the fabric layer, increased yarn width and decreased space between yarns favour a greater electromagnetic attenuation.

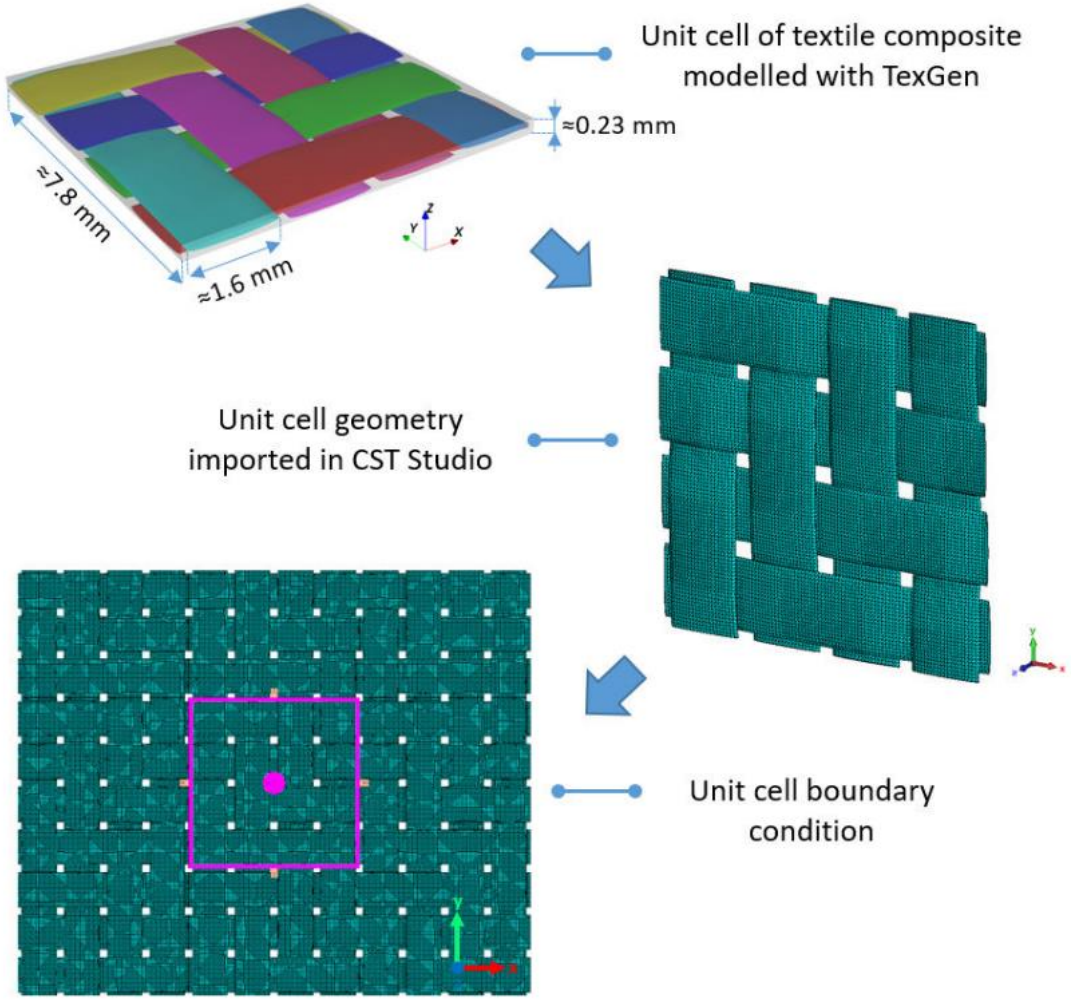


Figure 3.19: Simulation methodology for the mesoscale fabric layer.

Figure 3.21 compares the simulated results [S] with the measured [M] data. The average value of the transmission coefficient $|S_{21}|$ registered by the Vector Network Analyzer (VNA) is 54.5 dB against 55.9 dB of the simulation. In average, the simulation results are higher in SE compared to the experimental ones. However, the numerical model corresponds to a great extent to the measured data. Therefore, CST simulations can be used to describe the shielding behaviour of carbon fibre yarns at a mesoscale level.

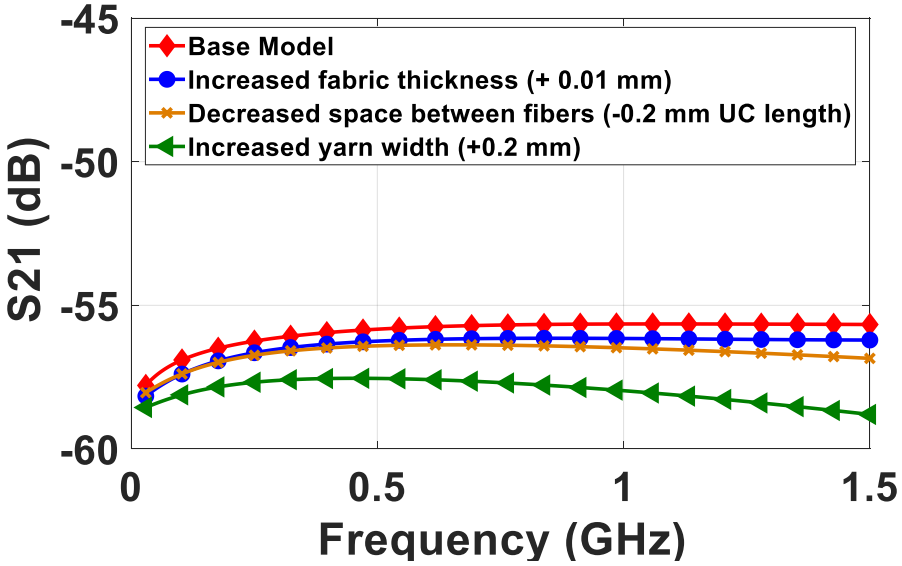


Figure 3.20: Effect of fabric thickness, yarn width and UC side length on simulated microwave transmission coefficient.

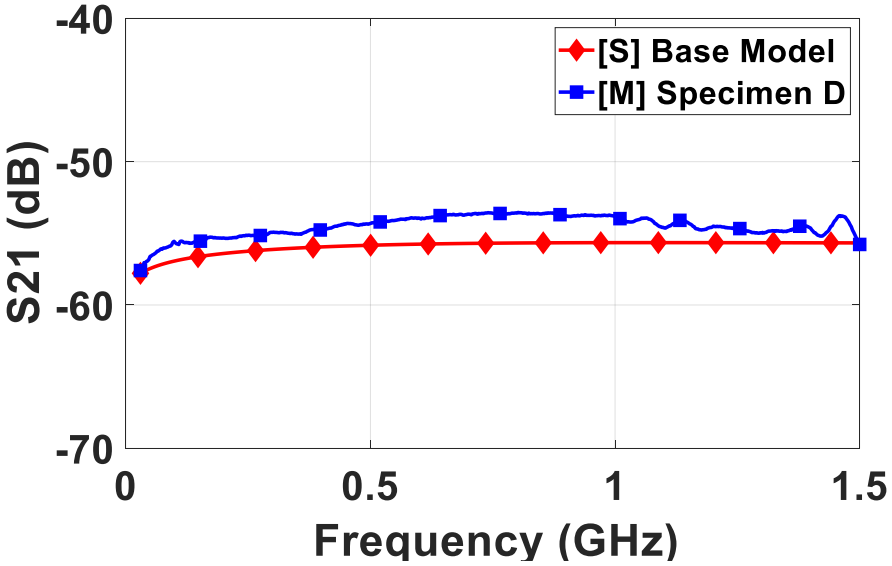


Figure 3.21: Measured [M] and simulated [S] transmission coefficient of TR30S fabric over 0.03-1.5 GHz.

3.5 Summary

The results of the experimental study show a significant ability of CFRP and carbon fibre cloth to obstruct electromagnetic radiation. A simple layer of 2/2 twill 3k dry carbon fibres fabric is able to shield more than 99.8% of the electromagnetic radiation. In CFRP samples, the presence of the resin reduces the contact between fibres, therefore the SE of CFRP composites increases with a higher fibre volume fraction, which ensures a greater continuity of conductive filler along the length and the

thickness of the material. A larger thickness and a greater number of fabric layers are not therefore an indication of higher conductivity, as shown in the case of specimen B. Instead, the conductivity is always related to the fibre volume fraction. However, a specimen with more layers exhibits a greater protection against electromagnetic radiation, proving that the SE is not only related to the conductivity of the material, but is also dependent on the power dissipated along the thickness and on the power reflected at different interfaces. All samples measured, with the exception of specimen F have SE $> 99\%$. However, specimen F has a minimum SE $\simeq 60\%$. These values confirm that CFRP materials can be successfully used for EMI shielding applications.

CST Microwave Studio® provides an efficient platform for performing simulations of shielding materials. The simulation work described applies to the less generic case of CFRP materials, which were presented as simple geometrical elements with homogeneous conductivity. For specimen A, the 3D model offer a level of accuracy less than $\simeq 2$ dB compared to the experimental tests results. Therefore, it is possible to neglect the effect of a separate modelling for resin and fibres and the presented model can be used as a valid approximation in this range of frequencies. The model proves also that the re-reflections losses can be disregarded to a certain extent and that the approximation calculated with Simon formalism is adequate to describe the problem. An increase in thickness favours the difference between the simulated shielding effectiveness and experimental results. In a thicker specimen made of carbon fibres/epoxy composite, with more layers of fabric, possibly the number of interfaces at different impedance is greater, causing a more significant re-reflections mechanism. In this case, it may be appropriate to take into account the separate influence of matrix and fibres at mesoscopic scale. Another factor, that may have affected the output, depends on the application of Simon formalism to calculate the SE as an average of values.

Chapter 4

Modified waveguide-based method for microwave characterization of high-loss materials

A waveguide-based measurement configuration is proposed, as a modification to the traditional completely-filled waveguide technique, for microwave characterization of relatively thin and high-loss materials. This method is aimed to overcome the large measurement errors caused by gaps and cross-sectional distortions, which are of great concern when measuring high-loss samples, such as unidirectional carbon fibre reinforced polymer composite sheets. In this chapter, the influences of critical parameters, namely; dielectric constant, loss factor, material thickness and waveguide misalignment, on measured complex permittivity of several diverse samples, are fully investigated through numerical electromagnetic simulations and measurements at X-band (8.2-12.4 GHz). By the virtue of the electromagnetic properties associated with high-loss dielectric materials, it is found that this technique coupled with the NRW/Backer-Jarvis conversion procedure is a capable method for measuring high-loss dielectric materials [199].

4.1 Limitations to traditional characterization methods for high-loss materials

As proved by the study presented in Chapter 3, the volume conductivity of CFRPs was confirmed to be of the order of 10^4 S/m. This condition makes transmission/reflection line the most suitable for electromagnetic characterization of high-loss materials.

As previously explained in Section 2.3.3, the use of methods based on the reflection coefficient only, such as open-ended techniques, would lead to incorrect prediction of the permittivity, because of the high reflection of the electromagnetic field, which occurs at the interface between air and the first surface of the material under test. This was also amply demonstrated by the study of Chapter 3, where the primary mechanism of EMI shielding for carbon composites was due to the reflection loss SE_R. Thus, all four (S_{11}, S_{12}, S_{21}, S_{22}) or a pair (S_{11}, S_{21}) of the scattering parameters are needed to correctly assess the complex permittivity and the TR line method is particularly suited for this purpose.

The TR line method was presented in Section 2.3.2, and can also be defined as *loaded transmission line method* or *completely-filled transmission line method*. As such, it will be addressed throughout this work. The TR method provides measurements of reflection and transmission coefficients and offers high accuracy over a broad range of frequencies [71], [78], [200]. However, precise machining of the sample is required in order to reduce the measurement uncertainty caused by small imperfections, such as air gaps between the sample and the waveguide and any deviation from the required sample geometry [78], [201].

In the literature, several studies have demonstrated that samples with cross-sectional distortions and inaccuracies associated with their thicknesses can produce error in the resulting calculated complex permittivity [81], [201], [202]. Low-loss samples are less affected by the error in the complex permittivity calculation resulting from such distortions [203]–[205]. Conversely, the presence of air gaps is of considerable concern when measuring high-loss materials, where the generated higher-order modes significantly affect the distribution of the reflected and transmitted signals [136], [201], [203]. For example, in the case of undesired gaps between the sample and the transmission line walls, a non-negligible amount of energy associated with these modes flows through the gaps around the sample [203]. Gaps with dimension $\leq 1\%$ of the waveguide aperture have been found to produce significant errors and could affect the calculated dielectric properties by as much as 50% [81], [203].

An example illustrating the issues caused by the aforementioned uncertainties is provided by the case of a high-loss carbon fibre reinforced polymer (CFRP) sheet. A CFRP laminate is by definition an inhomogeneous material, made of a dielectric polymer matrix and conductive carbon fibre reinforcements. A lack of contact between the conductive reinforcements and waveguide walls can produce critical errors, when the electric field is directed along the fibres. This lack of contact can also be caused by the polymeric matrix (e.g., resin pockets). In addition, shaping a sample in order to

tightly fit inside a waveguide can lead to alteration of its geometrical features (e.g., yarns pull-out, delamination), and consequently, its electromagnetic properties.

Several solutions have been proposed to overcome the air gap issue, including simple perturbation formulas for air gap correction [136], filling the air gap with conducting paste (e.g., silver-based paste) [203] and more recently with non-conducting paste [206], or using a partially-filled waveguide technique [205]. The first solution considers only the distorted dominant mode in the waveguide, and consequently is valid over a very small range of material parameters and gap sizes. Conductive paste is effective for air gaps but it does not address the issues related to the alteration of the sample and its physical properties after machining or hand cut. The latter solution is bound to cause additional undesired higher-order modes.

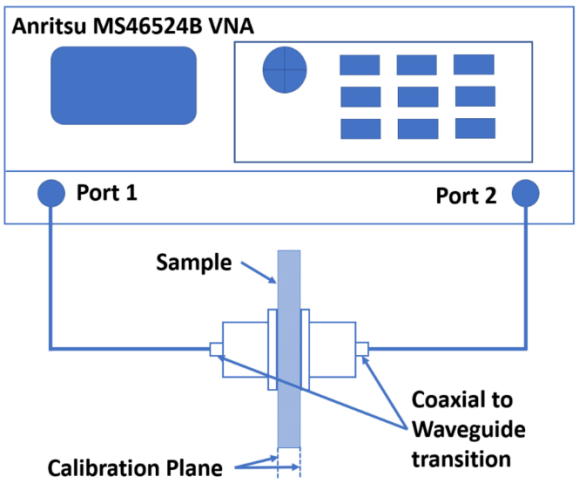


Figure 4.1: Clamped waveguide method measurement setup.

Considering the limitation of the loaded waveguide technique for evaluating high-loss dielectric materials, in this work a modification to the waveguide-based measurement method is proposed, which can be effective for this class of materials. The schematic of the method is shown in Figure 4.1, which consists of properly aligning and placing two flanged open-ended rectangular waveguides on both sides of the sample. Hereon, this method is referred to as the “clamped waveguide” method. In this arrangement, the electromagnetic waves are not confined within the interior of the waveguide walls and part of the radiation is guided along the sample plane (i.e., between the sample and the two waveguide flanges acting as a parallel-plate transmission line). However, we take advantage of the fact that this guided radiation decreases significantly in lossy materials, such that the fields remain primarily within the waveguide aperture region. A comparative study between using the standard completely-filled waveguide and the clamped waveguide methods, for high-loss and polarizing materials, such as a unidirectional CFRP sheet, is presented in this study as

well. The results show that the measurement accuracy associated with the latter method is significantly improved, since it overcomes the issues pertaining to cross-sectional distortions, as described earlier. The analysis was carried out over the X-band (8.2-12.4 GHz) frequency range and the effective complex permittivity for each chosen material was calculated using the NRW/Backer-Jarvis conversion procedure given in [71], [79], [80].

4.2 Clamped waveguide measurement approach

For a high-loss material, discontinuities in the measurement sample cause undesired reflections and transmissions that are unaccounted for by the models describing the same, leading to incorrect extraction of complex permittivity [201], [202], [204]. Hence, to properly estimate the dielectric properties of a sample a new arrangement was considered using samples with dimensions larger than the waveguide aperture and clamped between the flanges of two waveguide section, as shown in Figure 4.1. In this arrangement, the electromagnetic waves are no longer confined within the interior of the waveguide walls, as is the case for the completely-filled waveguide method. Instead, the electromagnetic waves can potentially become coupled into the material thickness and between the two flanges, creating a "dielectric-filled parallel-plate" transmission line. This causes a certain level of power leakage from the system, which for a given frequency will depend on the complex permittivity and thickness. However, if the sample is a high-loss and sufficiently thin, this energy loss can be neglected and the electric field can be considered to be primarily confined within the two waveguide apertures (i.e., resembling a completely-filled waveguide method), as illustrated in Figure 4.2.

Figure 4.2(a) shows the simulation setup for the clamped waveguide method, realized with CST Microwave Studio® [207]. Two open-ended rectangular waveguides with CPR90F flanges made of perfect electric conductor (PEC) are aligned and placed at both sides of a 150 mm × 200 mm × 1.5 mm dielectric sheet (8.2-12.4 GHz). The aperture of the X-band waveguide is of 22.86 mm × 10.16 mm, as indicated in Figure 4.2(a). The electric field distribution on the surface of the material was calculated for samples with ε_r' equal to 1.4, 8 and 59 and $tan\delta$ equal to 0.01, 0.4 and 0.8, as depicted in Figure 4.2(b)-(d), respectively. As expected, the electric field is no longer bounded within the waveguide aperture in the low-loss dielectric sample (see Figure 4.2(b)), and tends to propagate as guided waves between the flanges in the *x*-*y* plane, as well. Thus, power losses due to this phenomenon cannot be disregarded, which consequently renders this method not suitable for low-loss dielectric material characterization.

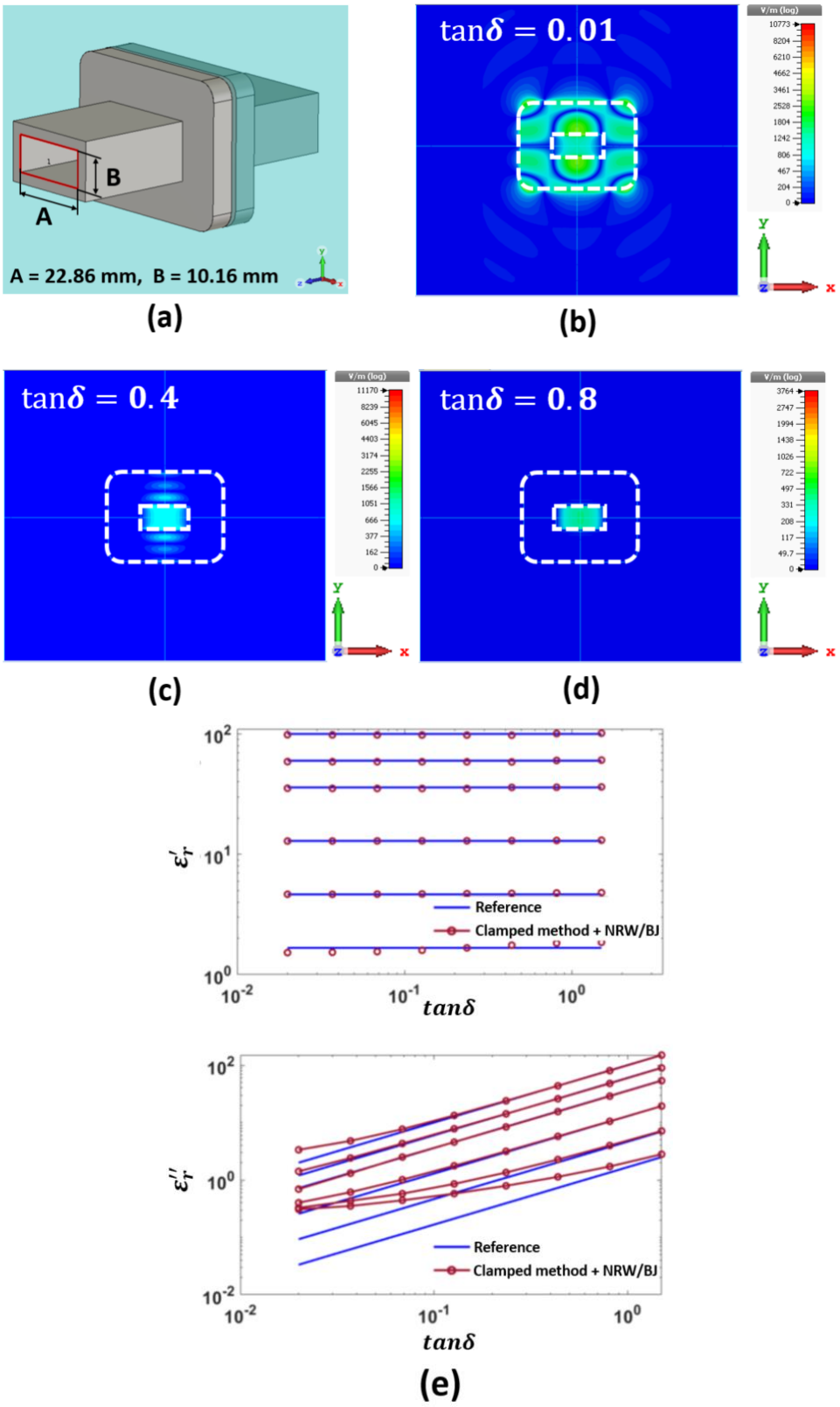


Figure 4.2: Diagram of the clamped method simulation setup, showing two open-ended waveguides with standard flanges. The field wave propagation is recorded at 10.3 GHz on the *x-y* plane for samples with thickness = 1.5 mm and $tan\delta = 0.01$ (b), $tan\delta = 0.4$ (c) and $tan\delta = 0.8$ (d). White dashed lines indicate waveguide flange perimeters; (e) Simulated dielectric constant and loss factor as function of $tan\delta$ with clamped method and NRW/BJ compared to reference values.

However, the amplitude of the guided waves between the two waveguide flanges, decreases as the material loss tangent increases, as seen in Figure 4.2(c). This continues, as a function of increasing loss factor, until the electric field remains well within the waveguide aperture, as shown in Figure 4.2(d). Consequently, this allows using the NRW/Backer-Jarvis method for extracting the complex permittivity of such material.

To further demonstrate this fact, let us consider the numerical simulations provided in Figure 4.2(e), which shows the simulated dielectric constant and loss factor for the clamped waveguide method coupled with the NRW/Backer-Jarvis method compared with reference values as function of the loss tangent. A wide range of complex permittivity was chosen and the loss tangent varies from low-loss material to high-loss materials, i.e. from 0.02 to 1.5. Figure 4.2(e) clearly show the applicability of the NRW/Backer-Jarvis conversion method to the clamped waveguide method only for high lossy materials, for which both dielectric constant and loss factor can be correctly estimated.

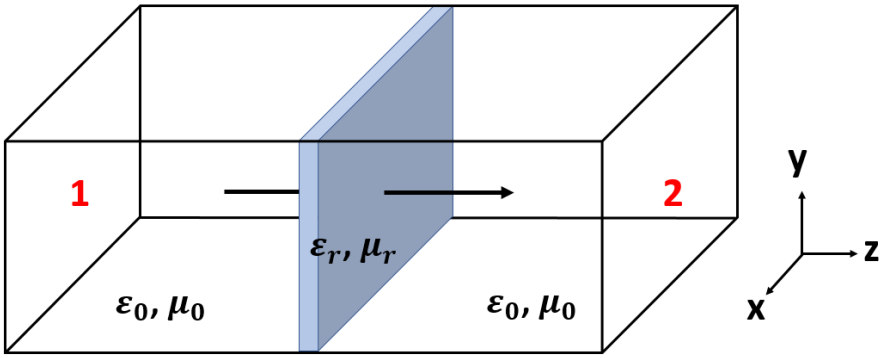


Figure 4.3: Schematic of the two-port completely-filled waveguide method, showing a rectangular waveguide filled with a homogeneous dielectric sheet with planar dimensions equal to the waveguide cross-section.

Numerical simulations and experimental measurements are presented in the following sections for several materials with different dielectric properties, in order to estimate the errors associated with this proposed clamped waveguide method as a function of dielectric constant, loss factor, material thickness and misalignments associated with the waveguide placements. It is important to compare the clamped method (in Figure 4.2(a)) with that of the completely-filled waveguide method [71], [79], as shown in Figure 4.3. In this way, the extent to which the former produces results that are inaccurate can be ascertained. The error in the calculated complex dielectric properties, for the clamped waveguide technique, is quantified for dielectric constant and loss factor according to the following expressions:

$$\frac{\Delta\varepsilon'}{\varepsilon'} = \left|\frac{\varepsilon'_C - \varepsilon'_{ref}}{\varepsilon'_{ref}}\right| \times 100 \tag{4.1}$$

$$\frac{\Delta\varepsilon''}{\varepsilon''} = \left|\frac{\varepsilon''_C - \varepsilon''_{ref}}{\varepsilon''_{ref}}\right| \times 100 \tag{4.2}$$

where $\Delta\varepsilon'$ and $\Delta\varepsilon''$ are the variations in dielectric constant and loss factor, respectively. Additionally, ε'_C and ε''_C are the dielectric constant and loss factor calculated with the clamped method, while ε'_{ref} and ε''_{ref} are the actual values of dielectric constant and loss factor used as reference.

4.3 NRW/Backer-Jarvis method applied to plug-loaded transmission line

Under the premises of Section 4.2, the NRW procedure can be also applied to the clamped waveguide method. Here below, the NRW/Backer Jarvis algorithm used for the conversion of the scattering parameters to permittivity is reported as per [71], [78].

Considering a two-port plug-loaded waveguide, as shown in Figure 4.4, the permittivity of low-loss solid materials can be successfully measured knowing the scattering parameters in reflection S_{11} and in transmission S_{21}. Having defined Γ_1 and Γ_2, as the reflection coefficient respectively at the air-plugs and the plug-sample boundaries:

$$\Gamma_1 = \frac{\eta_P + \eta_0}{\eta_P - \eta_0} \tag{4.3}$$

$$\Gamma_2 = \frac{\eta_S - \eta_P}{\eta_S + \eta_P} \tag{4.4}$$

and the exponential propagation coefficients in the plugs T_1 and the sample T_1 as:

$$T_1 = e^{-\gamma_P t_P} \tag{4.5}$$

$$T_2 = e^{-\gamma_S t_S} \tag{4.6}$$

where η_0, η_P and η_S are the wave impedances of the air, plug and sample, respectively, γ_P and γ_S are the propagation constants of plug and sample and t_P and t_S are the thicknesses of the plug and the sample, the scattering parameters can be defined by the following relationships:

$$S_{21} + S_{11} = \frac{(T_1^2\Gamma_2 + T_1^2\mathrm{T}_2 + \mathrm{T}_2\Gamma_1\Gamma_2 + \Gamma_1)}{(T_1^2\mathrm{T}_2\Gamma_1 + T_1^2\Gamma_1\Gamma_2 + \mathrm{T}_2\Gamma_2 + 1)} = \mathrm{V}_1 \tag{4.7}$$

$$S_{21} - S_{11} = \frac{(T_1^2\Gamma_2 - T_1^2\mathrm{T}_2 - \mathrm{T}_2\Gamma_1\Gamma_2 + \Gamma_1)}{(T_1^2\mathrm{T}_2\Gamma_1 - T_1^2\Gamma_1\Gamma_2 + \mathrm{T}_2\Gamma_2 + 1)} = \mathrm{V}_2 \tag{4.8}$$

Now, to have an estimation of the initial value of the complex permittivity of the sample ε_r^S, the scattering parameter can be measured directly with the VNA for the setup of Figure 4.4 and can be used to calculate the reflection Γ and transmission coefficient T:

$$X = \frac{1}{2}\frac{(1 - \Gamma_1 S_{21}^2 + \Gamma_1 S_{11}^2 - 2\Gamma_1 S_{11})T_1^4 + \Gamma_1^2 - 2\Gamma_1 S_{11} + S_{11}^2 - S_{21}^2}{T_1^2(\Gamma_1 - \Gamma_1 S_{21}^2 + \Gamma_1 S_{11}^2 - \Gamma_1^2 S_{11} - S_{11})} \tag{4.9}$$

$$\Gamma = X \pm \sqrt{X^2 - 1} \tag{4.10}$$

$$T = \frac{T_1^2\Gamma + \Gamma_1 - \mathrm{V}_1(1 + T_1^2\Gamma_1\Gamma)}{\mathrm{V}_1(\Gamma + T_1^2\Gamma_1) - T_1^2 - \Gamma_1\Gamma} \tag{4.11}$$

where $|\Gamma| < 1$ is required to find the correct root. From equation 4.10 and 4.11, the relative permeability μ_r^S and the relative permittivity ε_r^S of the sample can be derived as:

$$\frac{1}{\Lambda^2} = \left(\frac{\mu_r^S \varepsilon_r^S}{\lambda_0^2} - \frac{1}{\lambda_c^2}\right) = -\left(\frac{j}{2\pi t_S}\ln\left(\frac{1}{T}\right)\right)^2 \tag{4.12}$$

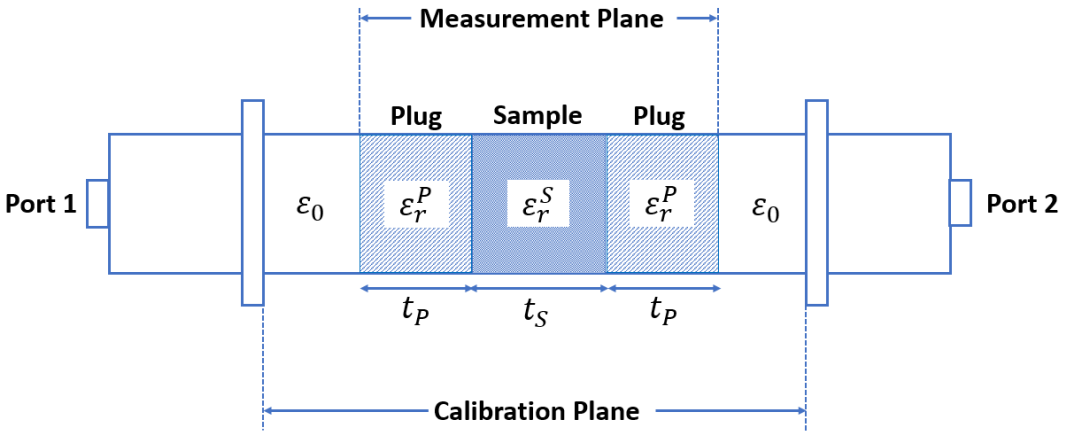


Figure 4.4: Diagram of the two-port plug-loaded completely-filled waveguide technique.

$$\mu_r^S = \mu_r^P \frac{1+\Gamma}{\Lambda(1-\Gamma)\sqrt{\frac{\mu_r^P \varepsilon_r^P}{\lambda_0^2} - \frac{1}{\lambda_c^2}}} \tag{4.13}$$

$$\varepsilon_r^S = \frac{\lambda_0^2}{\mu_r^S}\left(\frac{1}{\Lambda^2} + \frac{1}{\lambda_c^2}\right) \tag{4.14}$$

where λ_0 and λ_c correspond to the free-space wavelength and the waveguide cut-off wavelength.

Consequently, the complex value obtained for the sample permittivity ε_r^S is used as initial guess for a mean square error solving the following expression [71]:

$$S_{21}^2 - S_{11}^2 = \mathrm{V}_1\mathrm{V}_2 \tag{4.15}$$

where V_1 and V_2 are functions of ε_r^S, S_{11} and S_{21}.

From equation 4.15, the permittivity can be solved by the iterative method where the mean square error method for root determination is used. The algorithm is considered converged when $F(\varepsilon_r^S) = S_{21}^2 - S_{11}^2 - \mathrm{V}_1\mathrm{V}_2 = 0$.

4.4 Simulation results

4.4.1 Error due to material dielectric properties and thickness

To investigate the error resulting from the application of the clamped waveguide method, materials with different dielectric constants and loss factor were studied, as shown in Table 4.1. These include materials such as Neoprene foam and FR4 with low dielectric constant and loss factor, to materials with higher dielectric constant and loss factor such as carbon-filled rubber and CFRP. The permittivities used as reference are listed in Table 4.1 with subscript "*ref*" and were selected for the simulation to match the materials used in the measurement section except for FR4, whose values were taken from [201]. The complex permittivities chosen for the CFRP sheets (i.e., CFRP1 and CFRP2) are the ones measured for unidirectional CFRP sheets tested in the direction perpendicular to the fiber reinforcements.

Simulations were carried out at X-band (8.2-12.4 GHz) using CST Microwave Studio®, in order to determine the scattering parameters, S_{11} and S_{22} (reflection coefficients), S_{21} and S_{12} (transmission coefficients). This process simulates a two-port measurement performed with a vector network analyzer (VNA), as depicted in Figure 4.1. Using the simulated data, the dielectric properties were calculated through the Baker-Jarvis procedure, first, for the ideal model (L) and then for the clamped model (C), as reported in Table 4.1.

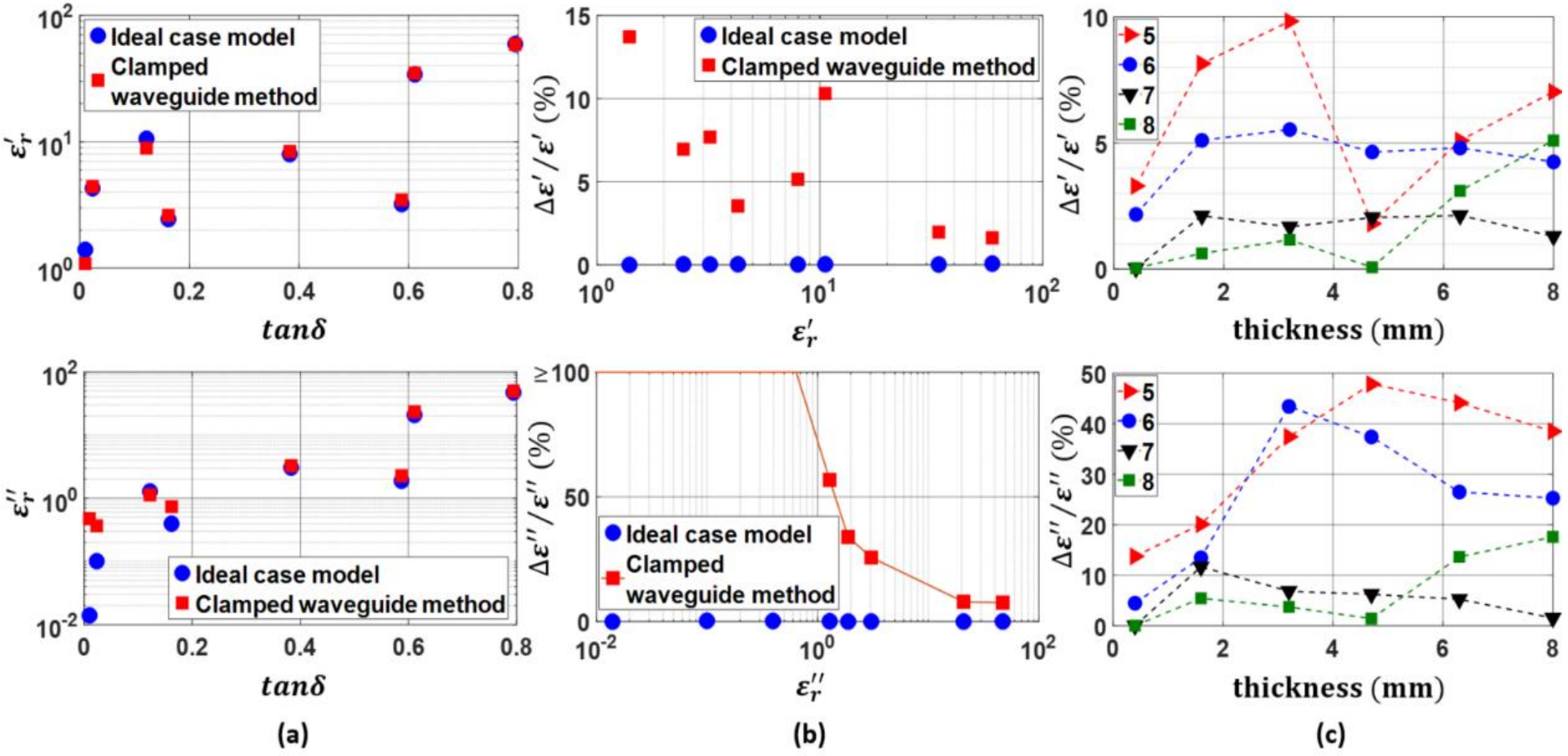


Figure 4.5: (a) Simulated dielectric constant and loss factor of ideal case model and clamped method; (b) error (%) in dielectric constant and loss factor of ideal case model and clamped method; (c) error (%) in dielectric constant and loss factor as function of sample thickness (materials are indicated with numbers reported in Table 4.1).

Finally, the resulting permittivities, averaged over X-band, are compared to calculate the errors, as per equations 4.1 and 4.2. As expected, the recalculated complex permittivities of the ideal model (i.e., completely-filled waveguide) are very close to the reference values (i.e., the error between ideal model and reference values is ~ 0). On the other hand, the simulated results for the clamped waveguide method are not exactly those of the reference values (and the ideal model), and vary as a function the complex permittivity of the sample used. This is due to the coupled fields in between the flanges, as explained earlier and being the focus of this investigation.

Table 4.1: Dielectric properties of materials chosen. Simulated results for ideal model (L) and clamped waveguide method (C).

Material	$\varepsilon_r'\|_{ref}$	$\varepsilon_r''\|_{ref}$	$tan\delta\|_r$	$\varepsilon_r'\|_L$	$\varepsilon_r''\|_L$	$tan\delta\|_L$	$\varepsilon_r'\|_C$	$\varepsilon_r''\|_C$	$tan\delta\|_C$
1 Neoprene foam	1.40	0.01	0.01	1.40	0.01	0.01	1.21	0.46	0.39
2 FR4	4.29	0.10	0.02	4.29	0.10	0.02	4.33	0.76	0.18
3 Antistatic polyethylene	2.44	0.40	0.16	2.44	0.40	0.16	2.61	0.91	0.35
4 Carbon-filled rubber	10.57	1.29	0.12	10.57	1.29	0.12	9.48	1.91	0.20
5 Carbon-filled polyethylene	3.22	1.89	0.59	3.22	1.89	0.59	3.35	2.53	0.76
6 Conductive ABS-PVC	7.97	3.05	0.38	7.97	3.05	0.38	8.12	3.84	0.47
7 CFRP1	34.13	20.86	0.61	34.12	20.85	0.61	33.93	22.51	0.66
8 CFRP2	59.36	47.15	0.79	59.40	47.12	0.79	59.66	46.41	0.78

In Figure 4.5(a), the calculated dielectric properties for the materials listed in Table 4.1 are reported as function of the loss tangent, in the same fashion as per Figure 4.2(e), but for a limited range of data points, as the simulations will be compared with the experimental study of Section 4.5. The results of Figure 4.5(a) and (b) clearly show that larger errors are associated with materials with lower dielectric constant and loss factor. While, for larger values of ε_r' and ε_r'' the complex permittivities calculated with the clamped waveguide method overlap the results of the ideal simulation. Figure 4.5(b) shows the errors in ε_r' and ε_r''. The results show that higher error is associated

with the calculated loss factor rather than the dielectric constant. The calculated errors for ε_r', even in case of low-loss materials, are less than 14% and as low as 2% for the CFRP samples. Overall, all samples show error in dielectric constant $\leq 8\%$, except for the Neoprene foam and the carbon-filled rubber samples. Conversely, the error for ε_r'' exceeds 100% for the Neoprene foam, the FR4 and the Antistatic polyethylene samples, since their loss factors are already very small and any error will seem significant. Additionally, the error decreases exponentially with increasing loss factor. For instance, for the CFRP1 and CFRP2 samples the error is 7.9% and 7.6%, respectively. The results clearly demonstrate that the clamped method is not suitable for measuring complex permittivity of low dielectric constant (low-loss) materials, as stated earlier (see Figure 4.2). In this method, the error associated with ε_r'' is greatly impacted by the additional losses in the *x-y* plane, and consequently ε_r'' is always overestimated.

Nevertheless, the clamped waveguide method provides a good characterization of high-loss materials, considering that in the literature samples with $tan\delta = 0.05$ have been reported to have errors $> 15\%$ for cross-sectional distortion of 0.5 mm in a loaded waveguide [201]. Also, samples with $\varepsilon_r = 155.9 - i175.7$ display errors up to 11% on the dielectric constant and 50% on the loss factor for a gap of 1% along the upper wall of the waveguide, when using the completely-filled waveguide method [81]. These results clearly illustrate the efficacy of the clamped waveguide method.

To investigate the impact of the sample thickness on the dielectric constant and loss factor, $\Delta\varepsilon_r'/\varepsilon_r'$ and $\Delta\varepsilon_r''/\varepsilon_r''$ were calculated for the materials with higher loss in Table 4.1 as function of thickness, and the results are presented in Figure 4.5(c). $\Delta\varepsilon_r'/\varepsilon_r'$ is very low and $\cong 0$ for CFRP samples when the thickness is ≤ 0.6 mm, maintaining a value $\leq 5\%$ for the other thicknesses. Overall, the error remains below 2.5% for the CFRP1 and the CFRP2 samples for thickness < 5 mm. The error reaches a maximum of 5.5% and 9.8% for the ABS-PVC and carbon-filled polyethylene samples respectively, in the range of thickness considered. $\Delta\varepsilon_r''/\varepsilon_r''$ is also nearly 0 for the higher loss samples with thicknesses less than 0.6 mm. In this case, the errors increase significantly for the low-loss samples (up to 44% for ABS-PVC and 50% for carbon-filled polyethylene). This is due to the overestimation of the loss factor, caused by the energy lost in the *x-y* plane, as mentioned earlier. However, it is important to observe that the error remains within 12% for the CFRP1 sample and 5% for the CFRP2 sample for thickness < 5 mm, respectively. This confirms the assumption that the clamped waveguide method is more suitable for measuring the complex permittivity of thin lossy materials.

4.4.2 Error in dielectric constant for fixed loss factor

To further investigate the limitation of the clamped waveguide method, the error over a wide range of dielectric constants ($\varepsilon_r' = 2$ to 80) was calculated for fixed loss factor values of $\varepsilon_r'' = 0.5$, 5 and 40, as shown in Figure 4.6. These values represent low-loss materials like PTFE to high-loss materials such as CFRP. Consistent with the previous results, the error in ε_r' decreases for higher values of both ε_r' and ε_r''. For instance, for a sample with $\varepsilon_r' = 40$, the calculated errors are 6.6%, 5.7% and 1.8% for the three considered loss factors, respectively. In the worst case of ε_r'' = 0.5, the errors remain below 10% for $\varepsilon_r' \geq 30$. The errors decrease exponentially as a function of increasing dielectric constant. However, for each curve it is possible to identify a peak in the error at lower values of ε_r' . This behavior seems to be affected by the choice of ε_r' rather than ε_r'' and may be related to the chosen frequency range, geometry and degree of polarization of the sample.

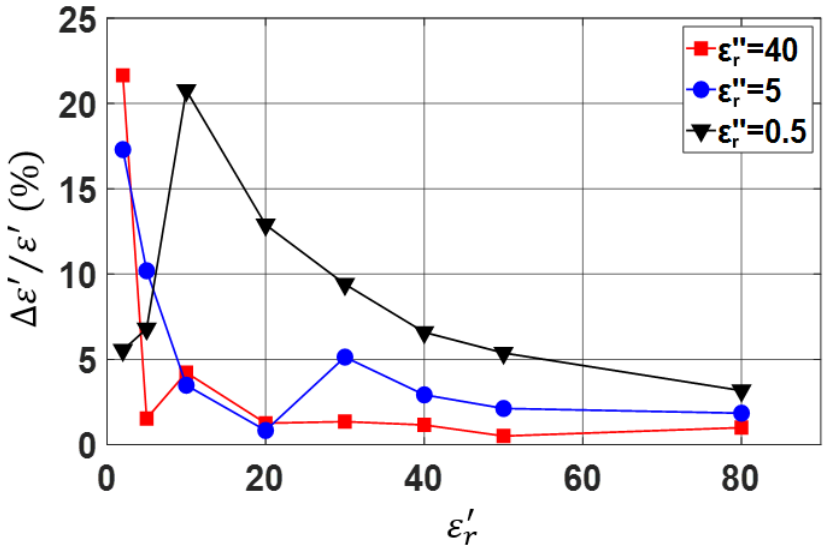


Figure 4.6: Error in ε_r' with fixed loss factor and thickness ($\varepsilon_r'' = 0.5$, 5 and 40, t = 2 mm).

4.4.3 Error in loss factor for fixed dielectric constant

A similar analysis was also carried out to evaluate the error over a wide range of loss factor values ($\varepsilon_r'' = 0.01$ to 50) values for dielectric constant values of $\varepsilon_r' = 2$, 10, 20 and 50. From the results in Figure 4.7, it can be observed that the error decreases exponentially as function of the loss factor and is significant for small values of ε_r''. In this case, however, the error is higher for higher values of the dielectric constant. For example, if ε_r'' = 30, the estimated error is of 4.6%, 6% and 7%, for $\varepsilon_r' = 10$, 20 and 50, respectively. Therefore, the error in loss factor for a fixed ε_r' is reduced in materials with higher values of ε_r'' and $tan\delta \geq 1$, while a higher dielectric constant primarily

affects the error in ε_r'. Considering a material with $\varepsilon_r' = 10$, the error is $< 10\%$ and continues to decrease for $\varepsilon_r'' > 10$. Once again, this confirms the assumption of Section 4.2, which stated that the clamped method can be a valid modification to the loaded waveguide technique in the characterization process of high-loss materials independent of their dielectric constant values.

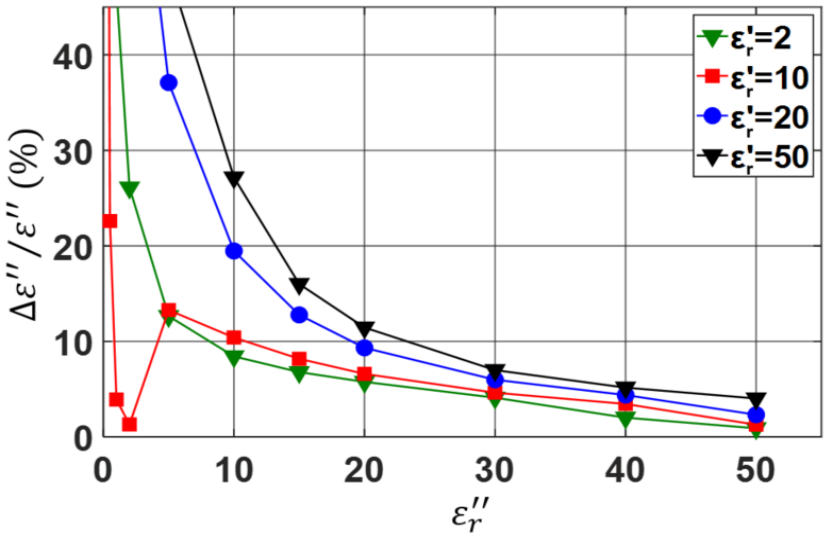


Figure 4.7: Error in loss factor with fixed dielectric constant and thickness ($\varepsilon_r' = 2$, 10, 20 and 30, t = 2 mm).

4.4.4 Error due to thickness

A wider range of thicknesses (0.3 mm to 10 mm) and loss tangent (0.07 to 1.5) were observed to estimate the dependence of the errors on dielectric constant and loss factor on the thickness. Thus, Figure 4.8 shows the errors in dielectric constant and loss factor as function of thickness for different values of $tan\delta$, having chosen a fixed dielectric constant $\varepsilon_r' = 20$. The values of $tan\delta$ represents each a material with different electromagnetic characteristic from low lossy to high lossy. As the material in this example becomes thicker, not necessarily for all $tan\delta$ the error increases. However, a peak can be observed for both curves at certain thicknesses. This may be the effect of the thickness being a multiple of one-half wavelength ($\lambda_m/2$) and yielding poor accuracy for that particular thickness.

The error in dielectric constant is inferior to 14.2% for all the materials and is inferior to 6.1% for $t_S < 5$ mm and $tan\delta > 0.44$ (i.e., $\varepsilon_r = 20 - i8.7$). The error in loss factor decreases drastically as the losses in the material increases. It is inferior to 16% in the whole range of thicknesses for $tan\delta \geq 0.81$, while it is reduced to less than 5.4% for $t_S < 4$ mm and $tan\delta = 1.5$.

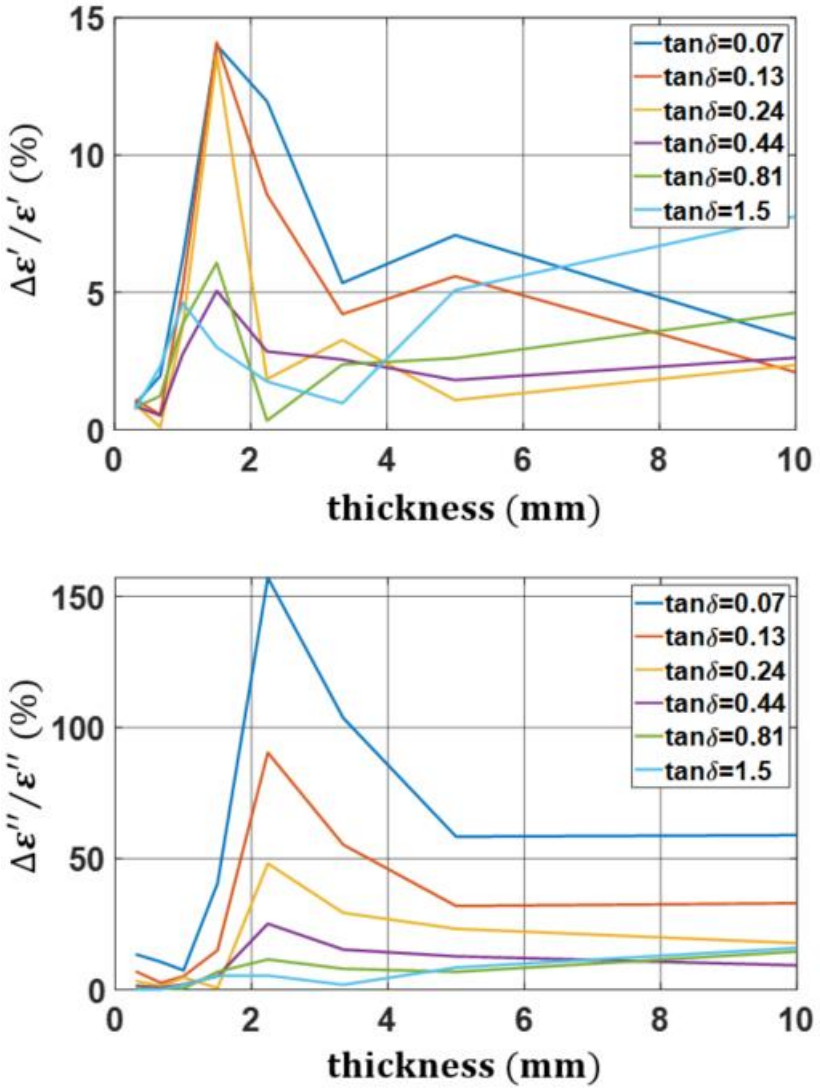


Figure 4.8: Error in dielectric constant and loss factor as function of thickness for fixed $\varepsilon_r = 12.9$.

4.4.5 Error due to waveguide misalignment

Considering the geometry of the waveguide setup of Figure 4.1, it is important to ensure proper alignment of the two open-ended waveguide apertures (i.e., their flanges) on both sides of the material. This is required in order to avoid issues caused by power leakage and undesired and unaccounted for reflections. Compared to the loaded waveguide technique, this required alignment can be more difficult to achieve practically.

The numerical simulations focused on two case scenarios of horizontal (d_x) and vertical misalignment (d_y), as illustrated in Figure 4.9. Two materials with medium to high-loss properties were chosen, such as the ABS-PVC and the CFRP1 in Table 4.1. Consequently, Figure 4.10 shows the error for ε_r' and ε_r'' for both cases, having

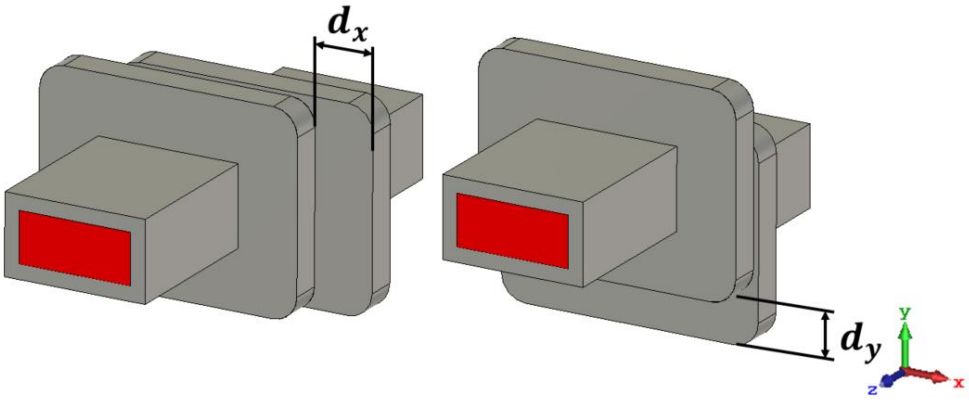


Figure 4.10: Horizontal (d_x) and vertical (d_y) misalignment of waveguides and their flanges.

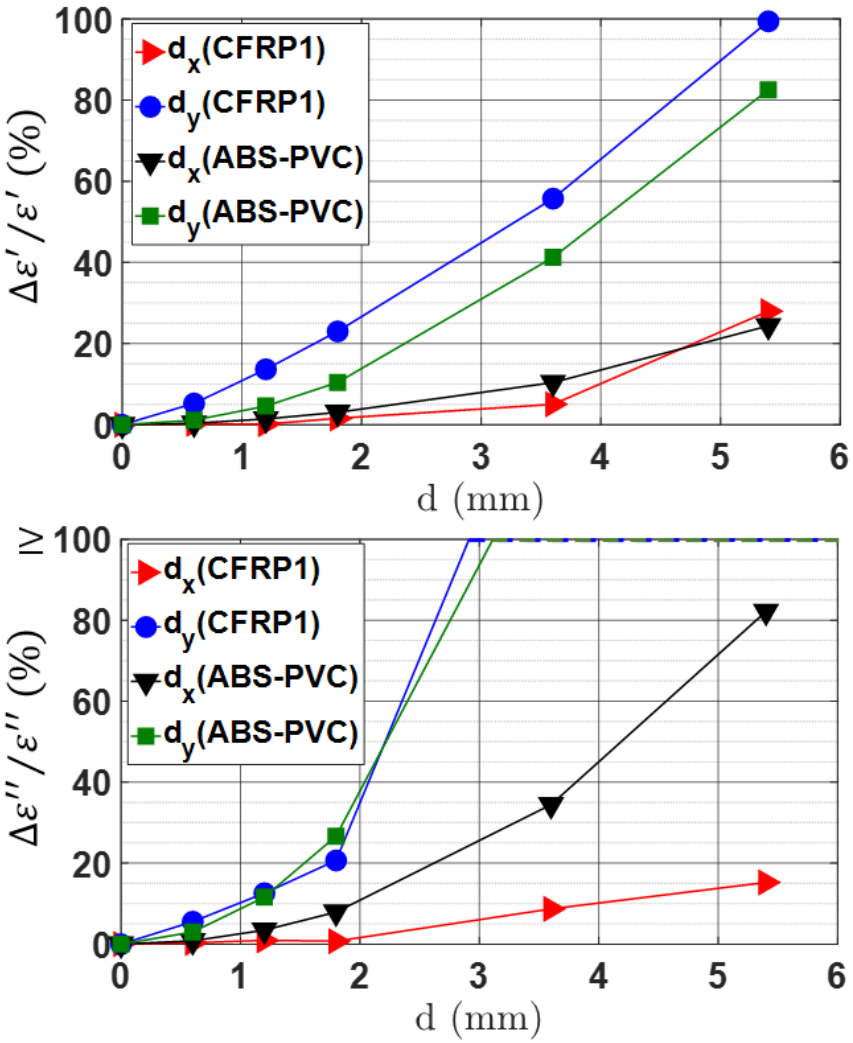


Figure 4.9: Error in dielectric constant and loss factor as function of horizontal and vertical misalignment of waveguides.

assumed initial error equal to 0 for perfect alignment ($d = 0$). The results show that a

vertical misalignment causes greater error for both materials, when determining the dielectric properties, compared to a horizontal misalignment. This is due to the fact that the dominant mode electric field in the waveguide is directed along the *y*-axis and has its maximum amplitude in the center of the waveguide aperture. Thus, the error increases faster as the misalignment d_y increases than for the case of horizontal movement d_x. Furthermore, significant inaccuracy ($\geq$ 100% for $d > 2$ mm) is found again on the loss factor determination, due to the energy loss caused by the misalignment and the resulting field leakage. For a misalignment of 0.6 mm, the error is found to be higher in case of vertical misalignment and varies from 1% to 6%. Whereas, for horizontal misalignment, the error stays below 1% for both dielectric constant and loss factor. Therefore, a vertical misalignment represents an important issue when conducting measurements with the clamped waveguide method, considering also that the estimation of the ε_r' seems to be more affected for lossy materials. In addition, if a combination of horizontal and vertical movement is considered, the dominant error is again the one due to the vertical movement. Hence, during the experimental measurements special attention must be paid in aligning the two open-ended waveguides.

4.5 Measurements results

To corroborate the numerical simulation results, and verify the efficacy of this method, measurements taken with the completely-filled waveguide method (L) [71], and the clamped waveguide method (C) were compared for several of the samples listed in Table 4.1, namely: Neoprene foam, carbon-filled rubber, carbon-filled polyethylene, conductive ABS-PVC and the CFRP. The composite samples were manufactured using 1 layer (CFRP1) and 2 layers (CFRP2) of Toray P235W-19 highly toughened carbon fiber-reinforced UD prepreg, impregnated in 37% epoxy resin (Torayca 3900-series), with density of 1.6 g/cm^3. A more detailed description of the CFRP samples is provided in Chapter 5.1. An Anritsu MS46524B Vector Network Analyzer (VNA) was used for the two-port vector S-parameter measurements. The waveguide ports were calibrated using a standard full two-port SSLT (short, shifted short, load, and thru) calibration technique [208].

4.5.1 Error due to dielectric properties

Figure 4.11 (a)-(b) and Table 4.2 show the experimental permittivities averaged over X-band. The errors in dielectric constant and loss factor for the clamped waveguide method were calculated using equations 4.1 and 4.2, with respect to the complex

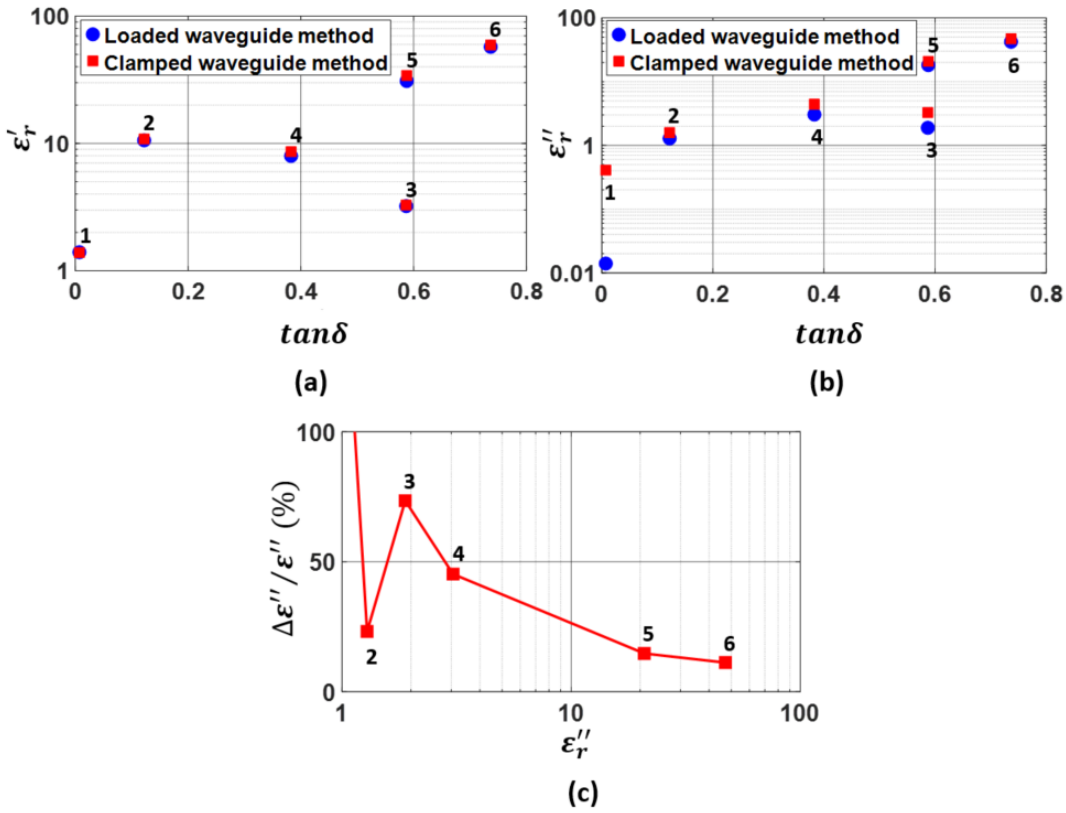


Figure 4.11: Measured dielectric constant (a) and loss factor, (b) with loaded and clamped transmission line, (c) and error in loss factor for clamped waveguide method.

permittivities obtained from the completely-filled waveguide method, in absence of referenced values.

Table 4.2: Complex dielectric permittivities calculated with loaded method (L) and clamped method (C) and relevant errors.

Material		$\varepsilon_r'\|_L$	$\varepsilon_r''\|_L$	$\varepsilon_r'\|_C$	$\varepsilon_r''\|_C$	$\frac{\Delta\varepsilon'}{\varepsilon'}$	$\frac{\Delta\varepsilon''}{\varepsilon''}$
1	**Neoprene foam**	1.39	0.01	1.41	0.41	1.6%	>100%
2	**Carbon rubber**	10.57	1.29	10.84	1.59	2.5%	23.2%
3	**Carbon-filled polyethylene**	3.22	1.89	3.28	3.28	1.9%	73.5%
4	**Conductive ABS-PVC**	7.97	3.05	8.62	4.43	8.1%	45.2%
5	**CFRP1**	30.94	18.19	34.13	20.86	10.3%	14.7%
6	**CFRP2**	57.37	42.27	59.36	47.15	3.5%	11.5%

As expected, the largest errors are obtained for the loss factor. In particular, similar to the simulation results, the imaginary part of the permittivity is considerably overestimated for Neoprene foam leading to error rate > 100%. As stated before, this

method is not suitable for low-loss materials. However, the large errors are also caused by the deviation of very small quantities (i.e., loss factor $\ll 1$). The error in loss factor decreases exponentially, similar to the trend seen in the simulation results, with the increasing dielectric constant and loss factor, up to 11.5% for the CFRP2 sample (see Figure 4.11(c)). As shown in Figure 4.11 and Table 4.2, ε_r'' is generally more difficult to estimate with the clamped method, unless the loss tangent reaches values close to unity (e.g., the CFRP sample has $tan\delta \cong 0.8$). On the other hand, the error associated with the real part of the permittivity is considerably lower. The difference in dielectric constant estimation between the two techniques remains below 10.3%.

Both the simulation and measurement results show similar trends. However, one must consider the fact that the simulations disregard factors related to sample physical properties and measurement set up (e.g., surface texture, non-homogenous material, imperfect alignment, air gaps). In reality, the permittivities measured with the completely-filled transmission lines are also subjected to error particularly for high-loss materials, as previously discussed in Section 4.2. This error can also become significant in the loaded waveguide method for the case of high-loss CFRP samples.

Hence, it can be of interest to compare the permittivities measured with both methods for a thin CFRP sample (i.e., CFRP2 with $t = 0.35$ mm) with the numerical simulation of the ideal case of Figure 4.3. The ideal model can be used as a substitute for the simulation setup of Figure 4.2(a), as the error between the two models is $\cong 0$ for thin CFRP, as seen in Figure 4.5(c). The permittivity values adopted in the ideal model are the ones reported in Table 4.2. Thus, Figure 4.12 shows the values of ε_r' and ε_r'' for measured and simulated results. The percent error can be calculated for both completely-filled and clamped waveguide line and averaged in the frequency range chosen. For instance, considering the clamped waveguide method, the error between the measured and simulated values is of $3.5\pm1.4\%$ for dielectric constant and $8.9\pm4.7\%$ for loss factor, while for the loaded waveguide method the errors are respectively $8.8\pm6\%$ and $21.9\pm9.3\%$. The error and standard deviation are greater in the case of the completely-filled waveguide method, as the experimental results varies more over frequency compared to the one measured with the clamped method. In addition, ε_r' shows an increase in value from 10.5 to 12.4 GHz. This behavior can be caused by the geometrical structure of the unidirectional high lossy CFRP, and any sample preparation issues in cutting and fitting samples inside a rectangular waveguide. This issue alone further shows the value of using the clamped waveguide method for measuring such composite materials.

Thus, the error in dielectric constant and loss factor for the CFRP samples calculated in Table 4.2 is likely overestimated due to the uncertainties on the completely-filled waveguide measurements when facing a high-loss material. Hence,

from both simulation and measured values, it is seen that the clamped waveguide method provides a good solution for electromagnetic characterization of high-loss material.

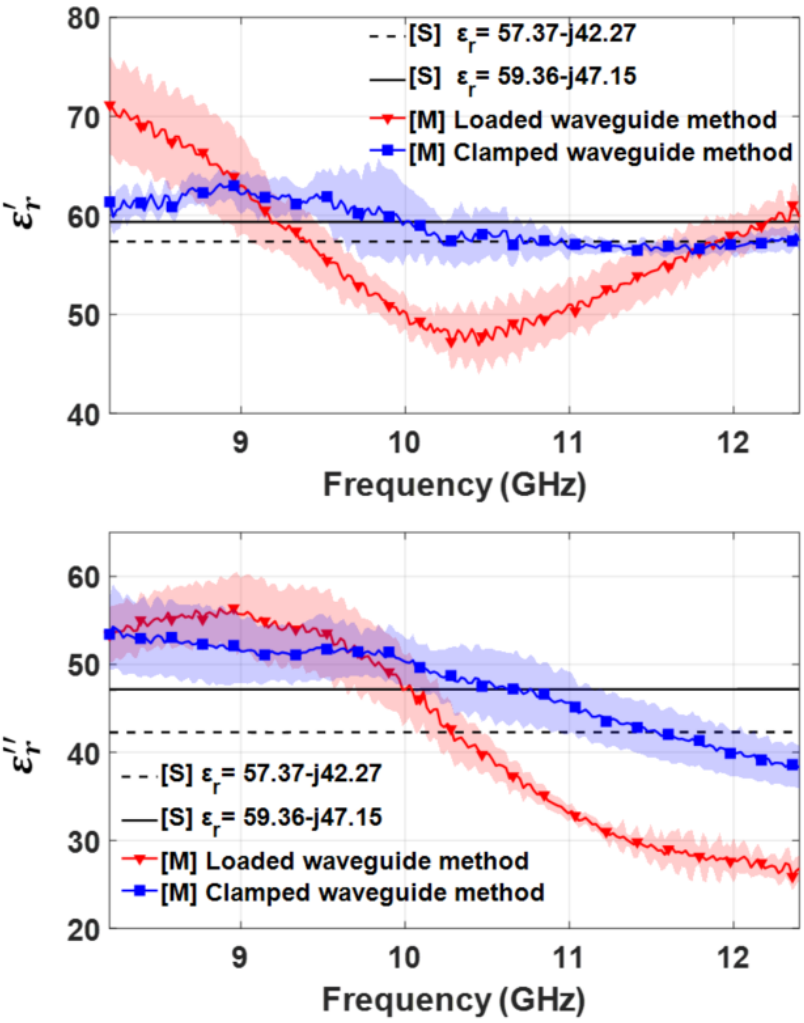


Figure 4.12: Simulated [S] and measured [M] permittivities for completely-filled and clamped waveguide method for CFRP sample with $t = 0.35$ mm.

4.5.2 Error due to material thickness

Figure Figure 4.13 shows the error in dielectric constant and loss factor as function of the thickness of the material. Three thicknesses were measured for the conductive ABS-PVC (1.6, 3.2 and 6.4 mm) and two for thin CFRP samples (0.23 mm and 0.35 mm). The results clearly indicate that the errors are reduced and close to 0 for the samples with higher loss factor and smaller thickness, even in the case of $\Delta\varepsilon''/\varepsilon''$. The errors in dielectric constant for conductive ABS-PVC are below 5.5%. However, the error in loss factor grows considerably following the simulation trend, reaching a peak of 74% for a thickness of 3.2 mm.

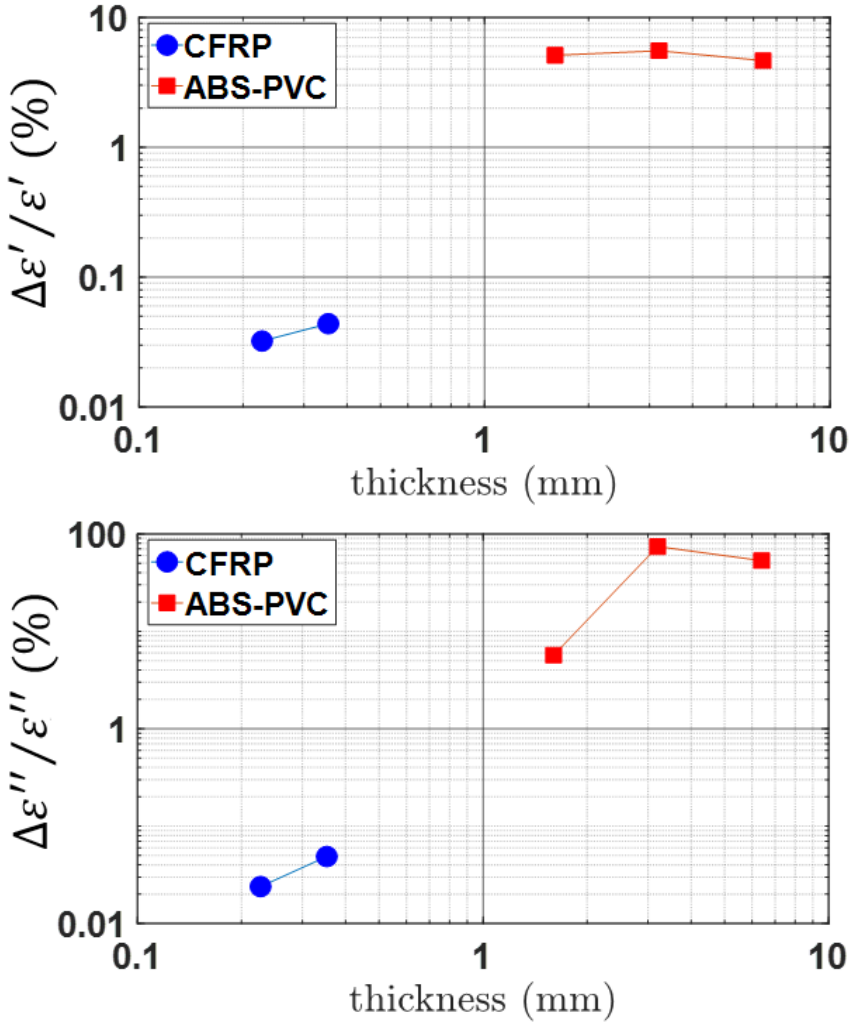


Figure 4.13: Error as function of sample thickness.

4.5.3 Error due to misalignment

The ABS-PVC sample with thickness of 1.6 mm was tested for vertical and horizontal misalignment of the waveguides, see Figure 4.14. The data points were taken according to a step of d =1.8 mm, corresponding to 1/16 of wavelength. Similar to the simulated results, the experimental results also showed larger errors in the determination of ε_r for misalignment in the vertical direction. In particular, the error in loss factor grows rapidly, reaching values ≥ 100% after only 2 mm, as what was simulated in Section 4.4.5. Lower errors are found in case of horizontal misalignment, where, within d_x =2 mm, the error in dielectric constant and loss factor stays below 1% and 5.3% respectively. The findings confirm that, when applying the clamped waveguide method, users must be particularly careful in avoiding vertical misalignment, while a certain degree of horizontal misalignment can be tolerated.

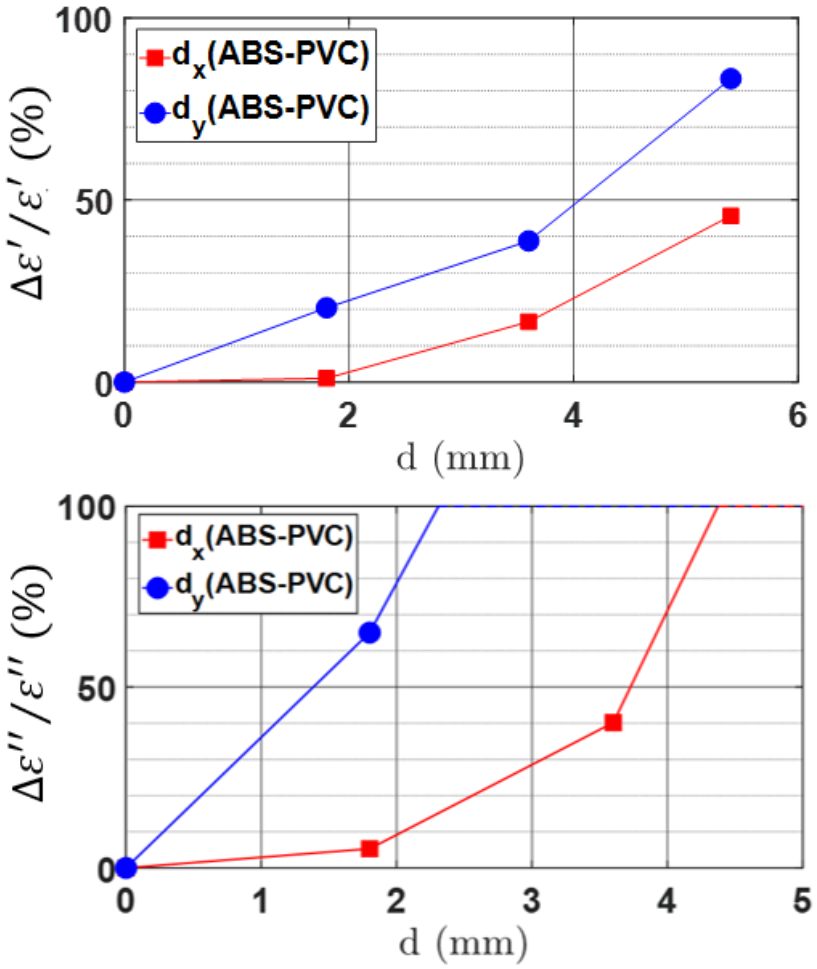


Figure 4.14: Error in dielectric constant and loss factor calculations as function of waveguide horizontal (d_x), and vertical misalignment (d_y).

4.6 Accuracy between simulations and measurements

Finally, it is important to remember that the errors presented in this study are due to the variation of small quantities. Figure 4.15 shows the data of Figures 4.5 and 4.11 plotted together (i.e. numerical simulations and measured data). From Figure 4.15 it is possible to observe that simulations and measurements are very close, as the completely-filled waveguide method provides for a robust recalculation of complex permittivity. The sample preparation always has imperfection, which much more significantly affects the measurement of high complex permittivity materials compared to low complex permittivity materials. In this work, it is demonstrated that for the former materials, when clamped between two waveguide flanges, which also desirably makes the measurement method completely nondestructive with no sample preparation required, the fields are very well confined within the waveguide apertures, resembling the electromagnetic situation in a completely-filled waveguide. As such,

the modified measurement procedure described in this work can be directly used for determining sample's complex permittivity. This will not be the case for low complex permittivity materials.

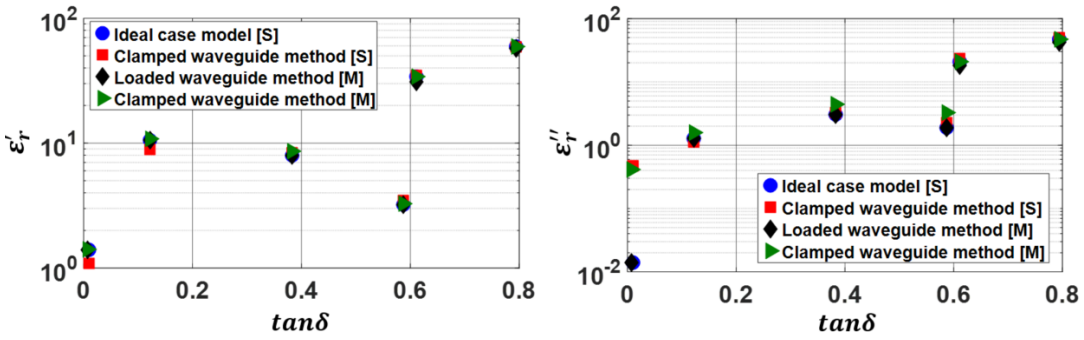


Figure 4.15: Dielectric constant and loss factor for simulations [S] and measured data [M] as function of $tan\delta$.

4.7 Summary and conclusion

Measurements of high dielectric constant and particularly high-loss factor materials (e.g., lossy composite sheets) is an important practical issue. However, methods by which to accurately accomplish this are significantly lacking. Additionally, composite sheets, having carbon fibre (extensively used in practice), present an additional constraint when using the completely-filled waveguide method since proper sample preparation becomes a significant challenge considering the presence of carbon fibres.

In this chapter, simulations and experimental measurements were conducted, in order to assess the applicability of the "waveguide clamped method" as a potential modification to the completely-filled waveguide technique. The method was found to be very useful for characterization of thin and high-loss materials, such as semiconductors, carbon fiber reinforced composites or carbon nanotube (CNT) composites. This modified method can be used with the NRW/Backer-Jarvis without requiring a new theoretical formulation for the extraction of the complex permittivity. In addition, the method itself is completely non-destructive with no sample preparation required.

Unexpectedly, in both numerical simulations and experimental tests, the dielectric constant (i.e., the real part of the complex permittivity) was closely estimated even for low-loss materials with errors in the same order as those experienced with the completely-filled waveguide technique. The error calculated experimentally does not exceed 4% for a sample with $tan\delta = 0.8$, and it decreases exponentially for greater value of ε_r' and ε_r''. On the other hand, the accuracy is degraded when estimating the loss factor using this method. However, as demonstrated in Sections 4.4 and 4.5, the

error decreases exponentially for materials with higher loss factors. An error in ε_r'' of 11.5% was measured for a sample with $tan\delta = 0.8$. In addition, both errors in ε_r' and ε_r'' are affected by the thickness of the sample and optimal results in the determination of the dielectric properties were found to be associated with small thicknesses (e.g., samples with $tan\delta = 0.6$ showed error of 0.04% for $t < 1$ mm).

The errors are due to the fact that the formulation for the completely-filled waveguide method do not account for the waveguide discontinuity in the clamped method. A more accurate analytical model that specifically accounts for discontinuities, leakage and higher-order modes, renders a more accurate recalculation of complex permittivity. However, as illustrated in this work, for thin and high-loss material this is not needed, since the expected errors are low due to concentration of the electromagnetic field within the waveguide aperture.

To reiterate, this work shows that the clamped method provides similar measurement to the ideal completely-filled waveguide method with errors in dielectric constant and loss-factor of less than 2% and 8%, respectively for materials with loss-tangent greater than 0.7. However, in practical implementation of the completely-filled waveguide method, the imperfections in sample geometry can result in errors of 15% on ε_r' and 26% on ε_r'' for materials with loss-tangent of 0.05 [201]. Furthermore, this error can significantly increase for higher complex permittivity [136], [201], [203]. Therefore, this proposed modification to the completely-filled waveguide method constitutes an improvement in the method's accuracy when measuring high complex permittivity materials.

Finally, particular attention must be paid in proper alignment of the waveguides, particularly in the direction of the maximum electric field.

Chapter 5

Wide-band microwave characterization of unidirectional CFRP sheets

After having established in Chapter 4 a reliable method for dielectric properties characterization of high-loss material, in this chapter, unidirectional composite sheets are tested in order to measure their complex permittivity.

The choice of unidirectional laminates is related to the observation reported in Chapter 3. When the composite material is subjected to radiation, the external electric field causes movement of electric charges in the conductive fibres. The movement follows the direction in which the electric field is polarized. If the composite laminate is composed by several layers of fibres oriented in different directions, or by several layers of woven fabric, there will always be movement of charges along the orientation of the electric field. This is due to the fact that the fibres are closely in contact with each other in more than one direction or arranged in more than one direction. Thus, more likely to promote movement of charges along the direction of the electric field. The movement of electric charges causes polarisation of the entire region and generates an electric field in opposition to the applied field, which repel the applied field from penetrating the material. As seen in Chapter 3, woven CFRP composites showed high ability of shielding the electromagnetic radiation.

Therefore, the use of a less complex structure, such as a unidirectional composite (i.e., with fibres oriented along a preferred direction) coupled with appropriate polarization of the electric field is the key to allow transmission of the signal through the CFRP composite, even if high lossy. If the electric field is directed perpendicularly to the fibres' orientation, the signal is able to penetrate the material, as the contact points between adjacent yarns decrease drastically.

In this section, the reflection and transmission coefficient of CFRP sheet are measured for parallel and perpendicular polarization of the electric field in respect to the fibres' orientation. A mesoscale numerical model of the CFRP sheet is also presented to determine the reflection and transmission properties of unidirectional CFRP. Subsequently, using this data, the dielectric properties (averaged over X-band and Ku-band) were calculated using the NRW/Backer-Jarvis procedure.

5.1 Materials

For the study, unidirectional composite sheets were manufactured using Toray P235W-19 highly toughened carbon fiber-reinforced UD prepreg, impregnated in 37% epoxy resin (Torayca 3900-series), with density of 1.6 g/cm^3. The carbon fiber/epoxy resin laminates were composed stacking along the same orientation, here indicated with 0°, 1 layer [0°], 2 layers $[0_2^\circ]$ and 4 layers $[0_4^\circ]$ of prepreg respectively. Each test specimen was cured by hot press. The sheets were processed at 190 °C under 0.6 MPa (90 psi) pressure for 6 hours, followed by a free-standing post-cure for 8 hours at 240 °C. This procedure ensures a nominally consistent volume fraction throughout the laminate. Three types of samples were obtained with thickness equal to 0.23 mm, 0.35 mm and 0.69 mm respectively, as shown in Table 5.1.

Table 5.1: Unidirectional CFRP sheets specifications.

Specimen	Lay up	Thickness [mm]
CFRP1	[0]	0.227
CFRP2	$[0_2]$	0.355
CFRP3	$[0_4]$	0.685

The electromagnetic properties of fibres and resin are reported in Table 5.2.

Table 5.2: CFRP properties of filler and polymer.

Material	Type	Electromagnetic properties
Epoxy resin	Torayca 3900	$\varepsilon_r' = 4$, $\mu_r = 1$
Carbon fibre	T800 24k	$\sigma = 70000$ S/m, $\mu_r = 1$

5.2 Mesoscale simulations of unidirectional CFRP sheets

In order to correctly assess the electromagnetic behaviour of unidirectional CFRP sheets, a step by step approach was considered, starting with simulation of a laminate made with only one layer of prepreg (i.e., CFRP1). This choice was made to avoid excessive computation time, as the running time of simulation increase with the number of mesh elements required to simulate more than one layer of prepreg and

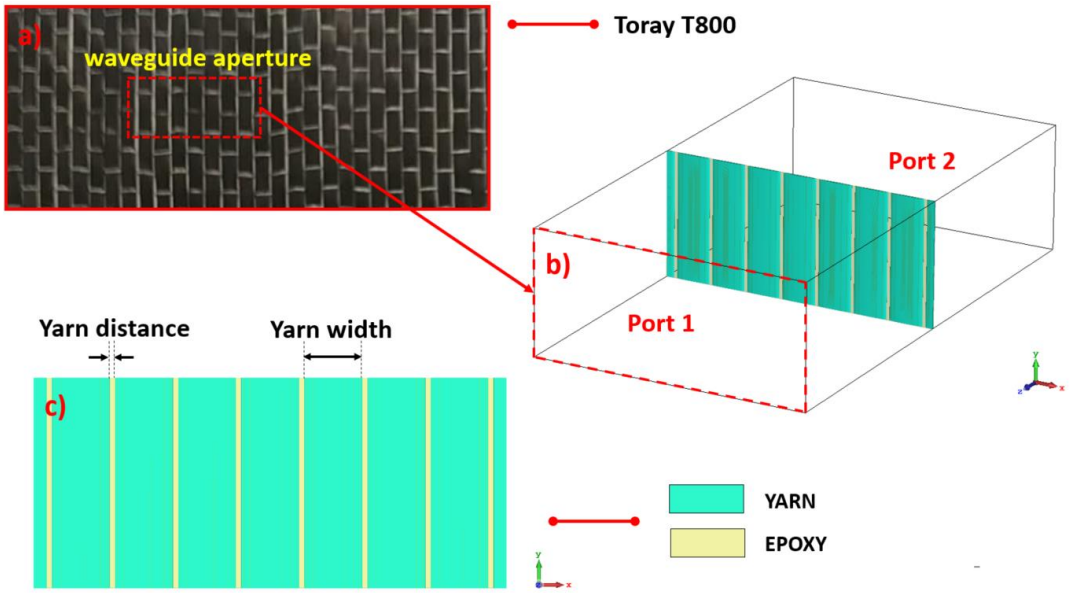


Figure 5.1: Simulation methodology for the mesoscale CFRP1 composite, inserted inside a WR90 waveguide: a) T800 carbon fibres, b) Simulated CFRP1 model inside a rectangular waveguide and c) particular of CFRP1 model with elliptical yarns (blue) and epoxy region (light green).

especially the element made of carbon fibre material. This is caused by the high conductivity of the carbon fibres, which is of the order of $\simeq 10^4 \div 10^5$. Nevertheless, full simulations of more than one layer will be compared with the experimental measurements results in Section 5.3.

Therefore, numerical simulations were conducted at X-band and Ku-band to assess the reflection and transmission coefficients S_{11} and S_{21} of the CFRP1 sample presented in Sections 4.5 and 5.1. The effects on the scattering parameters of fibres conductivity, yarn width, distance between yarns, yarn's thickness and shape of yarn cross-section are fully addressed for polarization of the electric field perpendicular and parallel to the fibres (or yarns) direction.

Table 5.3: CFRP1 model, geometric and electromagnetic parameters.

CFRP1 BASE MODEL	
YARN	$\sigma = 70000$ S/m, $\mu_r = 1$
EPOXY	$\varepsilon_r' = 4$, $\mu_r = 1$
YARN CROSS-SECTION	ELIPSE
YARN SPACING	0.3 mm
YARN WIDTH	2.4 mm
YARN THICKNESS	0.2 mm
BAND	X and Ku band

The completely-filled rectangular waveguide model shown in Fig. 4.3 is adopted. The homogenous material is replaced by a mesoscale model made of epoxy resin and conductive yarns, as illustrated in Figure 5.1. The frequency domain solver based on the Finite Integration Technique (FIT), which is a spatial discretization scheme to numerically solve Maxwell's equations on the geometry under simulation in their integral form [157].

The geometrical parameters, such as width of the yarns, distance between yarns and thickness of yarns, were measured with a micrometre with accuracy of $\pm$ 0.005 mm. This was possible due to having access to the dry unidirectional carbon fibre cloth T800, which is characterized by a high filament count for its yarns (i.e., Toray T800 24k), as depicted in Figure 5.1. As per Table 5.2, it was possible to define a base mesoscale model with geometrical and electromagnetic parameters reported in Table 5.3. Yarns made of carbon graphite with elliptical cross section were inserted inside a plate made of epoxy resin, with the assumption that the electromagnetic properties of carbon fibres are dominant over the epoxy resin, as the epoxy is non-conductive.

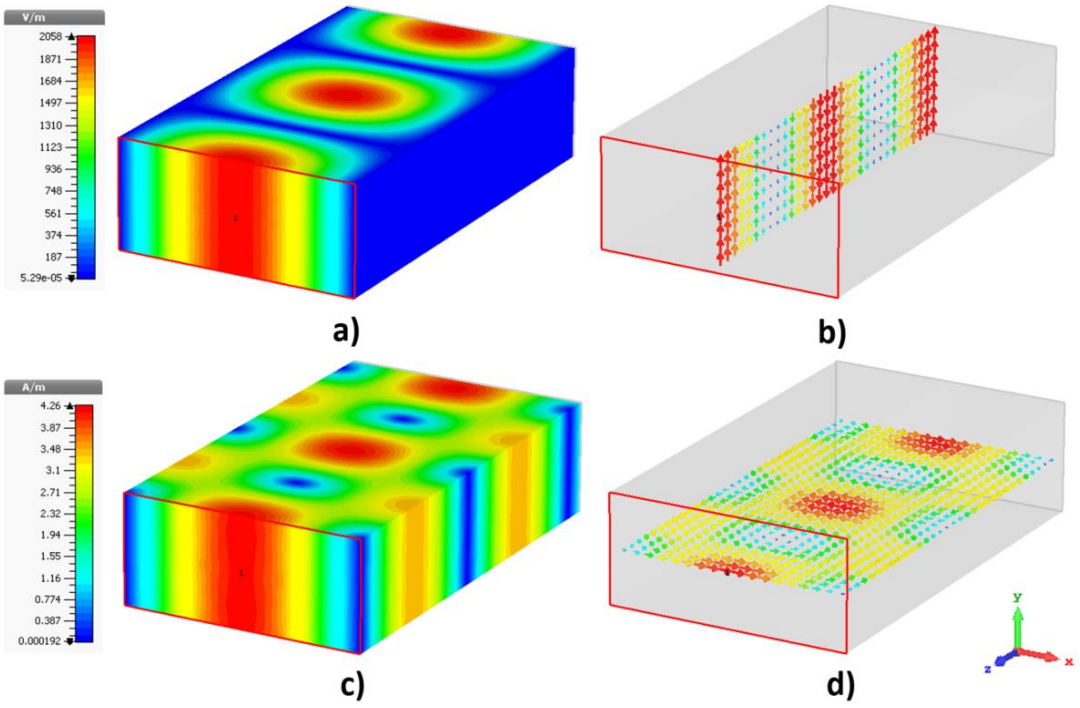


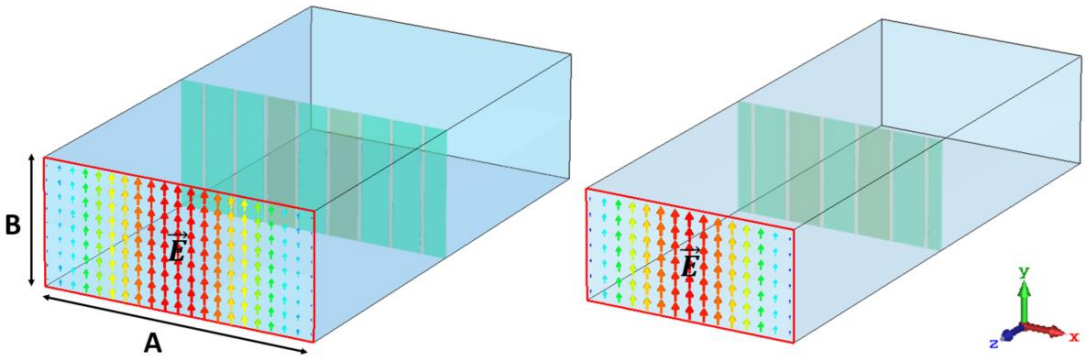
Figure 5.2: Propagation of TE_{10} in an empty WR-90 waveguide at 10.3 GHz: a) electric field pattern; b) **E** plotted on *y*-*z* cross-section; c) magnetic field pattern; d) **H** plotted on *x*-*z* cross-section.

5.2.1 Parallel polarization

A hollow waveguide is a transmission line that looks like an empty metallic pipe. It supports the propagation of transverse electric (TE) and transverse magnetic (TM)

modes. The notation TE_{mn} and TM_{mn} are commonly used to denote the type of wave and its mode, where m and n are the mode number in the horizontal and vertical directions respectively. The mode with the lowest cut-off frequency is called the fundamental mode or dominant mode. For a hollow rectangular waveguide the dominant mode is TE_{10}. Its electric field vector **E** and magnetic field vector **H** are directed perpendicularly to the direction of wave propagation (i.e., *z*-axis), and travel along the length of the waveguide as depicted in Figure 5.2. The electric field propagates oscillating along *y*-axis and is perpendicular to the magnetic field. Consequently, by convention the polarization of **E** is vertical and directed along *y*.

Therefore, to ensure a polarization parallel to the direction of the fibres, the yarns are also oriented along *y*. The models in Figure 5.3 are used for X-band (8.2 GHz to 12.4 GHz) and Ku-band (12.4 GHz to 18 GHz) simulations. The dimensions used are the standard for WR-90 and WR-62 waveguides and are indicated in Figure 5.3. A length of 40 mm has been considered for both waveguides. The boundary conditions are electric in all directions, so that the walls of the waveguide operate like a perfect



WR-90:
A = 22.86 mm, B = 10.16 mm

WR-62:
A = 15.8 mm, B = 7.9 mm

Figure 5.3: Parallel polarization models. WR-90 used for X-band simulations and WR-62 used for Ku-band simulations. **E** on port 1 is polarized along *y* and yarns are oriented along *y*. Material simulated: CFRP1.

electric conductor (PEC): all tangential electric fields and normal magnetic fluxes are set to zero. Two symmetry planes are considered along *y*-*z* and *x*-*z* plane, to reduce the computational time. The mesh is composed of tetrahedral elements, i.e., 117918 mesh elements for WR-90 and 65760 mesh elements for WR-62.

The calculated scattering parameters for the models of Figure 5.3 with CFRP1 (see Table 5.3) are shown in Figure 5.4. As expected, the result of a parallel polarization is low transmission and high reflection of the signal. This is caused by the difficulty of the TE waves to penetrate the material, which acts as a shield. Even if there is no contact between the yarns along *x* direction, this does not affect the flow of electric

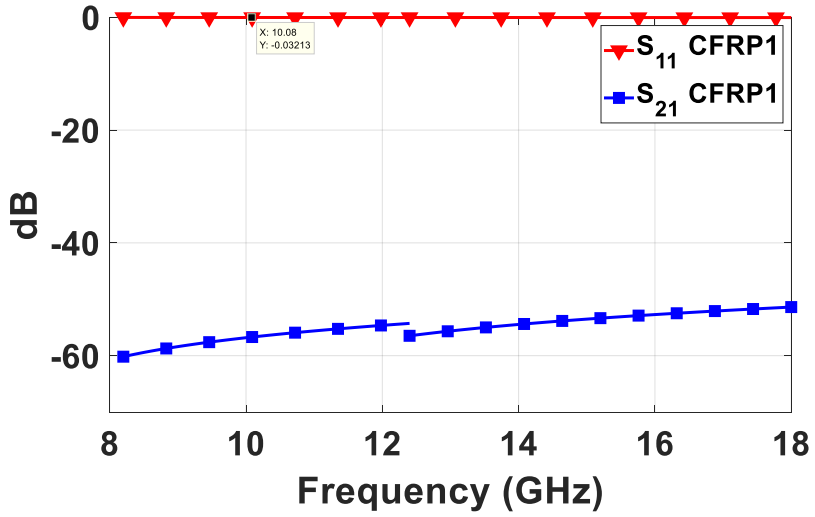


Figure 5.4: S_{11} and S_{21} calculated for CFRP1 over frequency range (8.2 to 18 GHz).

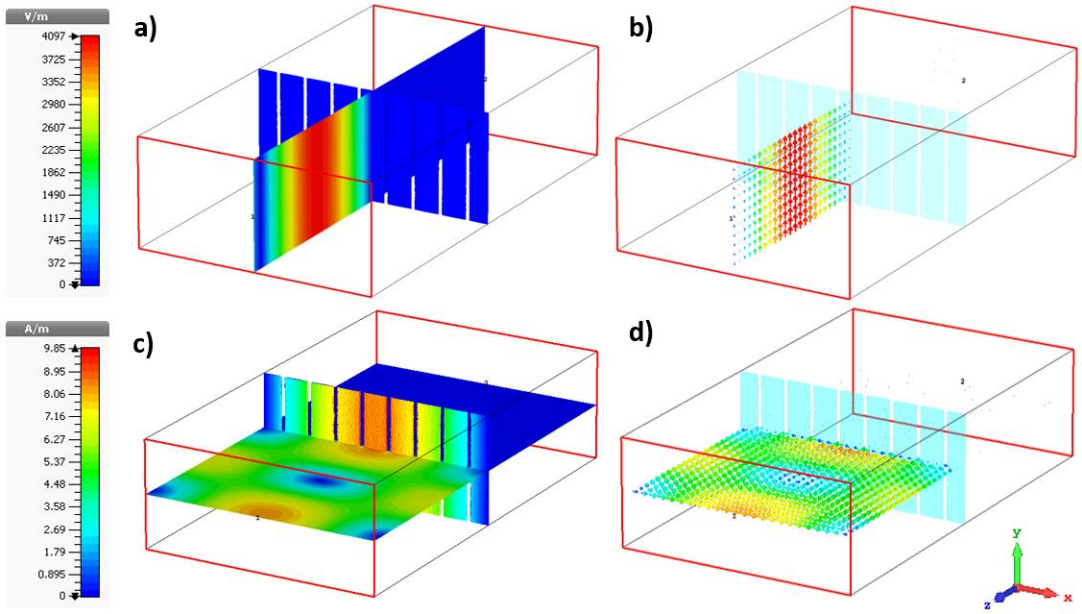


Figure 5.5: a) Electric field pattern; b) Electric field vector plotted on *y*-*z* cross-section; c) Magnetic field pattern; d) Magnetic field vector plotted on *x*-*z* cross-section. The fields are calculated at 10.3 GHz.

charges, as the electric current is directed along the direction of the electric field, i.e., along *y*.

An example of what happens to the electric and magnetic field pattern is reported in Figure 5.5, for the X-band case. The electromagnetic field transmitted through the sample is close to 0. Precisely, for X-band simulation, only the 0.15% of the signal is transmitted through the sample, while 99.63% of the signal is reflected back to Port 1 (the percentages presented are averaged over the band considered). A remaining third part of the signal is accepted in the structure (i.e., absorption loss). At Ku-band, the

0.21% of the signal is transmitted, while the 99.52% is reflected. The signal transmitted increases, as the $|S_{21}|$ (i.e., shielding effectiveness) decreases. Overall, the shielding effectiveness of CFRP1 averaged over the frequency band considered is equal to 55 dB. In the following sections, the effect of yarn conductivity, width, spacing, thickness, and cross-sectional shape is considered to evaluate how the scattering parameters varies over frequency. The permittivity of resin is considered constant and the one reported in Table 5.3, as it does not participate effectively in the shielding process, due to its dielectric behaviour.

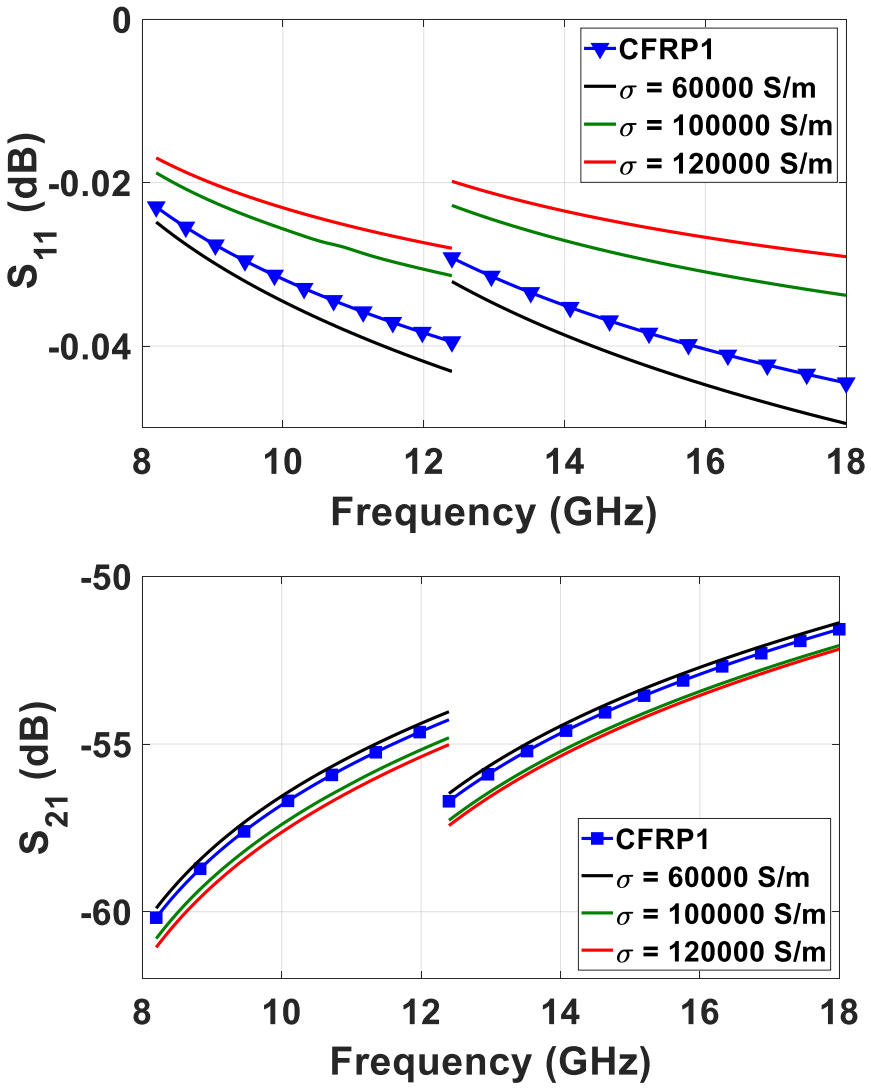


Figure 5.6: Reflection and transmission coefficient over frequency for σ = 60000, 70000, 100000 and 1200000 S/m.

Effect of fibre conductivity

The conductivity chosen for the base model of Table 5.3 is equal to 70000 S/m, as per technical datasheet. Hereafter, the base model is indicated as "CFRP1". The

conductivity of the yarns was made to vary between 60000 S/m and 120000 S/m, in order to verify its effect on the scattering parameters.

Figure 5.6 shows that an increment of conductivity is related to reduced transmission and increased reflection back to the source of the signal. This is expected, as a more conductive material, i.e., a material with lower resistivity, readily allows the passage of electric current. However, the variation of both S_{11} and S_{21} is not remarkable. Doubling the conductivity from 60000 S/m to 120000 S/m produces a decrement in S_{21} of $\simeq$ 1 dB and an increment in S_{11} $\simeq$ 0.01 dB (averaged over frequency band). A conductivity of 60000 S/m for the yarns in the simulated material generates a shielding effectiveness $>$ 50 dB, i.e., the material shields the 99.7% of the signal. Therefore, as a considerable part of the signal is already shielded, a further increase in conductivity does not overly affect both scattering parameters.

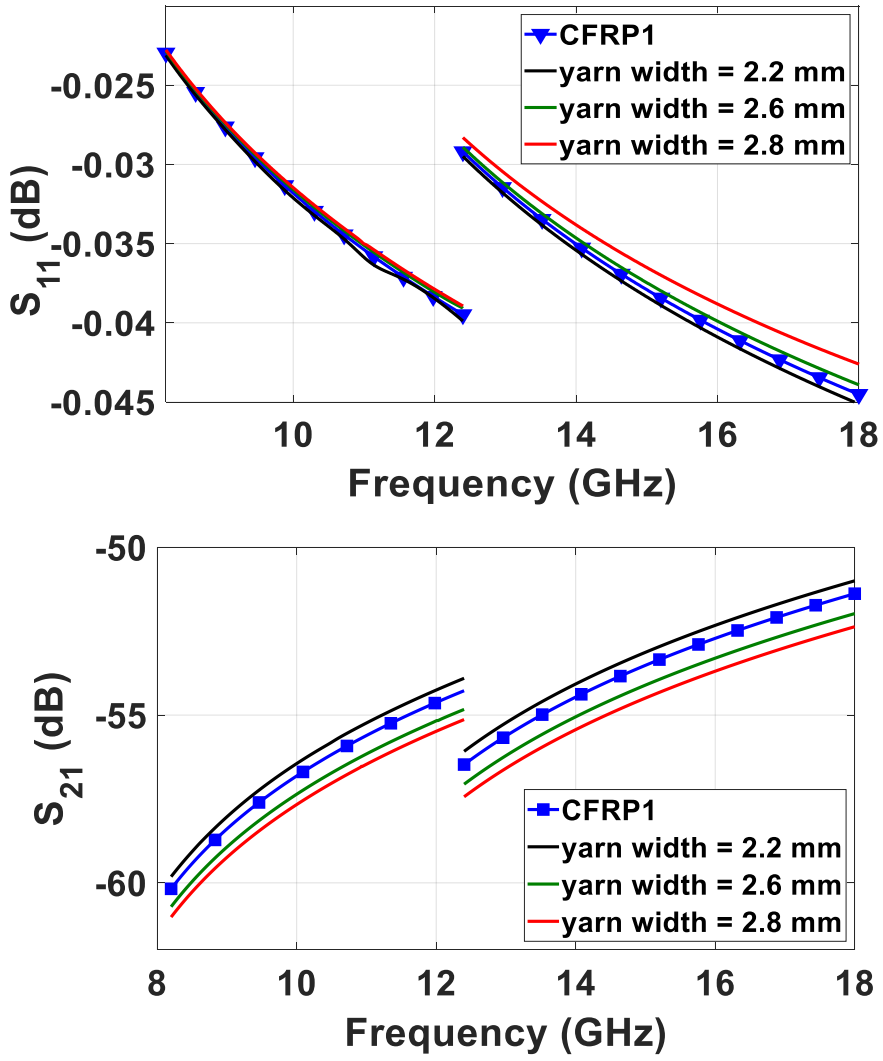


Figure 5.7: Reflection and transmission coefficient over frequency for yarn width = 2.2, 2.4, 2.6 and 2.8 mm.

Effect of yarn width

A similar outcome is found when changing the width of the yarn. The measured width is ≃ 2.4 mm. The width was made to vary from 2.2 mm to 2.8 mm with a step of 0.2 mm, keeping the spacing between the yarns unchanged and = 0.3 mm. Also in this case, the transmission coefficient decreases with increasing yarn's width, as the amount of reflecting surface increases. Figure 5.7 shows the S_{11} and S_{21} over frequency for the widths chosen. Similarly to the conductivity case, the S_{21} varies of ≃ 1 dB, as the yarn's width ranges from 2.2 mm to 2.8 mm. The S_{11} varies of 0.001-0.002 dB between the two extremes, as in this case a greater part of the signal is rather absorbed by the material then reflected, due to the increased dimension of the yarns.

Effect of yarn spacing

Measuring the dimension of the yarns spacing is a difficult task. As previously stated, the tools used was a micrometre with accuracy of ± 0.005 mm, and the particular structure of this unidirectional composite with high filament count resulted advantageous for taking measurements. However, more accurate methods such as travelling microscope and digital image processing can be used [209]. In literature, yarn spacing, also called pick length, has values that ranges from the order of micronmetre to millimetre length (e.g., 0.2-4 mm), for different yarn aspect ratios and fibre architectures [209]–[211]. The yarn spacing remains constant with the lamina thickness, decreases as the fibre volume fraction increases, and is affected by the yarn cross-section, i.e., if the cross-section varies from a round shape to a long and flat ellipse [211].

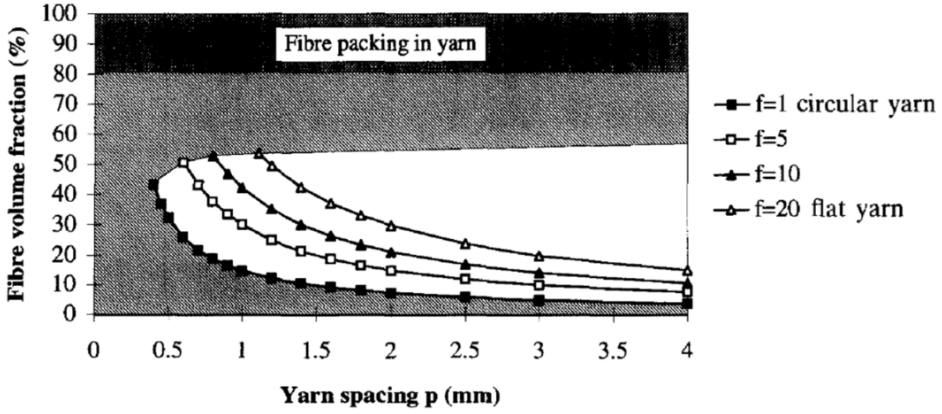


Figure 5.8: Fibre volume fraction as function of yarn spacing [211].

An example is given in Figure 5.8 [211], where the fibre volume fraction is reported as function of the yarn spacing, for several values of the yarn aspect ratio

indicated as f. The yarn spacing, indicated with p, for the base model was considered equal to:

$$p = \frac{\text{yarn width}}{8} = 0.3 \text{ mm} \tag{5.1}$$

considering that the yarn width is ≃ 2.4 mm and the prepreg resin content by weight percent is equal to 37% and resin spillage is expected after cure.

The yarn spacing was made to vary from 0.15 mm to 0.5 mm, keeping constant the value of yarn's width. The resulting reflection and transmission coefficients are reported in Figure 5.9. Unlike for the case of conductivity and yarn's width, in this case increasing the space between consecutive yarns produces a significant increment of the transmission coefficient. For instance, changing p from 0.15 mm to 0.5 mm causes an increment of ≃ 21 dB of S_{21}, considering the value averaged over frequency

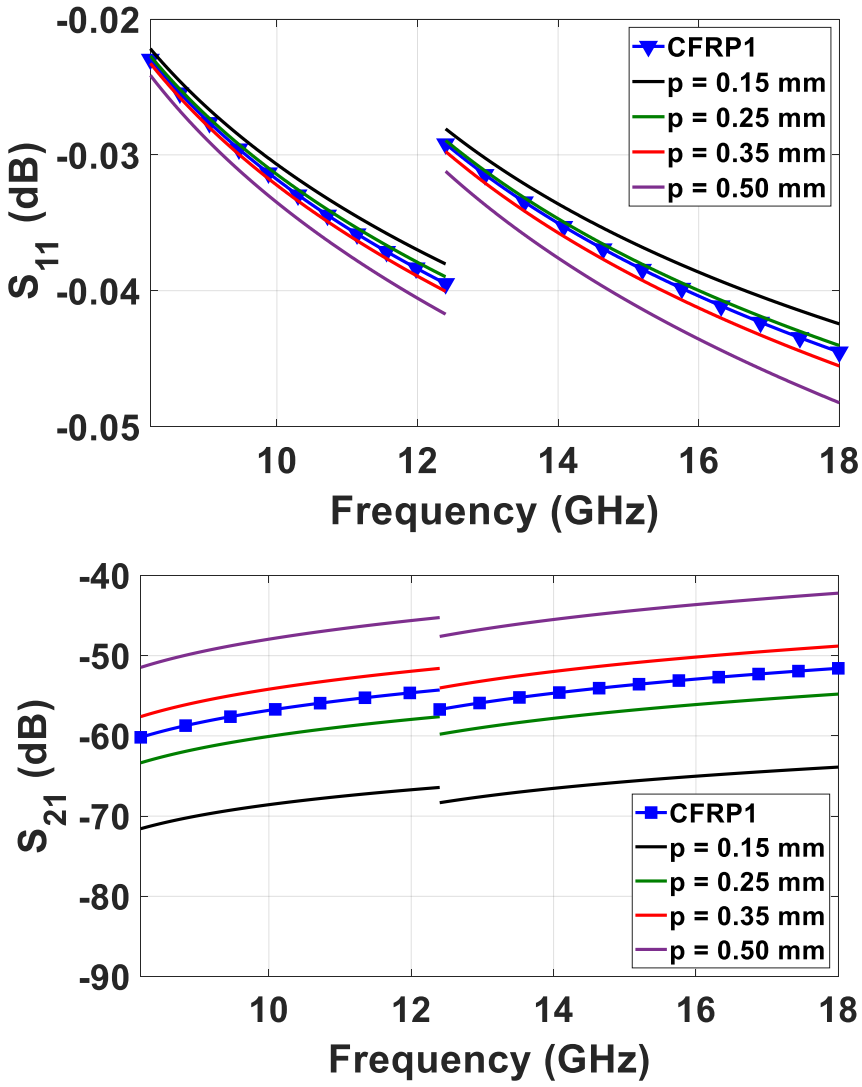


Figure 5.9: Reflection and transmission coefficient over frequency for p = 0.15, 0.25, 0.3, 0.35 and 0.5 mm.

band. Reducing the yarn spacing with constant yarn's width means tighten the yarns together and is more effective than increasing the width with constant d. The field propagates easily across the space between the yarns, which is filled with dielectric epoxy resin.

Effect of yarn thickness

Another parameter which influences the transmission coefficient is the thickness of the yarn, indicated in Figure 5.10 with t_{yarn}. The yarn thickness is limited by the total thickness of the material, which is ≃ 0.23 mm. Three thicknesses were considered, 0.10 mm, 0.15 mm and 0.20 mm. Varying t_{yarn} from 0.1 mm to 0.2 mm (i.e., doubling

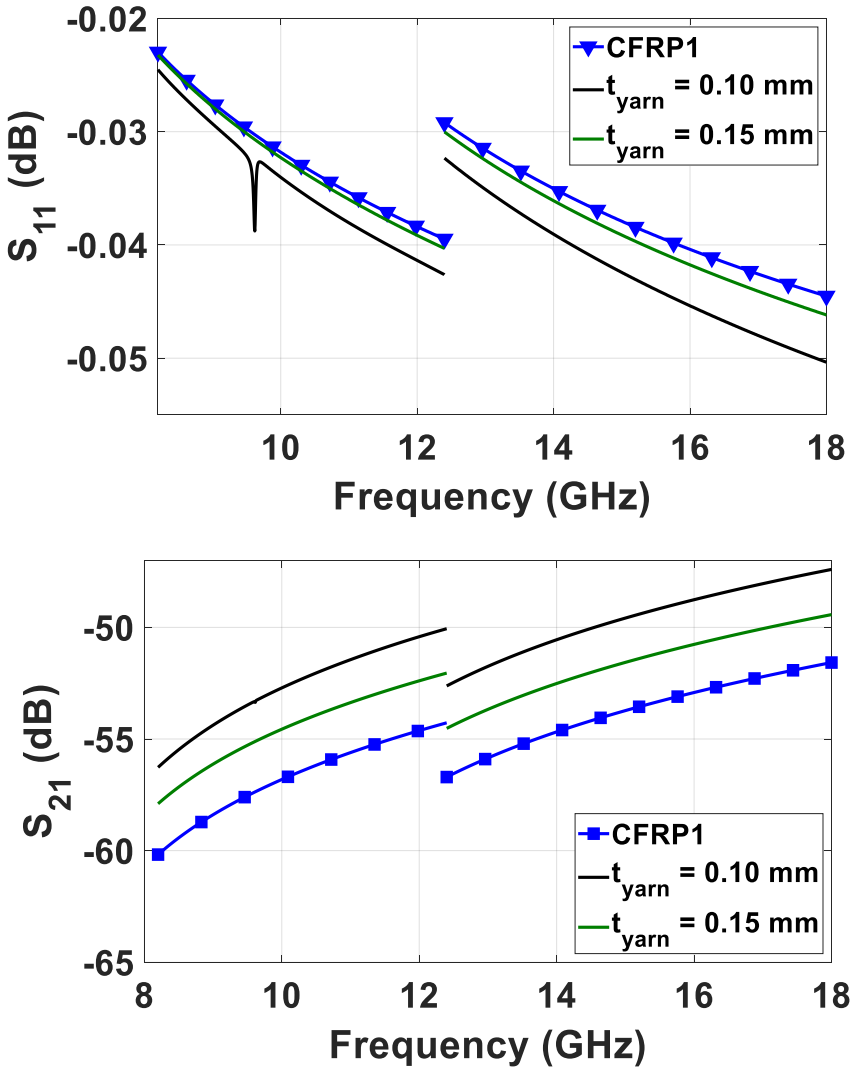


Figure 5.10: Reflection and transmission coefficient over frequency for $t_{yarn} = 0.10$, 0.15 and 0.20 mm.

the thickness), produces a decrement of ≃ 4 dB in average on the transmission of the signal, meaning that a thicker structure shields more energy.

Effect of yarn cross-section

For numerical models, the yarn cross-section shapes are usually assumed elliptical, lenticular or rectangular. The power-ellipse curve, which is a special form of the super-ellipse formulation (i.e., Lamé curve), is used to generate realistic yarn cross-sectional shapes [210]:

$$\left|\frac{x}{a}\right|^2 + \left|\frac{y}{b}\right|^{\frac{2}{n}} = 1 \tag{5.2}$$

where a is the length of the major semiaxis and b the length of the minor semiaxis. The entire range of exponents n gives realistic yarn cross-sectional shapes. For n = 1, the yarn shape describes an ellipse, for $n > 1$ a lenticular shape and for $0 < n < 1$ a rectangle with rounded edges. The chosen values of n are reported in Figure 5.11. Simulations were carried out for a lenticular shape with n = 2, 3 and 6, and for power-ellipses with n = 0.3, 0.6 and 0.9.

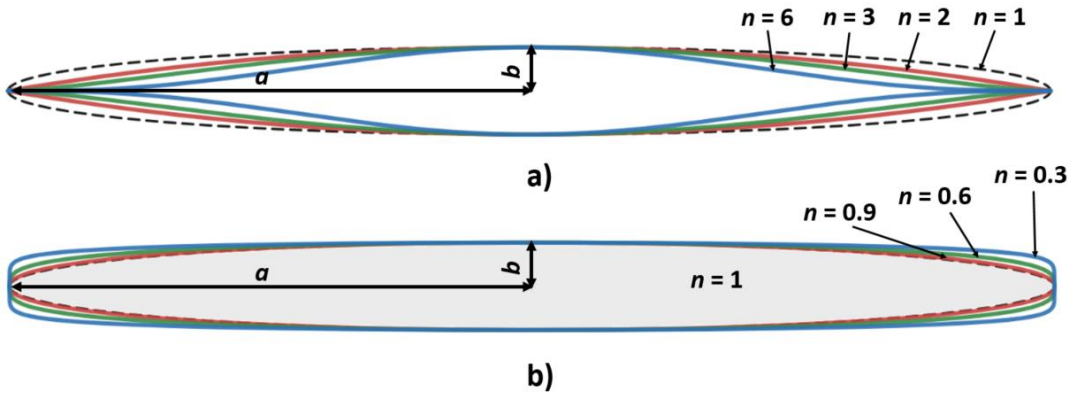


Figure 5.11: Power elliptical shapes for different exponents n: a) lenticular shape with n = 2, 3 and 6, b) n = 0.3, 0.6 and 0.9.

The results are shown in Figure 5.12 and 5.13. It is possible to observe that a power-ellipse cross-section always produces a lower value of S_{21} compared to an elliptical cross-section, both in the case of $n > 1$ and $0 < n < 1$ (i.e., the transmitted signal decreases). For a lenticular shape with n = 2, the transmitted signal decreases in average of ≃ 11 dB, as depicted in Figure 5.12. This means that the cross-sectional shape of the yarns can considerably affect the distribution of the signal. However, as the value of n increases, S_{11} and S_{21} tend to the ones measured for an elliptical cross-section. One would rather expect the opposite, as decreasing the value of n towards

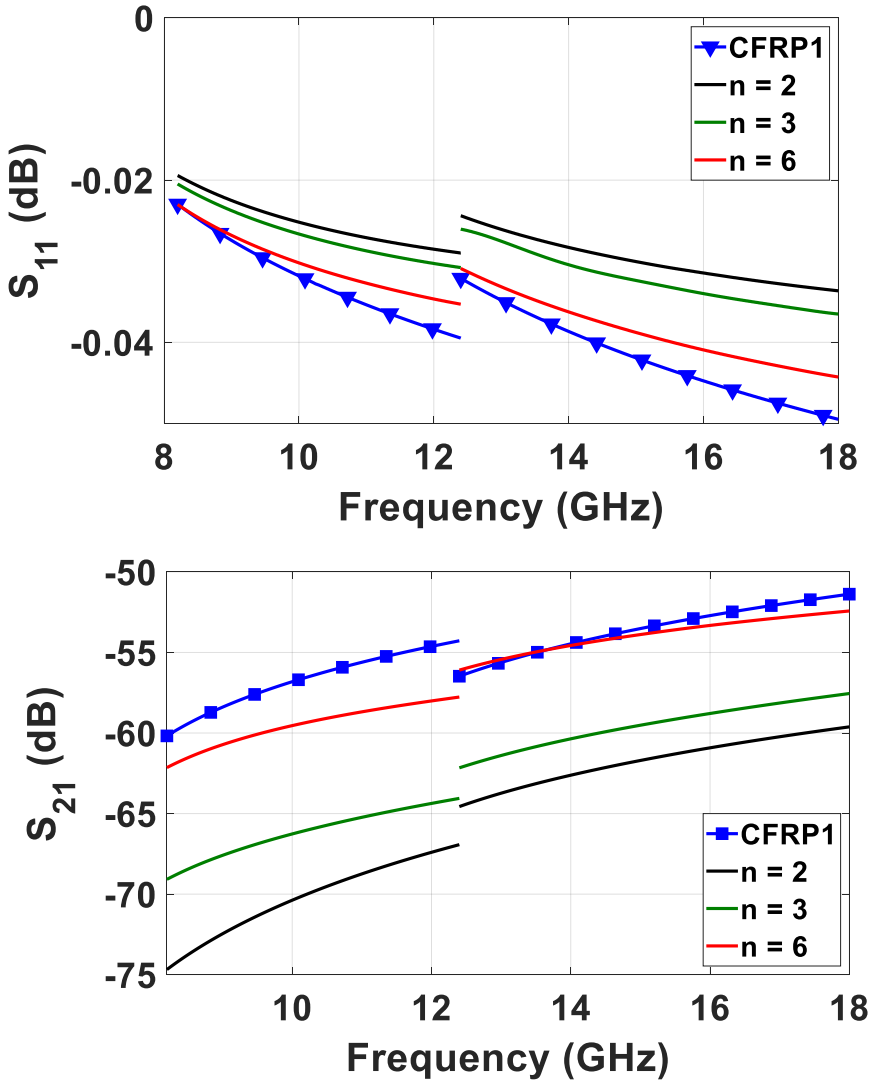


Figure 5.12: Reflection and transmission coefficient over frequency for *n* = 1, 2, 3 and 6.

the unity brings the shape of the cross-section back to an ellipse. Thus, it is possible to deduce that the lower S_{21} for *n* = 2 is determined by the change in the cross-sectional shape from convex to concave at its ends, resulting in a different distribution of the reflected signal.

For sake of clarity, Figure 5.14 shows the magnetic field distribution on *x*-*z* plane for *n* = 1, 2, 3 and 6 at X-band. In the *n* = 1 case, the rounder ends of the ellipse favour the transition of the electromagnetic field through the spacing between the yarns, as the vector field circles the edge of the yarn. This does not happen as the cross-section begins to take on a lenticular shape. The edges of the yarn, in their transition from round convex to pointed concave shape, hinder the path of the electric/magnetic field vector, conducing the field from one edge to the adjacent one, between two consecutive yarns. This behaviour can be particularly observed for the case of *n* = 3.

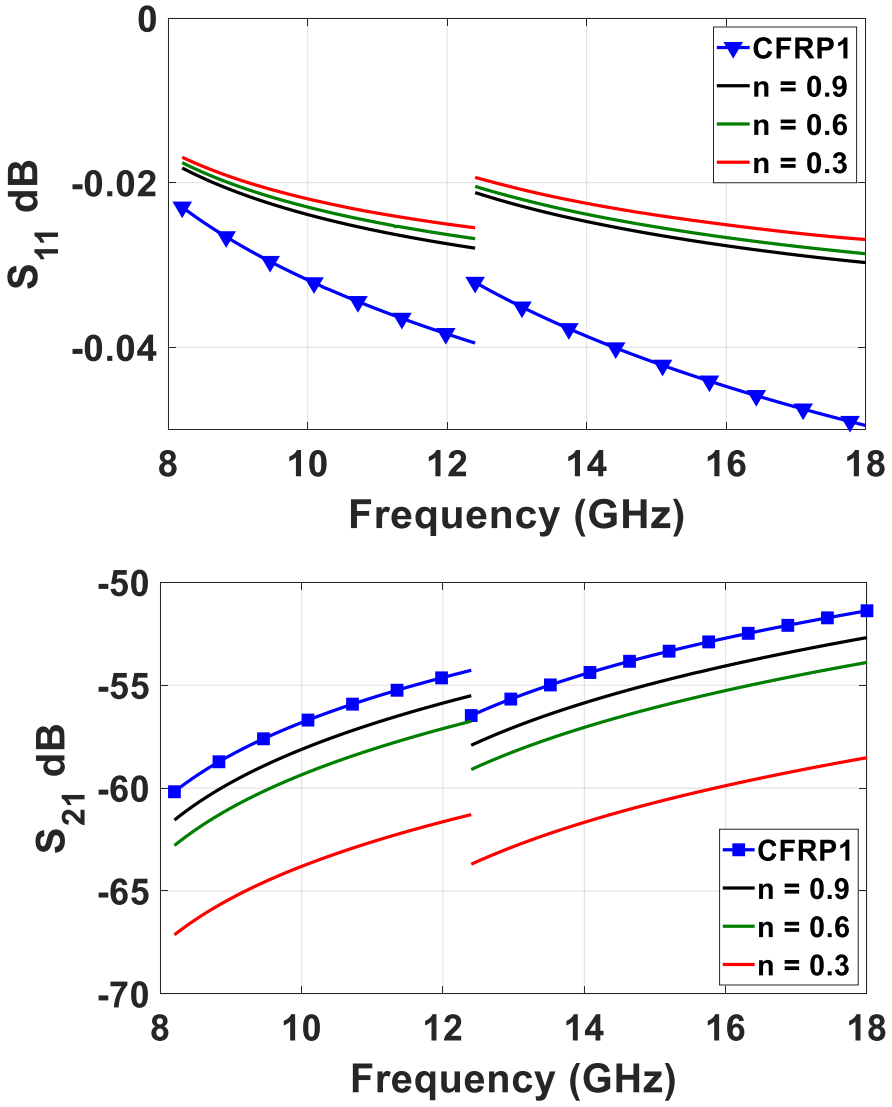


Figure 5.13: Reflection and transmission coefficient over frequency for n = 0.3, 0.6, 0.9 and 1.

However, as n increases the thickness of the yarn at its ends decreases (i.e., thinner edges and smaller cross-section area) and subsequently S_{21} increases again as well. Hence, even if initially a lenticular shape determines a significant increment of the shielding effectiveness of the sample, further increasing n reduces again the shielding effectiveness as the edges of the yarn become thinner.

Conversely, for $0 < n < 1$, to a decrement in value of the exponent corresponds a greater shielding effectiveness, as shown in Figure 5.13. The transmission coefficient decreases and the reflection coefficient increases. Between the base model CFRP1 and a model with n = 0.3 there is a difference of 7 dB in S_{21}. This behaviour can be easily explained acknowledging the fact that more the cross-section assumes a rectangular shape and the edges thicken, more radiation is reflected back to the source. This is due to two main causes: the area of the yarn cross-section is greater as n approaches 0, and

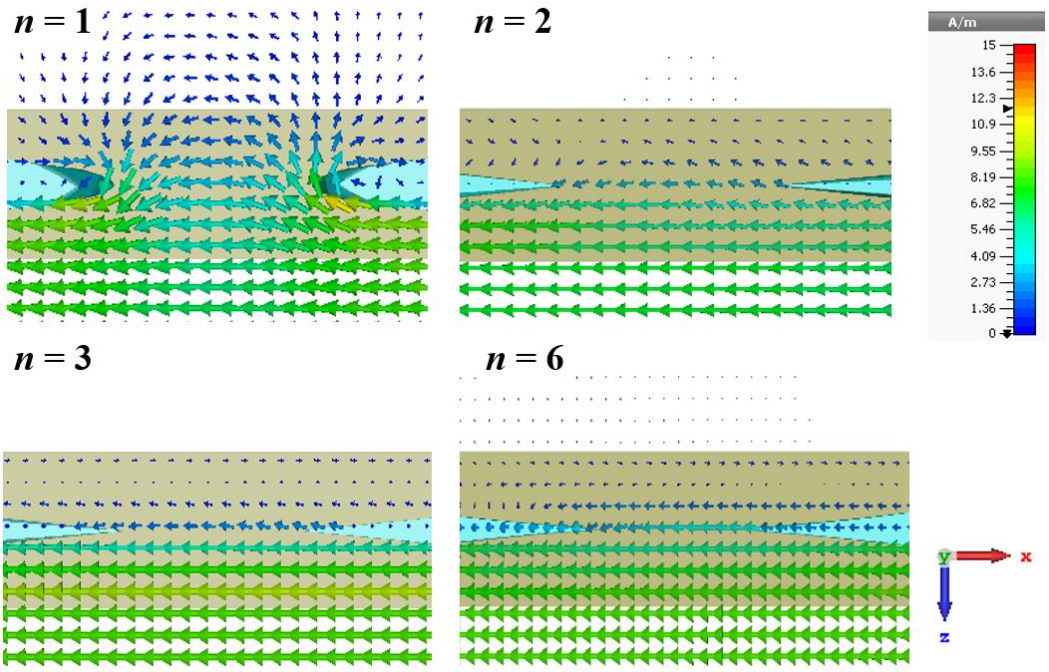
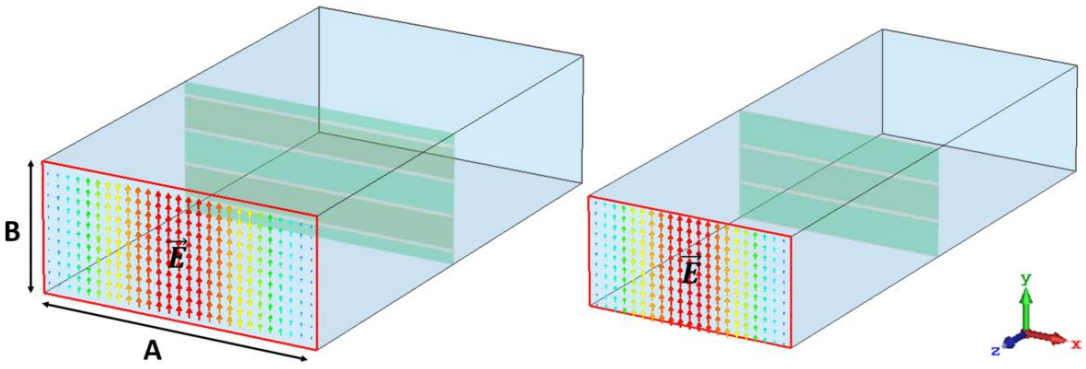


Figure 5.14: Magnetic field distribution at X-band between two consecutive yarns plotted on *x*-*z* plane for *n* = 1, 2, 3 and 6.

the path of the magnetic field around the edges is partially prevented by the more angular shape of the power-ellipse.

5.2.2 Perpendicular polarization

When the polarization of the electric field is perpendicular to the fibres, greater penetration of the signal through the material is expected. The case of perpendicular



WR-90:
A = 22.86 mm, B = 10.16 mm

WR-62:
A = 15.8 mm, B = 7.9 mm

Figure 5.15: Perpendicular polarization models for WR-90 and WR-62. **E** on Port 1 is polarized along *y* and yarns are oriented along *x*. Material simulated: CFRP1.

polarization was studied at X-band and Ku-band, using similar configurations to those presented in Section 5.2.1, where the only difference is the orientation of the yarns arranged along *x*-axis. The models used are presented in Figure 5.15.

The boundary conditions are electric in all directions. Two symmetry planes are considered along *y*-*z* and *x*-*z* plane, to reduce the computational time. The mesh is composed of tetrahedral elements, i.e., 110840 mesh elements for WR-90 and 13242 mesh elements for WR-62.

The calculated scattering parameters are shown in Figure 5.16. Unlike for the case of parallel polarization, when the electric field is perpendicular to the yarns a larger portion of the signal is transmitted from Port 1 to Port 2. For the base model, an average value of -3.2 dB and -3 dB were calculated for S_{11} and S_{21} respectively at X-band. While, -1.2 and -6.6 dB are the corresponding average values of S_{11} and S_{21} at Ku-band.

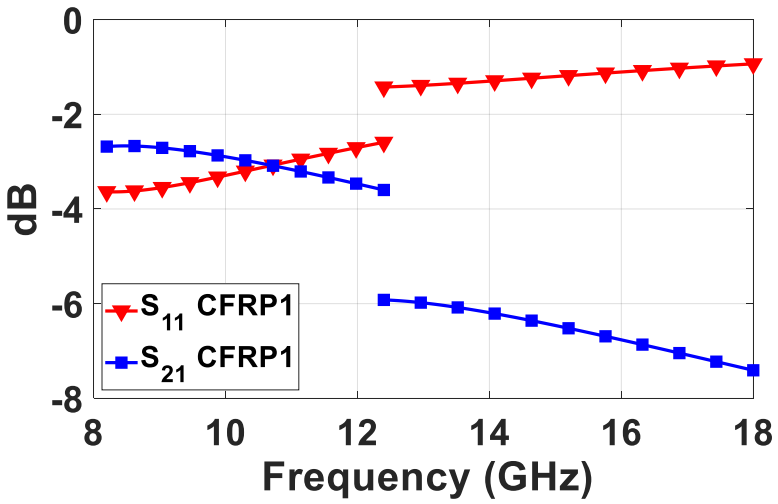


Figure 5.16: S_{11} and S_{21} calculated for CFRP1 with perpendicular polarization.

An example of what happens to the electric and magnetic field pattern is reported in Figures 5.17 and 5.18, for the X-band case. In this case, a significant part of the radiation is transmitted from Port 1 to Port 2. In addition, there is no continuity between the yarns along *y*-axis, therefore, the influence of the external electromagnetic field determines a concentration of positive/negative charge at the edges of each yarn, as shown in Figure 5.18, where the electric field is plotted on *y*-*z* plane between two consecutive yarns. As a consequence of the applied electric field, a higher charge density is found at the ends of the elliptical cross-section and since the electric field is proportional to the charge density, its value will be higher near the edges of the yarns.

Also in this case, the effect of yarn conductivity, width, spacing, thickness, and cross-sectional shape on the scattering parameters is reported in the following sections.

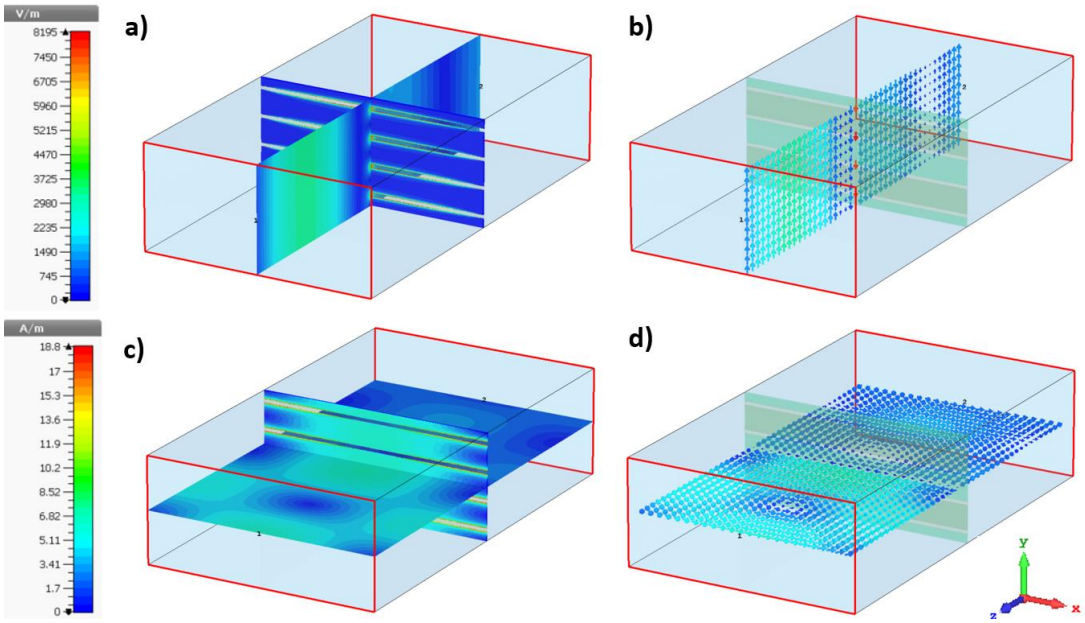


Figure 5.17: a) Electric field pattern; b) Electric field vector plotted on *y*-*z* cross-section; c) Magnetic field pattern; d) Magnetic field vector plotted on *x*-*z* cross-section. The fields are calculated at 10.3 GHz.

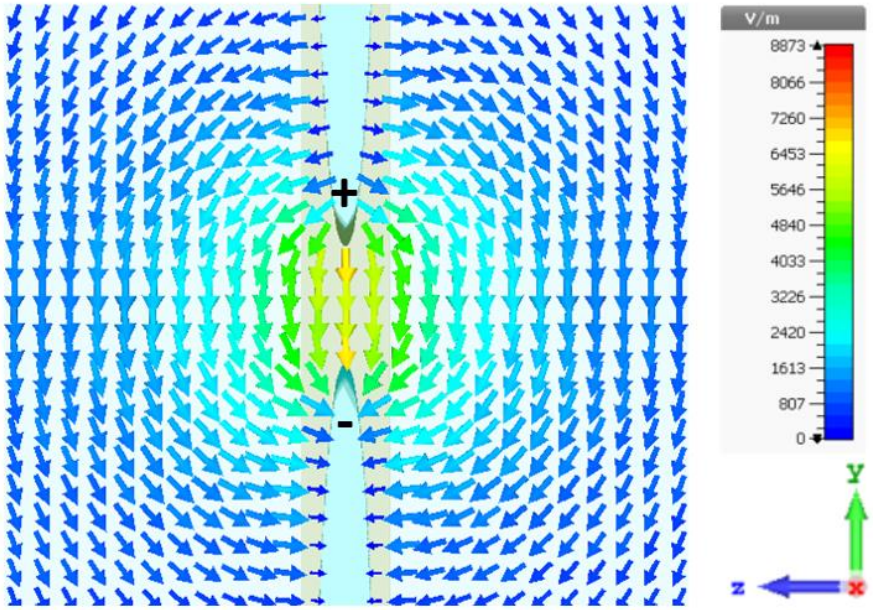


Figure 5.18: Electric field vector plotted on *y*-*z* plane at 10.3 GHz.

Effect of fibre conductivity

The conductivity of the yarns was made to vary in the same fashion as what done in Section 5.2.1. Differently to what was found for polarization parallel to fibres, the

conductivity of the yarns does not affect significantly the scattering parameters. The reason is due to the discontinuity between the conductive yarns along *y*-axis, as the movement of charges is hindered along *y*-axis. The calculated values overlap each other as demonstrated in Figure 5.19, for both reflection and transmission coefficient.

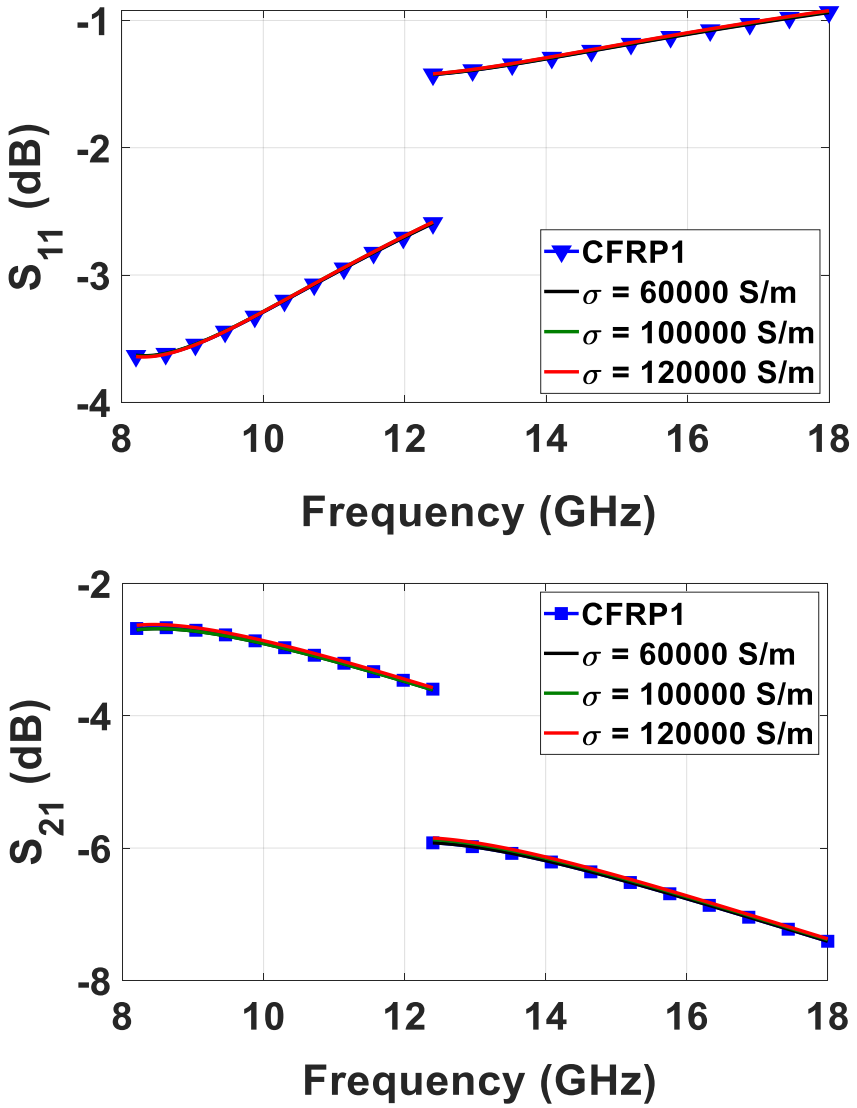


Figure 5.19: Reflection and transmission coefficient over frequency for $\sigma = 60000$, 70000, 100000 and 1200000 S/m.

Effect of yarn width

As previously done for the parallel case, the width was made to vary from 2.2 mm to 2.8 mm with a step of 0.2 mm, keeping the spacing between the yarns unchanged and $= 0.3$ mm. Also in this case, the transmission coefficient decreases with increasing

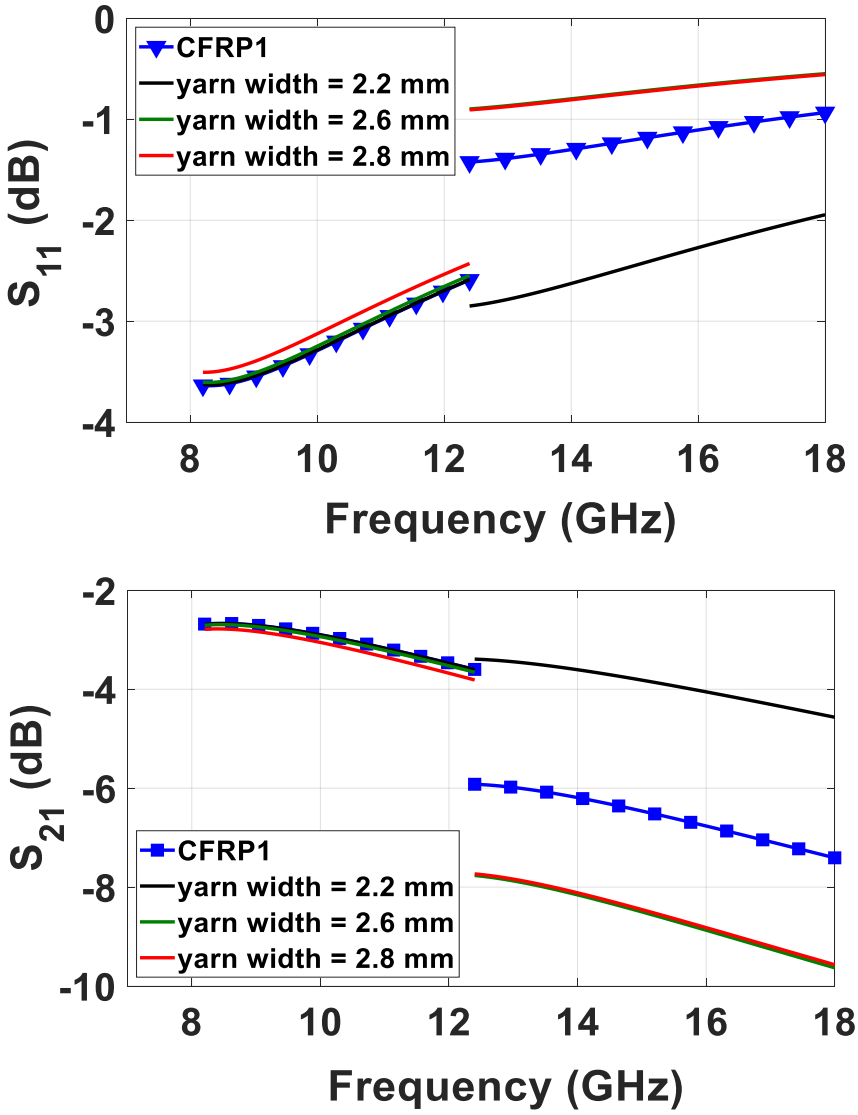


Figure 5.20: Reflection and transmission coefficient over frequency for yarn width = 2.2, 2.4, 2.6 and 2.8 mm.

yarn's width, as the amount of reflecting surface increases. However, the decrement/increment of the transmission/reflection coefficient is highly dependent upon the geometry of the system. When increasing the yarn's width, while keeping the spacing constant, the area of the yarns expands along *y*-axis, pushing the ones which are located close to the waveguide walls out of the waveguide aperture. In the X-band simulation, the upper and lower yarns are always in contact with the waveguide walls, when changing the width from 2.2 mm to a maximum of 2.8 mm. This contact is always ensured. However, in the Ku-band case, due to the smaller dimension of the aperture, the contact is maintained for 2.2 mm, then, for 2.4 mm the contact with the walls is lost as the upper and lower yarns move outside the waveguide frame. The

contact is consequently restored for width equal 2.6 mm and 2.8 mm as the subsequent yarns touch again the upper and lower wall of the waveguide.

This behaviour is shown in Figure 5.20. There is little variation at X-band for both coefficients as the upper and lower yarns are always in contact with the waveguide walls. Conversely, at Ku-band passing from a width of 2.2 mm to 2.8 mm produces a detectable variation of $\simeq$ 4.7 dB in average for the transmission coefficient and of $\simeq$ 1.7 dB in average for the reflection coefficient, as the initial upper and lower yarns are transitioning out of the aperture. This demonstrate that what influences the scattering parameters is not the width itself of the yarn, but the number of yarns seen by the waveguide aperture and the presence or absence of contact with the upper and lower waveguide walls. As a matter of fact, the values calculated for 2.6 mm and 2.8 mm are very close, i.e., once the contact is again re-established and the number of yarns seen by the waveguide is the same.

Effect of yarn spacing

As previously done for the parallel case, the yarn spacing was made to vary from 0.15 mm to 0.5 mm, keeping constant the value of yarns width. The resulting reflection and transmission coefficients are reported in Figure 5.21. Unlike for the case of polarization perpendicular to fibres, a significant increment of the transmission coefficient is not observed. However, considering the parameters calculated at X-band, a similar behaviour can be noticed. For instance, changing p from 0.15 mm to 0.5 mm causes an increment of $\simeq$ 3.8 dB of S_{21}, and a decrement of $\simeq$ 3.6 dB of S_{11}, considering both values averaged over frequency band. Also in this case, an important role is played by the number of yarns seen by the waveguide aperture and by the contact of the yarns with the upper and lower waveguide walls. At X-band, the number of yarns does not vary and the contact is always maintained. This is not the case when for a smaller aperture. At Ku-band, the number of yarns seen by the aperture decreases when varying p from 0.15 mm to 0.25 mm and the contact with the waveguide walls is lost. The contact with the walls is restored at p = 0.35 mm, where the upper and lower yarns are tangential the waveguide walls. Then, the portion of yarns section in contact with the waveguide walls further increases at p = 0.5 mm. From 0.15 mm to 0.25 mm the transmission slightly increases of 0.3 dB, then the transmitted signal does not vary significantly until the contact with the waveguide walls is restored (i.e., p = 0.35 mm) and decreases again once. Finally, the behaviour is similar to X-band, where the transmission increases/reflection decreases with p, as the number of yarns is constant and the contact is maintained.

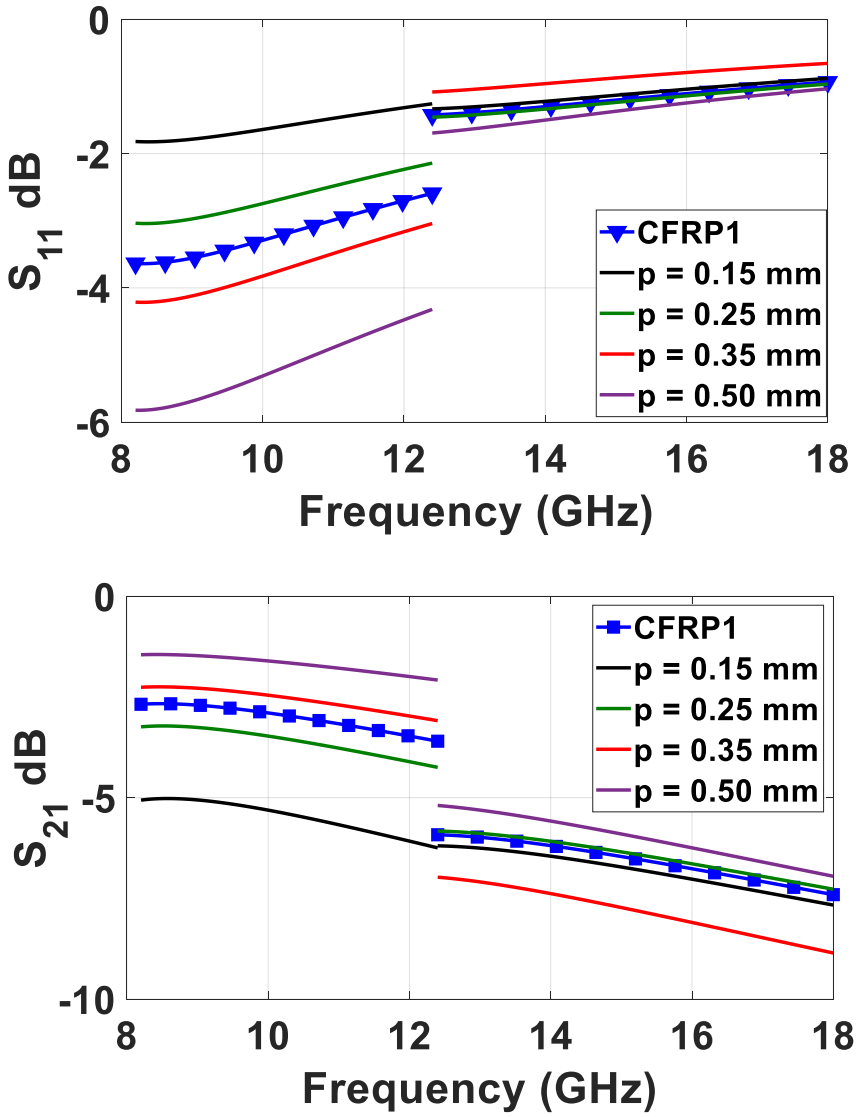


Figure 5.21: Reflection and transmission coefficient over frequency for p = 0.15, 0.25, 0.3, 0.35 and 0.5 mm.

From the observations on width and spacing of the yarns, it is possible to conclude that when the number of yarns seen by the waveguide aperture does not change and the contact with the upper and lower walls of the waveguide is maintained, to a decrement of the yarn's width or to an increment of yarn spacing corresponds a greater signal transmitted through the material. However, the spacing has a greater influence on the scattering parameters than the width. The number of the yarns seen by the aperture is also important. If the number of the yarns decreases, a greater quantity of the signal is transmitted. In addition, for the same number of yarns, the transmitted signal decreases when the space between the yarns (i.e., upper and lower yarns closest to the wall) and the wall is reduced, and so on until they touch the wall, subsequently, the transmitted signal increases again.

Effect of yarn thickness

Three thicknesses were considered, 0.10 mm, 0.15 mm and 0.20 mm. Varying t_{yarn} from 0.1 mm to 0.2 mm (i.e., doubling the thickness), produced a decrement of $\simeq 4$ dB in average on the transmission of the signal, for the polarization parallel to fibres. Also in the case of polarization perpendicular to fibres, a thicker structure shields more

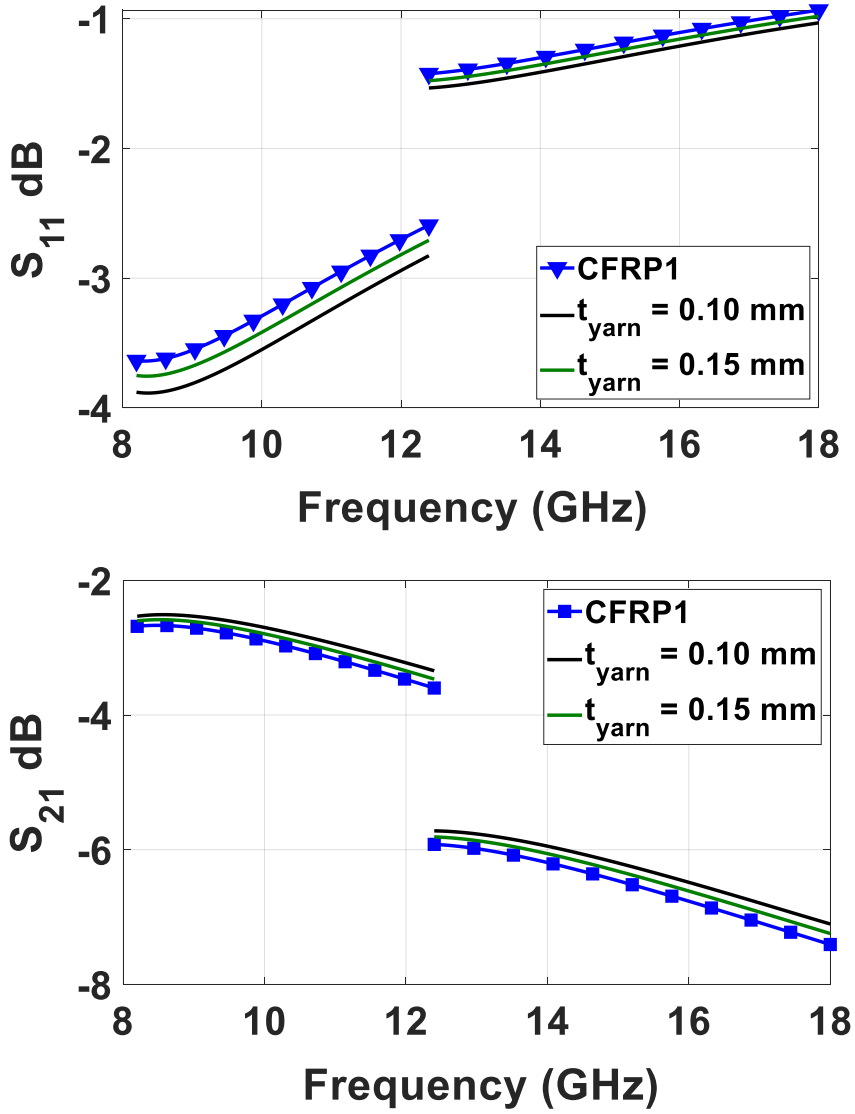


Figure 5.22: Reflection and transmission coefficient over frequency for $t_{yarn} = 0.10$, 0.15 and 0.20 mm.

energy, however, the decrement in transmitted signal is less evident and of the order of 10^{-1} dB, as shown in Figure 5.22. For thin and conductive structures, if the electric field is polarized perpendicularly to the structure, a small variation of thickness does not affect significantly the scattering parameters.

Effect of yarn cross-section

As previously done for the parallel case, the effect of the shape of the yarn's cross-section was taken into account also for polarization perpendicular to the fibres. The cases considered are the same reported in Figure 5.11. For the case of rectangular shape with rounded edges (i.e., $0 < n < 1$), three cases were observed with exponent $n =$

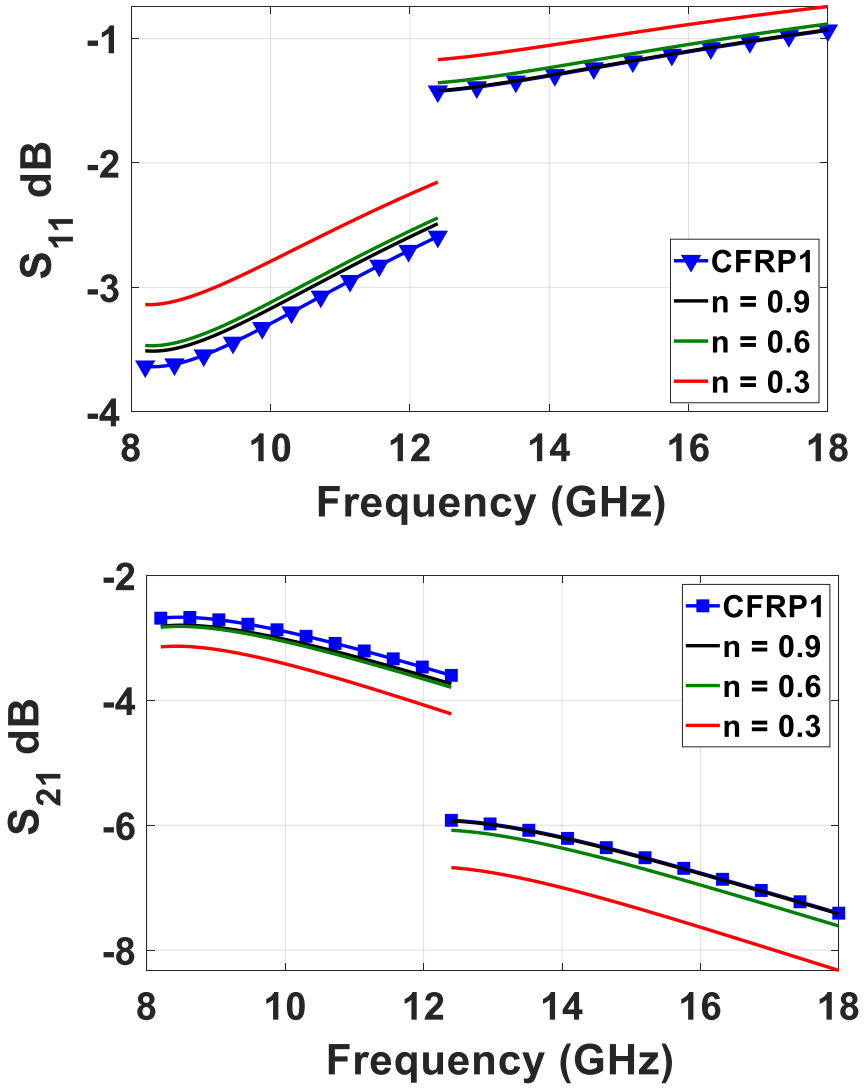


Figure 5.23: Reflection and transmission coefficient over frequency for n = 0.3, 0.6, 0.9 and 1.

0.3, 0.6, and 0.9, as depicted in Figure 5.23. Similarly to what happened in Section 5.2.1, to a thickening of the ellipse' edges corresponds a decrease of the transmission coefficient and an increase of the reflection coefficient, although these variations are not as significant as in the case of parallel polarization. As the flow of current is interrupted along *y*-axis.

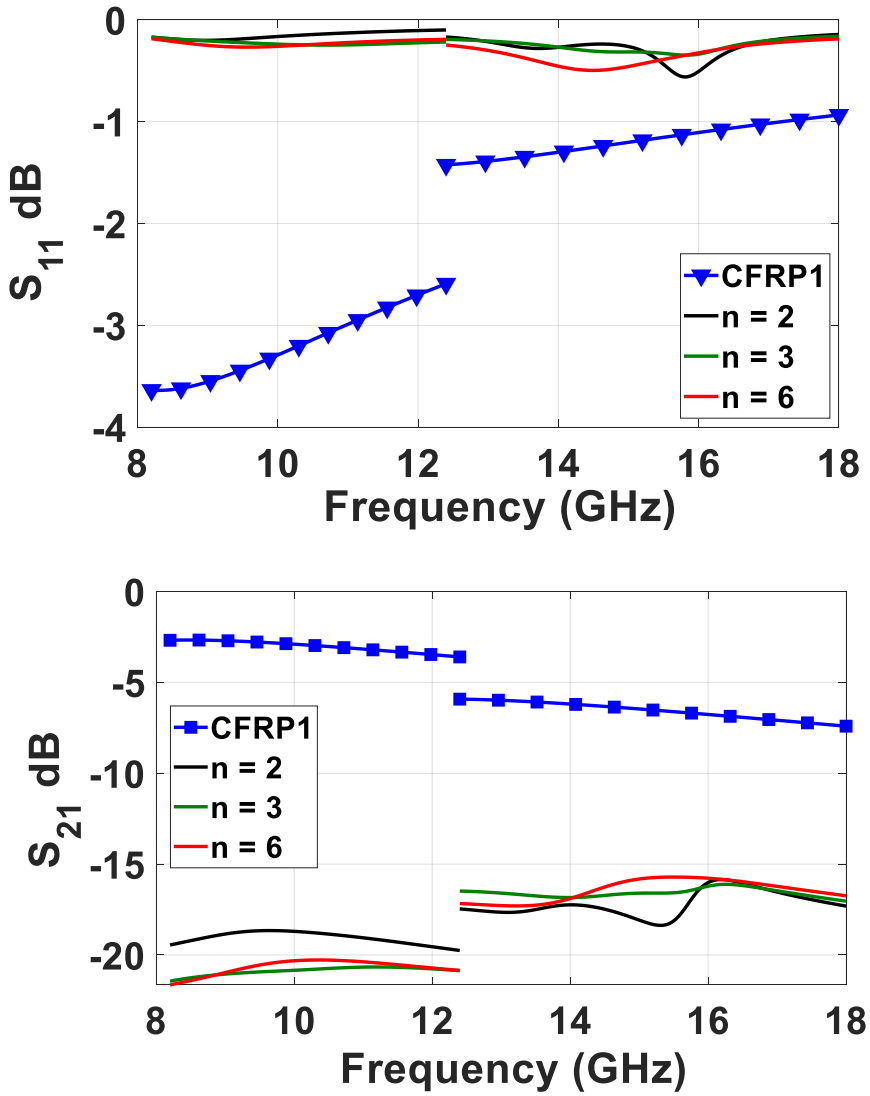


Figure 5.24: Reflection and transmission coefficient over frequency for n = 1, 2, 3 and 6.

The case of lenticular shape (i.e., $n > 1$) was studied for n = 2, 3 and 6. Unlike what happened in Section 5.2.1, the transmitted signal decreases considerably (the reflected signal increases), as shown in Figure 5.24. This leads to a significant increase in the shielding effectiveness once the shape of the yarn's cross-section assumes a lenticular frame with elongated corners. This is due to the dispersive power of a pointed conductor, that is observed in electrically charged conductors, and consists in the formation of a more intense electric field in proximity of the areas in which the surface of the conductor has a smaller radius of curvature (e.g., if the object is very pointed). The electric force that is exerted between the electrons leads them to the edges/corners of a conductor, where areas with a high concentration of charge appear. If the force is sufficient, this can make the electrons flee away from the pointed edges. In addition, if a pointed conductor is in contact with the plane surface of another

conductor, the electrons can be expelled from the strong field that is generated in the first and pass into the second, the reverse cannot happen. Figure 5.25 can be compared with Figure 5.18, to observe what happens to the electric field vector plotted on y-z

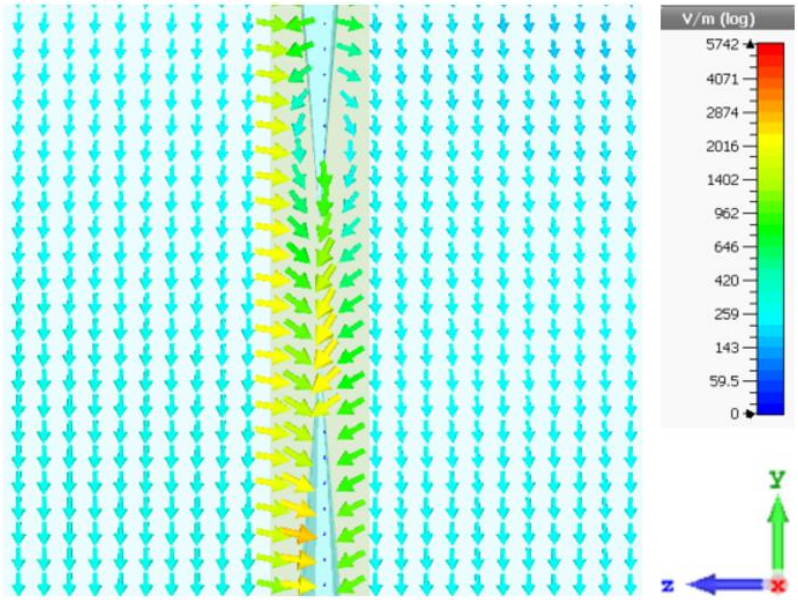


Figure 5.25: Electric field vector plotted on *y-z* plane at 10.3 GHz for lenticular yarn cross-section with for $n = 3$.

plane, between two consecutive yarns for $n = 3$. The flow of electric charges from one edge to another produces the effect similar to a continuous conductor, increasing considerably the shielding effectiveness. Therefore, it is important to take into account that the scattering parameters are more affected by the condition of $n > 1$ i.e., (cross-sectional lenticular shape) than $0 < n < 1$ and this can lead to great errors between numerical and experimental data, when adopting a mesoscale model.

5.3 Measurement methods

The materials presented in Section 5.1 were tested in order to measure the transmission and reflection coefficients and calculate the permittivities. An Anritsu MS4644A Vector Network Analyzer (VNA) was configured for two-port rectangular waveguide measurements first at X-band (8.2 - 12.4 GHz) and consequently at Ku-band (12.4 - 18 GHz). The waveguide ports were arranged according to the two experimental setups shown in Figure 5.26, after a SSLT (short-short-load-thru) calibration was performed, using the Pasternack calibration kit provided with the waveguides (i.e., WR90 and WR62) and CPR standard flanges.

The two transmission line techniques descripted in Chapter 4 were adopted in order to characterize the material. The first method, the plug-loaded transmission line,

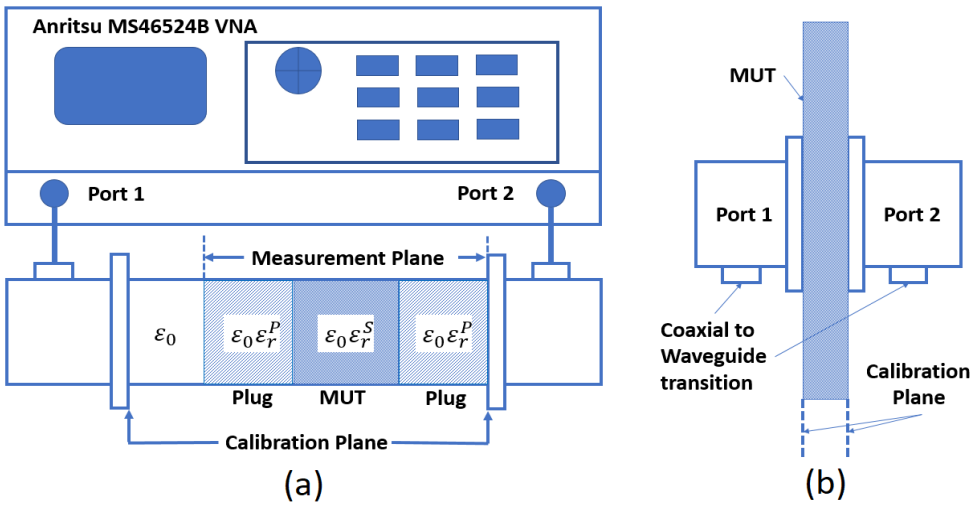


Figure 5.27: Geometry of the measurement setup for: (a) the two-port plug loaded transmission line method, and (b) clamped waveguide method.

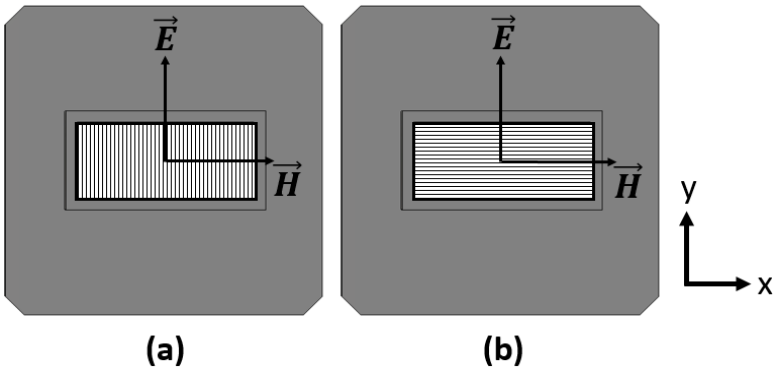


Figure 5.26: (a) MUT cross section with fibres parallel to the electric field, and (b) MUT cross section with fibres perpendicular to the electric field.

consists in positioning the sample of dimensions equal to the rectangular waveguide cross-section between two plastic plugs of known dielectric properties ($\varepsilon_r^P = 2.64 - 0.016$), as per Figure 5.26; a detailed description of this technique can be found in Section 4.3 and [71]. For the second measurement method, composite sheets of dimensions of $\simeq$ 200 mm × 200 mm were clamped between two rectangular waveguides, using the modified waveguide-based method discussed in Chapter 4.

5.3.1 Method 1: Two-port plug-loaded transmission line

Two different series of samples where cut from each CFRP sheet: 5 samples along the fibres direction and 5 samples in direction perpendicular to the fibres (30 samples in total), in order to achieve parallel and perpendicular polarization of the electric field vector of the dominant mode in the rectangular waveguide, as shown in Figure 5.27. For thicker laminates (CFRP2 and CFRP3) a water-jet cutting machine was employed for sake of precision, while samples obtained from CFRP1 were manually cut and

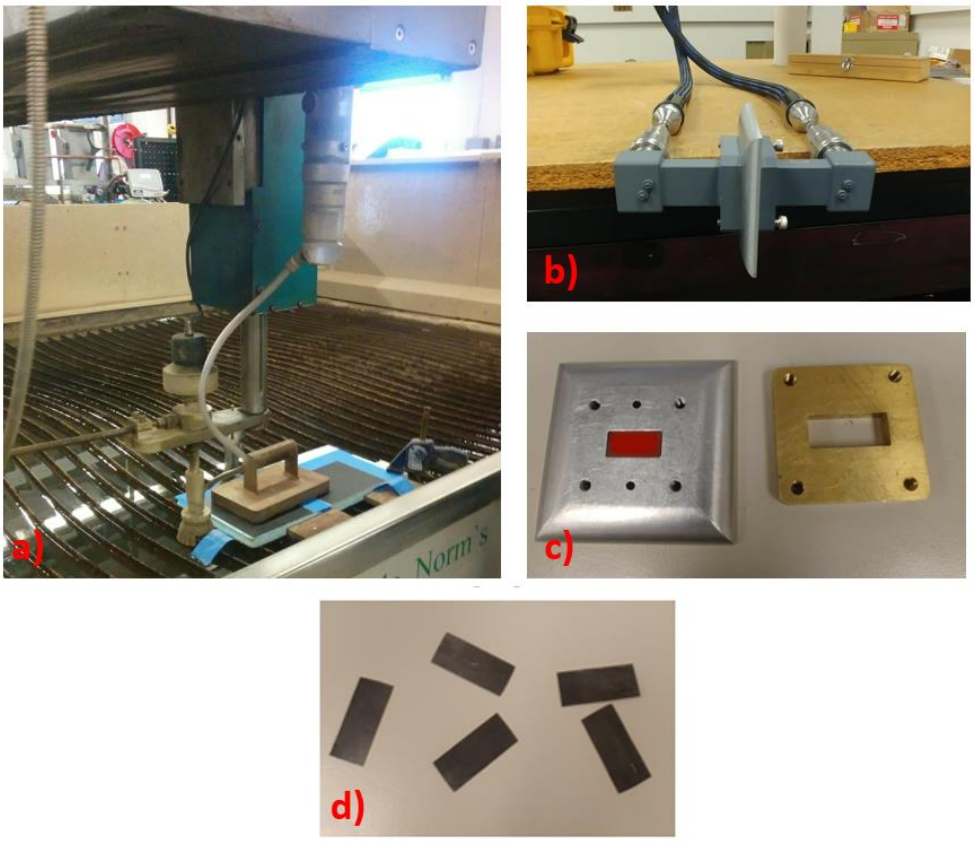


Figure 5.28: (a) Waterjet cutting process with composites in place, (b) example of plug-loaded line setup for WR62, (c) picture of shifts used for measurement at Ku-band on the left and X-band on the right, particular of red plug inserted in Ku-band shift; (d) CFRP1 samples for X-band waveguide (WR90) with fibres aligned along *x*-axis.

polished with sandpaper, due to their smaller thickness and the high risk of breakage during the waterjet process. Figure 5.28 shows: a) the waterjet cutting process used, b) the experimental setup with WR62, c) the shifts used between the two waveguides (Ku-band on the left and X-band on the right) and in red a shim/plug inserted inside the Ku-band shift, and d) a set of five samples cut from CFRP1 with fibres aligned along *x*-axis with dimensions compatible with WR90.

The average values of S_{11} and S_{21} are shown in Figure 5.29, in case of electric field vector perpendicular to the fibres and in Figure 5.30 for polarization parallel to the fibres. In case of perpendicular polarization, the calculated standard deviations (SD) do not exceed $SD \simeq 1.7$ dB (i.e., the maximum standard deviation observed is on specimen CFRP3-[0_4] at X-band). Figure 5.29 shows that the power transmitted from Port 1 to Port 2 decreases when increasing the thickness and the number of layers in the composite, i.e. the shielding effectiveness (SE) of the material increases. However, in case of parallel polarization, a similar expected behaviour was not observed.

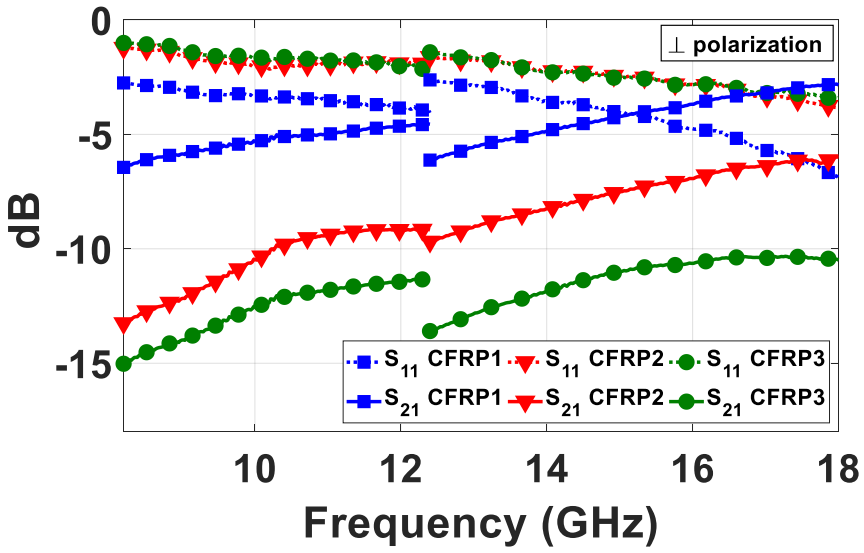


Figure 5.29: Average values of S_{11} and S_{21} over 8.2-18 GHz for perpendicular polarization measured with Method 1.

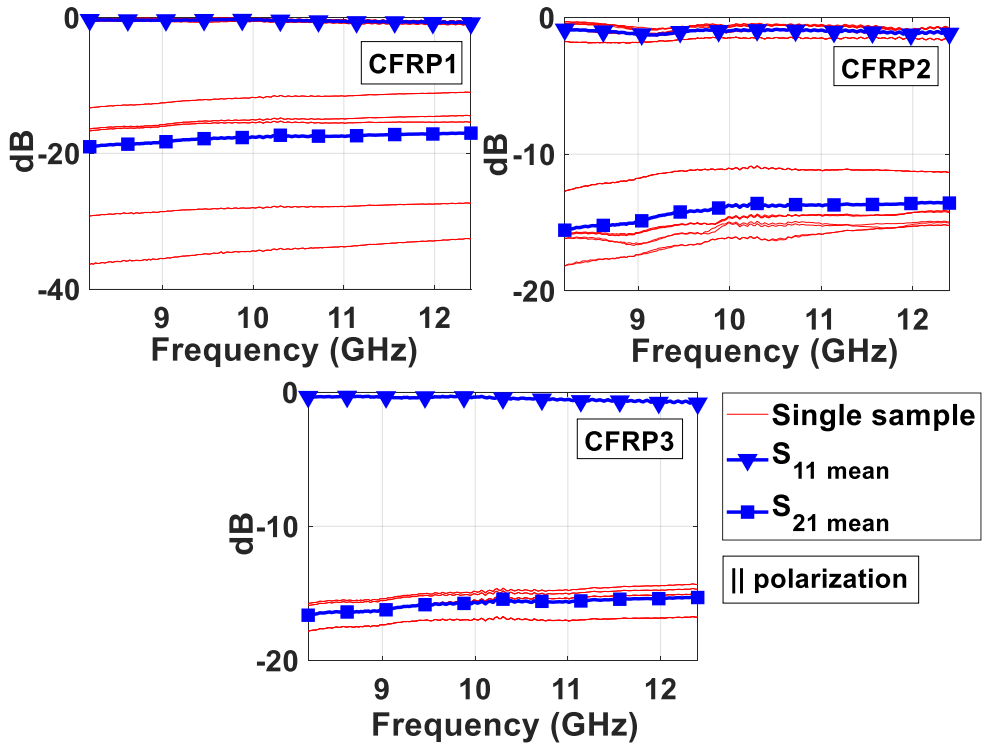


Figure 5.30: S_{11} and S_{21} measured for each sample in red and their average values over 8.2-12.4 GHz for parallel polarization with Method 1.

Figure 5.30 shows the average values of S_{11} and S_{21} of the single measurements for each sample for X-band. A significant difference in accuracy between the values obtained for the samples cut by water-jet and cut by hand can be observed. The standard deviation of the measured values has its maximum for CFRP1, i.e., $SD_{CFRP1} = 9.1$ dB and decreases for CFRP2 and CFRP3, with $SD_{CFRP2} = 2.1$ dB and $SD_{CFRP2} = 0.9$ dB. Even using the waterjet machine, the cut samples resulted more

accurate for CFRP3, whose greater thickness reduces the damage effects in the material during the cutting process. As extensively discussed in Chapter 4, the measurements of high lossy materials are subjected to errors due to the gaps between the sample and the waveguide, when the contact between the conductive fibres and the waveguide is interrupted along the larger dimension of the aperture. This is particularly evident for parallel polarization (i.e., the conductivity along the direction of the fibres is greater than transversally as discussed in Section 2.2). In addition, when the yarns of UD laminates are cut transversely, there is also a risk to stretch the fibres and widen the space between yarns.

This issue was less evident for perpendicular polarization where the cut is parallel to the fibres direction and there is less chance of fibres pull-out. Confirmation of the influence of the gaps and fibres pull-out on the measurements can be found in Figure 5.30, considering CFRP1 case. The edges of CFRP1 samples were refined with sand paper in order to fit the wave-guide cross-section and contrary to the samples cut by water-jet, the gaps between the specimen and waveguide were uneven for each, leading to a significant divergence of the measured data, e.g. the measured $|S_{21}|$ varies from 11.8 dB to 34.4 dB at 10.3 GHz. If the gaps along the larger dimension of the waveguide aperture are reduced, the S_{21} decreases. Hence, using the plug-loaded transmission line gives inaccuracy on the measured data, particularly in the case of parallel polarization. In addition, it can be observed in Figure 5.30 that the mean value of S_{21} for CFRP2 and CFRP3 are close, respectively -13.8 dB and -15.7 dB at 10.3 GHz. This is this is highly unlikely given the observations on the shielding effectiveness conducted on Chapter 3. To a higher number of layers should correspond a higher value of SE. These values are inferior to the maximum $|S_{21}|$ registered for CFRP1.

Consequently, this technique can produce unacceptably large errors for high-loss or highly reflecting samples, as the one considered in this study, particularly for electric field parallel to the fibres. Therefore, a second series of data were measured according to the clamped waveguide method. Composite sheets of bigger dimensions were clamped between the two waveguides, facilitating the measurement procedure and making it non-destructive, as there is no need of precise machining of samples.

5.3.2 Method 2: Clamped waveguide method

The average values of the scattering parameters for the two polarizations of the electric field are reported in Figures 5.31 and 5.32. Compared to the previous data, there is a substantial difference between the scattering parameters measured in the two electric field configurations, as the losses in the material increases. In case of perpendicular

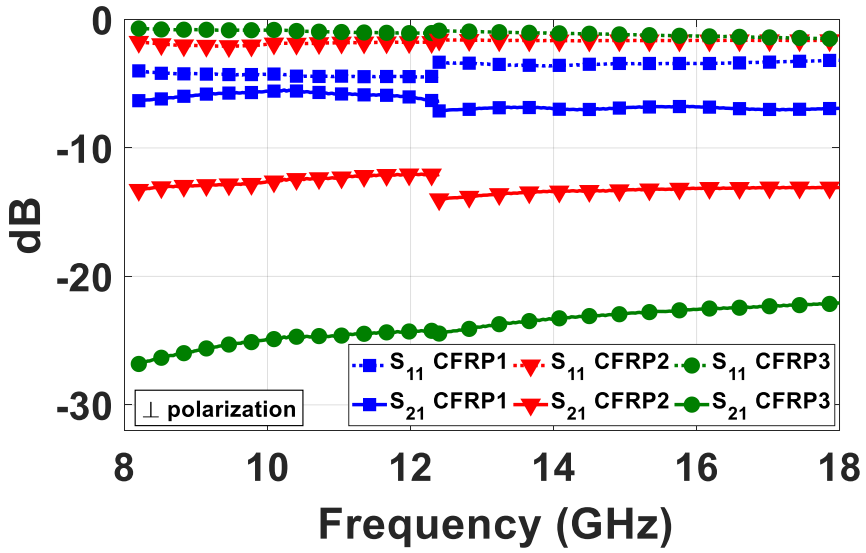


Figure 5.31: Average values of S_{11} and S_{21} over 8.2-18 GHz for perpendicular polarization measured with Method 2.

polarization, the calculated standard deviations do not exceed $SD \simeq 1.7$ dB (i.e., the maximum standard deviation observed is on specimen CFRP3-[0_4] at Ku-band). For this case, Table 5.4 shows the values of the reflection and transmission coefficients for the two measurement methods at fixed frequency points.

Table 5.4: S_{11} and S_{21} for plug-loaded (L) and clamped (C) waveguide method measured at fixed frequencies– polarization perpendicular to fibres.

Material	$S^L_{11_\perp}$	$S^C_{11_\perp}$	$S^L_{21_\perp}$	$S^C_{21_\perp}$	**Frequency (GHz)**
	-3.1	-4.2	-5.9	-5.9	9
CFRP1	-2.9	-3.5	-5.6	-6.9	13
	-5.7	-3.3	-3.2	-7.0	17
	-1.6	-2.0	-12.2	-12.9	9
CFRP2	-1.8	-1.8	-9.1	-13.7	13
	-3.4	-1.6	-6.4	-13.1	17
	-1.3	-0.8	-14.0	-25.8	9
CFRP3	-1.7	-1.0	-12.9	-23.9	13
	-3.2	-1.4	-10.4	-22.3	17

It can be observed that even in case of perpendicular polarization, when the UD composite is more transparent to the electromagnetic waves, the results differ between Method 1 and Method 2. In particular, the measured values of S_{11} and S_{21} denote a similar output at lower frequencies and when the specimen has a lower loss factor (i.e., CFRP1 and CFRP2). However, S_{21} diverges significantly for CFRP3, which is the laminate with the highest SE compared to the others. The high fibre density and the increased number of layers cause the CFRP3 sample to behave like a high-loss

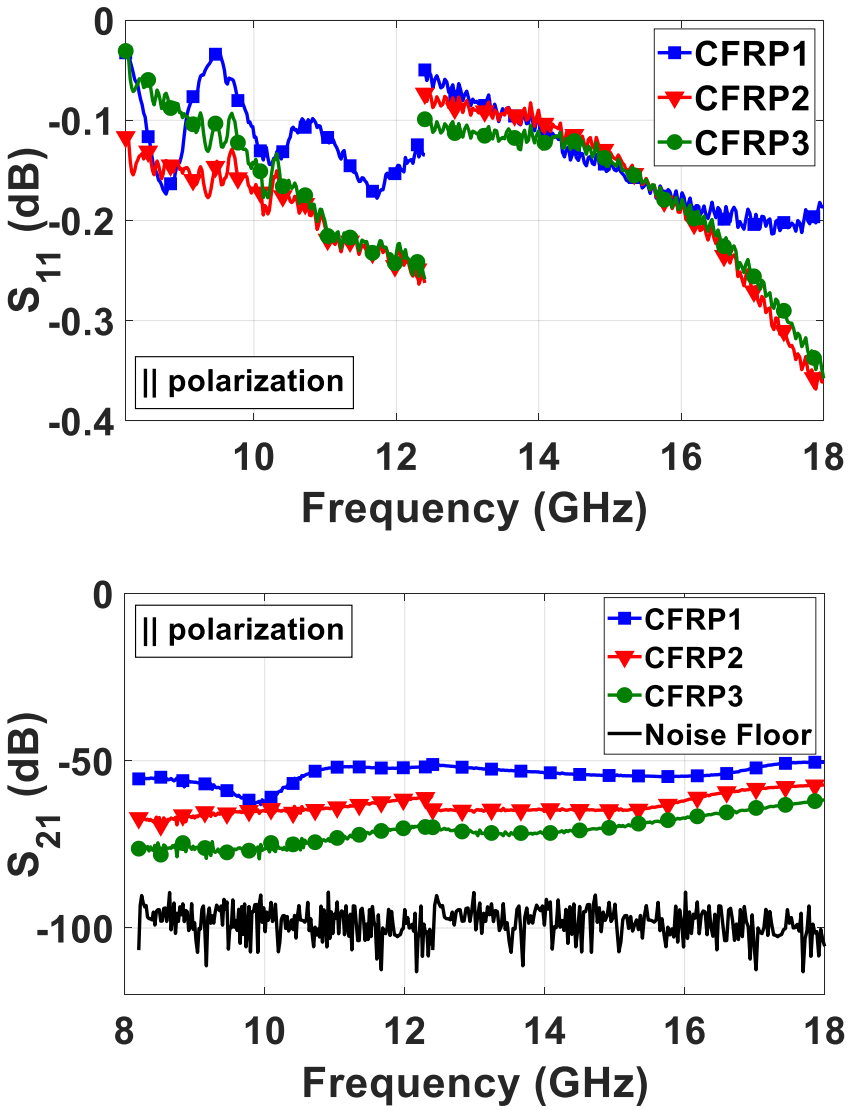


Figure 5.32: Average values of S_{11} and S_{21} over 8.2-18 GHz for parallel polarization measured with Method 2.

material, making the clamped waveguide method more accurate for its characterization.

Figure 5.32 shows S_{11} and S_{21} when the electric field is polarized in the direction of the fibres. The average standard deviation of the measured S_{21} has its maximum for CFRP3 at Ku-band, i.e., $SD_{CFRP3} = 5.5$ dB. However, for the other materials and frequency range the SD is below 3 dB for S_{21} and 0.06 dB for S_{11}. The measured values differs considerably from the one measured with the plug-loaded method and indicate that the high conductivity of the carbon fibres makes all three composite materials able to shield more than 99% of the radiation ($|S_{21}| > 50$ dB). Similarly, to what obtained in Chapter 3. Therefore, the clamped waveguide method seems to be more effective for describing the electromagnetic characteristics of CFRP and in general lossy materials. It is indeed expected a great difference in SE, when changing

the polarization of the electric field, and this technique was able to point out this behaviour.

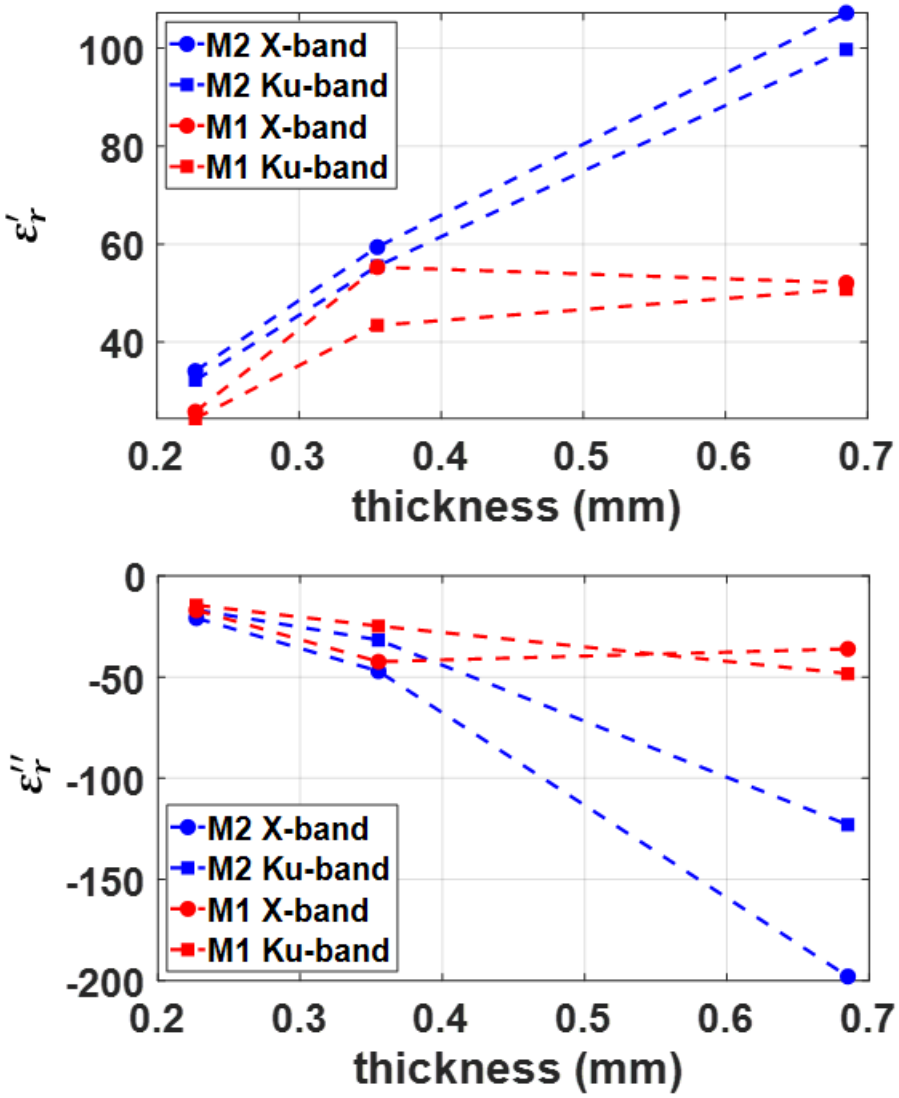


Figure 5.33: Dielectric constant and loss factor as function of thickness for Method 1 and Method 2. *M1 = Method 1 and M2 = Method 2

5.3.3 Complex permittivity

The NRW/Backer-Jarvis conversion method was used to extract the effective permittivity from the scattering parameters. The method was applied to both measurement techniques of Sections 5.3.1 and 5.3.2. The average values of complex permittivity are reported in Table 5.5, with the error in percentage between the two models for dielectric constant and loss factor.

Table 5.5: Measured complex permittivities over X-band and Ku-band and errors between two models, for electric field polarized perpendicularly to fibres.

Material	Method	ε_r X-band	ε_r Ku-band	$\frac{\Delta\varepsilon'}{\varepsilon'}$ X-band	$\frac{\Delta\varepsilon'}{\varepsilon'}$ Ku-band	$\frac{\Delta\varepsilon''}{\varepsilon''}$ X-band	$\frac{\Delta\varepsilon''}{\varepsilon''}$ Ku-band
CFRP1	1	30.9-18.2i	24.4-14.5i	10.3%	24.2%	14.7%	14.2%
	2	**34.1-20.9i**	**32.2-16.9i**				
CFRP2	1	57.4-42.3i	43.4-24.8i	3.5%	21.8%	11.5%	21.7%
	2	**59.4-47.2i**	**55.5-31.7i**				
CFRP3	1	52.1-36.1i	50.8-48.3i	51.4%	49.0%	81.8%	60.7%
	2	**107.2-197.9i**	**99.7-123.0i**				

Figure 5.33 shows the dielectric constant and loss factor as function of the thickness of the material. As expected, the results diverge between Method 1 and Method 2, as the thickness of the material increase (i.e., highest difference for CFRP3).

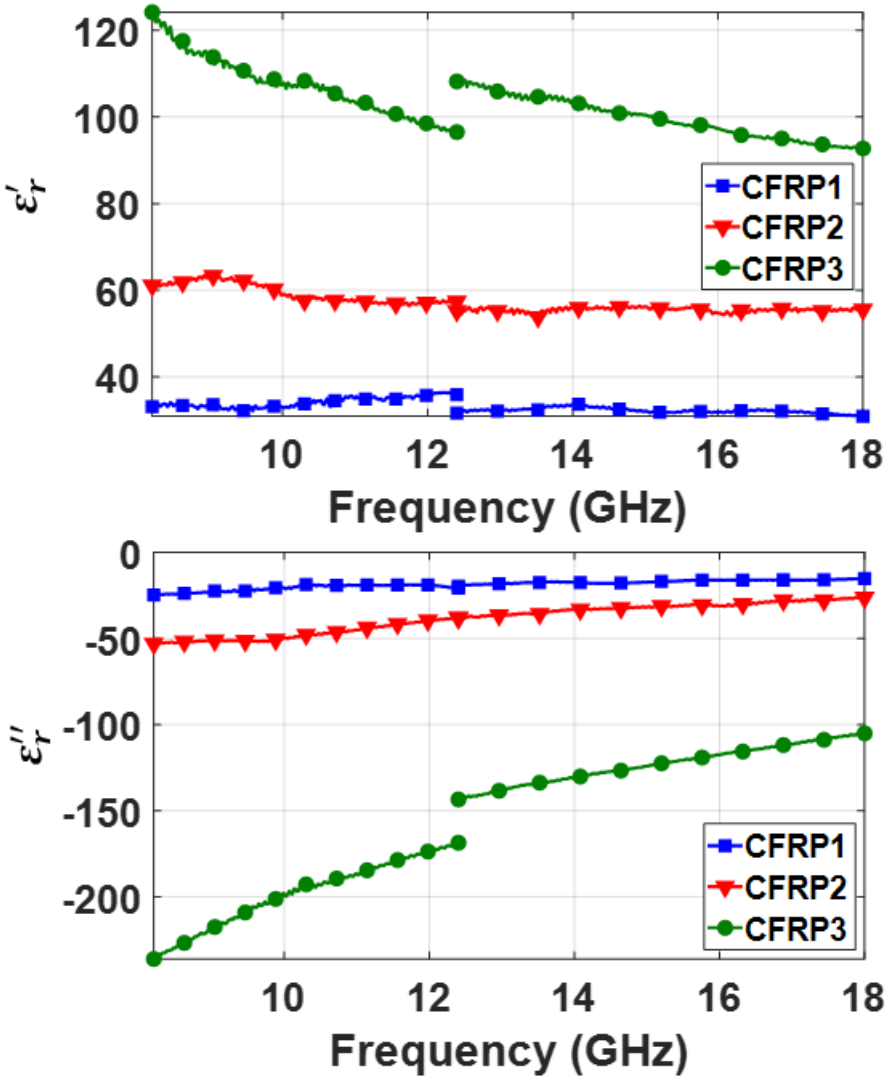


Figure 5.34: Dielectric constant and loss factor as function of frequency for Method 2. The loss factor is plotted with the negative sign.

As observed before, if the shielding effectiveness of the material is low (e.g., CFRP1 and CFRP2) both methods tend to provide similar outputs, considering the slopes of the curves of Figure 5.33. However, the combined effects of gaps and poor signal to noise ratio (SNR) progressively affects the quality of the data obtained with the plug-loaded method as the SE of the material increases. Conversely, these issues do not influence the clamped method. Hence, the NRW/Backer-Jarvis procedure was applied considering 0 offset from Port 1 and Port 2.

Figure 5.34 shows the real and imaginary part of the permittivity measured as function of the frequency for Method 2. Dielectric constant and loss factor increase with the number of layers of the laminate. The thickness of the composite once cured does not increase linearly with the number of plies, however, to a bigger increment of thickness corresponds a bigger increment of ε_r' and ε_r''. In addition, the dependence of ε_r' and ε_r'' on the frequency variation is more evident, as the number of layers increases. As it is to be expected the dielectric constant decreases over frequency.

5.3.4 Conductivity

The scarce transmission of the signal from Port 1 to Port 2 (<1%) and the lossy behavior of the composites in case of parallel polarization prevents the use of the NRW/Backer-Jarvis equations. In this case, the energy losses in the material are dominated by the conductivity term in the imaginary part of the permittivity. The conductivity of the material can be calculated through its relationship with the transmission coefficient using the Electromagnetic Interference (EMI) shielding theory applied to conductive plastics, seen in Section 3.2.4. The values of S_{21} reported in Figure 5.32 were processed using equation 3.20 and the resulting averages of the volume conductivity are listed in Table 5.6 for the tested samples.

Table 5.6: Average values of conductivity over X-band and Ku-band for CFRP1, CFRP2 and CFRP3 with electric field polarized along the fibre axis.

Material	Average σ (X-band) [S/m]	Average σ (Ku-band) [S/m]
CFRP1	5365	3779
CFRP2	4105	2930
CFRP3	1939	1204

The calculated conductivity is frequency dependent and decreases as the frequency increases. Considering that the specimens with a greater number of layers exhibits

higher attenuation upon transmission but the volume conductivities calculated with equation 3.20 are smaller in specimens with more plies, a great contribution to the SE is given by the absorption loss term, which is directly proportional to the thickness of the sample. The higher SE of CFRP2 and CFRP3 in accordance with equation 3.20 is due to a greater value of SE_A, as a consequence of a larger thickness of the samples.

5.4 Simulations results and discussion

5.4.1 Homogeneous model

Simulations were performed to assess the reflection and transmission coefficients S_{11} and S_{21} of the CFRP samples, adopting the values of the complex permittivities measured in Table 5.5 with the clamped waveguide method and the conductivities presented in Table 5.6. Using CST Microwave Studio®, a rectangular waveguide was filled with the sample of dimensions equal to the waveguide aperture. The sheet was modeled as a homogeneous material of known pemittivity/conductivity and magnetic permeability equal to free-space. The model adopted is the one presented in Chapter 4, Section 4.2, Figure 4.3. The simulations were repeated for X-band and Ku-band configurations.

For the case of polarization perpendicular to fibre axis, the materials were modelled according to the properties reported in Tables 5.1 and 5.5. The complex permittivities obtained with Method 1 and Method 2 were investigated for the perpendicular polarization case. In order to obtain accurate results, the frequency domain solver was used with convergence criteria of the adaptive mesh refinement for S-parameters below a threshold of 10^{-5}.

The results of the analysis are reported in Table 5.7, which shows the mean squared errors (MSE) between estimated values and actual values of S_{11} and S_{21} measured with the plug-loaded waveguide method (Method 1) and the clamped waveguide method (Method 2).

$$MSE = \frac{1}{n}\sum_{i=1}^{n}(S^{MEAS} - S^{SIM})^2 \tag{5.3}$$

$$MAPE = \left(\frac{1}{n}\sum_{i=1}^{n}\left|\frac{S^{MEAS} - S^{SIM}}{S^{MEAS}}\right|\right)100\% \tag{5.4}$$

The estimated scattering parameters present greater errors when the simulations are conducted using the permittivities measured from Method 1. In this case, the error in the evaluation of the transmission coefficients S_{21} increases significantly with frequency, having its maximum at Ku-band. Taking into account the mean absolute

percentage error (MAPE) of S_{21} for Method 1 and Method 2, the simulation gives an error of 13% for X-band calculations and of 52.7% for Ku-band using the permittivities measured with Method 1. The error found on the transmission coefficients is reduced to 2.8% for X-band and of 2.2% for Ku-band, using the permittivities measured with Method 2. Therefore, the errors between numerical and experimental values for Method 2 are inferior to the ones found for Method 1, confirming the better accuracy of the clamped transmission line.

Table 5.7: Mean squared errors between estimated values and measured values.

Material	**Method**	**MSE** $(S_{11})_X$	**MSE** $(S_{21})_X$	**MSE** $(S_{11})_{Ku}$	**MSE** $(S_{21})_{Ku}$
CFRP1	1	3.23	0.64	1.74	3.58
	2	**0.18**	**0.03**	**0.16**	**0.03**
CFRP2	1	0.11	1.96	1.83	18.78
	2	**0.15**	**0.22**	**0.30**	**0.07**
CFRP3	1	0.51	6.37	2.72	35.79
	2	**0.09**	**0.58**	**0.10**	**0.55**

Figure 5.35 shows the comparison between S_{11} and S_{21} simulated using the permittivities obtained with the clamped waveguide method and the actual measured values. The results are consistent with the experimental measurements, however, errors between simulation and measurements are present, which are more evident on the reflection coefficients. One of the causes can be attributed to the fact that the complex permittivities used for the numerical simulation have a different frequency dependent dispersion model compared to the one calculated with the NRW/Baker-Jarvis conversion method.

Finally, it is useful to quantify the amount of power reflected to Port 1, absorbed and transmitted to port 2 for the electric field in perpendicular configuration. In a Two-Port continuous transmission line, the power balance between Port 1 and Port 2 can be expressed as:

$$P_i = P_r + P_a + P_t + P_{loss} \tag{5.5}$$

where P_i, P_r, P_a and P_t are respectively the power in input, reflected, absorbed and transmitted through the material, while P_{loss} represents the power losses, which are equal to 0 in an ideal transmission line and $\neq 0$ considering the discontinuity in the

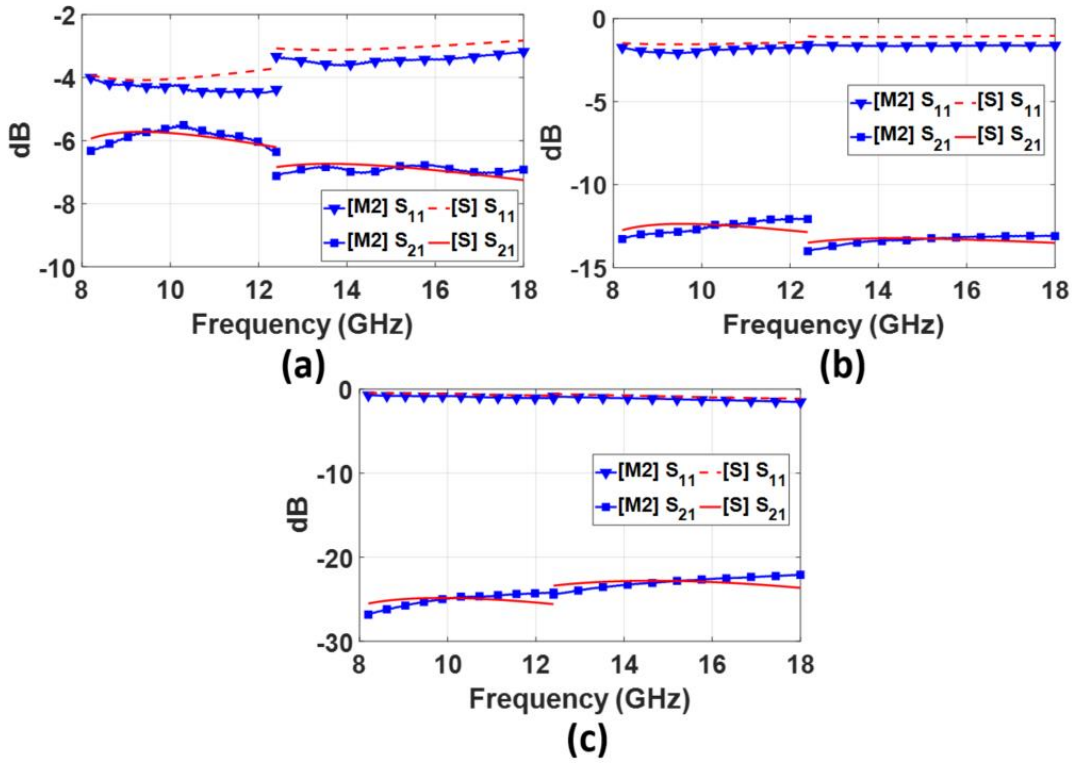


Figure 5.35: Simulated [S] and measured [M2] scattering parameters in perpendicular polarization for Method 2: (a) CFRP1, (b) CFRP2 and (c) CFRP3. *M2 = Method 2.

clamped transmission line. Therefore, knowing the values of the scattering parameters, the components of the power are given by the following equations:

$$P_r = P_i 10^{S_{11}/10} \tag{5.6}$$

$$P_t = P_i 10^{S_{21}/10} \tag{5.7}$$

Table 5.8 provides the percentages of the incident power that is reflected back to the source, transmitted though the material and absorbed/lost within the clamped waveguide method for CFRP1, CFRP2 and CFRP3. The power reflected increases and conversely the power transmitted decreases with the number of layers in the laminate, similarly also the power absorbed/lost decreases. Hence, the reflection loss becomes the primary shielding mechanism in perpendicular polarization as the number of layers of the structure increases. Even when the electric field vector is perpendicular to the fibre orientation, CFRP3 provides significant power attenuation. This is a consequence of the very high fibre density of the unidirectional prepreg used in this particular study. In addition, this shows that even using a convenient polarization of the electric field, the propagation of the electromagnetic radiation is hindered through CFRP composites. Therefore, the propagation of the signal can be limited to the first layers of the laminate. Consequently, CFRP composites can be effectively used as shielding

materials, and conversely, they are not suited for all those applications, which require signal transmission (i.e. microwave non-destructive testing, etc.).

Table 5.8: Power balance over 8.2 – 18 GHz for CFRP1, CFRP2 and CFRP3 in case of electric field polarized perpendicularly to fibre axis.

Material	Power reflected	Power transmitted	Power absorbed and Power losses
CFRP1	41.18%	23.11%	35.71%
CFRP2	66.70%	5.12%	28.17%
CFRP3	78.57%	0.41%	21.02%

The numerical simulation was repeated for the case of electric field parallel to the fibres. The conductivity and thickness of the homogenous slab were chosen according to Tables 5.1 and 5.6, in order to model CFRP1, CFRP2 and CFRP3. Table 5.9 and Figure 5.36 show respectively the mean absolute percentage errors and the comparison between numerical simulations and experimental measurements of S_{21}.

Table 5.9: MAPE between estimated values and measured values of S_{21} for Method 2.

Material	Method	MAPE $(S_{21})_X$	MAPE $(S_{21})_{Ku}$
CFRP1	2	8.6%	6.4%
CFRP2	2	6.3%	6.2%
CFRP3	2	5.9%	6.9%

The average conductivities calculated with the Simon formalism were used to define the electrical properties of the homogeneous sheet under analysis. As it can be seen from Figure 5.36, the errors between numerical model and experimental data are greater as the frequency increases for both X-band and Ku-band simulations and are related to different factors. The frequency dependent dispersion model of the conductivity is different in regards to the one calculated through the Simon formalism. Therefore, as the frequency increases it appears evident that the simulations does not match the experimental measurements. Furthermore, the multiple reflection mechanism that takes place because of impedance mismatches at the various interfaces

present inside the composite material, is not considered by the Simon formalism. Finally, this equation is used for a theoretical model of a conductive homogeneous sheet, while the actual CFRP composite is not homogeneous but consists of a series of plies.

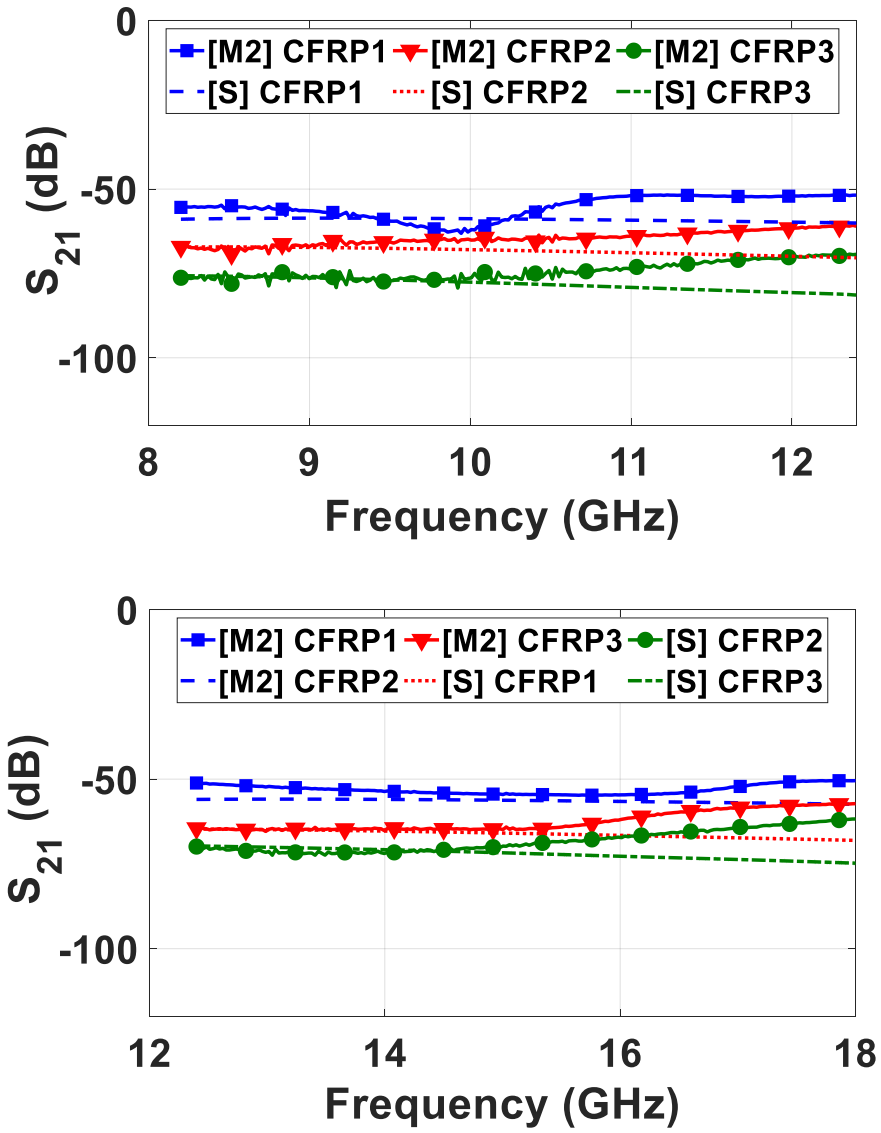


Figure 5.36: Simulated [S] and measured [M2] S_{21} in parallel polarization for Method 2 at X-band and Ku-band.

5.4.2 Mesoscale model

The homogenous model presumes the knowledge of the permittivity or conductivity of the material. In absence of these parameters, it is possible to use the mesoscale model for very thin materials. Simulations have been carried out for the case of CFRP1 (already presented in Section 5.2) and CFRP2.

Starting with the case of electric field polarized in the direction of the yarns, the model illustrated in Section 5.2, with geometrical and electrical characteristic descripted in Table 5.3 has been adopted for CFRP1. Figure 5.37 shows the comparison between simulated and measured data (with plotted standard deviations) for the transmission coefficient or shielding effectiveness of the material.

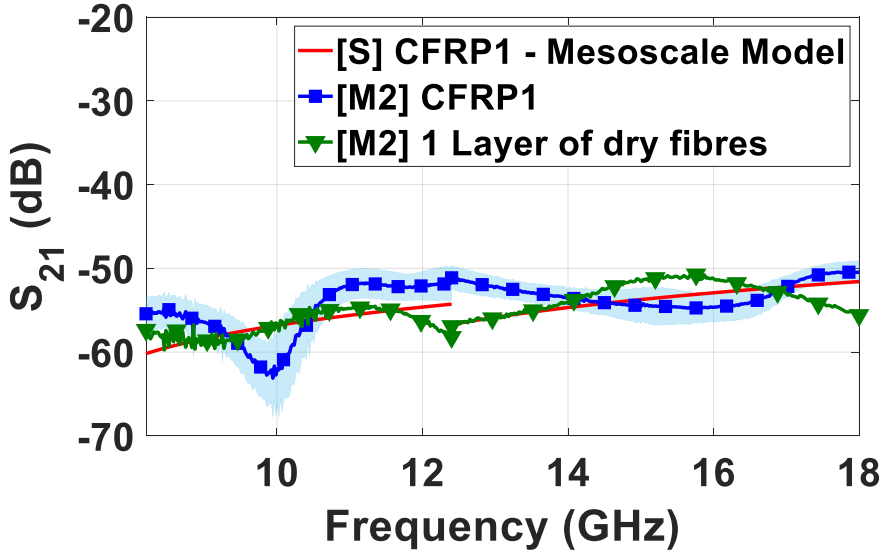


Figure 5.37: Simulated [S] and measured [M2] scattering parameters with electric field parallel to fibre axis for CFRP1.

As described in Section 5.1, CFRP1 was specially created with one layer of prepreg, to measure the permittivity of one layer only. This is important, as increasing the thickness and the number of layers of the prepreg does not correspond to a linear increment of permittivity or to a similar value in permittivity. The non-impregnated fibre unidirectional cloth was also available. As shown in Figure 5.37, comparing the measured S_{21} for the composite sheet (the standard deviation is represented for CFRP1) and the layer of dry fibre cloth, it is possible to observe that the average value of SE effectiveness for both is similar, over the band considered. This is a confirmation of the fact that the epoxy resin, being a dielectric material, does not contribute to the shielding. In addition, being only one layer of prepreg, the fibre weren't pressed excessively during the cure process, hence, the fibre volume fraction in this case is comparable to the dry cloth. The mesoscale model matches the measured data. Confirming, the parameter of choice reported in Table 5.3. The measured curves in the case of CFRP1 presents some minimum points or peaks (i.e., there seems to be a resonance at $\simeq$10 GHz). This is due to the fact that both samples are not perfectly rigid between the two waveguides, as the CFRP1 is very thin (i.e., 0.227 mm) and the fibre cloth is not a solid plate. During the experimental tests, it was possible to notice that

same behavior was less evident for the other samples, CFRP2 and CFRP3, which were thicker and provided an easier alignment between the flanges of the waveguides.

For CFRP2 simulation the parameters listed in Table 5.10 were adopted for the mesoscale model. A detail of the model made with 2 layers of prepreg (i.e., CFRP2) is reported in Figure 5.38.

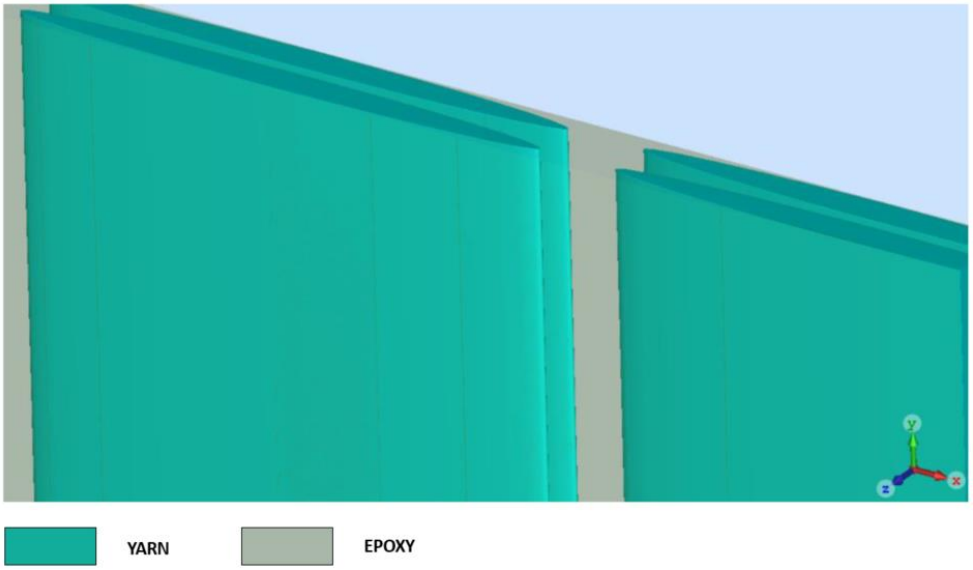


Figure 5.38: Simulated yarns in epoxy resin for CFRP2 model.

Table 5.10: CFRP1 model, geometric and electromagnetic parameters.

CFRP2 BASE MODEL	
YARN	$\sigma = 70000$ S/m, $\mu_r = 1$
EPOXY	$\varepsilon_r' = 4$, $\mu_r = 1$
YARN CROSS-SECTION	ELIPSE
YARN SPACING *X*-AXIS	0.30 mm
YARN SPACING *Z*-AXIS	0.05 mm
YARN WIDTH	2.40 mm
YARN THICKNESS	0.15 mm
EPOXY THICKNESS	0.36 mm
BAND	X and Ku band

The frequency domain solver was used with convergence criteria of the adaptive mesh refinement for S-parameters below a threshold of 10^{-5}. A mesh of 144329 tetrahedrons was adopted for X-band and 74984 tetrahedrons for Ku-band. Figure 5.39 shows the results. The simulated data match the measured values, particularly at X-band. In this simulation, the yarns were assumed to be perfectly aligned in *y* and *z* directions, which is not the case in reality. However, in case of polarization of the electric field in the direction of the yarns, this arrangement for thin sheets produces acceptable results.

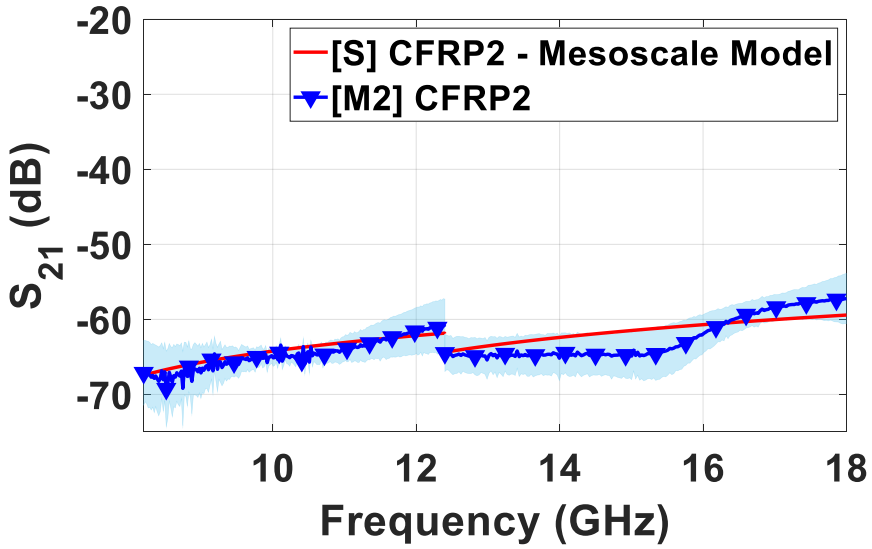


Figure 5.39: Simulated [S] and measured [M2] scattering parameters with electric field parallel to fibre axis for CFRP2.

The yarn spacing and alignment affect more evidently the case of polarization perpendicular to fibre axis. Figures 5.40 and 5.41 show the results for CFRP1 and CFRP2. In this case, a value of $p = 0.1$ was used, maintaining unchanged the other parameters. As the transmitted signal increases, the yarns spacing and the number of yarns have a greater influence on this case. The reflected and transmitted signal tend to be overestimated, as the model does not take into account the complexity of a composite laminate and the uncertainties related to the clamped waveguide model,

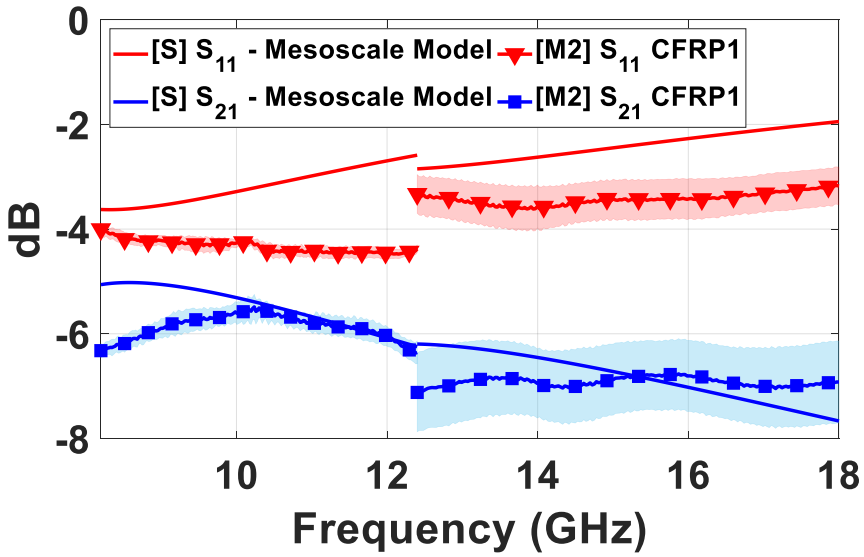


Figure 5.40: Simulated [S] and measured [M2] scattering parameters with electric field perpendicular to fibre axis for CFRP1.

which is more reliable as the conductivity of the material increases. It must be considered that the simulations disregard many uncertainties induced by the materials and setup geometry: non-smooth surface of sample, error in alignment, air gaps, errors in the sample length, guide losses and conductor mismatch, and uncertainty in the magnitude and phase of the scattering parameters measured by a vector network analyser.

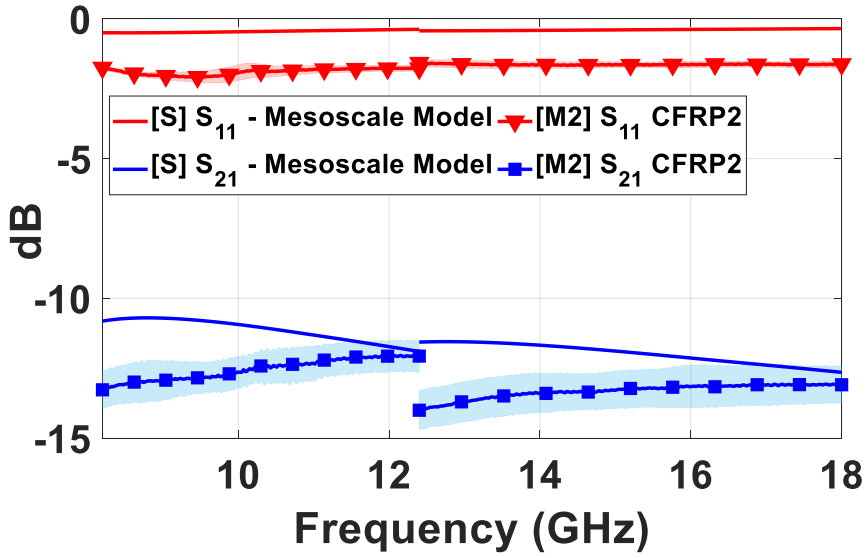


Figure 5.41: Simulated [S] and measured [M2] scattering parameters with electric field perpendicular to fibre axis for CFRP2.

Chapter 6

Free-space characterization and damage detection in unidirectional CFRP

As seen in Section 2.3.2, free-space methods are widely used for the characterization of dielectric materials, with the main advantage to allow high frequency and non-destructive measurements. A free-space measurement system, which include the use of horn antennas in transmitting and receiving configuration, has been extensively studied in literature (where the work of Ghodgaonkar et al. is well known) and used to determine the complex permittivity and complex permeability in several microwave-absorbing materials and dielectric composites [74], [75], [103]–[105], [110], [212]. However, few studies in literature address the characterization of CFRP composites due to the high reflectivity of this class of materials and are often limited to unidirectional samples and single ply architecture [134]. In this section, a unidirectional CFRP laminate will be characterized for polarization perpendicular to the fibre axis and the calculated permittivity will be used in the electromagnetic simulation, to reproduce several cases of damage scenarios, with the aim to verify if damage identification is feasible with a free-space method.

6.1 Free-space measurement system

A free-space measurement system was implemented for permittivity characterization as depicted in Figure 6.1. The system consists of two LB-28-20-C horn antennas, in transmission and reception, connected to a Hewlett Packard HP 8510C vector network analyser (VNA) in two-port configurations by means of 2.4 mm radio frequency (RF) coaxial cables. Additional elements are represented by the two antenna's holders, a sample holder made of dielectric material and a travel linear stage, to allow the

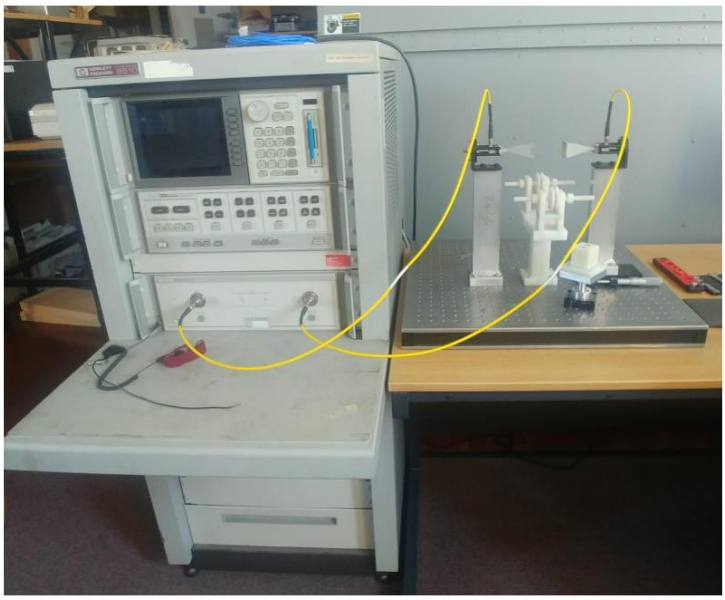


Figure 6.1: Free-space measurement system.

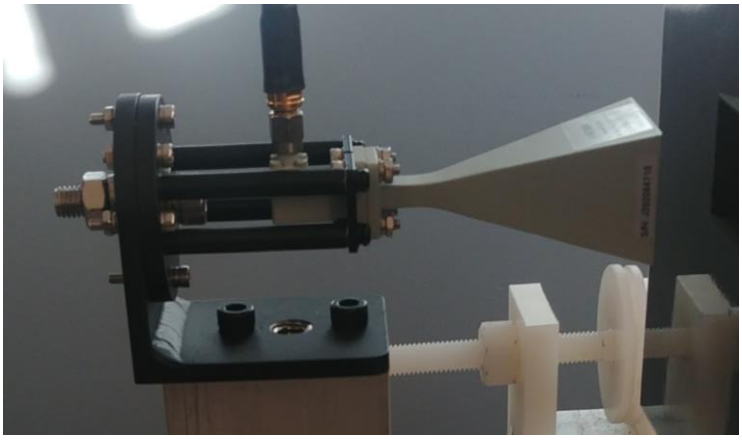


Figure 6.2: LB-28-20-C horn antenna with 2.4 mm female output and L type mounting bracket.

translation of one of the two antennas. The S-parameters S_{ij} are measured in free-space by the network analyser system consisting of a synthesized sweeper and a S-parameter test set. From the S_{ij} measurements, it will be possible to derive the reflection Γ and transmission T coefficients obtained by the signal scattered from and through a planar specimen.

A depiction of the LB-28-20-C horn antennas with the respective mounting bracket is given in Figure 6.2. Their frequency range is in the Ka-band (26.5-40 GHz). The horn antennas are placed on steel supports, refer to Figure 6.3, by means of L-type mounting brackets. One of the supports is kept fixed to the optical table. The other one is attached to the linear translation micrometer stage and is free to move along a linear

direction ranging up to 50 mm, as shown in Figure 6.4. The micrometer stage allows precision movements with resolution of 10 μm to one horn antenna, and this is needed for TRL calibration.

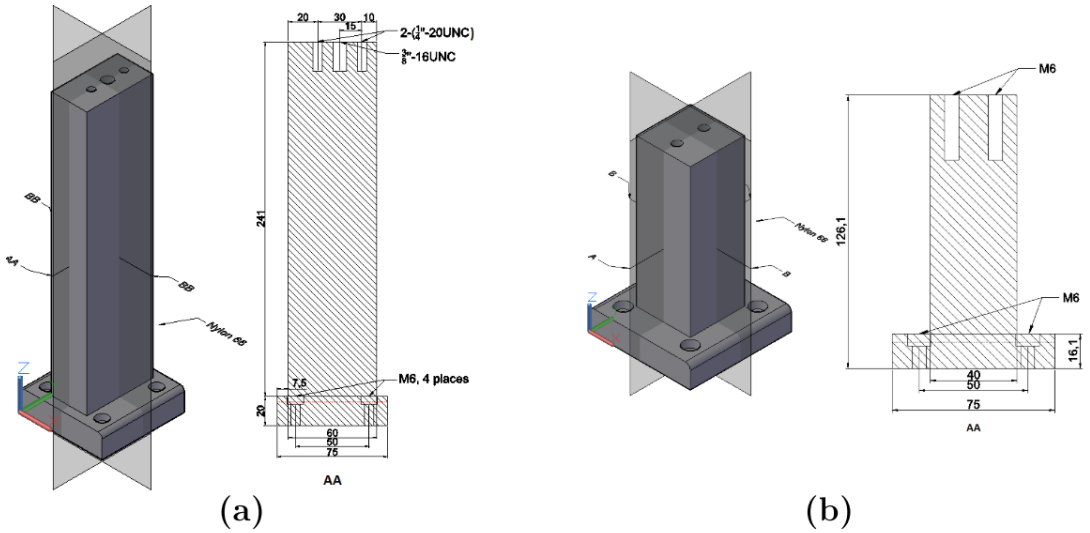


Figure 6.3: CAD for: (a) antenna base support; (b) specimen holder support.

The specimen holder is also fixed to the steel optical table through the support of Figure 6.3 and is machined to sustain a flat plate specimen with nominal dimensions of 200 mm by 200 mm. The upper part is composed of nylon 66 to avoid electromagnetic interference. The CAD model of the sample holder and the connection to the moving stage, with respective dimensions, are reported in Figure 6.5.



Figure 6.4: 50 mm travel linear translation stage with side mounted micrometer.

6.2 Materials

Three CFRP sheets were fabricated, the first two are made of discontinuous fibres, while the latter with unidirectional continuous fibres:

1. The first sample was realized stacking 10 layers of Optiveil 20301A 10 g/m^2 alternated with XPREG XA120 prepreg epoxy adhesive film (11 layers of adhesive resin). The carbon veil is composed of discontinuous carbon filaments

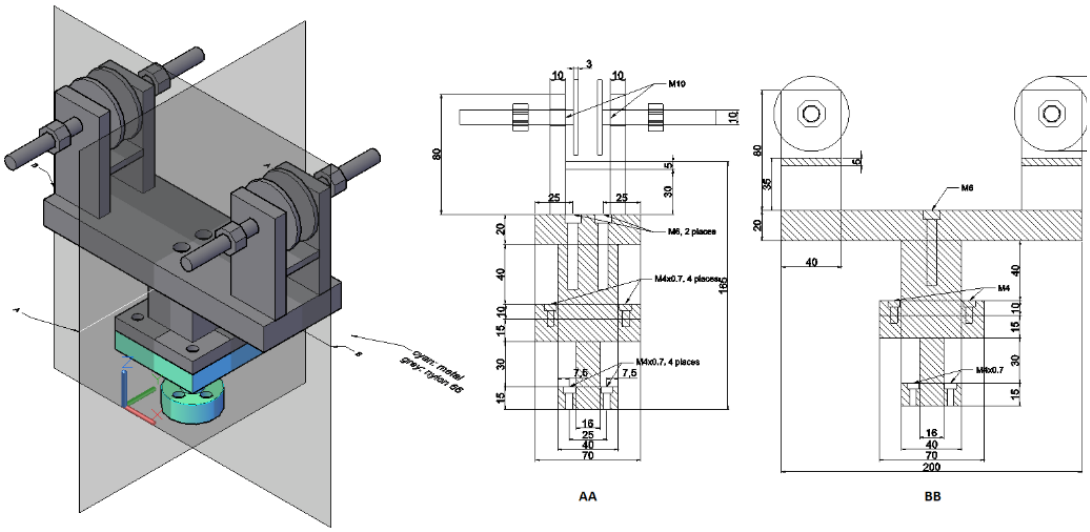


Figure 6.5: CAD for specimen support holder and junction to rotation stage.

with length ≃ 6 mm and diameter ≃ 7 µm in a PVA binder. The filaments are uniformly distributed with density of 10 g/m^2. Hereafter, this sample will be addressed as "C1".

2. The second sample was realized in the same way as C1, stacking 10 layers of Optiveil 20301A 34 g/m^2 alternated with XPREG XA120 prepreg epoxy adhesive film (11 layers of adhesive resin). The filaments are uniformly distributed with higher density of 34 g/m^2. Hereafter, this sample will be addressed as "C2".
3. The third sample was made of 8 layer of continuous UD carbon fibres Pyrofil TR50S 15K with light weight of 100 g/m^2 alternated with the same type of epoxy adhesive (9 layers). A free edge delamination was simulated including a PTFE patch of 30 mm × 80 mm between the second and the third layer. Hereafter, this sample will be addressed as "C3".

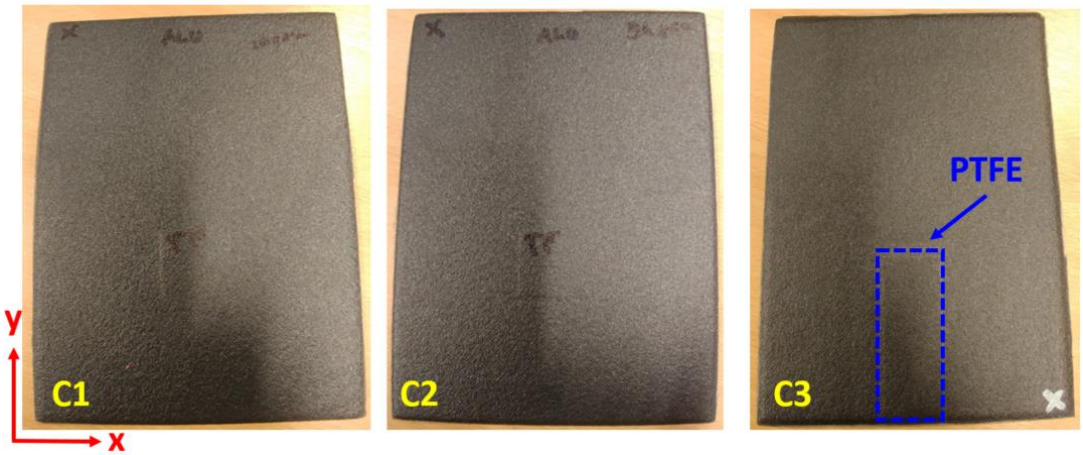


Figure 6.6: CFRP samples. C3 unidirectional fibres are directed long *y*-axis.

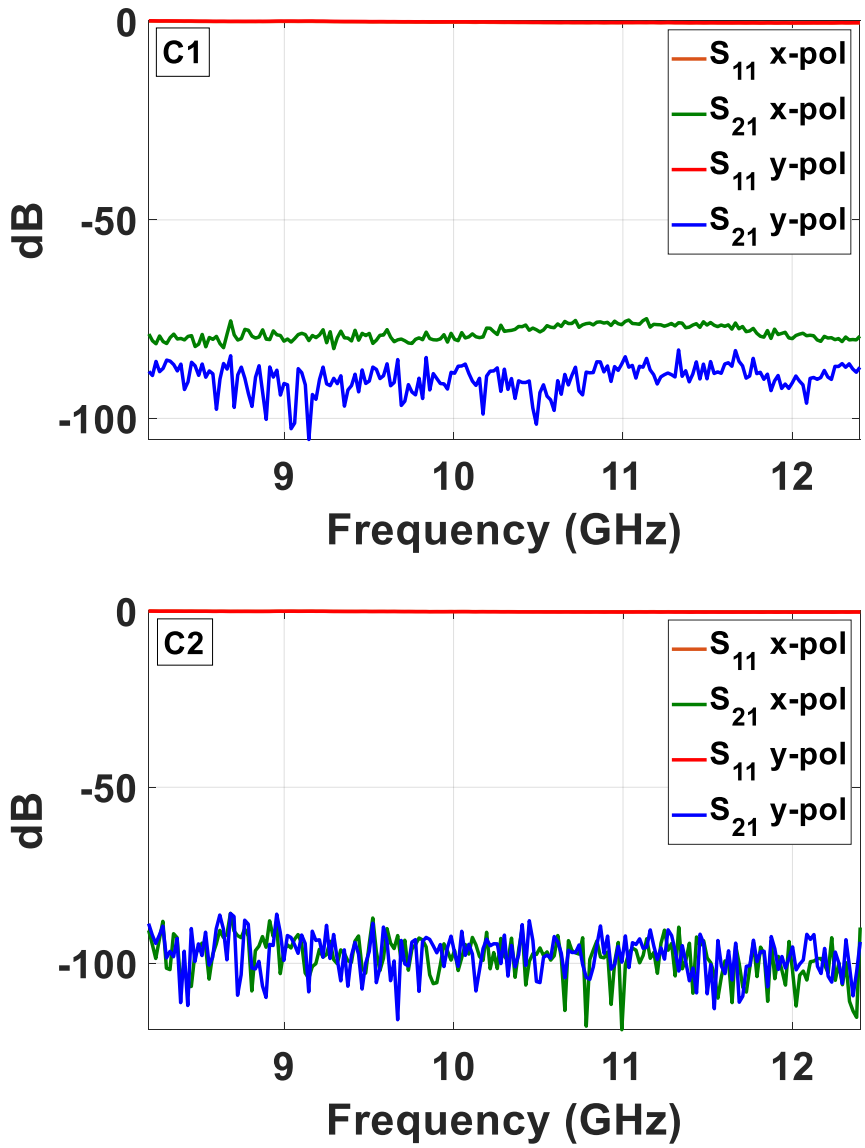


Figure 6.7: Measured S-parameters at X-band for C1 and C2.

Each sample underwent vacuum bagging and were cured in autoclave at 6 bar and 120°C for 1 hour. The samples are shown in Figure 6.6.

The S-parameters of the three samples have been characterized at X-band with the method explained in Chapter 4. Two polarizations of the electric field vector were adopted according to the coordinate system shown in Figure 6.6, i.e., along *x* and *y* axes. The results for C1 and C2 are shown in Figure 6.7. For the sample with lower fibre density C1, the transmission coefficient S_{21} measured with the two polarization does not coincide and is close to the noise floor. Even if the carbon veil fibre density should be approximatively constant in both *x* and *y* direction, the measurement shows that for *y*-pol the transmission decreases, indicating that along this direction the fibres have higher density. The S_{21} measured for C2 hits the noise floor, exceeding the

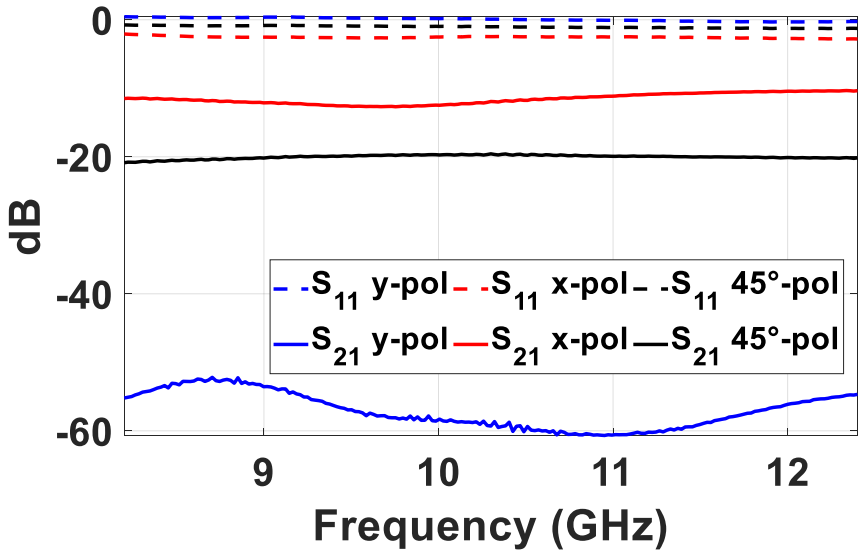


Figure 6.8: Measured S-parameters at X-band for C3 with different polarizations.

dynamic range. Both samples have high shielding effectiveness and the signal cannot pass through the material in both polarizations ($S_{11} \simeq 0$). On the other hand, the S-parameters measured for C3 are highly dependent upon the polarization of the incident wave. Figure 6.8 shows the S-parameters measured for polarization parallel (*y*-pol), perpendicular (*x*-pol) and oriented at 45° respect to fibre orientation. The transmission coefficient decreases (reflection increases) as the electric field vector becomes aligned with the fibres. If we consider the case of polarization perpendicular to the fibres, as previously done in Chapter 5 it is possible to extract the permittivity for C3: $\varepsilon_r(\mathrm{C3}) = 12.3 - i11.1$ at X-band.

6.3 TRL Calibration

To minimize the inaccuracies due to multiple reflections between the two horns via the surface of the sample, a two-port TRL (through-reflect-line) calibration technique is performed.

Errors resulting from imperfections in the measurement system (i.e., the network analyzer, test set, cables, adapters, fixtures, etc.) can be defined as either random or systematic. Systematic errors are the repeatable errors including mismatch, directivity, and tracking errors. These can be measured and then removed using a mathematical error model.

The systematic errors are determined from the difference between the measured and known responses of the standards. For example, considering the case of a two-port network analyzer, the error model must account for cross-talk between all ports, and three known impedance standards and a single transmission standard are required: the Short, Open, Load and Through (SOLT) calibration technique is adopted, which

involves an error model with twelve terms, requiring seven measurements of standards. This is further complicated if an object under test is not coaxially-connected, as any connected fixtures contribute to the measured S-parameters and comparable calibration standards may be difficult to fabricate.

Hence, alternative calibration methods are employed, particularly in the case of free-space measurements, such as the Through-Reflect-Line (TRL) calibration method. For a two-port VNA TRL calibration, a total of 10 measurements is needed to quantify eight unknowns denoted as ε. The eight TRL error terms are represented in the error model shown in Figure 6.9 [151].

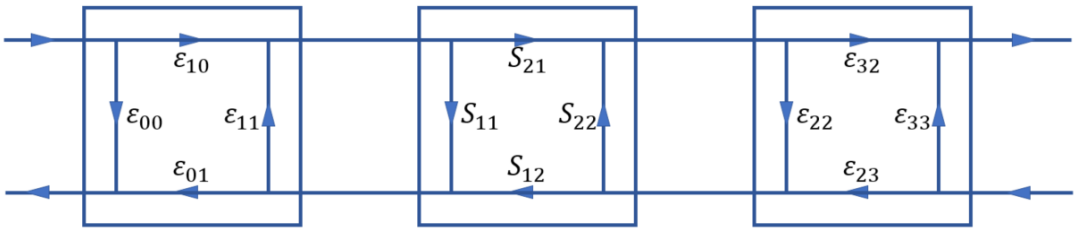


Figure 6.9: TRL error model [151].

The calibration standards needed are defined as Through, Reflect and Line. The standards need not be coaxial or waveguide-based; they can be implemented to work with other measurement setups and test fixtures, such as probe stations. The expected values for the calibration standard can be expressed as [150]:

$$\text{THRU: } [S] = \begin{bmatrix} 0 & 1 \\ 1 & 0 \end{bmatrix} \tag{6.1}$$

$$\text{LINE: } [S] = \begin{bmatrix} 0 & e^{-\gamma l} \\ e^{-\gamma l} & 0 \end{bmatrix} \tag{6.2}$$

$$\text{REFLECT: } S_{11} = S_{22} = \Gamma \tag{6.3}$$

where $[S]$ is the scattering matrix representing the two-port system, γ is the complex propagation constant of the transmission line, l is the length of the transmission line, and Γ is the complex reflection coefficient. Here, the transmission line is simply free space, and l is equal to one quarter of the wavelength at mid-band $\lambda_0/4$.

For the THRU step, a short length of transmission line (non-zero length THRU) is chosen: the total length between the two antenna apertures is equal to twice the fixed value $d = 11$ mm. As such, the calibration plane is identified in the middle point of this length. The REFLECT standard is obtained by placing a metal plate at the calibration plane between the two antennas and moving back the antenna connected to port 2 by a distance equal to the thickness of the metal plate t_{MP}, so that the total length between the two antennas is equal to: $2d + t_{MP}$. The LINE standard is achieved by

separating the antennas of an additional length equal to $\lambda_0/4 = 2.54$ mm, having chosen a frequency band from 27 GHz to 32 GHz. For the free-space measurement setup, the characteristic impedance adopted is the one of the free-space 377 Ω.

6.4 Permittivity extraction

The extraction of the permittivity is realized with the NIST iterative conversion method, derived from the Nicholson-Ross-Weir (NRW) method.

The NIST iterative method needs an initial guess that usually is obtained from the application of the NRW method. In absence of the approximate permittivity, the following procedure can be used.

Having defined the propagation constant in the air γ_0 and in the material γ as:

$$\gamma_0 = j\sqrt{\left(\frac{\omega}{c}\right)^2 - \left(\frac{2\pi}{\lambda_c}\right)^2} \tag{6.4}$$

$$\gamma = j\sqrt{\frac{\omega^2\mu_r\varepsilon_r}{c^2} - \left(\frac{2\pi}{\lambda_c}\right)^2} \tag{6.5}$$

$$\mathrm{c} = \frac{1}{\sqrt{\mu_0\varepsilon_0}} \tag{6.6}$$

where ω is the angular frequency, ε_r and μ_r the relative permittivity and permeability respectively, λ_c is the cut-off wavelength and c the velocity of light, it is possible to obtain the reflection Γ and transmission T coefficient as:

$$\Gamma = \frac{\frac{\gamma_0}{\mu_0} - \frac{\gamma}{\mu}}{\frac{\gamma_0}{\mu_0} + \frac{\gamma}{\mu}} = \frac{\gamma_0 - \gamma}{\gamma_0 + \gamma} \tag{6.7}$$

$$\mathrm{T} = e^{-\gamma L} \tag{6.8}$$

where L is the length of the sample and the relative permeably is assumed equal to 1.

Finally, known the measured scattering parameters, the permittivity can be extracted using an iterative method (i.e., Newton–Raphson iteration) to solve either one of the two following equations:

$$F^1(\varepsilon_r) = S_{11}S_{22} - S_{21}S_{12} - \left[e^{-2\gamma_0(L_{air}-L)}\right]\frac{T^2 - \Gamma^2}{1 - \Gamma^2T^2} \tag{6.9}$$

$$F^2(\varepsilon_r) = \frac{S_{21} + S_{12}}{2(1 - T^2\Gamma^2)} - T(1 - \Gamma^2)e^{-\mathrm{j}\gamma_0(L_{air}-L)} \tag{6.10}$$

where L_{air} is the total length of the air-line. The algorithm is considered converged when either of the two formulations is equal to 0.

An alternative method that can be employed to determine the material permittivity is the New Non-Iterative Conversion Method (NICM). This method is similar to the NRW conversion with the difference of defining the effective permittivity and permeability. First, the coefficients X, Γ and T are derived from the measured scattering parameters in a similar way to the NRW:

$$X = \frac{S_{11}^2 - S_{21}^2 + 1}{2S_{11}} \tag{6.11}$$

$$\Gamma = X \pm \sqrt{X^2 - 1} \tag{6.12}$$

$$\mathrm{T} = \frac{S_{11} + S_{21} - \Gamma}{1 - (S_{11} + S_{21})\Gamma} \tag{6.13}$$

where the latter is valid under the condition of $|\Gamma| < 1$ to find the correct root. Therefore, the effective permittivity and permeability can be determined as:

$$\mu_{eff} = \frac{1}{\Lambda}\left(\frac{1+\Gamma}{1-\Gamma}\right)\frac{1}{\sqrt{\frac{1}{\lambda_0^2} - \frac{1}{\lambda_c^2}}} \tag{6.14}$$

$$\varepsilon_{eff} = \frac{1}{\Lambda}\left(\frac{1-\Gamma}{1+\Gamma}\right)\frac{1}{\sqrt{\frac{1}{\lambda_0^2} - \frac{1}{\lambda_c^2}}} \tag{6.15}$$

where:

$$\frac{1}{\Lambda^2} = \left(\frac{\mu_r \varepsilon_r}{\lambda_0^2} - \frac{1}{\lambda_c^2}\right) = -\left(\frac{j}{2\pi L}\ln\left(\frac{1}{T}\right)\right)^2 \tag{6.16}$$

Being T a complex number, equation 6.16 has an infinite number of root, since the real part of $\ln\left(\frac{1}{T}\right)$ is unique and single valued but the imaginary part of $\ln\left(\frac{1}{T}\right)$ is equal $j(Arg\left(\frac{1}{T}\right) + 2\pi n)$, where $n = 0, \pm 1, \pm 2, \ldots$, and is the integer of the ratio of the sample length to the wavelength in the material (L/λ_m). For $n = 0$, and $-2\pi < Arg\left(\frac{1}{T}\right) < 0$, (L/λ_m) is between 0 and 1.

For a non-magnetic material $\mu_r = \mu_{eff} = 1$.

$$\varepsilon_r = \left(1 - \frac{\lambda_0^2}{\lambda_c^2}\right)\varepsilon_{eff} + \frac{\lambda_0^2}{\lambda_c^2}\frac{1}{\mu_{eff}} \tag{6.17}$$

$$\varepsilon_{eff} = \varepsilon_{eff}\left(\mu_{eff}\right)^n = \frac{1}{\left(\Lambda\sqrt{\frac{1}{\lambda_0^2} - \frac{1}{\lambda_c^2}}\right)^{n+1}}\left(\frac{1-\Gamma}{1+\Gamma}\right)^{1-n} \tag{6.18}$$

6.5 Measurements results

The experimental setup was calibrated using a TRL calibration in accordance with the parameters explained in Section 6.2. A schematic diagram of the experimental setup can be found in Figure 6.10.

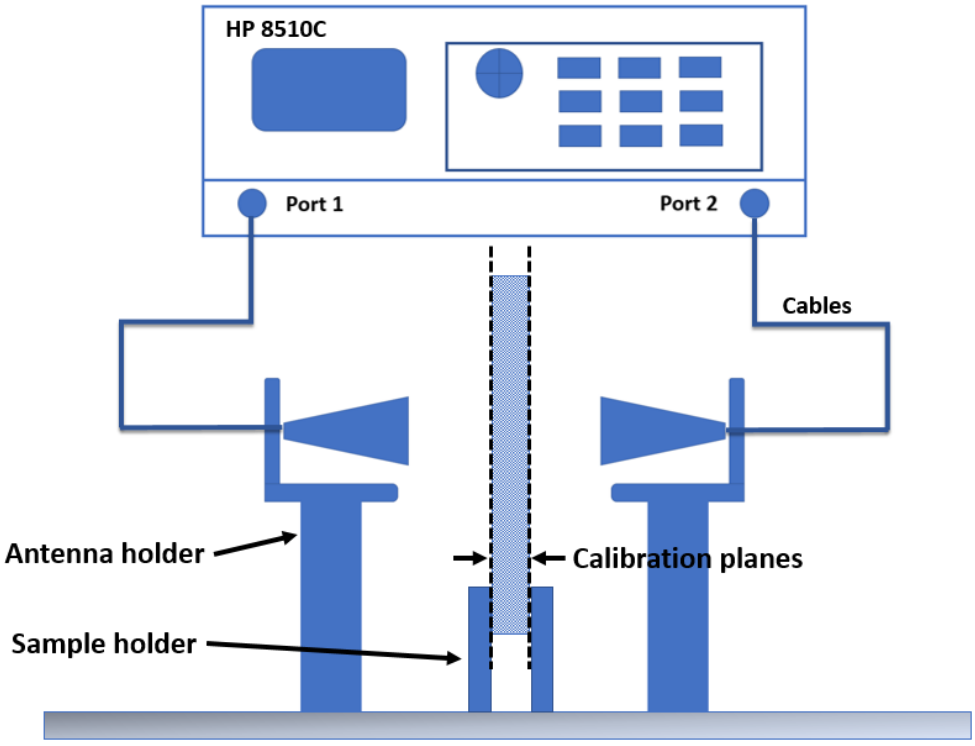


Figure 6.10: Schematic of experimental setup.

The frequency band of interest ranges from 27 GHz to 32 GHz. The sample is inserted between the two antennas along its *y* or *x*-axis to change the polarization of the electric field. The measurements are conducted in the near-field domain to avoid electromagnetic interferences from the surrounding area. Figure 6.11 represents the measurement system unloaded (no material inserted) with complete transmission of the signal from port 1 to port 2 ($S_{21} \simeq 0$).

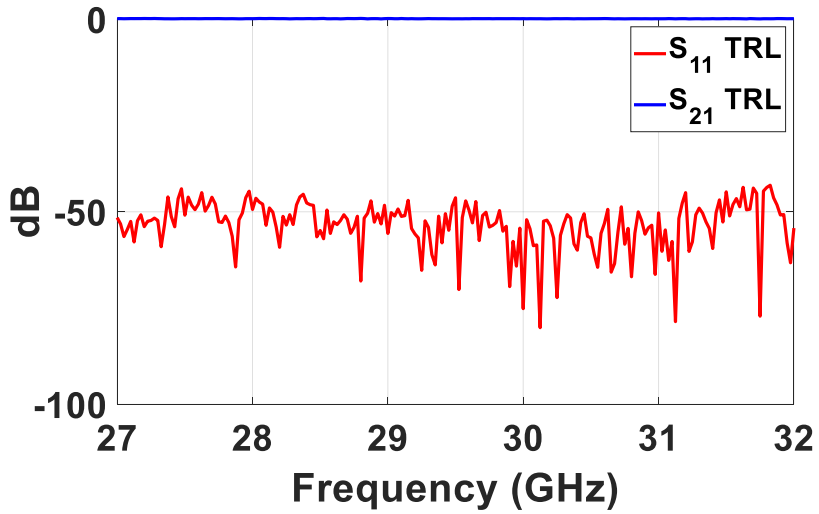


Figure 6.11: Reflection and transmission coefficient after TRL calibration and unloaded line.

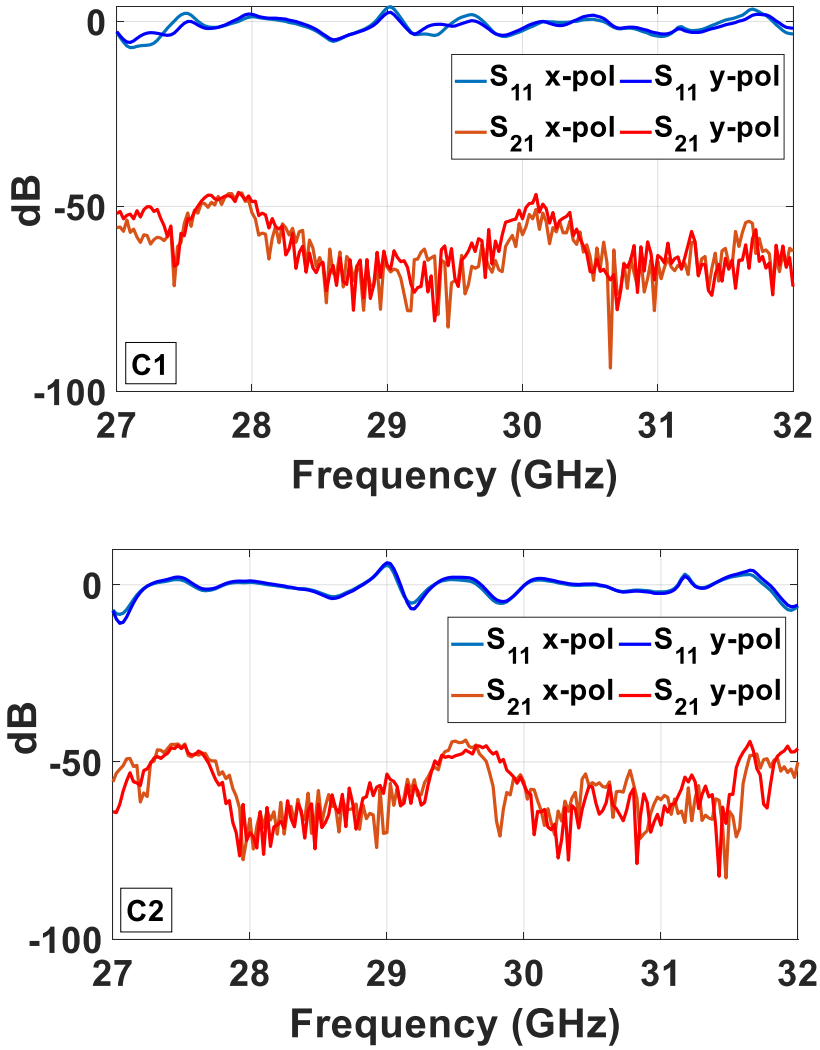


Figure 6.12: Reflection and transmission coefficients for C1 and C2 samples in vertical and horizontal polarization.

The signal is transmitted from port 1 to port 2 and the return loss is low.

C1 and C2 were tested in vertical polarization (y-pol) and horizontal polarization (x-pol), as shown in Figure 6.12. In both cases the measured values exceed the dynamic range as they are too close to the noise floor. This results confirms the findings obtained at X-band with the clamped waveguide method. The SE of these materials is high and the reflection coefficient oscillates around 0 value. Therefore, even if a defect was manufactured or embedded in the structure, it would not be seen by this type of microwave characterization.

A similar outcome is recorded for C3 in case of polarization parallel to the fibre direction, as seen in Figure 6.13. The value of $|S_{21}|$ is lower compared to the other two materials, however, also in this case the signal registered is close to the noise floor, due to the high conductivity of the fibres.

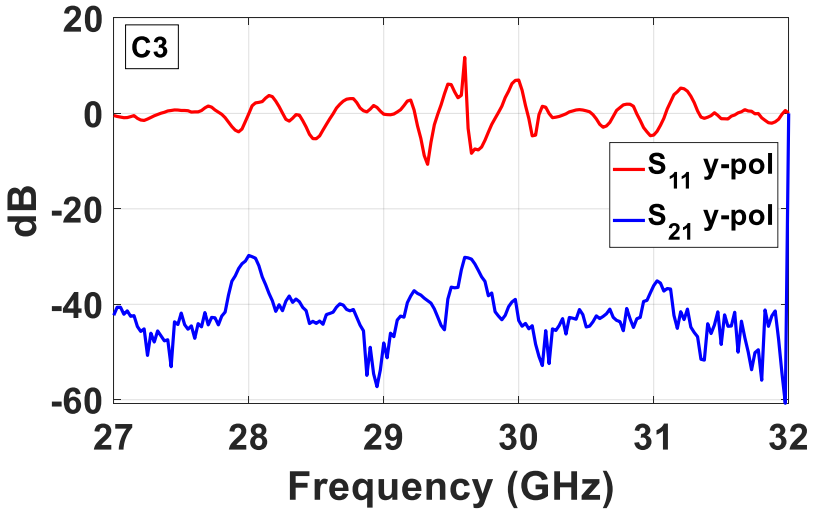


Figure 6.13: Reflection and transmission coefficient for C3 samples in vertical and polarization.

Conversely, perpendicular polarization relative to fibre direction allows for permittivity characterization and damage identification. Both sides of C3 where analysed. The patch defect inserted in the structure is between the second and the third layer on the side of port 2. The measurements are reported in Figures 6.14, 6.15 and 6.16 for the four scattering parameters S_{11}, S_{12}, S_{21}, and S_{22}. 30 measurements were realized on the healthy part of the structure and 30 measurements on the damaged area. The upper part shows the measurements with the plotted standard deviation, while the lower half the average S-parameters measured over frequency. Because of the orientation of the electric field, which is perpendicular to the fibres, transmission is allowed from port 1 to port 2 and the value of $|S_{21}|$ decreases sensibly in respect to the one measured in the parallel case.

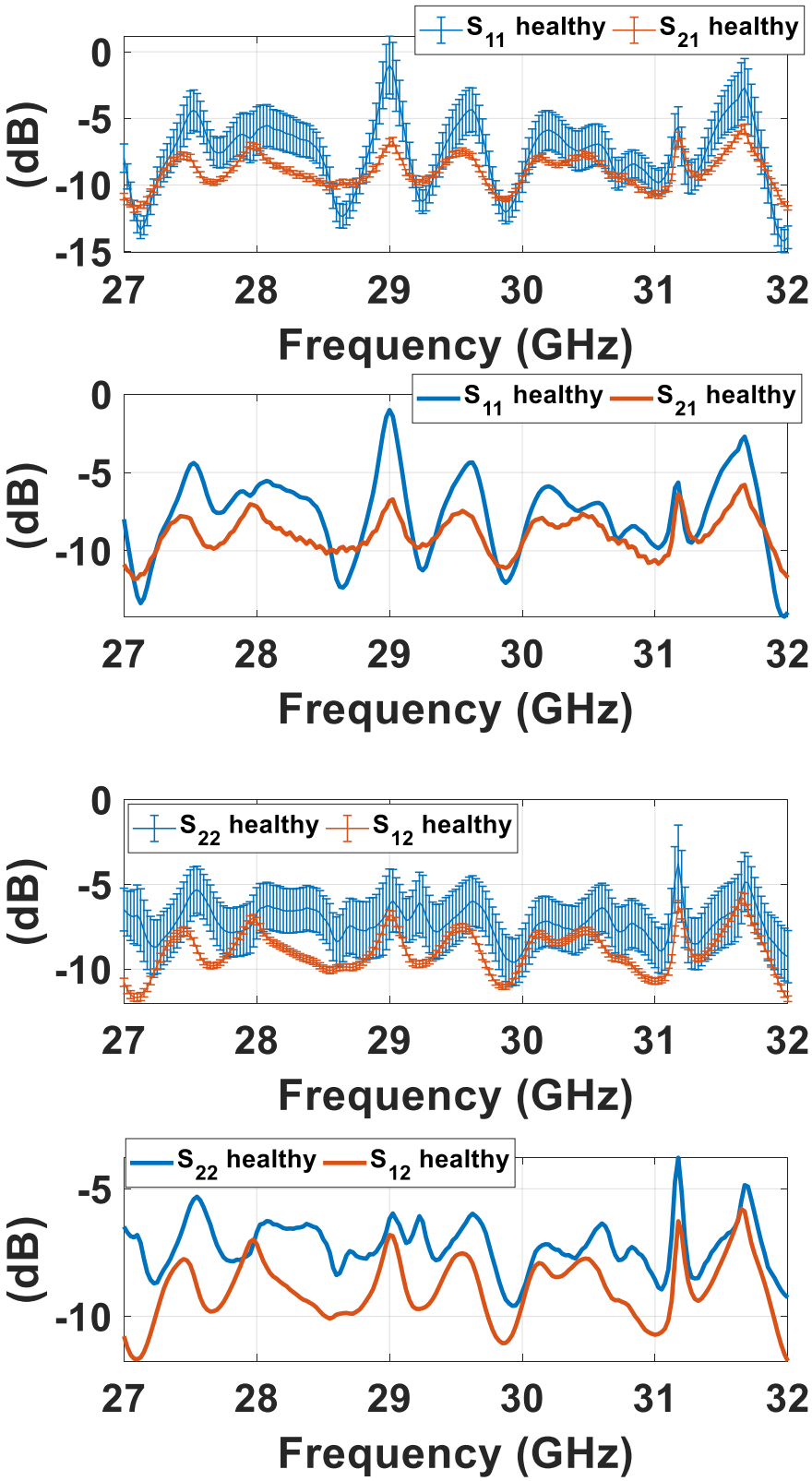


Figure 6.14: Reflection and transmission coefficients for healthy area of C3 sample in horizontal polarization.

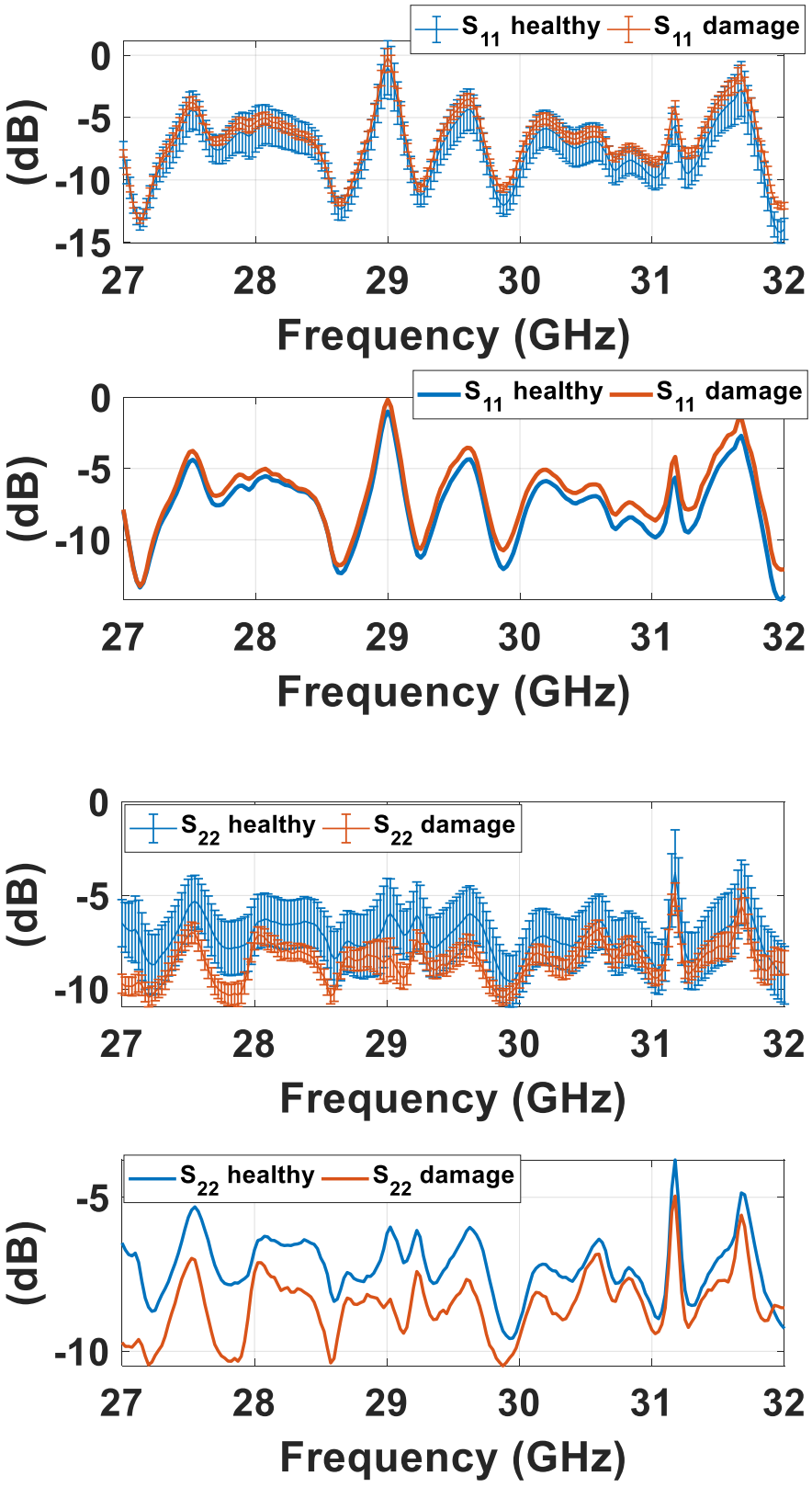


Figure 6.15: Reflection coefficients for healthy and damaged area of C3 sample in horizontal polarization.

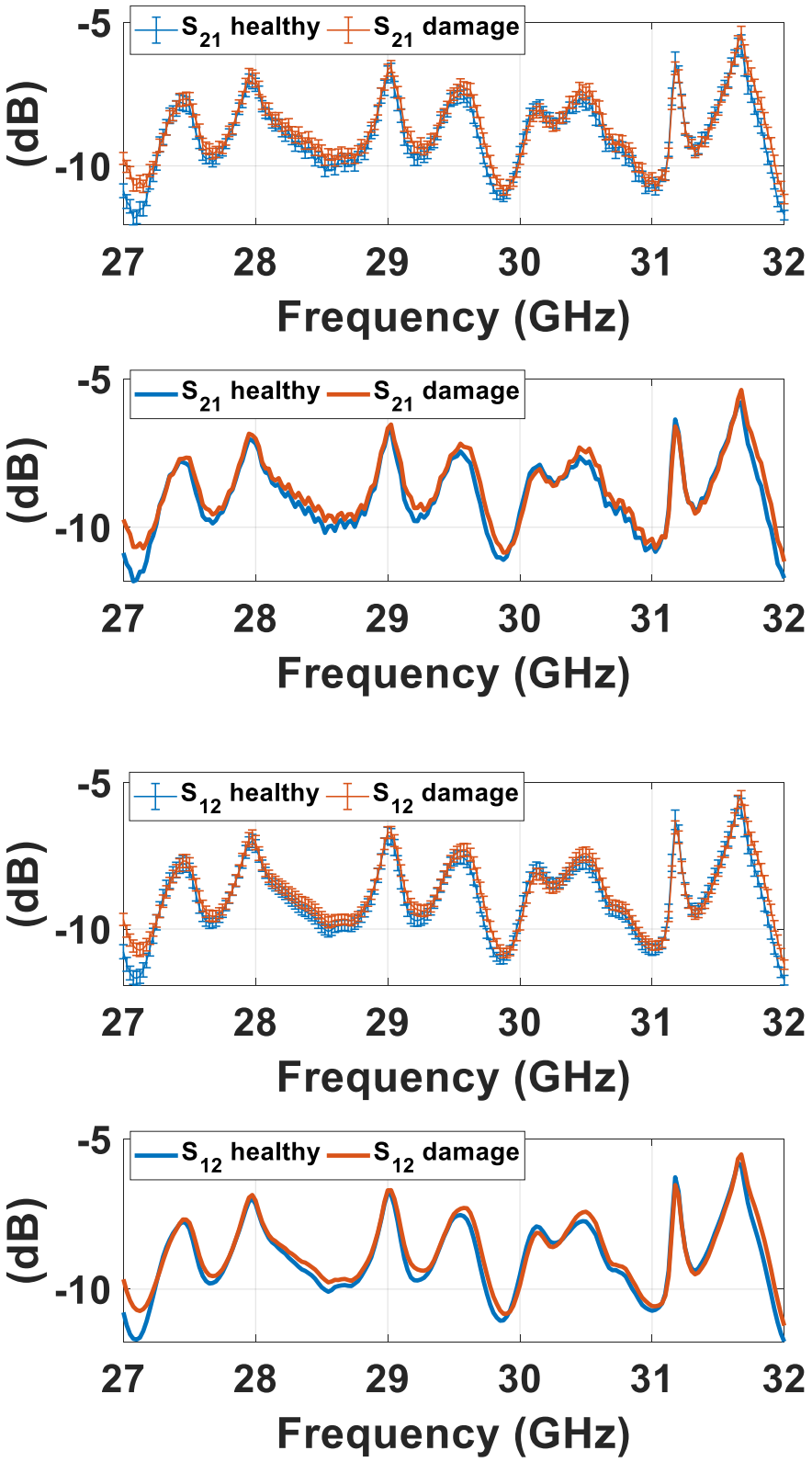


Figure 6.16: Transmission coefficients for healthy and damaged area of C3 sample in horizontal polarization.

Therefore, the reflection and transmission coefficient are close in value, as the portion of the signal transmitted and returned is close.

Particularly, good accuracy was reported on the measurements of the transmission coefficients S_{12} and S_{21}. Both coefficients displays the same values over frequency and the data have less dispersion compared to the ones measured for the reflection coefficients, as indicated by the standard deviation plotted on the graphics. Conversely, the reflection coefficients S_{11} and S_{22}, are more affected by the measurement dispersion and by possible EMI interferences on the signal. The antenna connected to port 1 is closer to the VNA, which is sustained by a metal structure and this can produce possible EMI interference.

Now, let us compare the healthy section of the sample and the damaged area. The first thing that can be noticed is that the standard deviation of the measured parameters on the latter is inferior to the one found for the healthy structure, even if the number of taken measurements is the same. This is due to the fact that the composite material is by definition anisotropic. Even if we assume the material to have the same physical properties along one direction, in this case *x*-axis, there are bound to be areas in which the material characteristic are not constant, as the fibres in reality are not perfectly straight or aligned. The measurements of the healthy material were recorded over a big area, changing the location of the antenna for each taken. The same procedure was applied to the damaged sector with the only noticeable difference that the patch area is smaller in size, allowing for less alteration in the material properties.

From the transmission measurements, no evident difference appears between the damaged and the healthy section. The same is true comparing the S_{11} for both cases, the same signal was recorded. The information on the damage is present only comparing the reflection coefficient on port 2 S_{22} for both cases. As shown in Figure 6.15. This is expected as on the side of the antenna connected to port 2, the delamination is closer to the surface.

6.5.1 Permittivity characterization

The NIST iterative method was applied with initial guess obtained from the X-band characterization in Section 6.2. The average values of S_{22} and S_{12}, shown in the from 6.14, were used for the permittivity extraction. The calculated permittivity over frequency is reported in Figure 6.17. The average value of the effective permittivity, calculated in the frequency range considered, is equal to $\varepsilon_r(\mathrm{C3}) = 9.3 - i2.7$. Note that this permittivity, as well as the ones characterized for the other composites presented in this work, cannot be used to describe the entire class of CFRP composites but it is inherent to this particular material. However, the values obtained in this work can be used to have an indication on the complex permittivity of UD composites in the direction transversal to the fibres. Furthermore, the calculated permittivity can be used

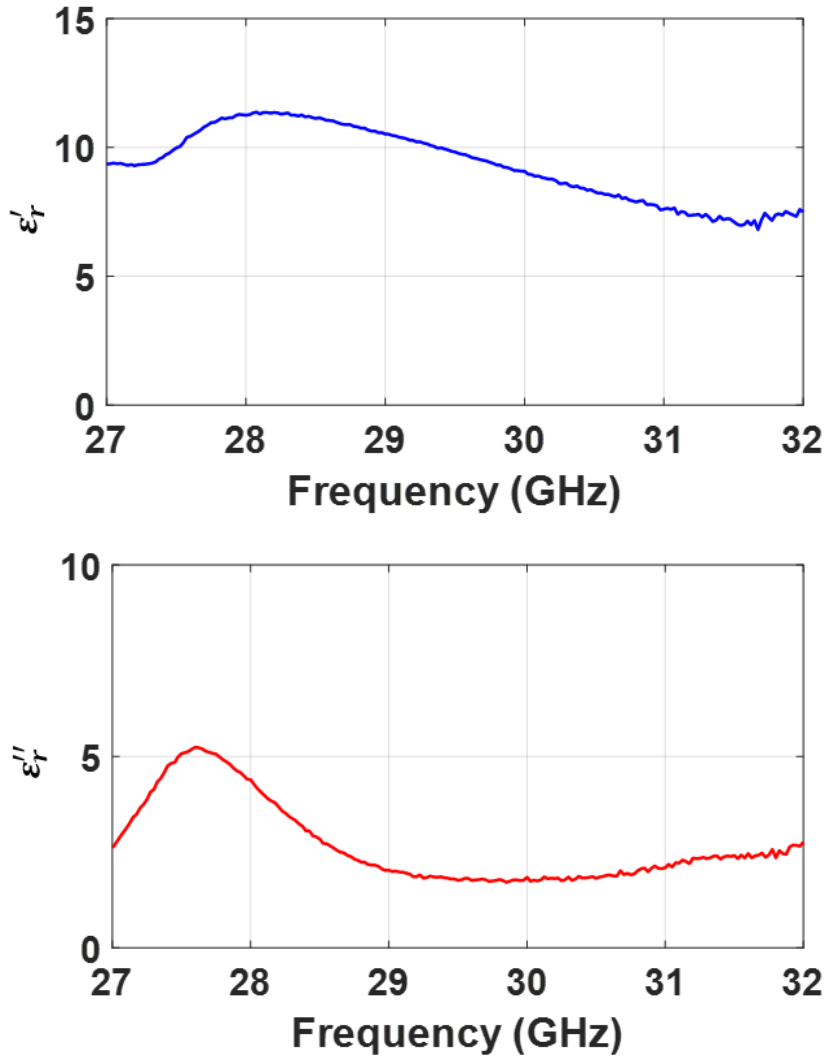


Figure 6.17: C3 permittivity estimation with free-space method.

in electromagnetic software, to simulate an anisotropic material along its three axis: a conductivity of $\simeq 10^4$ can be given along the fibre axis and the complex permittivity presented can be applied along the two directions orthogonal to the reinforcements.

Finally, note that the peak visible between 27 GHz and 28 GHz is probably due to the smoothing of the signal. For the permittivity calculation, the curve S_{12} for the healthy case, which can be found in Figures 6.14 and 6.16, was used. Smoothing the curve causes a drop in dB between 27 GHz and 27.5 GHz, as shown in Figure 6.18.

6.6 Damage identification, numerical simulation

Using the complex permittivity obtained by the experimental measurement, a numerical simulation was performed to examine whether the free-space method is appropriate for detection of defects. The chosen free-space method consists of two horn antennas in transmitting and receiving configuration in the near-field. The

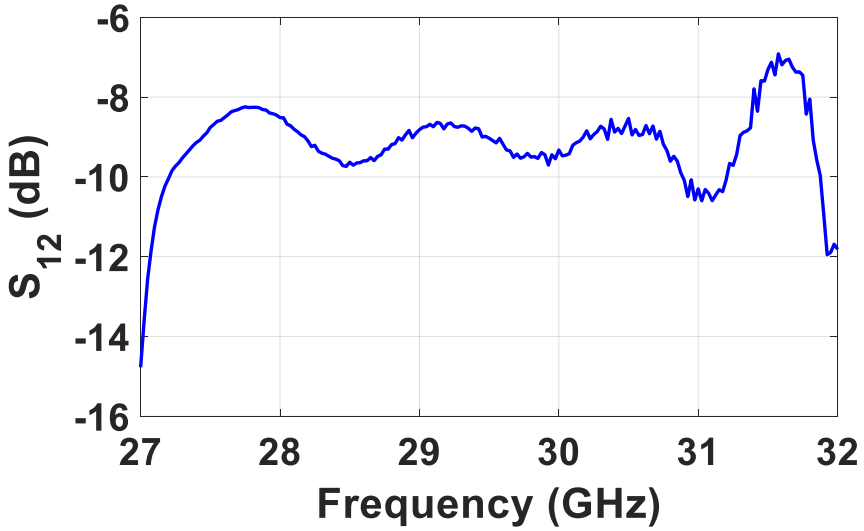


Figure 6.18: Carbon fibre fabric with in-plane waviness.

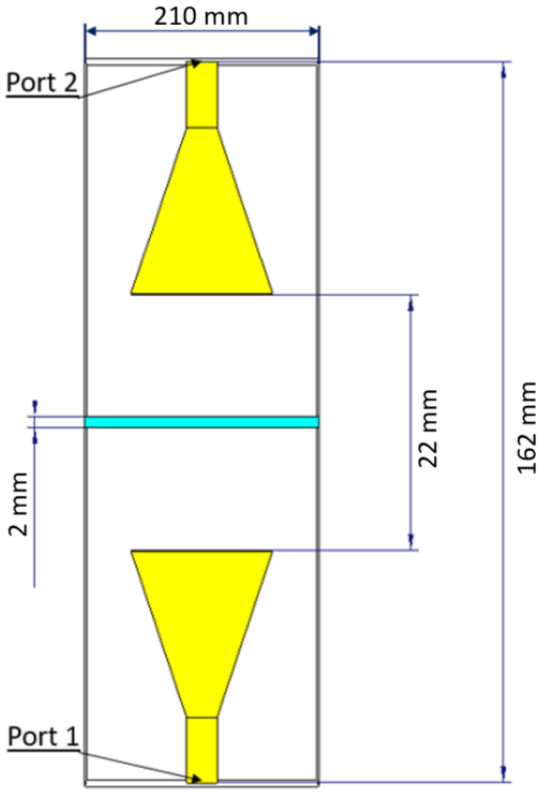


Figure 6.19: Free-space model used to calculate the S- parameter S21.

numerical model is shown in Figure 6.19 and was used for the damage simulations, considering normal incidence, vertical polarization of the electric field and a Gaussian-modulated sinusoidal RF pulse [V(t)] assigned to port 1. The reflection/transmission responses are obtained from power waves, in a frequency band ranging from 27 GHz to 32 GHz. The specimen of dimensions of 210 mm × 150 mm × 2 mm was placed between the two horn antennas, whose specifications are listed in Table 6.1.

Table 6.1: LB-28-20-C horn technical specification.

Frequency range (GHz)	26.5-40.0
Waveguide	WR28
Gain (dBi)	20
Polarization	Linear
Material	Cu
Size (mm)	32.1 × 40.4 × 94.0

The material has homogenous permittivity $\varepsilon_r(\mathrm{C3}) = 9.3 - i2.7$. To avoid numerical dispersion, the shortest wavelength of interest was spatially sampled at a rate of 10 mesh cells per wavelength.

Three damage configurations were considered for the aforementioned specimen. The aim is to know whether variations of the scattered signal can be detected due to the presence of a near-surface defect. A square element was used to simulate the case of delamination, surface defect (e.g., variation of thickness due to inclusion) and surface indentation. Type of defect and size are summarized in Table 6.2

Table 6.2: Damage types considered for simulation.

Type of defect	Execution	Dimension
Delamination	Rogers patch ($\varepsilon_r = 10.2 - i0.02$)	40 mm ×40 mm× 1.25 mm
Surface defect	$\varepsilon_r(\mathrm{C3}) = 9.3 - i2.7$	40 mm ×40 mm× 1.25 mm
Indentation	Air	40 mm ×40 mm× 1.25 mm

In case of inter-laminar defect, an artificial delamination of 1.25 mm in thickness was created filling the inset of with Rogers (permittivity can be seen in Table 6.2). In the case of surface defect and indentation, a square element was added or subtracted, respectively, to the sample surface facing the antenna connected to port 1. The scattering curves of the transmission coefficient for the undamaged and damaged models are reported in Figure 6.20. The sample with delamination exhibits greater power transmission through the specimen with respect to the undamaged model. This behaviour is expected, as part of the shielding material is missing, and the signal is facilitated to penetrate through the material. Conversely, the shielding effectiveness of the material increases due to the surface defect, as an additional element of minute thickness variation is added on the face of the sample facing the transmitting antenna,

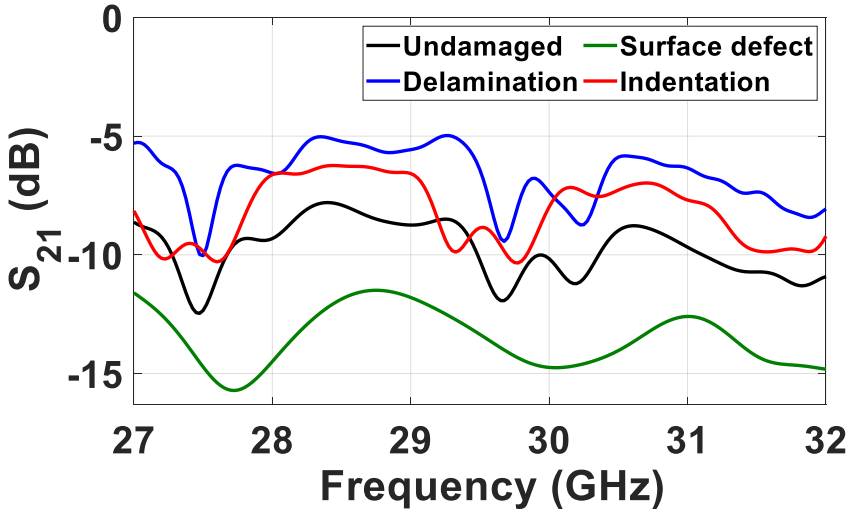


Figure 6.20: Comparison of the simulated transmission coefficient of damaged models with undamaged case, over 27-32 GHz.

increasing the reflection power of the sample. As for delamination, also the indentation provokes an decreased value of SE, as the material becomes thinner. For the undamaged model, the simulation required a mesh of 26000000 hexahedral elements and lasted ≃ 50 min with 2.6 GB of RAM needed.

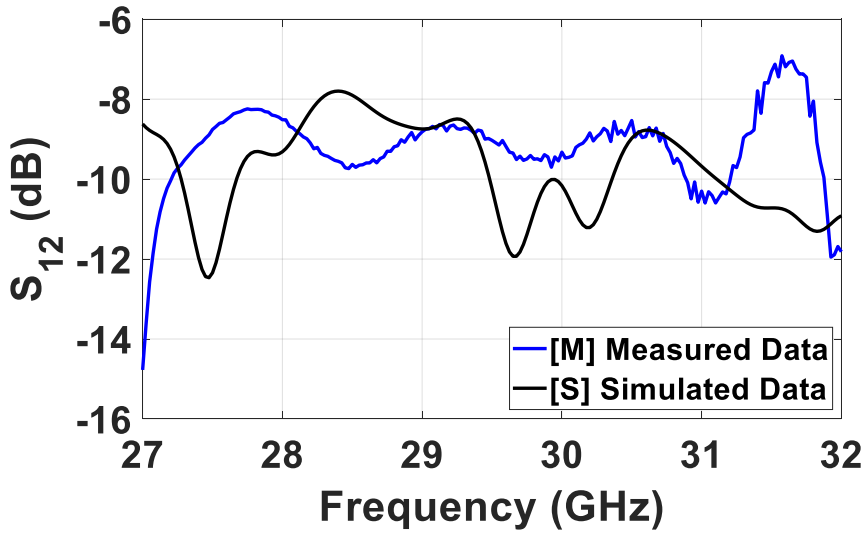


Figure 6.21: Comparison of measured [M] and simulated [S] transmission coefficient.

Figure 6.21 compares the experimental data of Figure 6.18, which were used for the extraction of the permittivity used in the EM simulations. The results allow for the EM software to be used instead of experimental measurement to simulate damage identification problems, as the permittivity extracted simulated to a good extent the actual measured value. In addition, from the analysis of Figure 6.20 it was possible to

assess the presence of the three damage cases, through changes in the magnitude of the transmission coefficient with respect to the undamaged model.

Consequently, an additional step was taken into simulating the three damage cases in presence of measurement error. In reality, the measure is subjected to errors such as uncertainty due to the measurement system, human factor, non-isotropic material, imperfect alignment of the antennas etc. This is confirmed by the standard deviation reported in the measurements.

Therefore, the same systematic errors were induced for the three damage cases and the measurements were recorded for a limited frequency range of interest. This comes from the observation of $S_{22\,healthy}$ and $S_{22\,damage}$ in Figure 6.15. It is possible to observe that as the frequency increases, more it is difficult to distinguish the two curves. Therefore, it is useful to analyse the signal around frequency point of interest (i.e., for example 28-28.5 GHz).

This was realized through simulations, inducing systematic errors on controlled parameters, such as permittivity, thickness of the material, geometry of the defect. For each damage case where collected $\simeq 100$ data point. The absolute value of the reflection coefficient was plotted as a function of the absolute value of the transmission

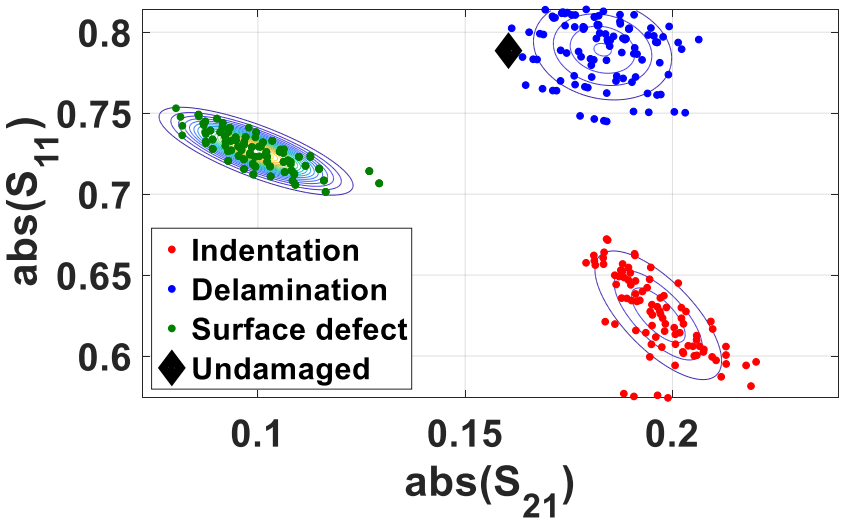


Figure 6.22: Comparison of the simulated three damage case (indentation, delamination and surface defect) with undamaged case, in presence of systematic errors.

coefficient in the smaller frequency range considered. In addition, a Gaussian mixture model (GMM) was used for data clustering. As seen in Figure 6.22, a cluster model is not necessary as the three damage cases can be easily differentiated. This observation is important, because allows for a better identification of the damage.

As previously seen in Section 6.5, the information about the delamination is found on the reflection coefficient S_{22}. However, from the observation of Figure 6.15 and

considering the larger standard deviation of S_{22} measured for the healthy area of the sample, this is not enough to confirm the presence of the free-edge delamination. Therefore, the same procedure as per 6.22 will be applied together with a *k*-means cluster to identify the data points belonging to the damaged and undamaged structure.

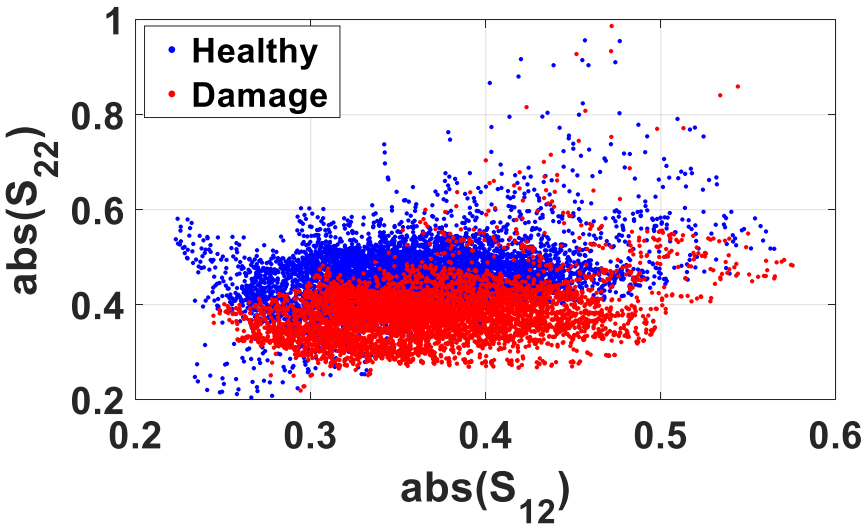


Figure 6.23: Comparison of healthy structure and free-edge delamination damage (27-32 GHz).

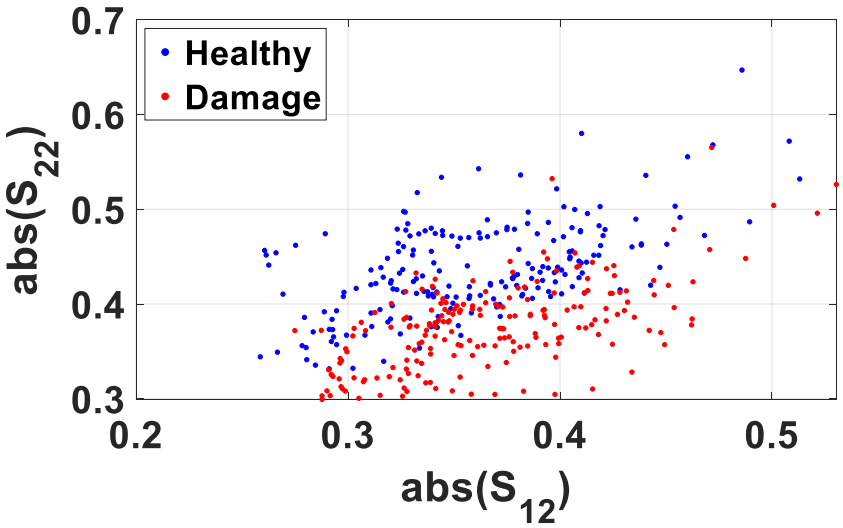


Figure 6.24: Comparison of average measured data of healthy structure and free-edge delamination damage (27-32 GHz).

6.7 Damage identification, experimental

The raw data of the reflection coefficient on port 2 (S_{22}) and the reverse transmission coefficient (S_{12}) are plotted as per Figure 6.22. As previously stated, a total of 30 measurements were collected for both healthy and damaged area of the sample.

Therefore, a total of 30×201= 6030 values are plotted in the frequency range from 27 GHz to 32 GHz, which express the magnitude of S_{22} as function of S_{12}, where 201 is the number of sampling points in the frequency range. The raw data are shown in Figure 6.23.

The data overlaps each other's due to the random errors that generate dispersion in the measurement. Even considering the averaged coefficients, it is difficult to differentiate the damage, see Figure 6.24.

As the information provided by the coefficients magnitude is not enough, there are two methods, which allows damage identification:

- Using smaller frequency intervals of interest with clustering, as seen previously in the simulations;
- Using the energy of the scattered signal.

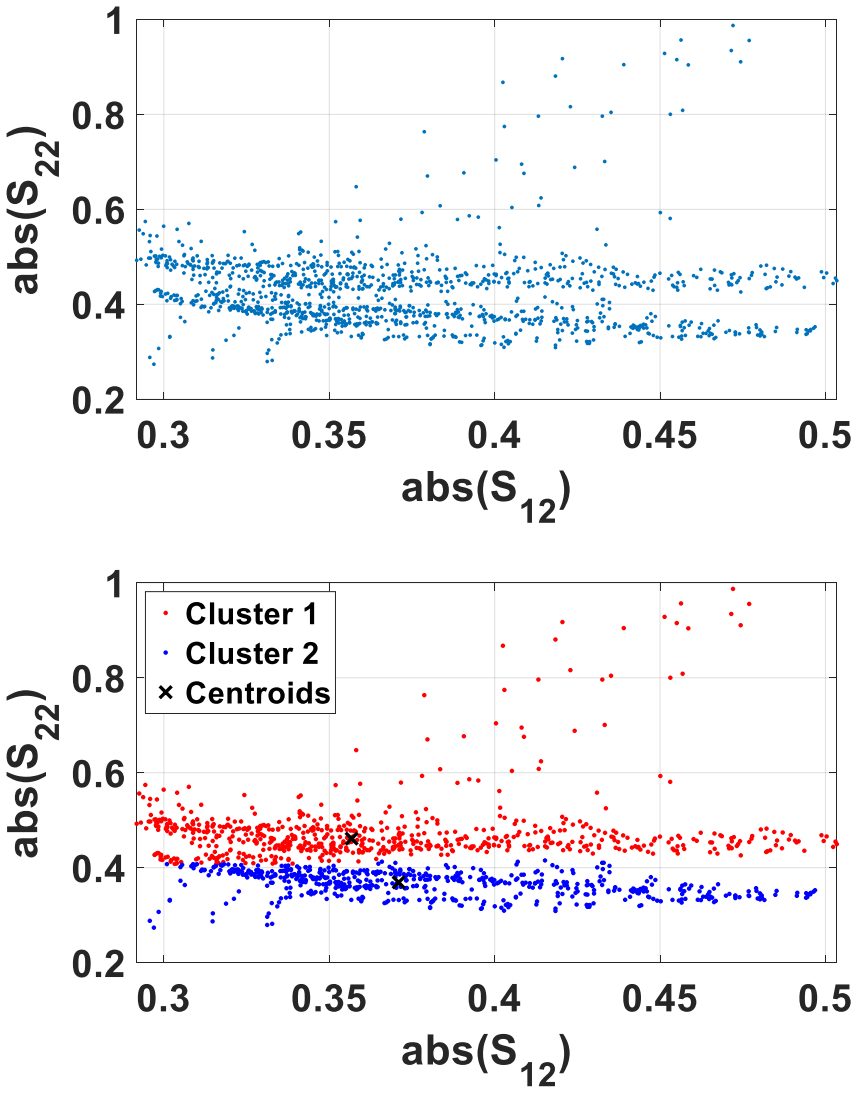


Figure 6.25: Pre and post processed data with *k*-means (28.7-29.2 GHz).

6.7.1 Reducing the frequency range

The frequency range is reduced to smaller intervals of interest. For example, the same values of Figure 6.23 are plotted in the reduced frequency range (28.7-29.2 GHz) in Figure 6.25.

Fig 6.25 shows the data before and after signal processing with the *k*-means clustering method. *k*-means clustering is a method of vector quantization that partition n observations into *k* clusters, where each observation belongs to the cluster with the nearest mean (cluster centroid) [213]. In this case, *K*-means partition the data in two clusters and choose the best arrangement out of five initializations. The results obtained in Figure 6.25 can be compared with the known data of Figure 6.26.
Some data points are not included, but generally the clustering method is able to interpret the two signals as independent. The process requires a series of measures.

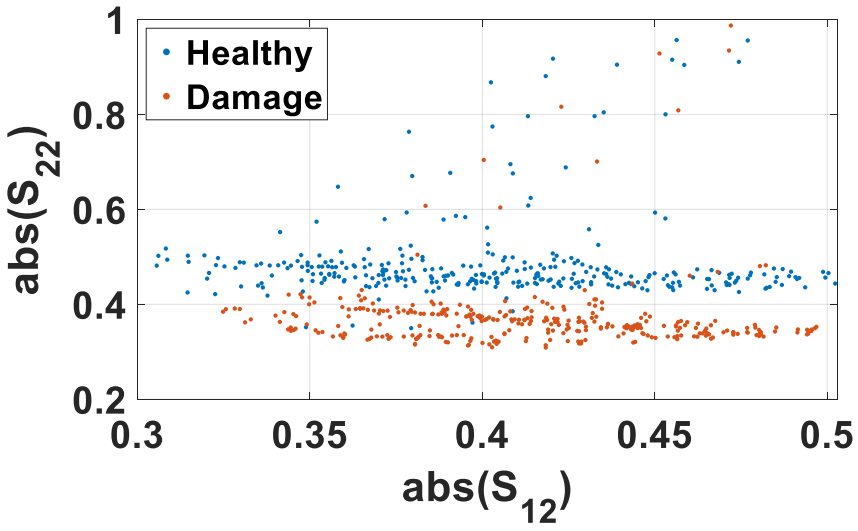


Figure 6.26: Comparison of healthy structure and free-edge delamination damage (28.7-29.2 GHz).

6.7.2 Energy of the scattered signal

The energy of a signal in the frequency domain can be defined as:

$$E_s^{Frequency} = |X[f]|^2 \tag{6.19}$$

The energy was calculated for the received S_{22} and transmitted S_{12} signal on port 2, and the reflection coefficient was plotted as function of the transmission coefficient for each measure. The results are shown in Figure 6.27. The healthy and the damaged area can be clearly differentiated from each other allowing for damage characterization of the free-edge delamination.

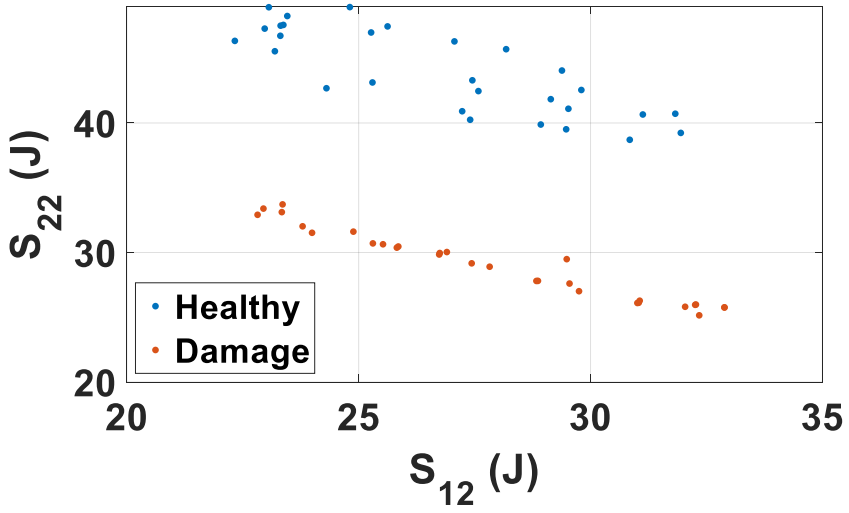


Figure 6.27: Comparison of healthy structure and free-edge delamination damage in terms of signal energy.

Chapter 7

Characterization of defects in carbon fabric and CFRP sheets using Synthetic Aperture Radar (SAR)

In this Chapter, synthetic aperture radar (SAR) imaging technique is applied to detect and characterize defects such as gaps, overlays, missing tow, fibre misalignment and fibre waviness in carbon fabric and CFRP laminates. Although, few studies are reported in literature about the application of microwave SAR imaging to carbon fibre composites, this technique shows great potential for these types of materials, as the yarns/tows present in the prepreg can be considered polarizing targets due to their linear orientation. Particularly in the case of unidirectional composites.

In fact, when an electric field strikes a composite material with uniform orientation of the fibres/yarns/tows, the amplitude of the scattered signal can be related the fibres yarns/tows direction and to the polarization of the electric field vector. The amplitude of the scattered signal is maximum when the electric field is oriented along the direction of the fibres. The dependence of the signal from the orientation of the fibres increases with the conductivity of the reinforcements (i.e., higher level of scattering). Thus, this method is very convenient in the case of carbon fibres.

The scattered signal changes with the orientation of a polarizing target and with differences in thickness of the materials, as demonstrated in literature [66], [125], [129]. Therefore, these assumptions makes this method particularly useful for real time application during the manufacturing process of composite materials, due to the good resolution and non-destructive nature of SAR methods, which involve the use of probes kept at a specific distance from the material under test (i.e., stand-off, lift-off distance).

The most evident example can be the application during manufacturing process such as automated fibre placement (AFP) or automated tape laying (ATL). As previously seen in Section 1.1.3., these manufacturing processes involve the deposition of a unidirectional tow (from 3 mm to 13 mm of width) or tape (up to 300 mm of width), using a roller on top of a preformed mould to produce more complex composite laminates (e.g., skins of aircraft wings). The roller moves on the same surface section according to same/different orientation each time (e.g., 0°,45°,45°,0°), to create several overlapping layers. Manufacturing defects generated during this procedure, such as missing tow, fibre misalignment, gaps, overlaps, fibre waviness and fibre wrinkling can be easily detected both because they produce unevenness in thickness and because a deviation of the reinforcement from the preferred path is registered by the scattered signal. The intensity of the scattered signal can be related to the polarization of the electric field in respect to the direction of the conductive fibres.

7.1 Electromagnetic waves polarization

Electromagnetic waves are described as transverse waves, where the electric field vector $\vec{E}$ and magnetic field vector $\vec{H}$ of a plane wave are perpendicular to each other and orthogonal to the direction of propagation of the wave $\vec{k}$. To describe the polarization of an electromagnetic wave, it is important to consider the direction along which the electric field $\vec{E}$ oscillates. The type of polarization of the wave is indicated by the projection of $\vec{E}$ on a plane perpendicular to $\vec{k}$.

The simplest type of polarization is linear, in this case $\vec{E}$ oscillates in one direction only (and $\vec{H}$ oscillates orthogonally). Linear polarization can be defined vertical or horizontal depending on the axis along which $\vec{E}$ oscillates. However, when $\vec{E}$ does not oscillate only along a single direction, it is useful to decompose the electric field into its components (i.e., into two waves with orthogonal polarization), as happens for vectors. If the components have the same amplitude, phase and period, the polarization remains linear (e.g, slant polarization). If the vector components have the same amplitude but are out of phase by a quarter of a period, the field is circularly polarized with the following convention for the sense of rotation: right-handed (+90°) or left-handed (-90°). In this case, $\vec{E}$ describes a complete circle in a wave period (i.e., the electric field vector rotates during propagation). If the components of the electric field do not have the same amplitude, elliptic polarization can be found.

7.2 Microwave SAR imaging

SAR imaging is generally performed using two orthogonally-polarized signals. The two signals can either be linearly-polarized and perpendicular to each other or circularly-polarized with left-hand and right-hand sense of rotation [125], [129], [214], [215]. These orthogonal signals can be generated using two separate probes or a single dual polarized antenna connected to a transceiver. The probe is raster scanned in a 2D rectangular surface with a fixed step over the area under test. The magnitude and phase of the backscattered signal are recorded, processed and organized using 3D SAR algorithms to produce a high spatial resolution image of the scanned target [120], [216]–[218]. The processed image relates the image intensity to the intensity of the backscattered signal.

7.2.1 Dual polarized antenna

Let us consider the case of a dual linearly polarized antenna, where the probe is able of transmitting and receiving two linearly polarized signals at each ports, with electric field vectors perpendicular to each other [125], [126], [214], [219]. A schematic diagram of a typical dual linearly polarized antenna, modelled as a four-port device, is reported in Figure 7.1. Two rectangular waveguides are defined as exciting ports, i.e., port 0 and port 3. Port 0 generates a dominant TE_{01} mode, while port 3 a TE_{10} mode. A square waveguide with dominant TE_{01} and TE_{10} modes is defined according to the type of dominant mode propagated as port 1 or port 2 respectively. The two dominant modes, TE_{01} and TE_{10}, have linear polarization with electric field vector perpendicular to each other. Thus, it is possible to define the two transversal

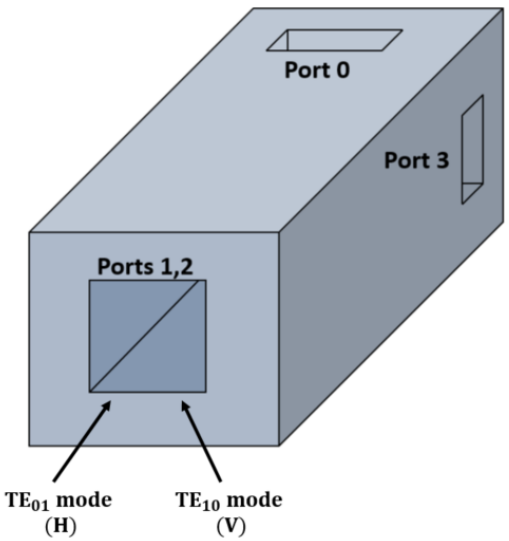


Figure 7.1: Schematic of a four-port dual polarized probe.

polarizations as linear vertical polarization (V) for port 1 excitation and horizontal polarization (H) for port 2, as shown in Figure 7.2.

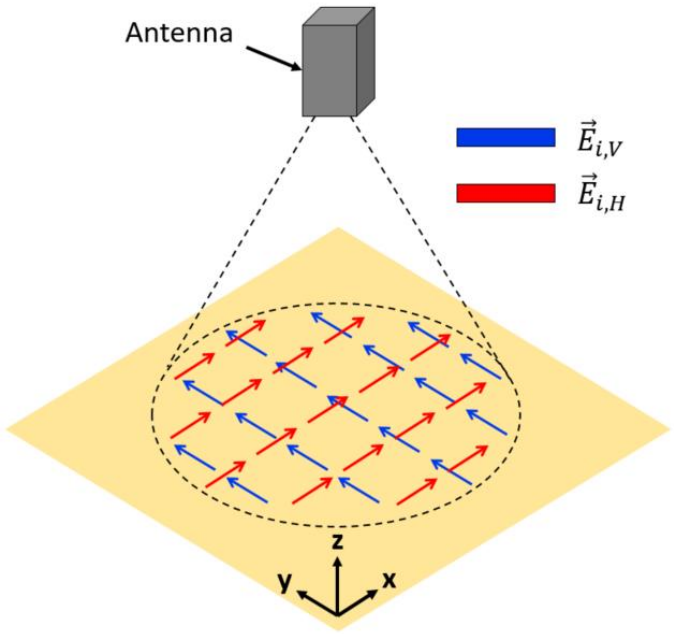


Figure 7.2: Dual linearly polarized probe illuminating a 2D target of interest. The blue arrows show the direction of the irradiating electric field $\vec{E}_i$ in case of vertical polarization, the red arrows in case of horizontal polarization.

The dual polarized antenna can be connected to a two-port vector network analyzer by means of its two rectangular waveguides (i.e., port 0 and port 3). At each port, the calibrated complex reflection coefficients can be read by the VNA, and it is possible to generate the S-parameters matrix *S*:

$$S = \begin{bmatrix} S_{11} & S_{21} \\ S_{12} & S_{22} \end{bmatrix} \tag{7.1}$$

where S_{ij} indicates the ratio between the signal received at port *i* and the signal transmitted from port *n*.

Using the alternative notations H and V to define the type of linear polarization, the signal scattered from a target can also be presented in terms of the linear polarimetric scattering matrix S_{Lin} that relates the scattered wave $\vec{E}_r$ with the incident wave $\vec{E}_i$. Thus, the S_{Lin} matrix seen by the square waveguide aperture can be written as:

$$S_{Lin} = \begin{bmatrix} S_{VV} & S_{HV} \\ S_{VH} & S_{HH} \end{bmatrix} \tag{7.2}$$

with:

$$\begin{bmatrix} E_{r,H} \\ E_{r,V} \end{bmatrix} = S_{Lin} \begin{bmatrix} E_{i,H} \\ E_{i,V} \end{bmatrix} \tag{7.3}$$

denoting $E_{r,H}$ and $E_{r,V}$ as the horizontal and vertical components of the electric field reflected by the target and $E_{i,H}$ and $E_{i,V}$ as the horizontal and vertical components of the electric field incident on the target. S_{Lin} components are the backscattering coefficients of the scatterer. For instance, the scattering parameter S_{HV} indicates the complex reflection coefficient obtained when irradiating with vertical polarization (port 1) and receiving with horizontal polarization (port 2).

Knowledge of the scattering matrix S_{Lin} permits calculation of the received magnitude, phase and direction of polarization of the scattered wave for any combinations of transmit and receive antenna polarization states. This process is called polarization synthesis. Therefore, the measurement system is valid for any orthogonally-polarized signals. For example, the case of left-hand (L) and right-hand (R) circular polarization can be derived adopting the proper mathematical conversion.

The conversion method is extensively explained in [126], and is used to transform linearly polarized S-parameters to circularly polarized S-parameters, using a derived matrix of mixed linear-circular polarized S-parameters. Having defined the latter as:

$$S_{VL} = \frac{1}{\sqrt{2}}(S_{VV} + jS_{VH}) \tag{7.4}$$

$$S_{HL} = \frac{1}{\sqrt{2}}(S_{HV} + jS_{HH}) \tag{7.5}$$

$$S_{VR} = \frac{1}{\sqrt{2}}(S_{VV} - jS_{VH}) \tag{7.6}$$

$$S_{HR} = \frac{1}{\sqrt{2}}(S_{HV} - jS_{HH}) \tag{7.7}$$

where, for instance, the scattering parameter S_{VR} indicates the ratio between the received signal vertically polarized along *y*-axis and transmitted signal with right-hand circular polarization.

The relationship between mixed linear-circular polarized S-parameters and S_{Lin} can be expressed in matrix form as:

$$\begin{bmatrix} S_{VL} & S_{HL} \\ S_{VR} & S_{HR} \end{bmatrix} = \frac{1}{\sqrt{2}} \begin{bmatrix} 1 & j \\ 1 & -j \end{bmatrix} \begin{bmatrix} S_{VV} & S_{HV} \\ S_{VH} & S_{HH} \end{bmatrix} \tag{7.8}$$

Subsequently, the same procedure can be used to convert the mixed S-parameters matrix to a circularly polarized matrix indicated as S_{Circ}. The conversion equation written in matrix form is:

$$S_{Circ} = \begin{bmatrix} S_{LL} & S_{RL} \\ S_{LR} & S_{RR} \end{bmatrix} = \frac{1}{\sqrt{2}} \begin{bmatrix} S_{VL} & S_{HL} \\ S_{VR} & S_{HR} \end{bmatrix} \begin{bmatrix} 1 & 1 \\ j & -j \end{bmatrix} \tag{7.9}$$

Finally, combining equations 7.8 and 7.9, S_{Circ} can be expressed as function of S_{Lin}:

$$S_{Circ} = \frac{1}{\sqrt{2}} \begin{bmatrix} 1 & j \\ 1 & -j \end{bmatrix} \begin{bmatrix} S_{VV} & S_{HV} \\ S_{VH} & S_{HH} \end{bmatrix} \begin{bmatrix} 1 & 1 \\ j & -j \end{bmatrix} \tag{7.10}$$

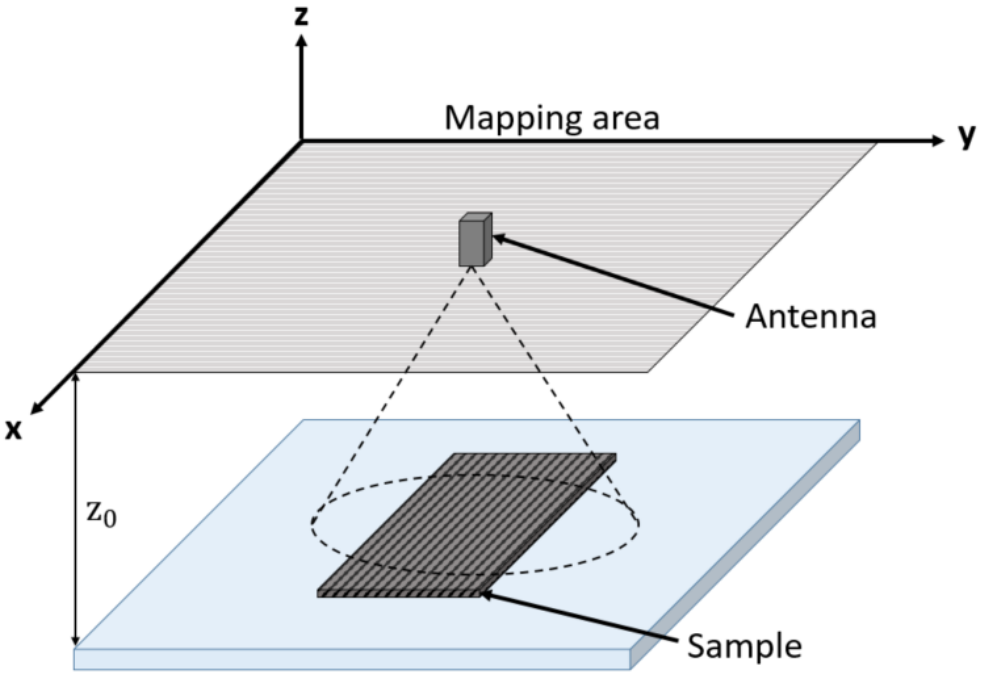


Figure 7.3: Dual polarized probe scanning the sample under test at stand-off distance z_0.

7.2.2 SAR polarimetry

As seen in the previous section, SAR polarimetry is generally performed transmitting and receiving waves at more than one polarization. In the case here described, the dual polarized probe completes a scan over a 2D raster grid (*x*-*y* plane) with fixed step and at a fixed stand-off distance z_0, as depicted in Figure 7.3. At each location the polarimetric S-parameters matrix is measured, and 3D SAR algorithms are employed to create a high-resolution wide-band image of the scanned area [120], [216]–[218]. The polarimetric scattering matrixes are studied to relate the type of polarization of the

transmitted wave with the intensity of the scattered signal [219]–[222]. In this case, since the carbon reinforcements are polarizing targets within the material (i.e., they are linearly distributed and conductive); the preferred direction of polarization of the electric field vector will be precisely along the direction of the reinforcements. Hence, any misalignment of the fibres from this preferred direction can be easily spotted in the post-processed microwave images.

For the experiment, a circularly polarized antenna courtesy of the Applied Microwave Nondestructive Testing Laboratory (AMNTL) of Iowa State University was employed [214]. The antenna is made of brass and consists of two standard Ka-band (26.5-40 GHz) rectangular waveguide (WR28) apertures as input ports (Port 0 and 3), connected to a square waveguide (port 1 and 2) by means of a septum polarizer (the schematic diagram can be found in Figure 7.1). The signal in input through each of the WR28 ports generates at the square waveguide aperture a transmitting wave with circular polarization, either a left-handed or right-handed. The geometry of the antenna and the calibration method to derive S_{VV}, S_{HV}, S_{VH} and S_{HH} from the pre-processed data were developed by AMNTL laboratory and are extensively explained in [214].

The antenna was connected to an Anritsu MS4644A VNA, which was configured for two-port measurements at 51 uniformly-spaced frequency points in the Ka-band. The material under test was secured onto a moving platform/table and a scanning step of 2 mm was selected. The scan time is related to the selected dimensions of the scanned area and decreases if the selected area is smaller or the sampling step size is bigger. For the measurements, a stand-off distance of $z_0 = 25 - 30$ mm was considered, according to the tested material. At each step, the S_{Circ} is determined, as well as the S_{Lin} derived from the former.

7.2.3 3D SAR algorithm

The 3-D SAR algorithm used is based on the *ω–k* algorithm and explained in [120], whose structure can be found in Figure 7.4. The NUFFT (non-uniform fast Fourier transform) algorithm is used, with $\sigma = 2$ and $m = 12$, where σ is the oversampling factor *m* is the overlap factor.

A cross-range NUFFT is performed, 2-D NUFFT consists in a more general Fourier transform by keeping the selection of (x', y') independent from the selection of (x, y), where (x', y') indicates the measurement sampling step size:

$$D(k_x, k_x, f) = \text{2D NUFFT}\{d(x', y', f)\} \tag{7.11}$$

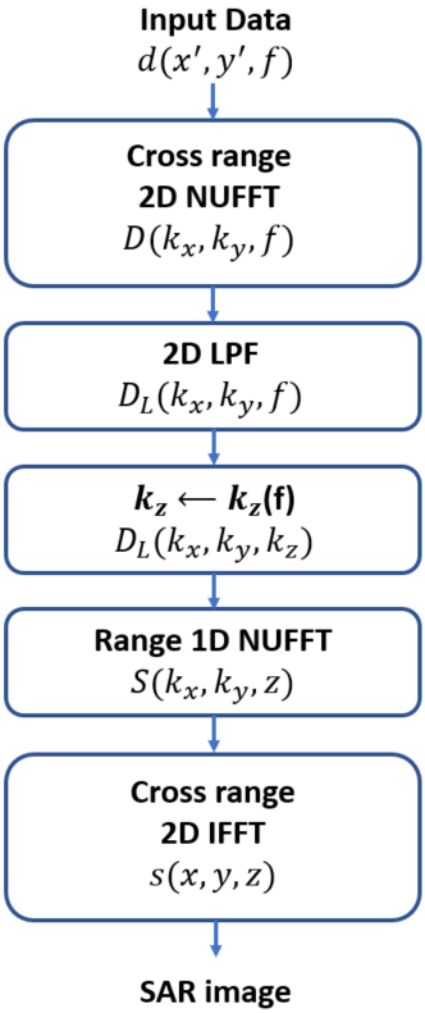


Figure 7.4: SAR ω–k algorithm used.

Then, the measurement data are low-pass filtered (LPF) to remove the resulting redundancy in the 2-D spectral domain occurring when the sampling step size is larger than $\simeq 0.05\,\lambda$ (image sampling step size or image pixel size).

$$D_L(k_x, k_x, f) = \text{LPF}\,\{D(k_x, k_x, f)\} \tag{7.12}$$

Subsequently, the inverse 1-D NUFFT is performed on D_L along the range spatial frequency discretization (k_z):

$$S(k_x, k_x, z) = \text{1D NUFFT}^{-1}\{D_L(k_x, k_x, k_z)\} \tag{7.13}$$

Finally, an high resolution image can be obtained from the inverse fast Fourier transform 2D IFFT of *S*.

7.3 Measurements

7.3.1 Detection of fibre misalignment and in-plane waviness

The first observation on the use of SAR polarimetry for carbon fibres NDT was carried out performing a scan over a short ribbon of carbon unidirectional fabric, where the unidirectional yarns were made to vary from their original distribution along *y*-axis to simulate in-plane waviness or fibre misalignment, in the way shown in Figure 7.5. The material used is cut from McMASTER unidirectional carbon fabrics weave P/N 1824N12, 0.36 mm thick. The sample of width equal to ≃1.5 cm was fixed on a flat aluminium plate, which can be used as an alternative substrate to a stacked sequence of conductive layers of carbon fabrics, in virtue of the high shielding effectiveness of carbon woven fabrics already shown in Chapter 3. The ribbon represents the ply of interest stacked on top of a substrate made of the previously laid composite sheets, whose effect is emulated by the metal plate.

The sample was scanned with the circularly polarized antenna presented in [214], with 2 mm sampling step size along *x* and *y* directions, to cover an area of 70 mm × 130 mm. The stand-off distance is 25 mm. S_{Lin} and S_{Circ} were determined over the frequency range (26.5-40 GHz) in 51 points.

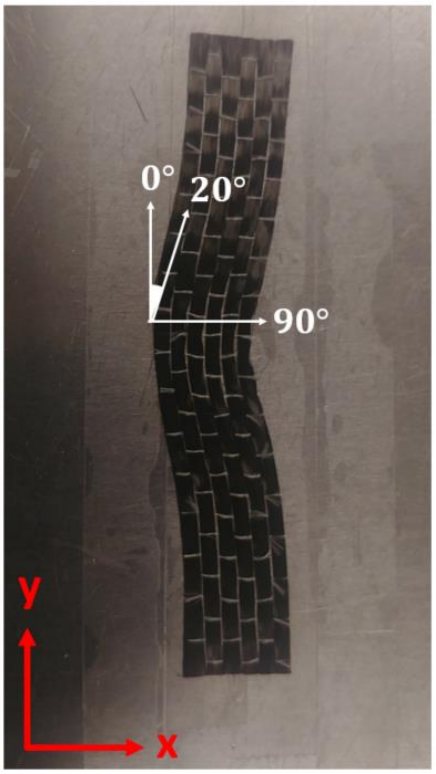


Figure 7.5: Carbon fibre ribbon with in-plane waviness (20° rotation), fixed on an aluminium plate.

An example of captured raw data is given by Figure 7.6, which shows the measured normalized magnitude of S_{VH} at fixed frequency points before SAR post-processing. At specific frequencies, it is already possible to point out that the magnitude of the S-parameter increases in correspondence of sectors where the yarns are not aligned with *y*-axis.

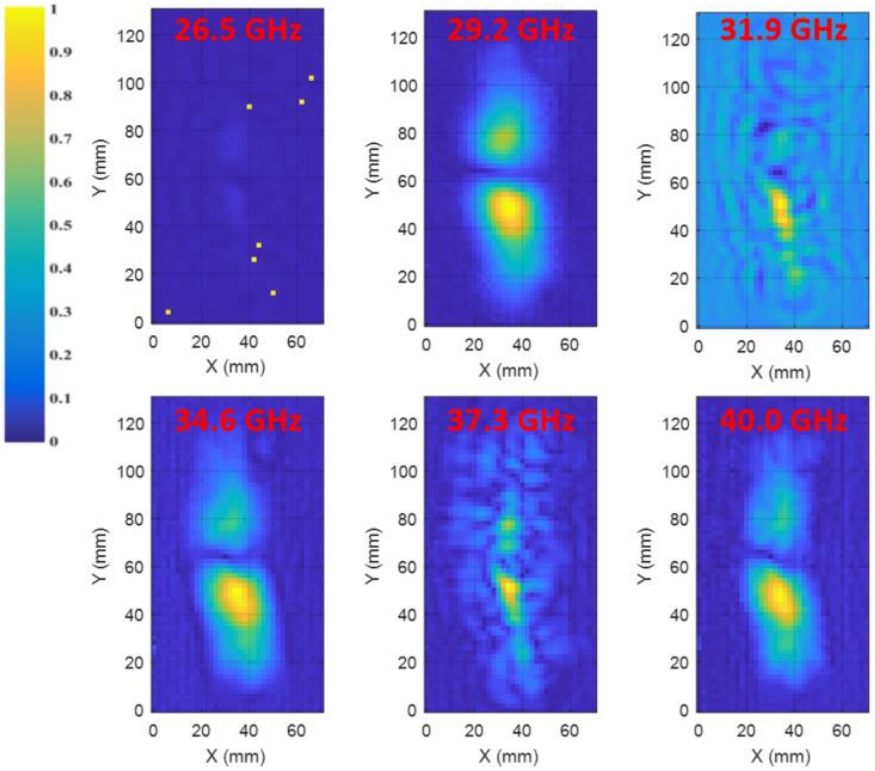


Figure 7.6: Raw measurement of S_{VH} for carbon unidirectional ribbon with in-plane waviness.

Subsequently, the raw data were resampled with spline method and resampling size of 2 mm along *x* and *y* directions. The wideband SAR algorithm seen in Section 7.1.3 was employed to produce images focused to the depth of the carbon unidirectional ribbon.

The post processed scattered coefficients of S_{Lin} and S_{Circ} are reported in Figure 7.7. The resulting SAR images shows the normalized magnitudes for the each element of the scattering matrices. As previously stated, the condition which allows spotting an eventual change in the direction of the fibres from their preferred orientation, i.e., *y*-axis in this case, is the one where the electric field vector is precisely aligned in the direction of the fibres, either in transmitting or receiving polarization.

Therefore, the cross-polarized coefficients S_{VH} and S_{HV}, which corresponds to the measurement obtained with the two orthogonal linearly polarized signals, are well-suited for detection of fibre misalignment, as the magnitude is only non-zero (i.e., the magnitude increases) where the fibres are not directed along *y*-axis. In addition, if we

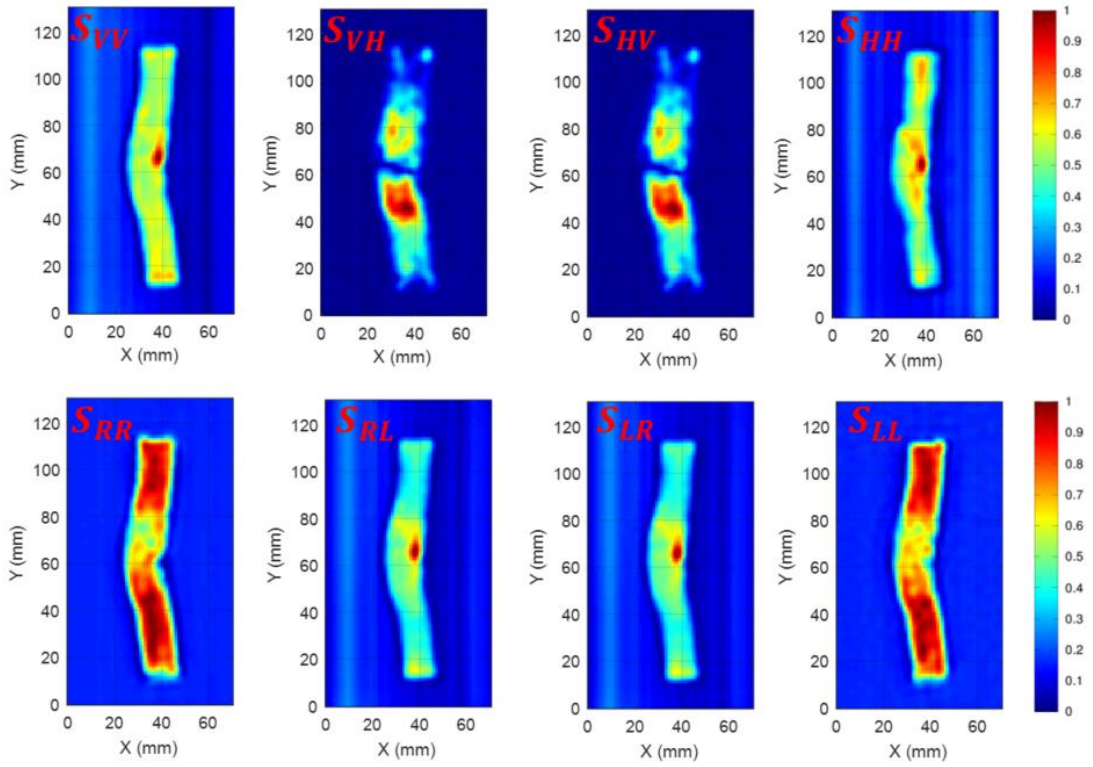


Figure 7.7: Normalized S-parameters magnitude SAR images of the carbon unidirectional ribbon with waviness.

consider an axis that passes through the horizontal mid-section of the sample in $y \simeq 62$ mm, it is also possible to observe an evident area at $\simeq 0$ magnitude between the curvature of the fibres. This happens because at the centre of the curvature the fibres are parallel to *y*-axis.

Hence, an image made with linear cross-polarization allows for easy detection of fibre waviness, as long as either the transmitted or received electric field vector is aligned along the orientation of the fibres. It is important to notice that the sample edges where manually cut and therefore frayed, especially at both upped and lower ends where the cut was done perpendicularly to the yarn orientation. This produces imaging artifacts, which would not be present in practice. Furthermore, the sample is not perfectly aligned along *y*-axis at both ends. However, this issue will be resolved using bigger specimen, as presented in the following paragraphs.

Another interesting finding can be observed for S_{VV}, S_{HH}, S_{RL} and S_{LR}. In the images, it is possible to observe a red point with increased magnitude. This is due to a uneven spot in the ribbon, where the fabric is thicker than other locations. Therefore, thickness variation can easily be spotted when transmitting and receiving using the same polarization in the case of linearly-polarized signals or using cross polarization in case of circularly-polarized signals.

Finally, considering the complex S-parameters S_{VH}, which carries the information to detect waviness/misalignment, it is possible to find information other than through

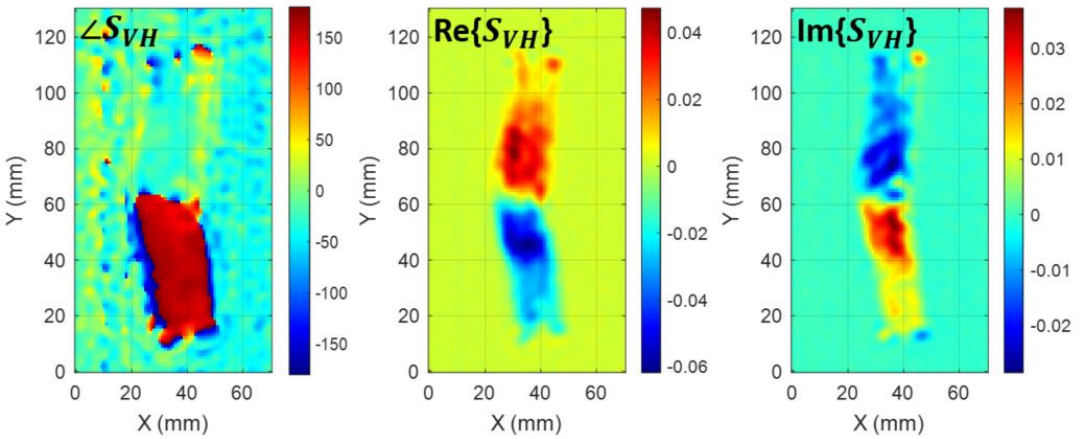


Figure 7.8: Phase (degrees), real part and imaginary part of S_{VH} SAR images.

the magnitude of the signal, also in the phase, real and imaginary part of the scattered coefficient. Figure 7.8 shows that the waviness can be detected also in the phase, real part or imaginary part of S_{VH}. It is possible to observe a change in phase in correspondence of the red-coloured section or lower half of the sample, while the phase is $\simeq 0$ in the remaining scanned area. The real part is negative in the lower half of the

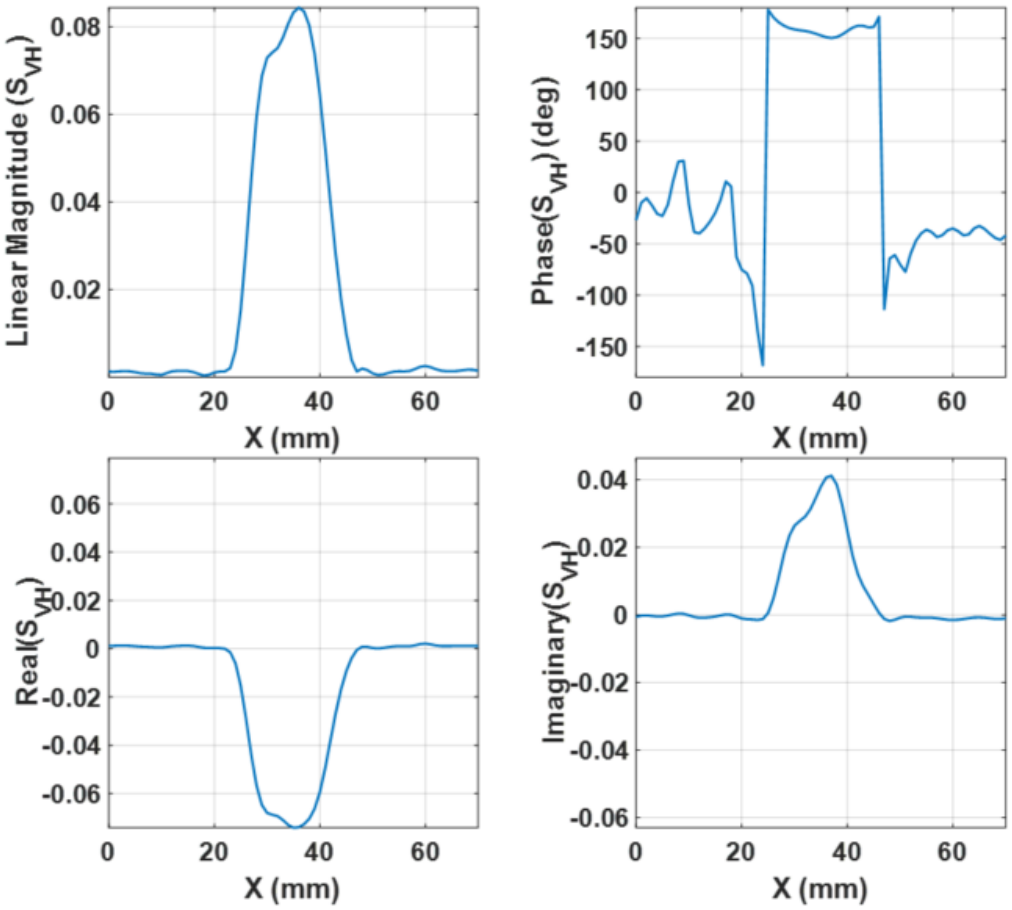


Figure 7.9: Normalized magnitude, phase in degrees, real part and imaginary part of S_{VH} as function of x at y = 46 mm.

sample while, crossing the imaginary axis at $y \simeq 62$ mm, changes sign and becomes positive for higher value of *y*. The real part is 0 in the rest of the scanned area and in the section at $y \simeq 62$ mm the signal oscillates around 0. The inverse is true for the imaginary part. An example of the value of phase, real part and imaginary part as function of *x* for fixed position $y \simeq 46$ mm is given in Figure 7.9. The maximum values of magnitude, phase and imaginary part (or minimum value in case of real part) are found approximately for the point of coordinates ($x \simeq 35$ mm, $y \simeq 46$ mm).

The fibre misalignment, other than being spotted by the SAR images, can also be related to the irradiating polarization that results in maximal scattering. The eigenvalues and eigenvectors of the scattering matrix can be calculated and, being the fibres polarizing targets, the eigenvectors with the largest eigenvalue represents the linear polarization along the orientation of the fibres. Therefore, it is possible to extract the orientation at each location in the image and characterize the degree of deviation of the fibres from the preferred path [120]. Figure 7.10 shows a polarimetric SAR image coloured according to the inclination of the fibres relatively to *y*-axis. It can be noticed that following the path of a yarn along *y*-axis, the fibres are first oriented along $0°$ relatively to *y*, than rotates of $\simeq 20°$ (positive if anticlockwise). Subsequently, the fibres rotate clockwisely to reach again $0°$ in correspondence of the mid-section. The rotation changes direction to $\simeq -20°$ (green coloured area). Passed the waviness area, the fibres are again aligned at $0°$ respect to *y*-axis.

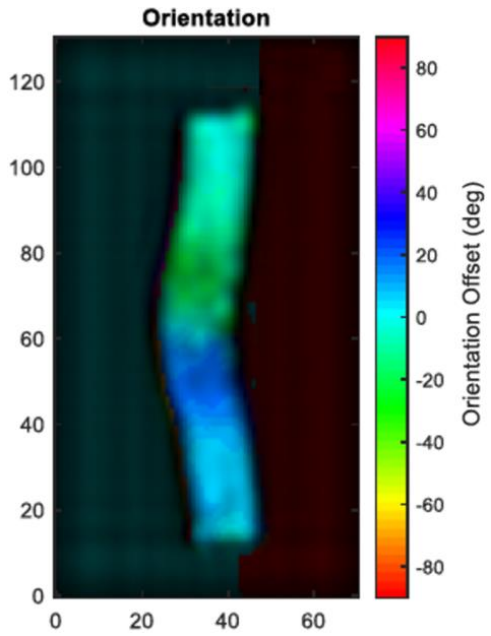


Figure 7.10: Polarimetric SAR image. The orientation of the fibres (in degrees) is represented in the form of a colored image and indicates the angle between the fibres direction and *y*-axis.

7.3.2 In-plane waviness

To evaluate the applicability of SAR polarimetry to fibre waviness detection in carbon fibres composites, a second larger specimen was realized from the same carbon fabric with in-plane waviness in its midsection, as reported in Figure 7.11.

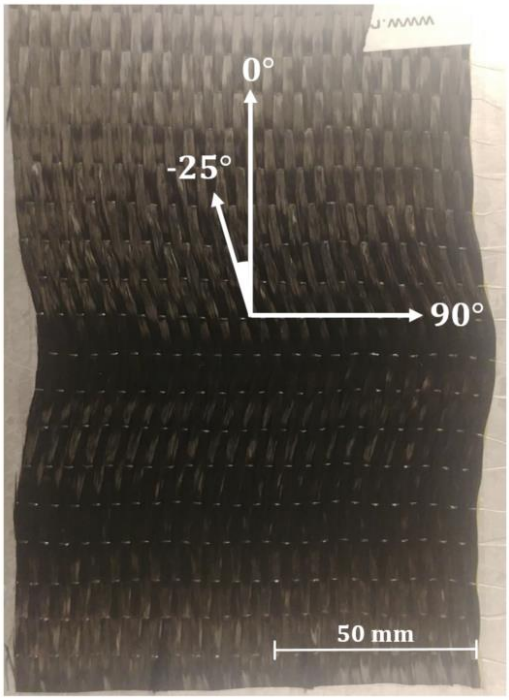


Figure 7.11: Carbon fibre fabric with in-plane waviness, ($\pm 25°$ rotation).

The sample with dimensions of 120 mm × 180 mm × 0.36 mm was secured on a flat aluminium plate. Even in absence of epoxy or a substrate made of carbon prepreg, the system of Figure 7.11 can emulate the case of a unidirectional carbon fibre prepreg being deposed on top of carbon prepreg layup. This is due to two reasons: first, as explained in the previous section, the conductivity of the aluminium plate replaces the one of a carbon substrate, secondly, the absence or presence of resin does not affect excessively the scattered signal, due to the dielectric nature of the polymer. The binding action exerted by the resin is obtained by holding the fabric in place with adhesive tape.

The same measurement conditions as 7.2.1 (i.e., step size, stand-off distance) are adopted. Considering that S_{VH} is the parameter of interest in case of waviness/misalignment, the normalized magnitude and imaginary part of S_{VH} were measured and are shown in Figure 7.12.

The results are even more significant than the ribbon case. Two coloured areas, which indicates the waviness of the fibres, can clearly be distinguished around the *x* symmetry axis of the sample. The areas, where no deviation is found (i.e., blue coloured in the case of normalized magnitude), consist of the metal background and

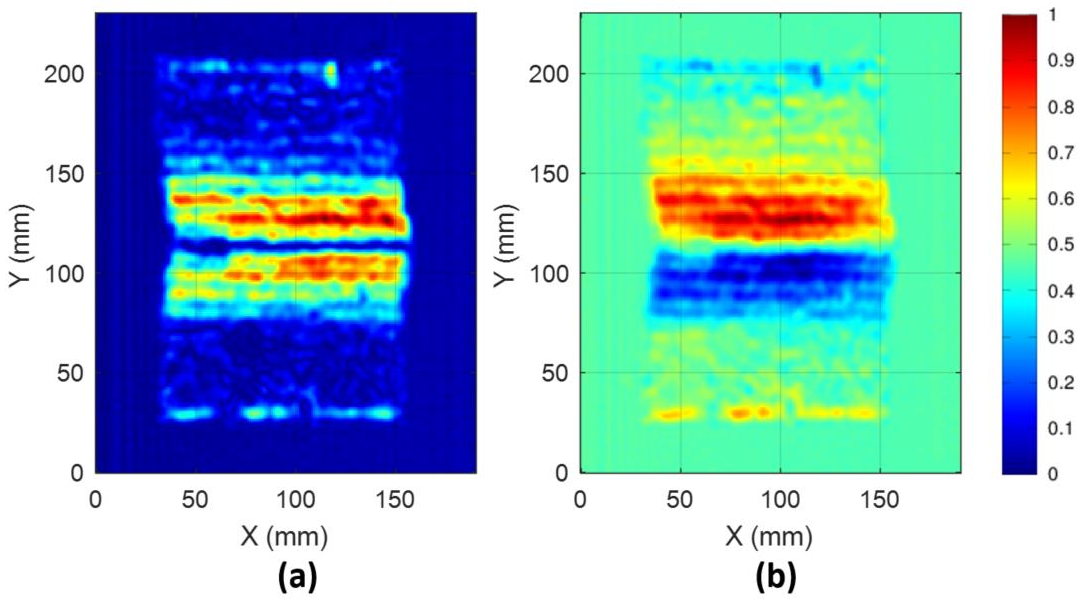


Figure 7.12: (a) Normalized magnitude and (b) imaginary part of S_{VH}.

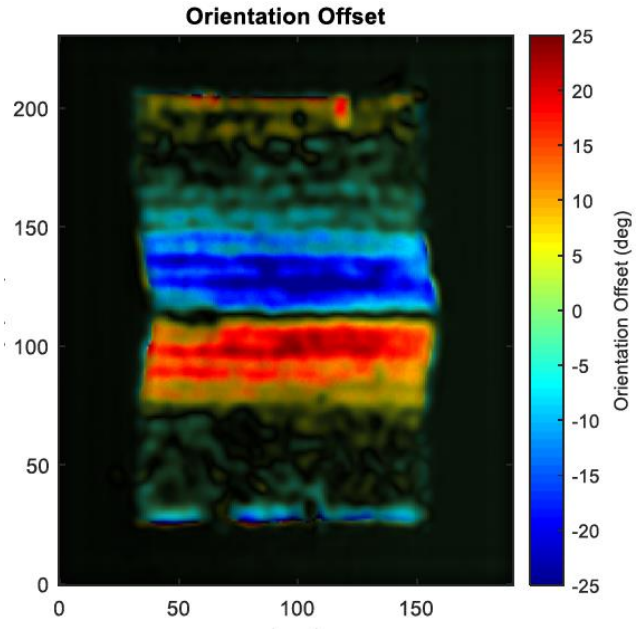


Figure 7.13: SAR image depicting the orientation of the fibres (in degrees) relative to *y*-axis.

the fibres aligned with *y*-axis. Imaging artifacts are again present at the upper and lower edges of the sample, where the fibres were manually cut, resulting in unevenness and fraying. The same does not happen to the lateral edges where the cut is sharper as it follows the direction of the fibres.

The orientation of the fibres is shown in Figure 7.13. The measured rotation angle of the fibres relative to *y*-axis is of $\simeq 25^{\circ}$ in clockwise and anticlockwise direction.

7.3.3 Fibre orientation

The same principle discussed for fibre in-plane waviness can be applied also to the case of fibre misalignment or involuntary variation in the fibre orientation. Therefore, two samples were prepared in the same fashion as what seen in Sections 7.2.1 and 7.2.1, where a bundle of yarns deviates from *y*-axis of a certain degree, red highlighted section in Figure 7.14. The first sample is backed by the aluminium plate only, the second is stacked over another layer of unidirectional fabric with fibre aligned in *y* direction.

Considering the convention adopted for fibre waviness in Section 7.2.2, if the angle between *y*-axis (considered 0°) and the direction of the fibre is due to clockwise rotation, then it will be considered positive. In the case of Figure 7.14, both orientation

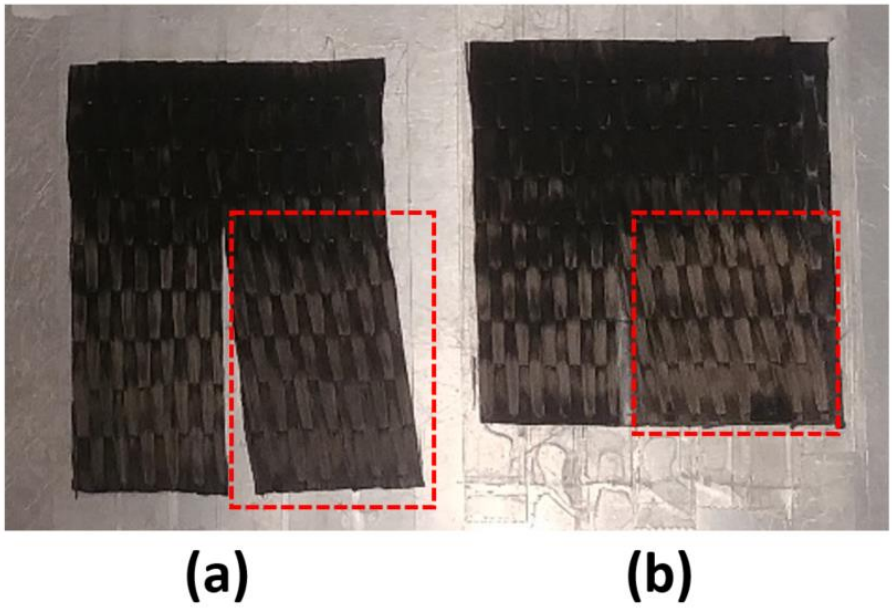


Figure 7.14: Carbon fibre fabric with wrong fibre orientation in the area highlighted in red for: (a) 1 layer of fabric, (b) 2 layers of fabric.

angles are therefore negative.

The scattering parameter S_{VH} is reported in Figure 7.15, while the orientation of the yarns in Figure 7.16. Also in this case, the higher magnitude of the coloured area in the SAR images is an indicator of the "wrong" direction assumed by the yarns. Also in this case, there are high intensity spots near the lower edge of sample (a) and at the upper edge of sample (b), due to the irregularity in the cut. The sample backed by a layer of unidirectional fabric does not show significant differences compared to the one directly fixed onto the aluminium plate. In addition, the SAR imaging technique works also if the deviation from y-axis involves a smaller portion of fibres. An example is given in Figure 7.17, where a small bundle of fibres overlaps the adjacent yarns.

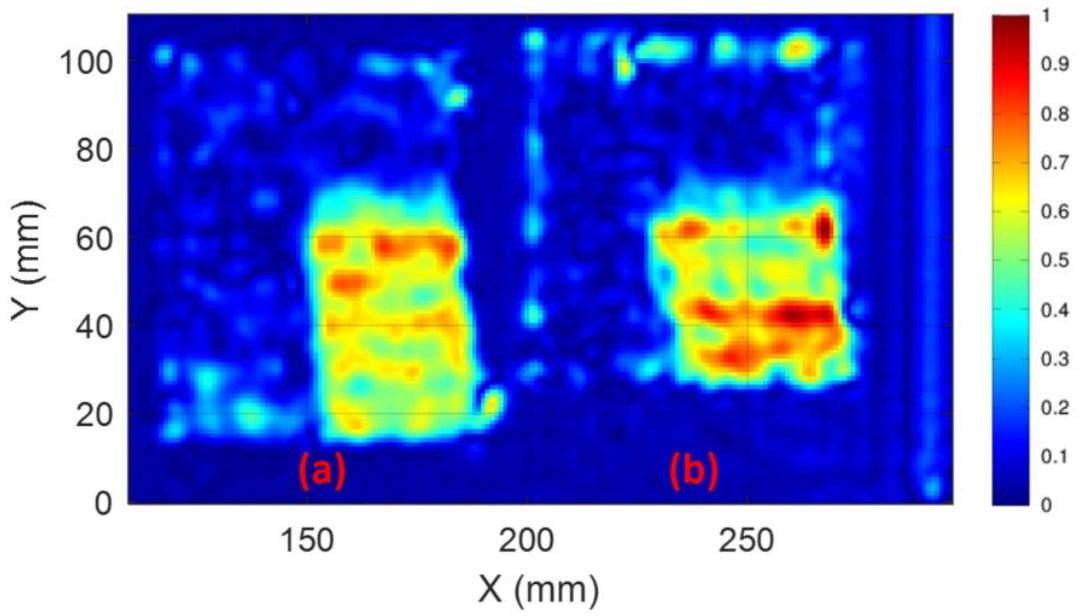


Figure 7.15: : Normalized magnitude of S_{VH} for: (a) 1 layer of fabric, (b) 2 layers of fabric.

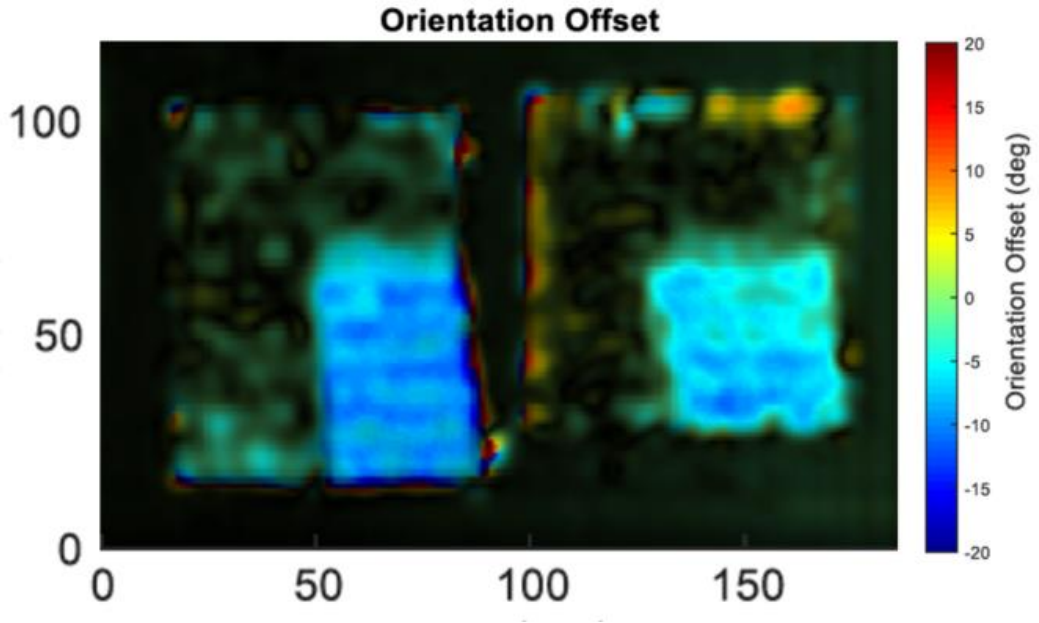


Figure 7.16: SAR images depicting the orientation of the fibres (in degrees) relative to *y*-axis.

7.3.4 Gaps, overlaps, missing tow

As seen in Chapter 1, other common manufacturing defects that can easily arise during AFP/ATL, involve gaps between yarns, overlaps, wrinkling and missing tow. As seen in the previous images, these type of defects can be the direct consequence of incorrect disposition of the fibres (fibre or ply misalignment). For instance, a deviation from the preferred path of the yarns can produce both gaps and overlaps at the same time. In Figure 7.18, a series of samples have been created, each with a specific defect:

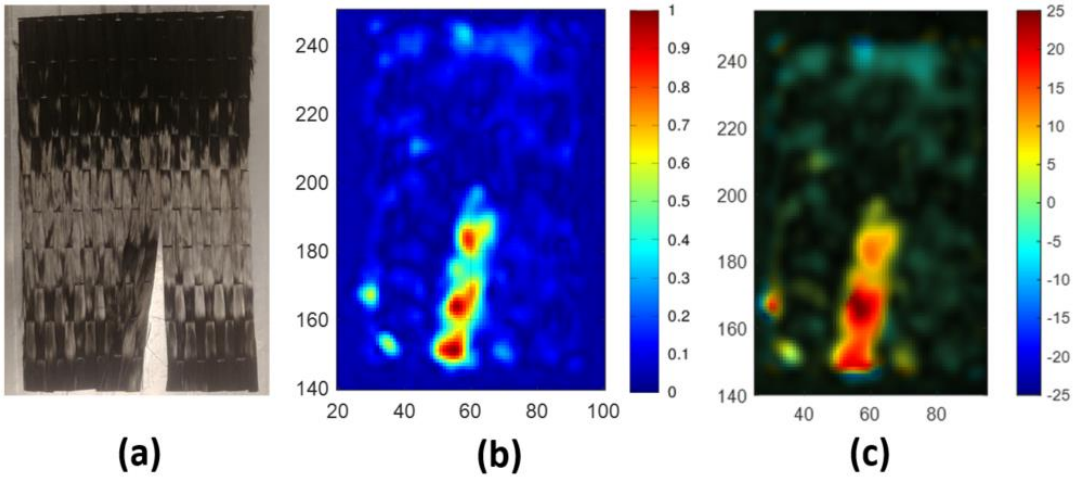


Figure 7.17: (a) sample with overlap, (b) S_{VH} SAR image and (c) SAR image depicting the orientation of the fibres (in degrees) relative to *y*-axis.

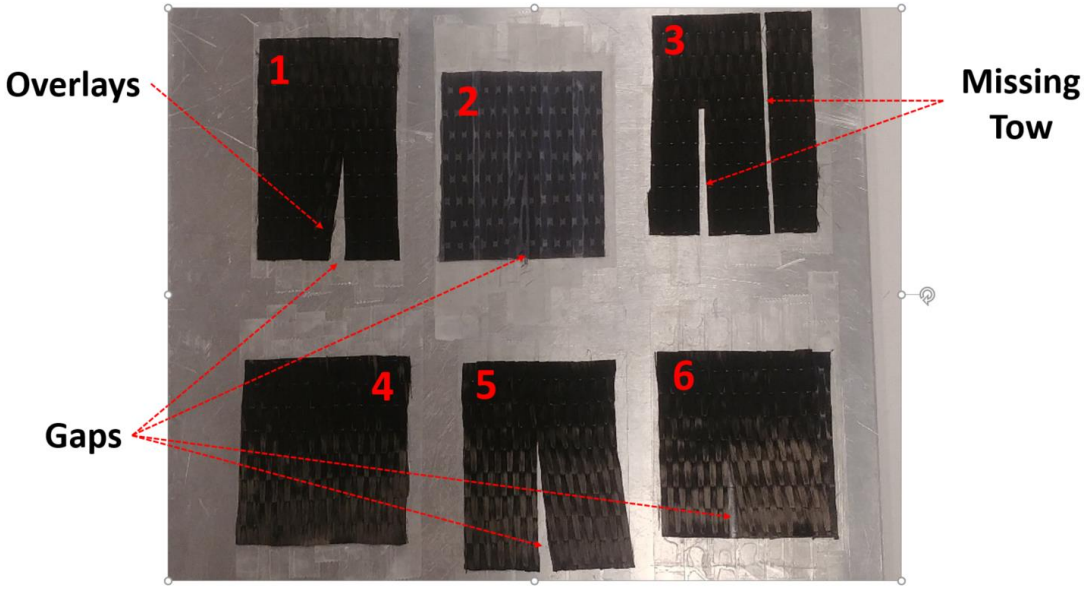


Figure 7.18: Samples with implemented common manufacturing defects that occur during AFP/ATL, such as gaps, overlaps, missing tow, fibre misalignment.

1. Gap and overlap;
2. Gap on top of a layer of UD carbon fibre fabric;
3. Missing tow;
4. Sample made of 2 layers of UD carbon fabric aligned along 0°: 1st layer with in-plane waviness, 2nd layer of "undamaged" UD carbon fibre fabric;
5. Gap and fibre misalignment;
6. Gap and fibre misalignment on top of UD carbon fibre fabric.

The material used is McMASTER unidirectional carbon fabrics P/N 1824N12, and the samples are backed by an aluminium metal plate.

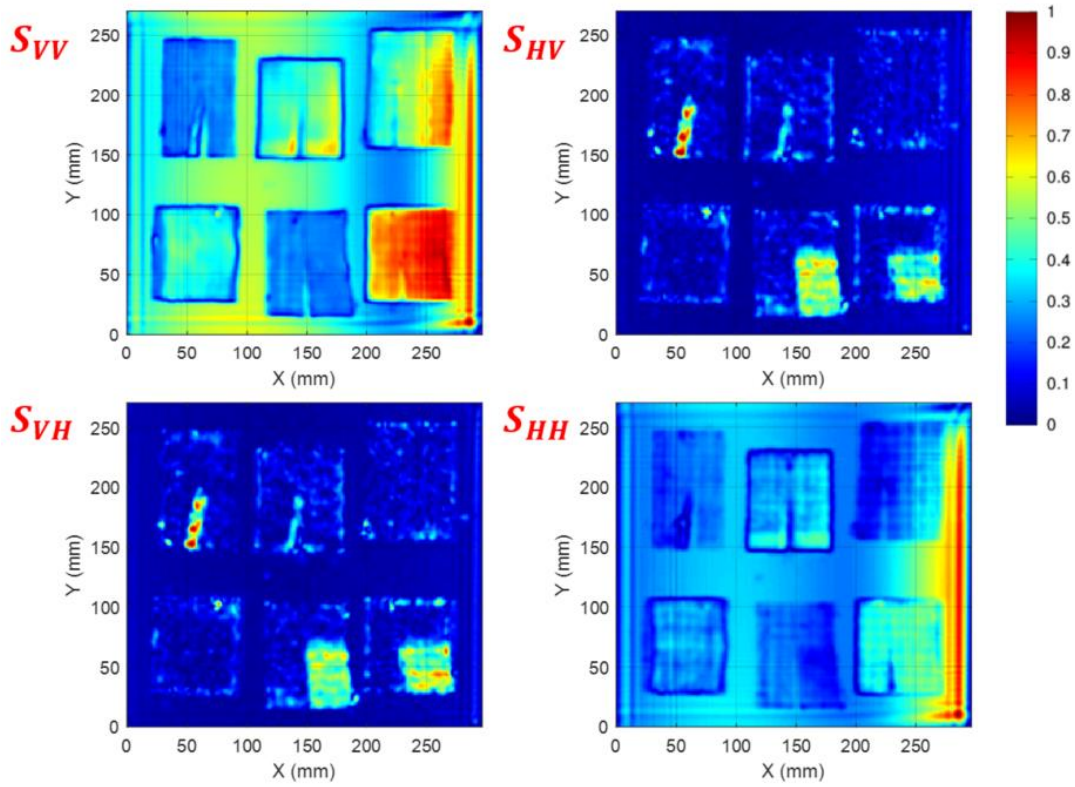


Figure 7.19: Normalized magnitude SAR images of S_{Lin} coefficients.

To characterize these types of defects, the sole use of S_{VH} is not sufficient. As seen in Figure 7.7, the combined use of S_{VV}, S_{HH}, S_{RL}, and S_{LR} can be useful to determine minute thickness variations, which can be found often, for instance, in presence of gaps and overlaps.

Figure 7.19 shows the normalized magnitudes SAR images of the scattering matrix S_{Lin} coefficients. The information on the fibre misalignment is still found within the S_{HV} or S_{VH}, while eventual gaps and overlaps are easily seen on S_{VV} or S_{HH}. However, in the case of sample 3 and 6 the scattered signal has been influenced by the proximity of the aluminium plate edge, i.e., the antenna during the raster scan operation was too close to the edge of the plate (the backing plate is not an ideally infinite plane).

A similar outcome can be observed considering the circularly polarized scattering matrix S_{Circ}. Its scattering parameters are shown in Figure 7.20. The effect provoked by the metal plate edge is present on S_{RL} or S_{LR}.

In conclusion, analysing each sample it is possible to make the following observations:

1. The gap is visible in S_{VV}, S_{LL}, S_{RL}, S_{RL} and S_{RR}, the overlap is visible in S_{VV}, S_{HH}, S_{RL} and S_{LR} (similar conclusion to Figure 7.7);
2. The gap is visible in S_{VV}, S_{HH}, S_{LL}, S_{RL}, S_{RL} and S_{RR}, albeit to a lesser extent;

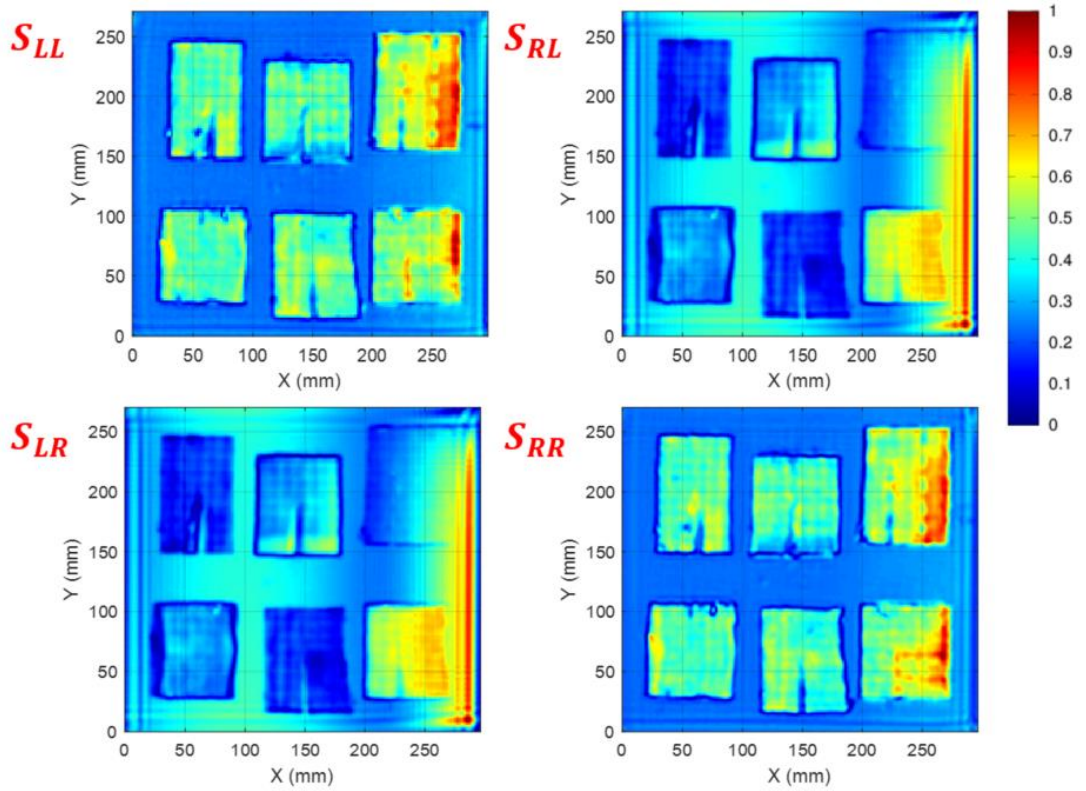


Figure 7.20: Normalized magnitude SAR images of S_{Circ} coefficients.

3. Sample 3 is influenced by the edge effect caused by the interaction of the transmitted signal with the metal plate edge. However, the missing tow can be partially detected through S_{VV}, S_{HH}, S_{RL} and S_{LR};
4. The contour of the first layers appears below the second layer to a certain extent for S_{VV}, S_{HH}, S_{RL} and S_{LR}.
5. The gap is visible in S_{VV}, S_{HH} and S_{Circ} (same findings as Sample 2);
6. The gap is visible in S_{VV}, S_{HH} and S_{Circ} (same findings as Sample 2 and 5).

Given these observations, it is possible to deduce the following:

- Gaps or negative variation of thickness in respect to the surface of the material are visible in S_{VV}, S_{HH} and S_{Circ};
- Overlaps or positive variation of thickness in respect to the surface of the material are visible in S_{VV}, S_{HH}, S_{RL} and S_{LR}.

It is also worth to learn more about what happens in the case of missing tow and hidden fibre waviness. Therefore, two additional samples of bigger dimensions were created to simulate these types of defects, see Figures 7.21 and 7.22. In the first sample, a series of defects such as gaps, missing yarn and round inclusion have been implemented. In the second sample fibre waviness was artificially created on the 1st layer oriented along 0° (y-axis), and then covered by a second layer stacked at 90°.

For the sample of Figure 7.21, the measured S-parameters of interest are reported in Figure 7.23. The information on flaws such as gaps and missing yarn or partially

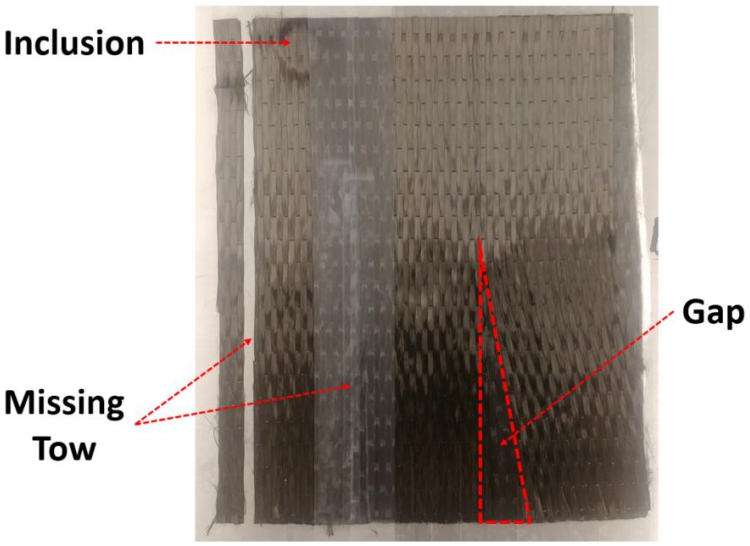


Figure 7.21: Carbon fabric sample with implemented missing tow, inclusion and gap.

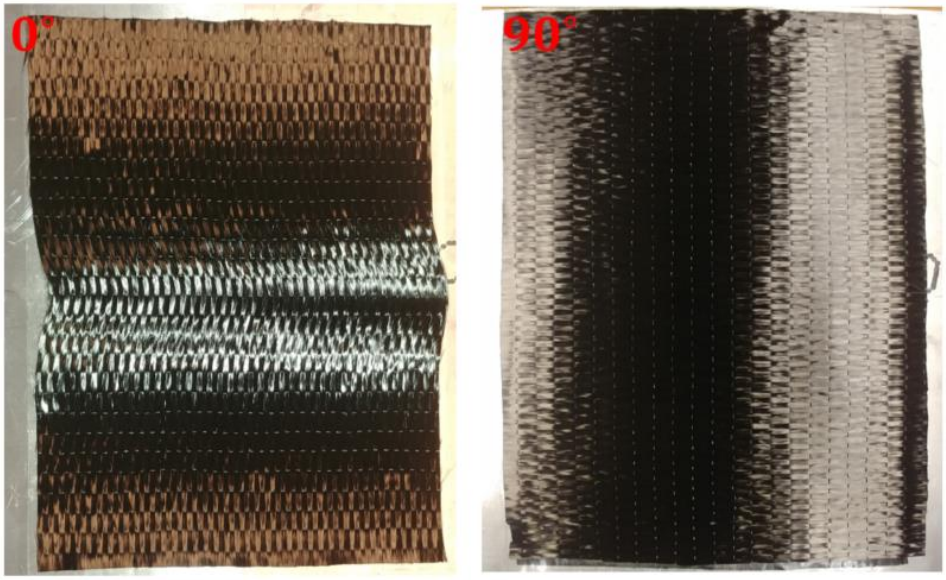


Figure 7.22: Carbon fabric sample with implemented in-plane fibre waviness on the 1st layer oriented along 0°, and covered by 2nd layer stacked at 90°.

missing yarn can be found on the S-parameters S_{VV}, S_{HH}, S_{RL} and S_{LR}. In fact, these types of defects involves surface thickness variation, as previously stated. The identification can be carried out also through the phase or the real or imaginary part of these coefficients. In case of orthogonal linearly-polarized excitation, the best results are obtained when the image corresponds to measurements made with the polarization vector of the transmitting and receiving signals aligned in the same direction. Conversely, in the case of circularly-polarized excitation, the best outputs comes from the "cross-polarized" S-parameters. S_{LR} is not reported in Figure 7.23, however, its results are similar to S_{RL}.

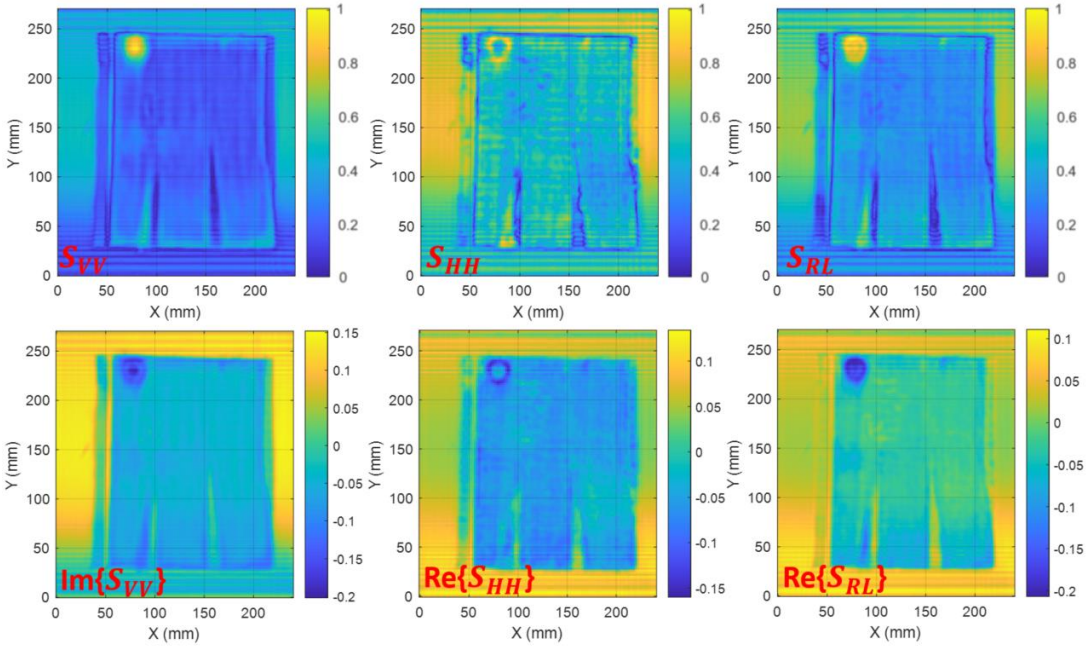


Figure 7.23: S-parameters of interest for the characterization of gaps and missing tow.

As seen in Section 7.2.2, in-plane waviness can be spotted easily reading the S-parameters S_{VH} and S_{HV}. It is of interest, to understand if the same can be done, if the waviness present on a substrate is covered by a layer of carbon fabric or prepreg, choosing a convenient polarization of the exciting signal. As shown in Figures 7.19 and 7.20 for the case of sample 4, the contour of the substrate layer is to some degree visible in S_{VV}, S_{HH}, S_{RL} and S_{LR}. The sample shown in Figure 7.22 is made of two layers with orientation of the fibres perpendicular to each other, i.e., $[0°, 90°]$. Thus, in this particular case, the best results should be obtained when the polarization vector of the transmitting and receiving signals is aligned in the same direction, and specifically along y (S_{VV}). If the transmitted wave is vertically polarized (y-axis), the electric field is perpendicular to the direction of the fibres of the 2nd layer (i.e., top layer), and can penetrate more easily through it. At the same, this type of polarization satisfy the condition of being aligned along the direction of the fibres in the layer displaying the in-plane waviness (polarizing target).

As shown in Figure 7.24, nothing can be detected using the S-parameters S_{VH} and S_{HV}. Figure 7.25 shows that the best results can be obtained using S_{VV} and S_{LR} (or alternatively S_{LR}). Also adopting S_{VV} with the antenna rotated of 45° degrees can be a solution to detect the substrate. The results shows that even though it is possible to define the contour of the substrate layer, the in-plane waviness cannot be detected. However, the purpose of this technique is to be used in real-time application during the manufacturing lay-up process, inspecting each layer as it is deposed. Therefore, this result does not take away the benefits brought by the application of SAR imaging.

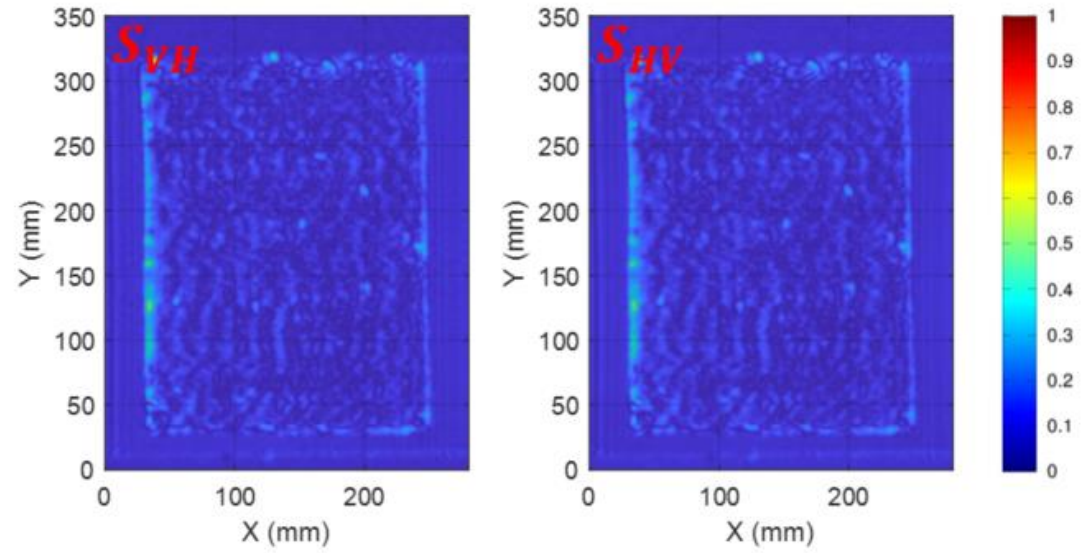


Figure 7.24: Normalized S_{VH} and S_{HV} magnitude SAR image.

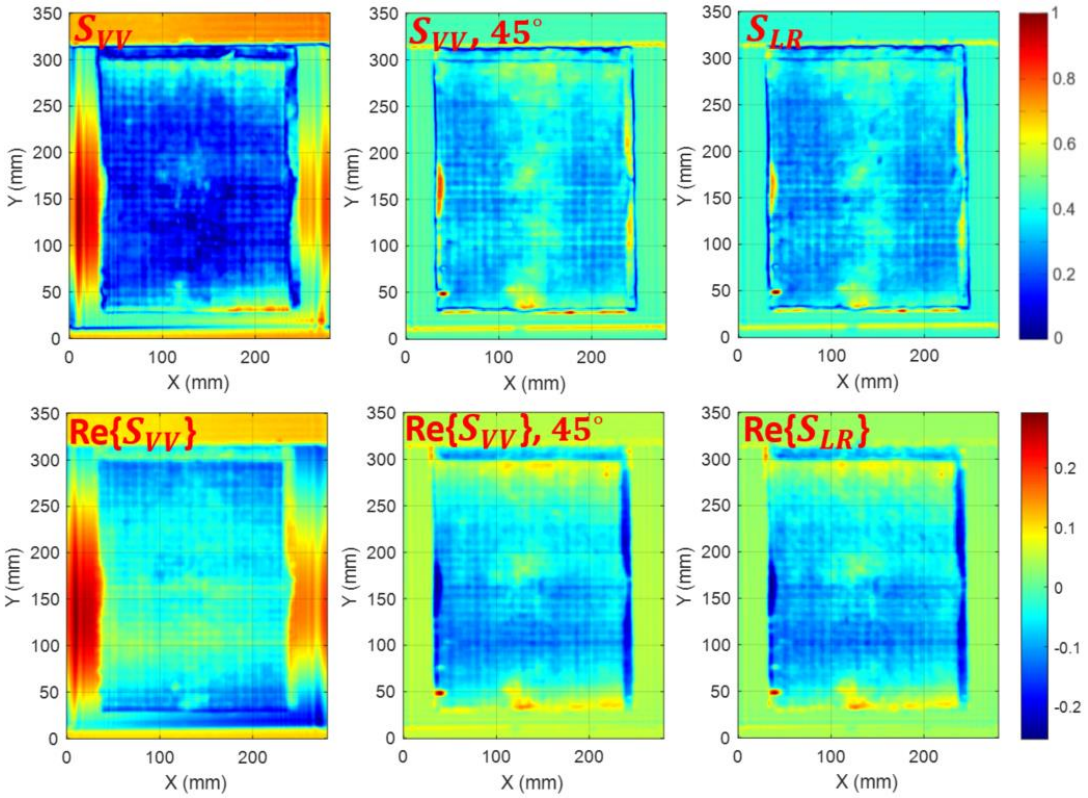


Figure 7.25: SAR image of interest for the characterization of embedded in-plane waviness.

7.3.5 Inclusion

Two CFRP samples with embedded inclusion were scanned over Ka-band. As observed in Figure 7.23, where a round inclusion is inserted between two layers of

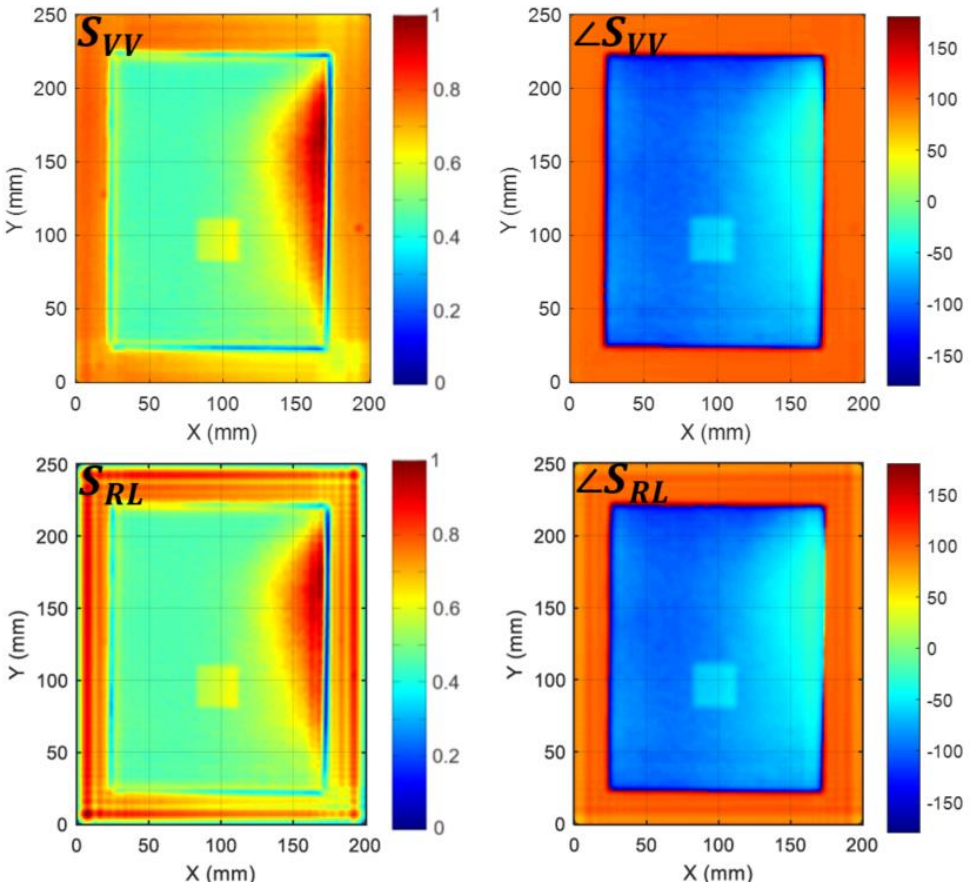


Figure 7.26: SAR images of interest for the characterization of embedded PTFE patch inside a CFRP with discontinuous fibres.

fabric, this type of defect can be spotted using S_{VV} and S_{HH} for linear orthogonal polarization or S_{RL} and S_{LR} for circular right-hand and left-hand polarization. Both these pair of coefficients provide information on minute thickness variation.

Two CFRP sheets were fabricated, made respectively of discontinuous fibres and unidirectional fibres:

4. The first sample was realized stacking 10 layers of Optiveil 20301A 34 g/m^2 alternated with XPREG XA120 prepreg epoxy adhesive film (11 layers of adhesive resin). The carbon veil is composed of discontinuous carbon filaments with length ≃ 6 mm and diameter ≃ 7 μm in a PVA binder. The filaments are uniformly distributed with density of 34 g/m^2. A PTFE patch of 20 mm × 20 mm was inserted between the third and the fourth layer.
5. The second sample is made of 8 layer of continuous UD carbon fibres Pyrofil TR50S 15K with light weight of 100 g/m^2 alternated with the same type of adhesive (9 layers). A free edge delamination was simulated including a PTFE patch of 30 mm × 80 mm between the second and the third layer.

The samples underwent vacuum bagging and were cured in autoclave at 6 bar and 120°C for 1 hour. The samples were scanned at Ka-band with a circularly polarized

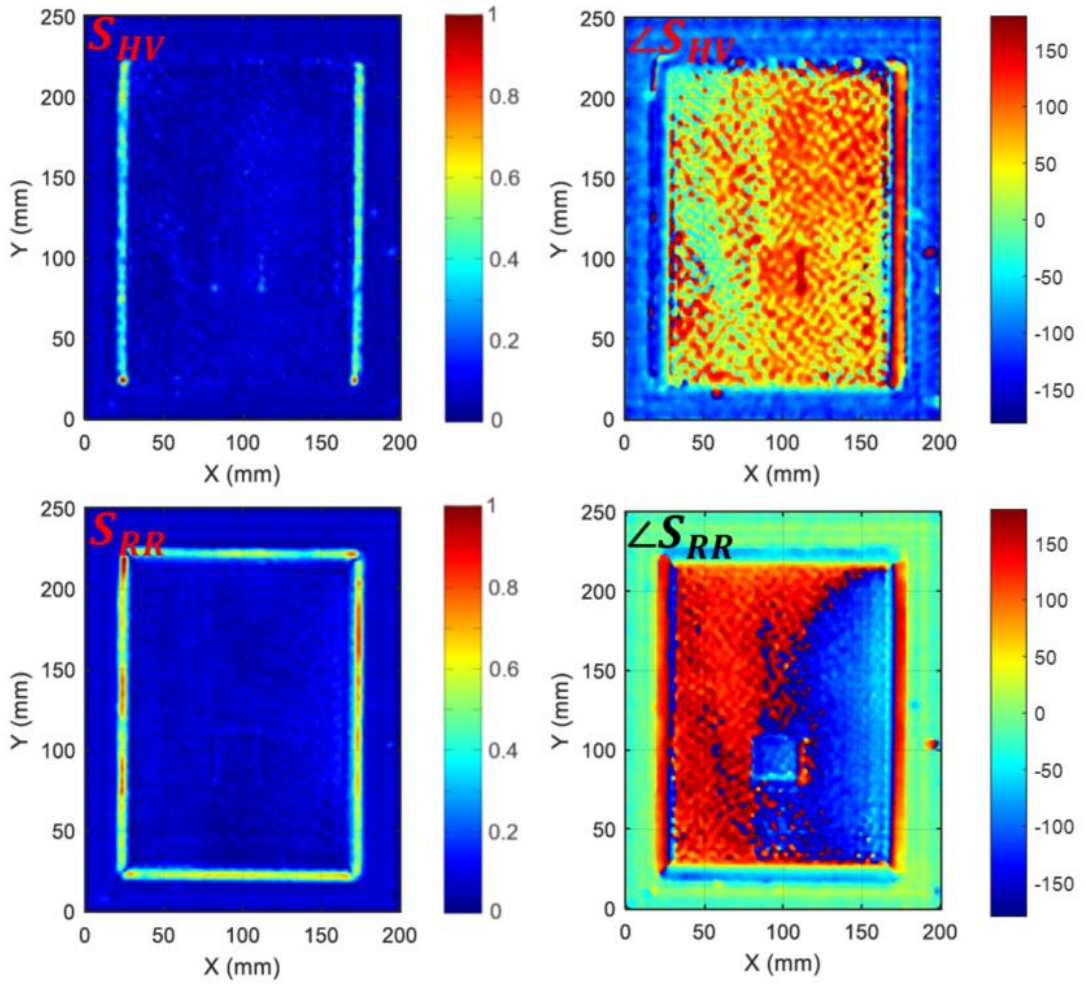


Figure 7.27: Normalized magnitude and phase of S_{HH} and S_{RR} for CFRP with discontinuous fibres.

antenna, with stand-off $z_0 = 20$ mm. The measured scattering parameters of interest are reported in Figures 7.26 and 7.28 for the carbon veil CFRP composite and the unidirectional CFRP, respectively.

A square patch is clearly visible in Figure 7.26 for the first sample. The thickness of the composite is $\simeq 2$ mm and the insertion of the thin PTFE patch produces a changing in thickness locally. The findings confirm that this type of defect can be easily characterized using S_{VV}/S_{HH} or S_{RL}/S_{LR}, which produces very similar SAR images, having the material the same physical properties in x and y direction. Conversely, the information on S_{VH}/S_{HV} or S_{LL}/S_{RR} is not enough to determine clearly the defect, even though it is possible to recognize the shape of the patch, particularly on the phase, as reported in Figure 7.27.

There is evidence of the PTFE patch also in the second sample (see Figure 7.28 and 7.29). However, the signal is non-uniform, as the UD samples is polarized along y-axis. Higher intensity is registered along the vertical section where the patch is inserted. This behaviour can be either represented by a possible delamination in

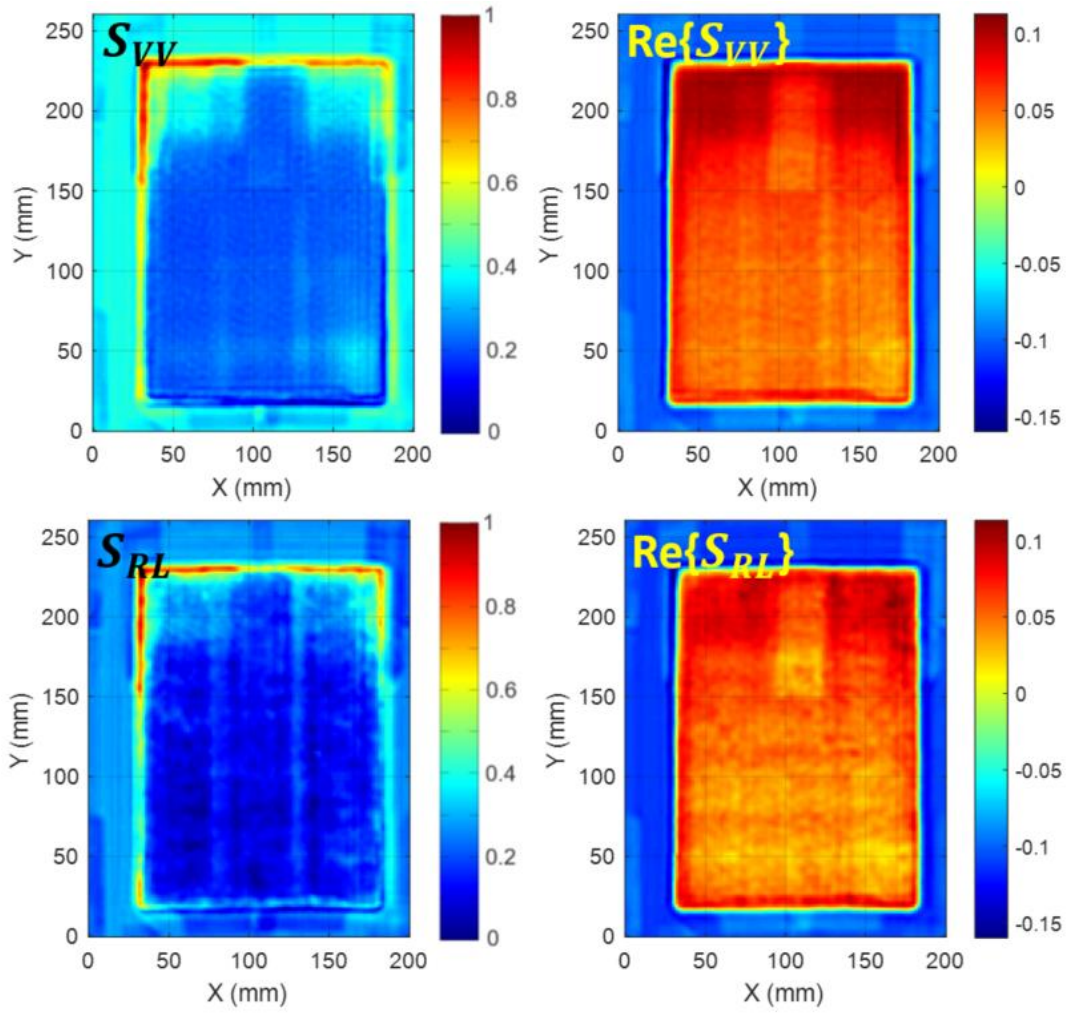


Figure 7.28: Normalized magnitude and real part of S_{VV} and S_{RL} for CFRP with unidirectional continuous fibres.

correspondence of the inserted patch, extending along the y-axis, or the effect produced by the long continuous polarized yarns. The latter does not affect the CFRP

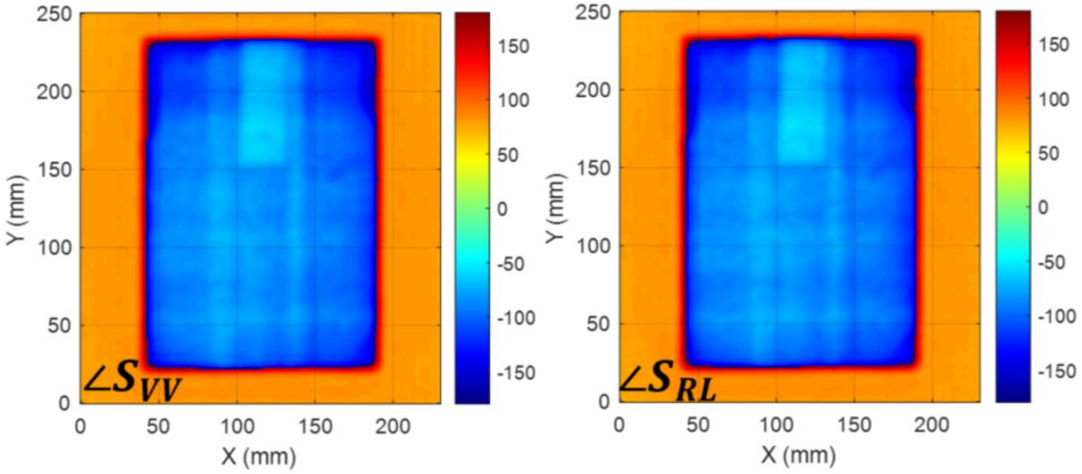


Figure 7.29: Phase of S_{VV} and S_{RL} for CFRP with unidirectional continuous fibres.

made with carbon veil, as the fibres are discontinuous and evenly distributed in *x* and *y* direction.

7.3.6 Out-of-plane fibre waviness

Finally, it is worth to consider SAR polarimetry in the case of out-of-plane waviness. In practice, if out-of-plane waviness were present within a composite laminate, it would be difficult to characterize this defect using SAR imaging, due to the scarce penetration of the signal. However, the same is not true in the case of other composite materials, such as fiberglass. For the latter, although the glass fibres are non-conductive, when they are arranged in a continuous configuration, they can become polarizing targets as well. The sample in Figure 7.30 was prepared with McMASTER unidirectional carbon fabrics 1824N12 and was scanned with the same procedure explained in 7.2.1.
The results are shown in Figure 7.31. These images clearly demonstrate the capability of SAR polarimetry to characterize out-of-plane fibre orientation.



Figure 7.30: CFRP unidirectional fabric sample with out-of-plane fibre waviness.

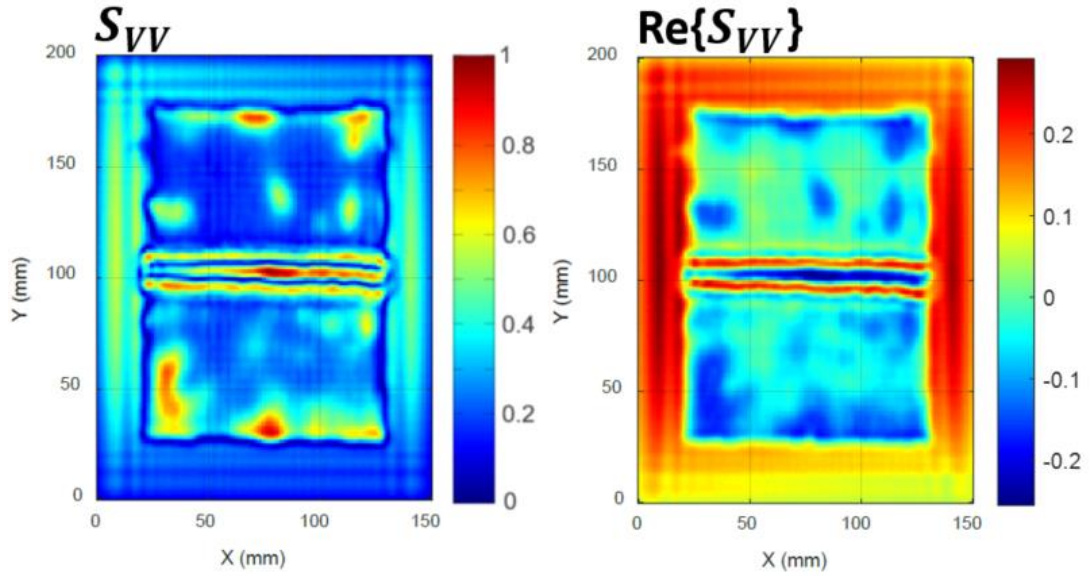


Figure 7.31: SAR images of out-of-plane fibre waviness.

Conclusion and suggestions for further work

The focus of this study has been to improve the methods of characterization of high-loss materials, such as carbon fibre composites. Measurements of high dielectric constant and particularly high-loss factor materials is an important practical issue. However, methods by which to accurately accomplish this are significantly lacking. Composite sheets, having carbon fibre (extensively used in practice), present an additional constraint when using characterization methods which require machining of the sample. Proper sample preparation becomes a significant challenge considering the structure and anisotropy of carbon fibres. Furthermore, carbon fibre composites have represented a limitation to the application of microwave NDT, due to the high conductivity of the fibres, which does not allow signal propagation in the material and, consequently, hinders a volume analysis of the sample. In the following section, an overview of this work's findings and their comparison with other existing techniques is presented. In addition, future possible routes and applications related to this study are considered.

Clamped waveguide method

As extensively explained in Chapter 4, the clamped waveguide method was adopted to overcome the issue of characterization of high lossy materials, such as semiconductors, carbon fiber reinforced composites or carbon nanotube (CNT) composites. The complex permittivity's extraction can be realized using the NRW/Backer-Jarvis without requiring a new theoretical formulation tailored for the geometry of the clamped method. The method itself is completely non-destructive and requires no preparation/machining of the sample. In both numerical simulations and experimental tests, the dielectric constant was closely estimated even for low-loss materials with errors in the same order as those experienced with the completely-filled waveguide technique. The error calculated experimentally does not exceed 4% for a sample with $tan\delta = 0.8$, and it decreases exponentially for greater value of ε_r' and ε_r''. The error on the loss factor, albeit high for low-loss materials, decreases exponentially for materials with higher loss factors. An error in ε_r'' of 11.5% was measured for a sample with $tan\delta = 0.8$. In addition, both errors in ε_r' and ε_r'' are affected by the thickness of the sample and optimal results in the determination of the dielectric properties were found to be associated with small thicknesses (e.g., samples with $tan\delta = 0.6$ showed error of 0.04% for $t < 1$ mm).

Currently, a broadband method with high accuracy for the determination of the complex permittivity of high loss materials represents a challenge. As a matter of fact, non-resonant methods developed so far include open-ended transmission line (rectangular and coaxial probes) [72], [73], free space method [74], [75], and loaded transmission line method [59]. Open-ended probes are employed to measure the reflection coefficient and are particularly useful for non-destructive testing, however, they have the disadvantage of providing only reflection measurement and are affected by air gaps. This technique is not applicable to high-loss materials, being hindered by the high reflection loss of the CFRP. Free space methods allow measurements of both reflection and transmission coefficients, however, a large and flat sample is required, and multiple reflections phenomena occur between the antenna and the surface of sample, as well as diffraction effects at the sample edges making it less accurate compared to the clamped method. Finally, as extensively explained in Chapter 4 and 5, where both methods are compared, the loaded transmission line method gives inaccurate estimation of the complex permittivity of high loss materials, as shown clearly in Figure 5.30. The cause is related to the perfect machining of the sample required for such technique, which can be partially overcome using conductive paste. In addition, it is very important to take into consideration that this technique is destructive compared to the clamped method. On the other hand, resonant methods, i.e. cavity resonators [68], open-ended [223] and planar resonant transmission line [67], can be used for characterization of high-loss materials, however, there are limitations to narrow band frequencies only and limitations on the loss characteristics of the materials that can be measured. Furthermore, precise sample preparation and positioning is required [69], [70], making them destructive.

The non-destructive and easy application of the clamped method is its strong feature. The errors documented in Chapter 4 are due to the NRW/Backer-Jarvis conversion procedure, which does not account for the waveguide discontinuity in the clamped method. This opens the way for further investigation on this research topic. The numerical/experimental validation of this characterization method can be followed by a more accurate mathematical model that specifically accounts for discontinuities, leakage and higher-order modes, in order to obtain a more accurate recalculation of complex permittivity.

The research topic is also pointing out the lack of theoretical approach for the determination of the complex permittivity in composite materials. While this was not the aim of this project, as today, mixing formula and mathematical models able to predict the permittivity of heterogeneous materials composed by conductive elements are still at their initial stage [224].

SAR polarimetry applied to CFRP

The results demonstrated the effectiveness of using a simple cross-polarization measurement to detect surface defects such as:

- Fibre misalignment (e.g., deviation of fibres, in-plane fibre waviness);
- Gaps and overlaps;
- Missing tow;
- Out-of-plane fibre waviness.

The effectiveness of SAR polarimetry is due to the geometrical distribution in continuous yarns of the conductive fibres, particularly in unidirectional laminates, making them perfect polarizing targets and an interesting subject of study for 3D SAR polarimetry.

Chapter 7 shows that it is possible to create accurate electromagnetic images, which are able to spot the typologies of defects mentioned above, with respect to the scattering parameters obtained. Particularly, the combined use of S_{VV}, S_{HH}, S_{RL}, and S_{LR} is useful to determine minute thickness variations, which can be found often, for instance, in presence of gaps and overlaps. On the other hand, the information on the fibre misalignment is found through the S_{HV} or S_{VH} parameters, i.e., when the scattered signal is obtained irradiating the surface of the material with a signal characterized by polarization perpendicular to the received one. The shape and extent of the flaws can be easily recorded through SAR images.

Considering that this method is applicable to the first layers of the CFRP laminate, SAR imaging finds its optimal use in real-time manufacturing inspections, e.g., during automated manufacturing processes such as automated fibre placement (AFP) and automated tape laying (ATL). This would require the manufacturing of a real-time detection tailored probe or array of probes. Therefore, new research applications shall aim to make this method applicable at market/industry level, and to produce standardized procedures for non-destructive testing.

Current industry standard for inspection during AFP/ATL processes is primarily visual/manual. Manual inspection is generally time consuming and requires the presence of highly trained personnel. The traceability of findings is reduced and human factor can be an issue. The time cost of visual/manual inspection and rework is significant, with estimates placing percentage of machine time dedicated to laydown being as low as 24%, and is proportional to the size of the produced part. Therefore, to avoid large cost and time of production, other inspection techniques have been developed [225]:

- Thermographic monitoring: based on a thermal camera combined with image processing that can analyze the visible temperature difference between the laid

tow and the substrate; the images can be difficult to interpret due to different emissivities and reflections from surfaces;

- Profilometry: laser projections onto a surface are used to infer surface features from pattern deviation. However, the accuracy of defect identification and quality of data are affected by the material type;
- Eddy currents: able to provide subsurface data. The defects identification is affected by the size of the defect and some defects such as fold and bridging can be detected but not distinguished from other defects;
- Machine learning: iteration on neural network architectures has produced models able to achieve human or near human levels of performance. A drawback is the large amounts of data required to train the deep object detection algorithms.

As the industry is continuously striving to improve the quality and precision of the detected data and widening detectable defect classes, SAR imaging represents a new opportunity for future market applications and challenges the abovementioned techniques. As demonstrated in Chapter 7, SAR polarimetry is able to:

- Detect with precision most common manufacturing flaws;
- Distinguish among classes of defects;
- Reduce costs and production times, being real-time and easy to apply;
- The training of specialized personnel would not require extensive knowledge;
- Assure traceability of data;
- Be paired with other NDT methods, such as thermography (i.e., microwave thermography) and machine learning.

All of these features would drastically increase the quality of layup.

Lastly, it is of research interest the application of SAR polarimetry for out-of-plane waviness in dielectric composites. This technique can be easily extended to other classes of dielectric composites such as fiberglass, being the glass fibres polarizing targets [226]. In this case, also volume characterization is now possible as the signal propagation is allowed inside the material. Embedded out-of-plane waviness is an example of future application studies of this technique.

List of publications and conferences:

- Munalli, D., Dimitrakis, G., Chronopoulos, D., Greedy, S. and Long, A., 2019. Electromagnetic shielding effectiveness of carbon fibre reinforced composites. Composites Part B: Engineering, 173, p.106906.
- Munalli, D., Al Qaseer, M.T. and Zoughi, R., 2022. Modified Waveguide-Based Method for Microwave Characterization of High-Loss Materials. IEEE Transactions on Instrumentation and Measurement.
- Dvorsky, M., Munalli, D., Al Qaseer, M. T., and Zoughi, R., 2022. Application of Microwave Polarimetry to the Characterization of Fiber Misalignment in Composites. IEEE Open Journal of Instrumentation and Measurement, 1, 1-9.
- Munalli, D., Chronopoulos, D. and Greedy, S., 2018. Electromagnetic shielding effectiveness of fiber-reinforced composites: a preliminary study.
- Munalli, D., Dimitrakis, G., Chronopoulos, D., Greedy, S. and Long, A., 2019, November. The use of free-space microwave non-destructive techniques: simulation of damage detection in carbon fibre reinforced composites. In *11 th Symposium on NDT in Aerospace, Saclay* (pp. 1-10).

Bibliography

[1] J. M. Corum, R. L. Battiste, K. C. Liu, and M. B. Ruggles, “Basic Properties of Reference Crossply Carbon-Fiber Composite,” 2000. doi: 10.2172/777662.

[2] P. D. Mangalgiri, “Composite materials for aerospace applications,” *Bull. Mater. Sci.*, vol. 22, no. No. 3, pp. 657–664, 1999, doi: 10.1088/1755-1315/166/1/012006.

[3] B. T. C. Miller, M. J. Chajes, D. R. Mertz, J. N. Hastings, and S. Member, “STRENGTHENING OF A STEEL BRIDGE GIRDER USING CFRP PLATES,” *J. Bridg. Eng.*, vol. 6, no. 6, pp. 514–522, 2001, doi: 10.1061/(ASCE)1084-0702(2001)6.

[4] M. A. Muflikhun, T. Yokozeki, and T. Aoki, “The strain performance of thin CFRP-SPCC hybrid laminates for automobile structures,” *Compos. Struct.*, vol. 220, no. September 2018, pp. 11–18, 2019, doi: 10.1016/j.compstruct.2019.03.094.

[5] F. Ahmad, J. W. Hong, H. S. Choi, and M. K. Park, “Hygro effects on the low-velocity impact behavior of unidirectional CFRP composite plates for aircraft applications,” *Compos. Struct.*, vol. 135, pp. 276–285, 2016, doi: 10.1016/j.compstruct.2015.09.040.

[6] J. Pora and B. Cedex, “Composite Materials in the Airbus A380 - From History to Future -,” pp. 1–10.

[7] R. Schutze and H. C. Goetting, “Development of adaptive CFRP struts for vibration suppression in high-loaded lightweight structures,” *Spacecr. Struct. Mater. Mech. Eng.*, vol. 386, pp. 199–205, 1996.

[8] A. Fink, P. P. Camanho, J. M. Andrés, E. Pfeiffer, and A. Obst, “Hybrid CFRP/titanium bolted joints: Performance assessment and application to a spacecraft payload adaptor,” *Compos. Sci. Technol.*, vol. 70, no. 2, pp. 305–317, 2010, doi: 10.1016/j.compscitech.2009.11.002.

[9] A. Francesconi, C. Giacomuzzo, S. Kibe, Y. Nagao, and M. Higashide, “Effects of high-speed impacts on CFRP plates for space applications,” *Adv. Sp. Res.*, vol. 50, no. 5, pp. 539–548, 2012, doi: 10.1016/j.asr.2012.05.012.

[10] D. Gay and S. V Hoa, *Composite materials: design and applications*. CRC press, 2007.

[11] J. Cao *et al.*, “Characterization of mechanical behavior of woven fabrics: Experimental methods and benchmark results,” *Compos. Part A Appl. Sci. Manuf.*, vol. 39, no. 6, pp. 1037–1053, 2008, doi: 10.1016/j.compositesa.2008.02.016.

[12] D. From, “Improvements Embedding in Epoxy Resin Methods,” *Machinery*, vol. 4, no. From the Department of Anatomy, University of Washington, Seattle, pp. 409–414, 1961.

[13] M. Altin Karataş and H. Gökkaya, “A review on machinability of carbon fiber reinforced polymer (CFRP) and glass fiber reinforced polymer (GFRP) composite materials,” *Def. Technol.*, vol. 14, no. 4, pp. 318–326, 2018, doi: 10.1016/j.dt.2018.02.001.

[14] A. Hammami, R. Gauvin, F. Trochu, O. Touret, and P. Ferland, “Analysis of the Edge Effect on Flow Patterns in Liquid Composites Molding,” *Appl. Compos. Mater.*, vol. 5, no. 3, pp. 161–173, 1998, doi: 10.1023/A:1008887400832.

[15] A. Hammami, R. Gauvin, and F. Trochu, “Modeling the edge effect in liquid composites molding,” *Compos. Part A Appl. Sci. Manuf.*, vol. 29, no. 5–6, pp. 603–609, 1998, doi: 10.1016/S1359-835X(97)00120-6.

[16] M. K. O. Kang and W. O. O. I. L. Lee, “Analysis of Resin Transfer/Compression Molding Process,” *Polym. Compos.*, vol. 20, no. 2, pp. 293–304, 1999.

[17] K. Yassin and M. Hojjati, “Processing of thermoplastic matrix composites through automated fiber placement and tape laying methods: A review,” *J. Thermoplast. Compos. Mater.*, vol. 31, no. 12, pp. 1676–1725, 2018, doi: 10.1177/0892705717738305.

[18] S. T. Peters, *Composite filament winding*. ASM International, 2011.

[19] D. Munalli, G. Dimitrakis, D. Chronopoulos, S. Greedy, and A. Long, “The use of free-space microwave non-destructive techniques_ simulation of damage detection in carbon fibre reinforced composites,” *Conf. Proc. 11th Symp. NDT Aerosp.*, pp. 1–10, 2019.

[20] W. F. Smith, “Principles of materials science and engineering,” 1986.

[21] F. Heinecke and C. Willberg, “Manufacturing-induced imperfections in composite parts manufactured via automated fiber placement,” *J. Compos. Sci.*, vol. 3, no. 2, pp. 1–24, 2019, doi: 10.3390/jcs3020056.

[22] S. Sun, Z. Han, H. Fu, H. Jin, J. S. Dhupia, and Y. Wang, “Defect characteristics and online detection techniques during manufacturing of FRPs using automated fiber placement: A review,” *Polymers (Basel).*, vol. 12, no. 6, p. 1337, 2020.

[23] A. Sawicki and P. Minguett, “The effect of intraply overlaps and gaps upon the compression strength of composite laminates,” in *39th AIAA/ASME/ASCE/AHS/ASC Structures, Structural Dynamics, and Materials Conference and Exhibit*, 1998, p. 1786.

[24] A. Sawicki, E. Schulze, L. R. Fitzwater, and K. Harris, “Structural qualification of V-22 EMD tow-placed aft fuselage,” in *ANNUAL FORUM PROCEEDINGS-AMERICAN HELICOPTER SOCIETY*, 1995, vol. 51, p. 1641.

[25] P. Kulkarni, K. D. Mali, and S. Singh, “An overview of the formation of fibre waviness and its effect on the mechanical performance of fibre reinforced polymer composites,” *Compos. Part A Appl. Sci. Manuf.*, vol. 137, no. May, p. 106013, 2020, doi: 10.1016/j.compositesa.2020.106013.

[26] P. Kulkarni, K. D. Mali, and S. Singh, “An overview of the formation of fibre waviness and its effect on the mechanical performance of fibre reinforced polymer composites,” *Compos. Part A Appl. Sci. Manuf.*, vol. 137, no. May, p. 106013, 2020, doi: 10.1016/j.compositesa.2020.106013.

[27] M. P. De Goeje and K. E. D. Wapenaar, “Non-destructive inspection of carbon fibre-reinforced plastics using eddy current methods,” *Composites*, vol. 23, no. 3, pp. 147–157, 1992.

[28] T. Aastroem, “From fifteen to two hundred NDT-methods in fifty years,” in *17th World Conference on Nondestructive Testing*, 2008, pp. 25–28.

[29] M. R. Jolly *et al.*, “Review of non-destructive testing (NDT) techniques and their applicability to thick walled composites,” *Procedia CIRP*, vol. 38, pp. 129–136, 2015.

[30] F. A. A. (FAA), *Aviation Maintenance Technician Handbook-General: FAA-H-8083-30*. Aviation Supplies & Academics, Incorporated, 2008.

[31] A. Circular, “Acceptable Methods, Techniques, and Practices–Aircraft Inspections and Repair,” *Vol. FAA Circ. AC*, 1998.

[32] M. Trimm, “An overview of nondestructive evaluation methods,” *Pract. Fail. Anal.*,

vol. 3, no. 3, pp. 17–31, 2003.

[33] J. Cheng, J. Qiu, H. Ji, E. Wang, T. Takagi, and T. Uchimoto, “Application of low frequency ECT method in noncontact detection and visualization of CFRP material,” *Compos. Part B Eng.*, vol. 110, pp. 141–152, 2017.

[34] J. Summerscales, *Non-destructive testing of fibre-reinforced plastics composites*, vol. 2. Springer Science & Business Media, 1990.

[35] V. Dattoma, R. Marcuccio, C. Pappalettere, and G. M. Smith, “Thermographic investigation of sandwich structure made of composite material,” *NDT E Int.*, vol. 34, no. 8, pp. 515–520, 2001.

[36] S. Gholizadeh, “A review of non-destructive testing methods of composite materials,” *Procedia Struct. Integr.*, vol. 1, pp. 50–57, 2016.

[37] M. E. Ibrahim, “Nondestructive evaluation of thick-section composites and sandwich structures: A review,” *Compos. Part A Appl. Sci. Manuf.*, vol. 64, pp. 36–48, 2014.

[38] C. Soutis, “Fibre reinforced composites in aircraft construction,” *Prog. Aerosp. Sci.*, vol. 41, no. 2, pp. 143–151, 2005, doi: 10.1016/j.paerosci.2005.02.004.

[39] S. Kharkovsky and R. Zoughi, “Microwave and millimeter wave nondestructive testing and evaluation-Overview and recent advances,” *IEEE Instrum. Meas. Mag.*, vol. 10, no. 2, pp. 26–38, 2007.

[40] J. Blitz, *Electrical and magnetic methods of non-destructive testing*. Springer Science & Business Media, 2012.

[41] J. D. Jackson, “Classical electrodynamics.” American Association of Physics Teachers, 1999.

[42] A. Amiet and P. Jewsbury, “Free space microwave permittivity and permeability measurements,” *Asia-Pacific Microw. Conf. Proceedings, APMC*, no. November, p. 13, 2000, doi: 10.1109/apmc.2000.925852.

[43] B. Lambert, “Dielectric Spectroscopy,” 2006. .

[44] L.-F. Chen, C. K. Ong, C. P. Neo, V. V Varadan, and V. K. Varadan, *Microwave electronics: measurement and materials characterization*. John Wiley & Sons, 2004.

[45] D. Munalli, G. Dimitrakis, D. Chronopoulos, S. Greedy, and A. Long, “Electromagnetic shielding effectiveness of carbon fibre reinforced composites,” *Compos. Part B Eng.*, vol. 173, 2019, doi: 10.1016/j.compositesb.2019.106906.

[46] D. Munalli, D. Chronopoulos, and S. Greedy, “Electromagnetic shielding effectiveness of fiber-reinforced composites: A preliminary study,” *9th Eur. Work. Struct. Heal. Monit. EWSHM 2018*, pp. 1–12, 2018.

[47] L. Jylhä and A. Sihvola, “Equation for the effective permittivity of particle-filled composites for material design applications,” *J. Phys. D. Appl. Phys.*, vol. 40, no. 16, pp. 4966–4973, 2007, doi: 10.1088/0022-3727/40/16/032.

[48] Z. Li, A. Haigh, C. Soutis, and A. Gibson, “X-band microwave characterisation and analysis of carbon fibre-reinforced polymer composites,” *Compos. Struct.*, vol. 208, no. October 2018, pp. 224–232, 2019, doi: 10.1016/j.compstruct.2018.09.099.

[49] W. B. Westphal and A. Sils, *Dielectric constant and loss data*, Vol. 72, N. Air Force Materials Laboratory, Air Force Systems Command, 1972.

[50] “MatWeb.” http://www.matweb.com/search/QuickText.aspx.

[51] Y. C. Shin, E. Novin, and H. Kim, “Electrical and thermal conductivities of carbon fiber composites with high concentrations of carbon nanotubes,” *Int. J. Precis. Eng. Manuf.*, vol. 16, no. 3, pp. 465–470, 2015, doi: 10.1007/s12541-015-0063-8.

[52] “MatWeb.” .

[53] D. Balageas, C. P. Fritzen, and A. Guemes, *Structural health monitoring*, Vol. 90. John Wiley & Sons, 2010.

[54] P. Banerjee and J. L. Schmidt, “Electrical conductivity modeling and validation in unidirectional carbon fiber reinforced polymer composites,” 2013.

[55] R. D. Chippendale and I. O. Golosnoy, “Percolation effects in electrical conductivity of carbon fibre composites,” in *IET 8th International Conference on Computation in Electromagnetics (CEM 2011)*, 2011, pp. 1–2.

[56] A. B. Constantine, *Antenna theory: analysis and design*. Wiley-Interscience, 2005.

[57] R. Zoughi, *Microwave non-destructive testing and evaluation principles*, vol. 4. Springer Science & Business Media, 2000.

[58] Y. Wang and M. N. Afsar, “Measurement of complex permittivity of liquids using waveguide techniques,” *Prog. Electromagn. Res.*, vol. 42, pp. 131–142, 2003, doi: 10.2528/PIER03010602.

[59] R. Zoughi *et al.*, “Microwave dielectric properties and Targeted heating of polypropylene nano-composites containing carbon nanotubes and carbon black,” *Polymer (Guildf).*, vol. 179, p. 121658, 2019, doi: 10.1016/j.polymer.2019.121658.

[60] S. Clerjon and J. L. Damez, “Microwave sensing for an objective evaluation of meat ageing,” *J. Food Eng.*, vol. 94, no. 3–4, pp. 379–389, 2009, doi: 10.1016/j.jfoodeng.2009.04.004.

[61] A. Hashemi, K. E. Kurtis, K. M. Donnell, and R. Zoughi, “Empirical multiphase dielectric mixing model for cement-based materials containing alkali-silica reaction gel,” *IEEE Trans. Instrum. Meas.*, vol. 66, no. 9, pp. 2428–2436, 2017, doi: 10.1109/TIM.2017.2707927.

[62] S. Trabelsi, A. W. Kraszewski, and S. O. Nelson, “Nondestructive microwave characterization for determining the bulk density and moisture content of shelled corn,” *Meas. Sci. Technol.*, vol. 9, no. 9, pp. 1548–1556, 1998, doi: 10.1088/0957-0233/9/9/026.

[63] K. J. Bois, A. D. Benally, P. S. Nowak, and R. Zoughi, “Cure-state monitoring and water-to-cement ratio determination of fresh portland cement-based materials using near-field microwave techniques,” *IEEE Trans. Instrum. Meas.*, vol. 47, no. 3, pp. 628–637, 1998, doi: 10.1109/19.744313.

[64] S. S. Yoon, J. W. Lee, T. K. Lee, and J. H. Roh, “Insensitivity Characteristics in the Dual Polarization of Deployable CFRP Reflector Antennas for SAR,” *IEEE Trans. Antennas Propag.*, vol. 66, no. 1, pp. 88–95, 2018, doi: 10.1109/TAP.2017.2772315.

[65] M. Ghasr, S. Kharkovsky, R. Zoughi, and R. Austin, “Comparison of near-field millimeter wave probes for detecting corrosion pit under paint,” *IEEE Trans. Instrum. Meas.*, vol. 54, no. 4, pp. 1497–1504, 2005, doi: 10.1109/TIM.2005.851086.

[66] B. Akuthota, D. Hughes, R. Zoughi, J. Myers, and A. Nanni, “Near-Field Microwave Detection of Disbond in Carbon Fiber Reinforced Polymer Composites Used for Strengthening Cement-Based Structures and Disbond Repair Verification,” *J. Mater. Civ. Eng.*, vol. 16, no. 6, pp. 540–546, 2004, doi: 10.1061/(asce)0899-

1561(2004)16:6(540).

[67] K. T. Muhammed Shafi, A. K. Jha, and M. J. Akhtar, “Improved Planar Resonant RF Sensor for Retrieval of Permittivity and Permeability of Materials,” *IEEE Sens. J.*, vol. 17, no. 17, pp. 5479–5486, 2017, doi: 10.1109/JSEN.2017.2724942.

[68] J. Sheen, “Microwave measurements of dielectric properties using a closed cylindrical cavity dielectric resonator,” *IEEE Trans. Dielectr. Electr. Insul.*, vol. 14, no. 5, pp. 1139–1144, 2007, doi: 10.1109/TDEI.2007.4339473.

[69] U. C. Hasar, “A generalized formulation for permittivity extraction of low-to-high-loss materials from transmission measurement,” *IEEE Trans. Microw. Theory Tech.*, vol. 58, no. 2, pp. 411–418, 2010, doi: 10.1109/TMTT.2009.2038443.

[70] V. N. Egorov, *Resonance methods for microwave studies of dielectrics (Review)*, vol. 50, no. 2. 2007.

[71] K. J. Bois, L. F. Handjojo, A. D. Benally, K. Mubarak, and R. Zoughi, “Dielectric plug-loaded two-port transmission line measurement technique for dielectric property characterization of granular and liquid materials,” *IEEE Trans. Instrum. Meas.*, vol. 48, no. 6, pp. 1141–1148, 1999, doi: 10.1109/19.816128.

[72] S. Ganchev, N. Qaddoumi, and R. Zoughi, “Detection optimization of disbond in layered composites with varying thicknesses using an open-ended rectangular waveguide,” *CPEM Dig. Conf. Precis. Electromagn. Meas.*, pp. 69–70, 1994, doi: 10.1109/cpem.1994.333287.

[73] S. Bakhtiari, S. I. Ganchev, and R. Zoughi, “Analysis of Radiation from an Open-Ended Coaxial Line into Stratified Dielectrics,” *IEEE Trans. Microw. Theory Tech.*, vol. 42, no. 7, pp. 1261–1267, 1994, doi: 10.1109/22.299765.

[74] D. K. Ghodgaonkar, V. V. Varadan, and V. K. Varadan, “A Free-Space Method for Measurement of Dielectric Constants and Loss Tangents at Microwave Frequencies,” *IEEE Trans. Instrum. Meas.*, vol. 38, no. 3, pp. 789–793, 1989, doi: 10.1109/19.32194.

[75] D. K. Ghodgaonkar, V. V. Varadan, and V. K. Varadan, “Free-Space Measurement of Complex Permittivity and Complex Permeability of Magnetic Materials at Microwave Frequencies,” *IEEE Trans. Instrum. Meas.*, vol. 39, no. 2, pp. 387–394, 1990, doi: 10.1109/19.52520.

[76] D. K. Ghodgaonkar, N. A. Ali, and L. Giubbolini, “Microwave nondestructive testing of composite materials using free-space microwave measurement techniques,” in *15th World Conference on Non-Destructive Testing*, 2000, pp. 15–21.

[77] J. Baker-Jarvis, B. Jones, M. Janezic, R. G. Geyer, J. H. Grosvenor, and C. M. Weil, “Dielectric and magnetic measurements: A survey of nondestructive, quasi-nondestructive, and process-control techniques,” *Res. Nondestruct. Eval.*, vol. 7, no. 2–3, pp. 117–136, 1995, doi: 10.1080/09349849509409572.

[78] K. C. Yaw, “Measurement of dielectric material properties,” *Application Note. Rohde & Schwarz*. pp. 1–35, 2012.

[79] J. Baker-Jarvis, E. J. Vanzura, and W. A. Kissick, “Improved technique for determining complex permittivity with the transmission/reflection method,” *IEEE Trans. Microw. Theory Tech.*, vol. 38, no. 8, pp. 1096–1103, 1990, doi: 10.1109/22.57336.

[80] W. B. Weir, “Automatic Measurement of Complex Dielectric Constant and Permeability at Microwave Frequencies,” *Proc. IEEE*, vol. 62, no. 1, pp. 33–36, 1974, doi: 10.1109/PROC.1974.9382.

[81] T. C. Williams, M. A. Stuchly, and P. Saville, “Modified transmission-reflection method for measuring constitutive parameters of thin flexible high-loss materials,” *IEEE Trans. Microw. Theory Tech.*, vol. 51, no. 5, pp. 1560–1566, 2003, doi: 10.1109/TMTT.2003.810139.

[82] Z. Li, A. Haigh, C. Soutis, A. Gibson, and R. Sloan, “Dielectric constant of a three-dimensional woven glass fibre composite: Analysis and measurement,” *Compos. Struct.*, vol. 180, pp. 853–861, 2017, doi: 10.1016/j.compstruct.2017.08.061.

[83] L. Handjojo a, K. J. Bois a, J. Bauer b, R. Hamilton b, and R. Zoughi a, “Broad-band lVIICROWAVE dielectric property characterization and nondestructive inspection of various glass specimens,” *Nondestruct. Test. Eval.*, vol. 16, no. 1, pp. 55–69, 2000.

[84] R. Zoughi, *Microwave N on-Destructive Testing and Evaluation*. 2000.

[85] S. Trabelsi, A. W. Kraszewski, and S. O. Nelson, “Simultaneous determination of density and water content of particulate materials by microwave sensors,” *Electron. Lett.*, vol. 33, no. 10, pp. 874–876, 1997.

[86] S. Trabelsi, A. W. Krazsewski, and S. O. Nelson, “Unified calibration method for nondestructive dielectric sensing of moisture content in granular materials,” *Electron. Lett.*, vol. 35, no. 16, pp. 1346–1347, 1999.

[87] S. Trabelsi, A. W. Kraszewski, and S. O. Nelson, “New calibration technique for microwave moisture sensors,” *IEEE Trans. Instrum. Meas.*, vol. 50, no. 4, pp. 877–881, 2001.

[88] S. Bakhtiari and R. Zoughi, “Microwave thickness measurement of lossy layered dielectric slabs using incoherent reflectivity,” *Res. Nondestruct. Eval.*, vol. 2, no. 3, pp. 157–168, 1990.

[89] S. Bakhtiari, S. I. Ganchev, and R. Zoughi, “Open-ended rectangular waveguide for nondestructive thickness measurement and variation detection of lossy dielectric slabs backed by a conducting plate,” *IEEE Trans. Instrum. Meas.*, vol. 42, no. 1, pp. 19–24, 1993.

[90] K. J. Bois, A. Benally, P. S. Nowak, and R. Zoughi, “Microwave nondestructive determination of sand-to-cement ratio in mortar,” *Res. Nondestruct. Eval.*, vol. 9, no. 4, pp. 227–238, 1997, doi: 10.1080/09349849709414476.

[91] S. I. Ganchev, S. Bakhtiari, N. Qaddoumi, D. Brandenburg, and R. Zoughi, “Microwave Diagnosis of Rubber Compounds,” *IEEE Trans. Microw. Theory Tech.*, vol. 42, no. 1, pp. 18–24, 1994, doi: 10.1109/22.265523.

[92] S. I. Ganchev, N. Qaddoumi, E. Ranu, and R. Zoughi, “Microwave Detection Optimization of Disbond in Layered Dielectrics with Varying Thickness,” *IEEE Trans. Instrum. Meas.*, vol. 44, no. 2, pp. 326–328, 1995, doi: 10.1109/19.377843.

[93] S. Bakhtiari, N. Qaddoumi, S. I. Ganchev, and R. Zoughi, “Microwave noncontact examination of disbond and thickness variation in stratified composite media,” *IEEE Trans. Microw. Theory Tech.*, vol. 42, no. 3, pp. 389–395, 1994.

[94] S. Gray, S. Ganchev, N. Qaddoumi, G. Beauregard, D. Radford, and R. Zoughi, “Porosity level estimation in polymer composites using microwaves,” *Mater. Eval.*, vol. 53, no. 3, pp. 404–408, 1995.

[95] D. Hughes *et al.*, “Microwave nondestructive detection of corrosion under thin paint and primer in aluminum panels,” *Subsurf. Sens. Technol. Appl.*, vol. 2, no. 4, pp. 435–471, 2001.

[96] N. N. Qaddoumi, L. F. Handjojo, T. S. Bigelow, J. K. Easter, A. V Bray, and R. Zoughi, "Microwave corrosion detection using open ended rectangular waveguide sensors," 2000.

[97] N. Qaddoumi, A. Shroyer, and R. Zoughi, "Microwave detection of rust under paint and composite laminates," *J. Res. Nondestruct. Eval.*, vol. 9, no. 4, pp. 201–212, 1997.

[98] N. Wang and R. Zoughi, "Moment method solution for modeling the interaction of open ended coaxial probes and surface cracks in metals," 2002.

[99] N. Qaddoumi, E. Ranu, J. D. McColskey, R. Mirshahi, and R. Zoughi, "Microwave detection of stress-induced fatigue cracks in steel and potential for crack opening determination," *J. Res. Nondestruct. Eval.*, vol. 12, no. 2, pp. 87–103, 2000.

[100] C.-Y. Yeh and R. Zoughi, "A novel microwave method for detection of long surface cracks in metals," *IEEE Trans. Instrum. Meas.*, vol. 43, no. 5, pp. 719–725, 1994.

[101] W. Shalaby and R. Zoughi, "Microwave compressive strength estimation of cement paste using monopole probes," *Res. Nondestruct. Eval.*, vol. 7, no. 2–3, pp. 101–115, 1995.

[102] M. Frank, L. Handjojo, N. Qaddoumi, K. Bois, and R. Zoughi, "Microwave evaluation of anisotropy in glass and reflection properties of glass fibers under static load," vol. 57, no. March, pp. 57–62, 2008, doi: 10.1063/1.1301983.

[103] M. H. Umari, D. K. Ghodgaonkar, V. V Varadan, and V. K. Varadan, "A free-space bistatic calibration technique for the measurement of parallel and perpendicular reflection coefficients of planar samples," *IEEE Trans. Instrum. Meas.*, vol. 40, no. 1, pp. 19–24, 1991.

[104] V. V Varadan, R. D. Hollinger, D. K. Ghodgaonkar, and V. K. Varadan, "Free-space, broadband measurements of high-temperature, complex dielectric properties at microwave frequencies," *IEEE Trans. Instrum. Meas.*, vol. 40, no. 5, pp. 842–846, 1991.

[105] I. S. Seo and W. S. Chin, "Characterization of electromagnetic properties of polymeric composite materials with free space method," *Compos. Struct.*, vol. 66, no. 1–4, pp. 533–542, 2004.

[106] J. W. Schultz, *Focused beam methods: measuring microwave materials in free space*. John Schultz, 2012.

[107] H. M. A. Al-Mattarneh, D. K. Ghodgaonkar, and W. M. B. W. A. Majid, "Microwave nondestructive testing for classification of Malaysian timber using free-space techniques," *6th Int. Symp. Signal Process. Its Appl. ISSPA 2001 - Proceedings; 6 Tutorials Commun. Image Process. Signal Anal.*, vol. 2, pp. 450–453, 2001, doi: 10.1109/ISSPA.2001.950177.

[108] U. C. Hasar, "Non-destructive testing of hardened cement specimens at microwave frequencies using a simple free-space method," *NDT E Int.*, vol. 42, no. 6, pp. 550–557, 2009, doi: 10.1016/j.ndteint.2009.04.004.

[109] G. Koutsoukis, I. Alic, A. Vavouliotis, F. Kienberger, and K. Haddadi, "Roll-to-roll in-line implementation of microwave free-space non-destructive evaluation of conductive composite thin layer materials," *Appl. Sci.*, vol. 11, no. 1, p. 378, 2021.

[110] D. K. Ghodgaonkar, N. Hj Hamzah, K. F. Hj Che Kasim, and Z. Awang, "Microwave nondestructive testing of coatings and paints using free-space microwave measurement system," *4th Natl. Conf. Telecommun. Technol. NCTT 2003 - Proc.*, pp. 67–70, 2003,

doi: 10.1109/NCTT.2003.1188304.

[111] M. J. Horst, “Design of a microwave imaging system for rapid wideband imaging,” 2016.

[112] M. T. Ghasr, S. Kharkovsky, R. Zoughi, and R. Austin, “Comparison of near-field millimeter-wave probes for detecting corrosion precursor pitting under paint,” *IEEE Trans. Instrum. Meas.*, vol. 54, no. 4, pp. 1497–1504, 2005.

[113] C. Huber, H. Abiri, S. I. Ganchev, and R. Zoughi, “Modeling of surface hairline-crack detection in metals under coatings using an open-ended rectangular waveguide,” *IEEE Trans. Microw. Theory Tech.*, vol. 45, no. 11, pp. 2049–2057, 1997.

[114] D. Hughes, M. Kazemi, K. Marler, R. Zoughi, J. Myers, and A. Nanni, “Microwave detection of delaminations between fiber reinforced polymer (FRP) composite and hardened cement paste,” in *AIP Conference Proceedings*, 2002, vol. 615, no. 1, pp. 512–519.

[115] J. T. Case, “Microwave and millimeter wave imaging using synthetic aperture focusing and holographical techniques,” 2005.

[116] G. Zheng, R. Zhang, S. Li, H. Zhou, and Y. Shi, “A hyperlens-embedded solid immersion lens for beam focusing beyond the diffraction limit,” *IEEE Photonics Technol. Lett.*, vol. 23, no. 17, pp. 1234–1236, 2011.

[117] S. Kharkovsky, R. Zoughi, and F. L. Hepburn, “Comparison of Focused and Near-Field Imaging of Spray on Foam Insulation (SOFI) at Millimeter Wave Frequencies,” 2007.

[118] S. Kharkovsky, J. T. Case, R. Zoughi, and F. Hepburn, “Millimeter wave detection of localized anomalies in the space shuttle external fuel tank insulating foam and acreage heat tiles,” in *2005 IEEE Instrumentationand Measurement Technology Conference Proceedings*, 2005, vol. 2, pp. 1527–1530.

[119] J. T. Case, J. Robbins, S. Kharkovsky, F. Hepburn, and R. Zoughi, “Microwave and millimeter wave imaging of the space shuttle external fuel tank spray on foam insulation (SOFI) using synthetic aperture focusing techniques (SAFT),” in *AIP Conference Proceedings*, 2006, vol. 820, no. 1, pp. 1546–1553.

[120] J. T. Case, M. T. Ghasr, and R. Zoughi, “Optimum two-dimensional uniform spatial sampling for microwave SAR-based NDE imaging systems,” *IEEE Trans. Instrum. Meas.*, vol. 60, no. 12, pp. 3806–3815, 2011.

[121] M. T. Ghasr, J. T. Case, and R. Zoughi, “Novel reflectometer for millimeter-wave 3-D holographic imaging,” *IEEE Trans. Instrum. Meas.*, vol. 63, no. 5, pp. 1328–1336, 2014.

[122] J. C. Curlander and R. N. McDonough, *Synthetic aperture radar*, vol. 11. Wiley, New York, 1991.

[123] Z. Xu and K.-S. Chen, “On signal modeling of moon-based synthetic aperture radar (SAR) imaging of earth,” *Remote Sens.*, vol. 10, no. 3, p. 486, 2018.

[124] Y. K. Chan and V. Koo, “An introduction to synthetic aperture radar (SAR),” *Prog. Electromagn. Res. B*, vol. 2, pp. 27–60, 2008.

[125] M. Dvorsky, M. T. Al Qaseer, and R. Zoughi, “Crack sizing using dual-polarized microwave SAR imaging,” *I2MTC 2020 - Int. Instrum. Meas. Technol. Conf. Proc.*, pp. 1–6, 2020, doi: 10.1109/I2MTC43012.2020.9129478.

[126] M. Dvorsky, M. T. Al Qaseer, and R. Zoughi, “Detection and Orientation Estimation

of Short Cracks Using Circularly Polarized Microwave SAR Imaging," *IEEE Trans. Instrum. Meas.*, vol. 69, no. 9, pp. 7252–7263, 2020, doi: 10.1109/TIM.2020.2978317.

[127] T. H. Kim, R. James, and R. M. Narayanan, "High-resolution nondestructive testing of multilayer dielectric materials using wideband microwave synthetic aperture radar imaging," *Nondestruct. Charact. Monit. Adv. Mater. Aerospace, Civ. Infrastruct. 2017*, vol. 10169, p. 1016903, 2017, doi: 10.1117/12.2259798.

[128] M. Nezadal, J. Schür, and L.-P. Schmidt, "Non-destructive testing of glass fibre reinforced plastics with a full polarimetric imaging system," in *2014 39th International Conference on Infrared, Millimeter, and Terahertz waves (IRMMW-THz)*, 2014, pp. 1–2.

[129] S. Kharkovsky, A. C. Ryley, V. Stephen, and R. Zoughi, "Dual-polarized microwave near-field reflectometer for noninvasive inspection of carbon fiber reinforced polymer-strengthened structures," *IEEE Trans. Instrum. Meas.*, vol. 57, no. 1, pp. 168–175, 2008, doi: 10.1109/TIM.2007.909497.

[130] A. Katsounaros, K. Z. Rajab, Y. Hao, M. Mann, and W. I. Milne, "X-band characterization of multi-walled carbon nanotube films," *Proc. - 2011 Int. Conf. Electromagn. Adv. Appl. ICEAA'11*, pp. 516–519, 2011, doi: 10.1109/ICEAA.2011.6046394.

[131] L. Wang, S. Member, R. Zhou, H. Xin, and S. Member, "Multiwalled Carbon Nanotube Papers Using Rectangular Waveguides," *Carbon N. Y.*, vol. 56, no. 2, pp. 499–506, 2008.

[132] H. C. Kim and S. K. See, "Electrical properties of unidirectional carbon-epoxy composites in wide frequency band," *J. Phys. D. Appl. Phys.*, vol. 23, no. 7, pp. 916–921, 1990, doi: 10.1088/0022-3727/23/7/026.

[133] Z. Delecki and M. Hamid, "Simple Method for Determination of the Complex Dielectric Constant.," *J. Microw. Power Electromagn. Energy*, vol. 23, no. 1, pp. 53–58, 1988, doi: 10.1080/08327823.1988.11688037.

[134] E. J. Riley, K. L. Koudela, and R. M. Narayanan, "Characterization of the electromagnetic parameter uncertainty in single-ply unidirectional carbon-fiber-reinforced-polymer laminas," *Compos. Part B Eng.*, vol. 162, no. June 2018, pp. 361–368, 2019, doi: 10.1016/j.compositesb.2018.10.089.

[135] A. Galehdar, K. J. Nicholson, W. S. T. Rowe, and K. Ghorbani, "The conductivity of unidirectional and quasi isotropic carbon fiber composites," *Eur. Microw. Week 2010, EuMW2010 Connect. World, Conf. Proc. - Eur. Microw. Conf. EuMC 2010*, no. September, pp. 882–885, 2010.

[136] K. S. Champlin and G. H. Glover, "Influence of waveguide contact on measured complex permittivity of semiconductors," *J. Appl. Phys.*, vol. 37, no. 6, pp. 2355–2360, 1966, doi: 10.1063/1.1708817.

[137] S. S. Yoon, J. W. Lee, T. K. Lee, J. H. Roh, H. I. Kim, and D. W. Yi, "Conductivity Evaluation of a Newly Proposed Material for a SAR Reflector Antenna," *J. Electromagn. Eng. Sci.*, vol. 14, no. 3, pp. 293–298, 2014, doi: 10.5515/jkiees.2014.14.3.293.

[138] A. Galehdar, W. S. T. Rowe, K. Ghorbani, P. J. Callus, S. John, and C. H. Wang, "The effect of ply orientation on the performance of antennas in or on carbon fiber composites," *Prog. Electromagn. Res.*, vol. 116, no. April, pp. 123–136, 2011, doi: 10.2528/PIER11031512.

[139] S. S. Yoon, J. W. Lee, T. K. Lee, and D. W. Yi, “A study on measurement system for electrical characteristics of anisotropic composite material,” *2016 URSI Asia-Pacific Radio Sci. Conf. URSI AP-RASC 2016*, no. 3, pp. 1150–1151, 2016, doi: 10.1109/URSIAP-RASC.2016.7601138.

[140] Z. Li and Z. Meng, “A review of the radio frequency non-destructive testing for carbon-fibre composites,” *Meas. Sci. Rev.*, vol. 16, no. 2, pp. 68–76, 2016, doi: 10.1515/msr-2016-0010.

[141] Z. Li, A. Haigh, C. Soutis, and A. Gibson, “Principles and Applications of Microwave Testing for Woven and Non-Woven Carbon Fibre-Reinforced Polymer Composites: a Topical Review,” *Appl. Compos. Mater.*, vol. 25, no. 4, pp. 965–982, 2018, doi: 10.1007/s10443-018-9733-x.

[142] S. Kharkovsky and R. Zoughi, “Application of near-field microwave and millimeter wave nondestructive testing for evaluation of fiber breakage and orientation evaluation in CFRP composite patches,” *AIP Conf. Proc.*, vol. 760, pp. 554–561, 2005, doi: 10.1063/1.1916724.

[143] S. H. Yang, K. B. Kim, H. G. Oh, and J. S. Kang, “Non-contact detection of impact damage in CFRP composites using millimeter-wave reflection and considering carbon fiber direction,” *NDT E Int.*, vol. 57, pp. 45–51, 2013, doi: 10.1016/j.ndteint.2013.03.006.

[144] S. H. Yang, K. B. Kim, H. G. Oh, and J. S. Kang, “Non-contact detection of impact damage in CFRP composites using millimeter-wave reflection and considering carbon fiber direction,” *NDT E Int.*, vol. 57, pp. 45–51, 2013, doi: 10.1016/j.ndteint.2013.03.006.

[145] M. Tabib-Azar, P. S. Pathak, G. Ponchak, and S. LeClair, “Nondestructive superresolution imaging of defects and nonuniformities in metals, semiconductors, dielectrics, composites, and plants using evanescent microwaves,” *Rev. Sci. Instrum.*, vol. 70, no. 6, pp. 2783–2792, 1999, doi: 10.1063/1.1149795.

[146] S. Gubinelli *et al.*, “An ultra-wideband radar approach to nondestructive testing,” *Proc. - IEEE Int. Conf. Ultra-Wideband*, pp. 303–308, 2014, doi: 10.1109/ICUWB.2014.6958997.

[147] A. Foudazi, “Development of active microwave thermography for structural health monitoring,” 2017.

[148] K. Sam-Ang, D. Didier, B. Florin, and B. Franck, “Comparison between microwave infrared thermography and CO 2 laser infrared thermography in defect detection in applications with CFRP,” *Mater. Sci. Appl.*, vol. 2013, 2013.

[149] R. Mavaddat, “Network scattering parameters,” 1996.

[150] C. E. Kintner, “Free-Space Measurements of Dielectrics and Three-Dimensional Periodic Metamaterials,” 2017.

[151] A. Note, “Keysight Technologies In-fixture Microstrip Device Measurements Using TRL Calibration.”

[152] “electronics-notes.” https://www.electronics-notes.com/articles/antennas-propagation/rf-feeders-transmission-lines/waveguide-modes-te-tm-tem.php.

[153] V. Rodriguez, “Basic Rules for Indoor Anechoic Chamber Design [Measurements Corner],” *IEEE Antennas Propag. Mag.*, vol. 58, no. 6, pp. 82–93, 2016, doi: 10.1109/MAP.2016.2609821.

[154] Z. Xiong and Z. Chen, "Modeling of Tapered Anechoic Chambers," *2018 AMTA 2018 Proceedings, AMTA 2018*, pp. 1–4, 2019.

[155] F. B. J. Leferink, "Using reverberation chambers for EM measurements," *SoftCOM 2010 - Int. Conf. Software, Telecommun. Comput. Networks*, pp. 1–5, 2010.

[156] "Ibdonline Camere riverberanti," [Online]. Available: http://www.ibdonline.it/CamereRiverberanti.html.

[157] T. Weiland, "A discretization model for the solution of Maxwell's equations for six-component fields," *Arch. Elektron. und Uebertragungstechnik*, vol. 31, pp. 116–120, 1977.

[158] F. Edelvik, R. Schuhmann, and T. Weiland, "A general stability analysis of FIT/FDTD applied to lossy dielectrics and lumped elements," *Int. J. Numer. Model. Electron. Networks, Devices Fields*, vol. 17, no. 4, pp. 407–419, 2004.

[159] B. Krietenstein, R. Schuhmann, P. Thoma, and T. Weiland, "The perfect boundary approximation technique facing the big challenge of high precision field computation," in *Proceedings of the XIX International Linear Accelerator Conference (LINAC 98), Chicago, USA*, 1998, pp. 860–862.

[160] M. Clemens and T. Weiland, "Magnetic field simulation using conformal FIT formulations," *IEEE Trans. Magn.*, vol. 38, no. 2, pp. 389–392, 2002.

[161] H. W. Ott, *Electromagnetic compatibility engineering*. John Wiley & Sons, 2011.

[162] N. Leitgeb, J. Schröttner, and M. Böhm, "Does 'electromagnetic pollution' cause illness?," *Wiener Medizinische Wochenschrift*, vol. 155, no. 9, pp. 237–241, 2005.

[163] A. Balmori, "Electromagnetic pollution from phone masts. Effects on wildlife," *Pathophysiology*, vol. 16, no. 2–3, pp. 191–199, 2009.

[164] Z. Kubík and J. Skála, "Shielding effectiveness simulation of small perforated shielding enclosures using fem," *Energies*, vol. 9, no. 3, p. 129, 2016.

[165] W. J. Rea *et al.*, "Electromagnetic field sensitivity," *J. Bioelectr.*, vol. 10, no. 1–2, pp. 241–256, 1991.

[166] S. Yang, K. Lozano, A. Lomeli, H. D. Foltz, and R. Jones, "Electromagnetic interference shielding effectiveness of carbon nanofiber/LCP composites," *Compos. Part A Appl. Sci. Manuf.*, vol. 36, no. 5, pp. 691–697, 2005.

[167] E. Håkansson, A. Amiet, and A. Kaynak, "Electromagnetic shielding properties of polypyrrole/polyester composites in the 1–18 GHz frequency range," *Synth. Met.*, vol. 156, no. 14–15, pp. 917–925, 2006.

[168] J.-M. Thomassin, C. Jerome, T. Pardoen, C. Bailly, I. Huynen, and C. Detrembleur, "Polymer/carbon based composites as electromagnetic interference (EMI) shielding materials," *Mater. Sci. Eng. R Reports*, vol. 74, no. 7, pp. 211–232, 2013.

[169] D. D. L. Chung, "Materials for electromagnetic interference shielding," *Mater. Chem. Phys.*, p. 123587, 2020.

[170] S. A. Schelkunoff, "Electromagnetic waves," 1943.

[171] R. B. Schulz, V. C. Plantz, and D. R. Brush, "Shielding theory and practice," *IEEE Trans. Electromagn. Compat.*, vol. 30, no. 3, pp. 187–201, 1988.

[172] D. M. Bigg, "The effect of chemical exposure on the EMI shielding of conductive plastics," *Polym. Compos.*, vol. 8, no. 1, pp. 1–7, 1987.

[173] W. S. Jou, T. L. Wu, S. K. Chiu, and W. H. Cheng, "Electromagnetic shielding of nylon-66 composites applied to laser modules," *J. Electron. Mater.*, vol. 30, no. 10, pp. 1287–1293, 2001.

[174] Y. Yang, M. C. Gupta, and K. L. Dudley, "Towards cost-efficient EMI shielding materials using carbon nanostructure-based nanocomposites," *Nanotechnology*, vol. 18, no. 34, p. 345701, 2007.

[175] S.-S. Tzeng and F.-Y. Chang, "EMI shielding effectiveness of metal-coated carbon fiber-reinforced ABS composites," *Mater. Sci. Eng. A*, vol. 302, no. 2, pp. 258–267, 2001.

[176] J. Wu and D. D. L. Chung, "Increasing the electromagnetic interference shielding effectiveness of carbon fiber polymer–matrix composite by using activated carbon fibers," *Carbon N. Y.*, vol. 40, no. 3, pp. 445–447, 2002.

[177] M.-S. Cao, W.-L. Song, Z.-L. Hou, B. Wen, and J. Yuan, "The effects of temperature and frequency on the dielectric properties, electromagnetic interference shielding and microwave-absorption of short carbon fiber/silica composites," *Carbon N. Y.*, vol. 48, no. 3, pp. 788–796, 2010.

[178] N. C. Das, D. Khastgir, T. K. Chaki, and A. Chakraborty, "Electromagnetic interference shielding effectiveness of carbon black and carbon fibre filled EVA and NR based composites," *Compos. part A Appl. Sci. Manuf.*, vol. 31, no. 10, pp. 1069–1081, 2000.

[179] M. H. Al-Saleh and U. Sundararaj, "Electromagnetic interference shielding mechanisms of CNT/polymer composites," *Carbon N. Y.*, vol. 47, no. 7, pp. 1738–1746, 2009.

[180] L. Li and D. D. L. Chung, "Electrical and mechanical properties of electrically conductive polyethersulfone composites," *Composites*, vol. 25, no. 3, pp. 215–224, 1994.

[181] D. D. L. Chung, "Electromagnetic interference shielding effectiveness of carbon materials," *Carbon N. Y.*, vol. 39, no. 2, pp. 279–285, 2001.

[182] X. Luo and D. D. L. Chung, "Electromagnetic interference shielding using continuous carbon-fiber carbon-matrix and polymer-matrix composites," *Compos. Part B Eng.*, vol. 30, no. 3, pp. 227–231, 1999.

[183] D. D. L. Chung, "Carbon materials for structural self-sensing, electromagnetic shielding and thermal interfacing," *Carbon N. Y.*, vol. 50, no. 9, pp. 3342–3353, 2012.

[184] "Standard Test Method for Measuring the Electromagnetic Shielding Effectiveness of Planar Materials." https://www.astm.org/d4935-18.html.

[185] Y. M. Lee and K. J. Madden, "Mil-Std-907B Modifies Mil-Std-285 Emi test procedures," in *IEEE International Symposium on Electromagnetic Compatibility*, 1990, pp. 238–240.

[186] Y. M. Lee, "Comparison of SE measurements between MIL-STD-285 and the ASTM Standard E1851," in *1998 IEEE EMC Symposium. International Symposium on Electromagnetic Compatibility. Symposium Record (Cat. No. 98CH36253)*, 1998, vol. 2, pp. 1053–1058.

[187] G. Wypych, *Handbook of fillers*, vol. 92. ChemTec Pub. Toronto, 2010.

[188] T. W. Więckowski and J. M. Janukiewicz, "Methods for evaluating the shielding effectiveness of textiles," *Fibres Text. East. Eur.*, no. 5 (59), pp. 18–22, 2006.

[189] S. Kovar, J. Valouch, H. Urbancokova, M. Adámek, and V. Mach, “Simulation of shielding effectiveness of materials using cst studio,” *WSEAS Trans. Commun.*, vol. 16, pp. 131–136, 2017.

[190] I. Munteanu and I. Hänninen, “Recent advances in CST STUDIO SUITE for antenna simulation,” in *2012 6th European Conference on Antennas and Propagation (EUCAP)*, 2012, pp. 1301–1305.

[191] M. Rütschlin and T. Wittig, “State of the art antenna simulation with CST STUDIO SUITE,” in *2015 9th European Conference on Antennas and Propagation (EuCAP)*, 2015, pp. 1–5.

[192] H. Saadi and R. Oussaid, “Materials effect on shielding effectiveness,” in *2007 IEEE International Conference on Signal Processing and Communications*, 2007, pp. 999–1002.

[193] P. Saini, V. Choudhary, B. P. Singh, R. B. Mathur, and S. K. Dhawan, “Polyaniline–MWCNT nanocomposites for microwave absorption and EMI shielding,” *Mater. Chem. Phys.*, vol. 113, no. 2–3, pp. 919–926, 2009.

[194] Z. Liu *et al.*, “Reflection and absorption contributions to the electromagnetic interference shielding of single-walled carbon nanotube/polyurethane composites,” *Carbon N. Y.*, vol. 45, no. 4, pp. 821–827, 2007.

[195] N. Quievy *et al.*, “Electromagnetic absorption properties of carbon nanotube nanocomposite foam filling honeycomb waveguide structures,” *IEEE Trans. Electromagn. Compat.*, vol. 54, no. 1, pp. 43–51, 2012.

[196] R. M. Simon, “EMI shielding through conductive plastics,” *Polym. Plast. Technol. Eng.*, vol. 17, no. 1, pp. 1–10, 1981.

[197] G. Lu, X. Li, and H. Jiang, “Electrical and shielding properties of ABS resin filled with nickel-coated carbon fibers,” *Compos. Sci. Technol.*, vol. 56, no. 2, pp. 193–200, 1996.

[198] A. C. Long and L. Brown, “Modelling the geometry of textile reinforcements for composites: TexGen,” in *Composite reinforcements for optimum performance*, Elsevier, 2011, pp. 239–264.

[199] D. Munalli, M. T. Al Qaseer, and R. Zoughi, “Modified Waveguide-Based Method for Microwave Characterization of High-Loss Materials,” *IEEE Trans. Instrum. Meas.*, 2022.

[200] S. Dubrovskiy and K. Gareev, “Measurement method for detecting magnetic and dielectric properties of composite materials at microwave frequencies,” *Proc. 2015 IEEE North West Russ. Sect. Young Res. Electr. Electron. Eng. Conf. ElConRusNW 2015*, pp. 24–26, 2015, doi: 10.1109/EIConRusNW.2015.7102223.

[201] A. Foudazi and K. M. Donnell, “Effect of sample preparation on microwave material characterization by loaded waveguide technique,” *IEEE Trans. Instrum. Meas.*, vol. 65, no. 7, pp. 1669–1677, 2016, doi: 10.1109/TIM.2016.2540840.

[202] R. G. Fehlen, “Air gap error compensation for coaxial transmission line method of electromagnetic material characterization,” M.S. thesis, Dept Elect. and Comp. Eng., Air Force Institute of Technology, Ohio, 2006.

[203] S. B. Wilson, “Modal analysis of the ‘gap effect’ in waveguide dielectric measurements,” *IEEE Trans. Microw. Theory Tech.*, vol. 36, no. 4, pp. 752–756, 2009, doi: 10.1109/vissof.2009.5336427.

[204] M. A. Hindy, A. A. Mitkees, and A. El Sohly, “Modal analyses of loaded waveguides

for microwave diagnostics of semiconductors," *Midwest Symp. Circuits Syst.*, pp. 1042–1045, 1989, doi: 10.1109/mwscas.1989.102032.

[205] A. Bogle, M. Havrilla, D. Nyquis, L. Kempel, and E. Rothwell, "Electromagnetic material characterization using a partially-filled rectangular waveguide," *J. Electromagn. Waves Appl.*, vol. 19, no. 10, pp. 1291–1306, 2005, doi: 10.1163/156939305775525909.

[206] M. P. Parkhomenko, D. S. Kalenov, I. S. Eremin, N. A. Fedoseev, V. M. Kolesnikova, and Y. L. Barinov, "Usage and Experimental Tests of the Modified Waveguide Method for Measurement of the Complex Permittivity and Permeability of Materials," *Phys. Wave Phenom.*, vol. 27, no. 4, pp. 299–306, 2019, doi: 10.3103/S1541308X19040101.

[207] "CST-Computer Simulation Technology." https://www.3ds.com/.

[208] D. Rytting, "Network analyzer error models and calibration methods," *White Paper*. pp. 1–44, 1998.

[209] A. T. M. S. Islam and M. P. U. Bandara, "Yarn Spacing Measurement in Woven Fabrics with Specific Reference to Start-up Marks," *J. Text. Inst.*, vol. 87, no. 1, pp. 107–119, 1996, doi: 10.1080/00405009608659060.

[210] R. Naik, "Failure Analysis of Woven and Braided Fabric Reinforced Composites," *J. Compos. Mater.*, vol. 29, pp. 2334–2361, 1995.

[211] P. Vandeurzen, J. Ivens, and I. Verpoest, "A three-dimensional micromechanical analysis of woven-fabric composites: II. Elastic analysis," *Compos. Sci. Technol.*, vol. 56, no. 11, pp. 1317–1327, 1996, doi: 10.1016/S0266-3538(96)00091-7.

[212] J. Musil and F. Zacek, "Microwave measurements of complex permittivity by free space methods and their applications," *NASA STI/Recon Tech. Rep. A*, vol. 87, 1986.

[213] "scholar." .

[214] M. Dvorsky, M. T. Al Qaseer, and R. Zoughi, "Calibration of a Dual-Polarized Probe Using the 16-Term Calibration Model," *IEEE Trans. Instrum. Meas.*, vol. 70, 2021, doi: 10.1109/TIM.2021.3076854.

[215] M. A. Abou-Khousa, M. S. U. Rahman, and X. Xingyu, "Dual-polarized microwave imaging probe," *IEEE Sens. J.*, vol. 19, no. 5, pp. 1767–1776, 2018.

[216] X. Dong and Y. Zhang, "A novel compressive sensing algorithm for SAR imaging," *IEEE J. Sel. Top. Appl. earth Obs. Remote Sens.*, vol. 7, no. 2, pp. 708–720, 2013.

[217] P. Berardino, G. Fornaro, R. Lanari, and E. Sansosti, "A new algorithm for surface deformation monitoring based on small baseline differential SAR interferograms," *IEEE Trans. Geosci. Remote Sens.*, vol. 40, no. 11, pp. 2375–2383, 2002.

[218] F. Dellinger, J. Delon, Y. Gousseau, J. Michel, and F. Tupin, "SAR-SIFT: a SIFT-like algorithm for SAR images," *IEEE Trans. Geosci. Remote Sens.*, vol. 53, no. 1, pp. 453–466, 2014.

[219] M. Dvorsky, G. S. Member, M. Tayeb, A. Qaseer, and S. Member, "Synthetic Aperture Radar 3-D Polarimetry," vol. 71, 2022.

[220] J. J. Van Zyl, *Synthetic aperture radar polarimetry*, vol. 2. John Wiley & Sons, 2011.

[221] J. J. Van Zyl, M. Arii, and Y. Kim, "Model-based decomposition of polarimetric SAR covariance matrices constrained for nonnegative eigenvalues," *IEEE Trans. Geosci. Remote Sens.*, vol. 49, no. 9, pp. 3452–3459, 2011.

[222] W.-M. Boerner, “Basics of sar polarimetry i,” UIC-ECE COMMUNICATIONS CHICAGO IL COMMUNICATIONS, SENSING AND NAVIGATION LAB, 2007.

[223] D. Xu, L. Liu, and Z. Jiang, “Measurement of the Dielectric Properties of Biological Substances Using an Improved Open-Ended Coaxial Line Resonator Method,” *IEEE Trans. Microw. Theory Tech.*, vol. MTT-35, no. 12, pp. 1424–1428, 1987, doi: 10.1109/TMTT.1987.1133870.

[224] A. H. Sihvola, *Electromagnetic mixing formulas and applications*, no. 47. Iet, 1999.

[225] A. Brasington, C. Sacco, J. Halbritter, R. Wehbe, and R. Harik, “Automated fiber placement: A review of history, current technologies, and future paths forward,” *Compos. Part C Open Access*, vol. 6, no. June, p. 100182, 2021, doi: 10.1016/j.jcomc.2021.100182.

[226] M. Dvorsky, D. Munalli, M. T. Al Qaseer, and R. Zoughi, “Application of Microwave Polarimetry to the Characterization of Fiber Misalignment in Composites,” *IEEE Open J. Instrum. Meas.*, vol. 1, no. June, pp. 1–9, 2022, doi: 10.1109/ojim.2022.3184347.

Appendix I

Matlab Codes

Iterative method

This algorithm uses an iterative method to extract permittivity from reflection and transmission measurement data. It accepts complex-valued scattering parameter data and returns complex ε_r.

```
%--------------------------%
%--- Inversion code NIST for free-space----%
%
% Script that calculates the permeability & permittivity
% of a sample material using either the S11 & S21 or S22 & S12
% parameters obtained from a Ka-Band Horn system & the
% Network Analyzer.

close all; % Close all graphs presently open


%------------------IMPORT S-PARAM & DEFINE CONSTANTS----------------
--%

file_name = input('File containing S_11 data (real/imag format):
','s');
[F, S11r, S11i, S21r, S21i] = import_real_imag_hvs(file_name);
S11 = complex(S11r, S21i);
S21 = complex(S21r, S21i);
eps_guess = input('Initial guess for relative epsilon: ');


%---------------SMOOTHING OF MEASURED DATA-----------------------
---%

PFC=5;
S11_real_fit = polyfit(F,real(S11),PFC);
S11_real_val = polyval(S11_real_fit, F);
S11_imag_fit = polyfit(F,imag(S11),PFC);
S11_imag_val = polyval(S11_imag_fit, F);

S11_smooth = S11_real_val + i.*S11_imag_val;

S11new = S11_smooth(1:(length(S11_smooth))); % Average between every
2 succesive data points.

S21_real_fit = polyfit(F,real(S21),PFC);
S21_real_val = polyval(S21_real_fit, F);
S21_imag_fit = polyfit(F,imag(S21),PFC);
S21_imag_val = polyval(S21_imag_fit, F);

S21_smooth = S21_real_val + i.*S21_imag_val;

S21new = S21_smooth(1:(length(S21_smooth)));
```

```
%-----------------------PLOT SMOOTH VS ORIGINAL ------------------%

figure
plot(F,mag2db(abs(S11)),F,mag2db(abs(S21)));
hold on
plot(F,mag2db(abs(S11_smooth)),F,mag2db(abs(S21_smooth)));
hold off
xlabel('Frequency(GHz)');
ylabel('dB');


%-----------------------DEFINE VARIABLES-------------------------%

th=1.75*10^(-3) ; %th material in m
Lair=22*10^(-3); %th air in m
c=299792458; % Speed of light in vacuum (m/s)
Fc=21.077; %cut-off frequency in GHz
lc=c/(Fc*10^9); % cut-off wavelength in m
eo=8.8542*10^(-12);
uo=4*pi*10^(-7) ;
lo=c./(F.*10^9); % wavelength free space in m
w=(2*pi).*(F.*10^9); %angular frequency in Hz


%-----------------------DEFINE propagation constant y------------%

y0=1i*sqrt((w./c).^2-(2*pi/lc)^2); % propagation constant in air

y= @(Er) 1i*sqrt(((w./c).^2).*(Er)-(2*pi/lc)^2); % propagation
constant in material


%-----------------------DEFINE reflection coeff G----------------%

G = @(Er) (y0-y(Er))./(y0+y(Er));

%-----------------------DEFINE transmission coeff T--------------%

T = @(Er) exp(-y(Er).*th);

%-----------------------DEFINE permittivity----------------------%

A=S11new.*S11new-(S21new.*S21new);
C= @(Er) T(Er).^2;
D= @(Er) G(Er).^2;
B= @(Er) (C(Er)-D(Er))./(1-D(Er).*C(Er)); % equations will allow the
determination of the permittivity

% Method 1 Transm and Refl
fx = @(Er) A-(B(Er).*(exp(y0.*(-2)*(Lair-th))));


% Method 2 Refl
fx2 = @(Er) (S21new./(1-C(Er).*D(Er)))-(T(Er)-
T(Er).*D(Er)).*(exp(y0.*(th-Lair)));

%optimization with either one of fx or fx2

options = optimset(optimset('fsolve'), 'TolFun', 1.0e-12,
'TolX',1.0e-12);
```

```
Er1 = fsolve(fx, eps_guess, options);


Real_perm=mean(real(Er1(1:201,1))) % Average value real part of
permittivity
Im_perm=mean(abs(imag(Er1(1:201,1)))) % Average value im part of
permittivity
LossFactor=Im_perm/Real_perm % Average value loss factor of
permittivity
```

New non-iterative method

This algorithm uses a method to extract permittivity from reflection and transmission measurement data. It accepts complex-valued scattering parameter data and returns complex ε_r.

```
%--------------------------%
%---Inversion code New NICM free-space----%
%
% Script that calculates the permeability & permittivity
% of a sample material using either the S11 & S21 or S22 & S12
% parameters obtained from a Ka-Band Horn system & the
% Network Analyzer.

close all; % Close all graphs presently open


%-----------------IMPORT S-PARAM & DEFINE CONSTANTS--------------%

file_name = input('File containing S_11 data (real/imag format):
','s');
[F, S11r, S11i, S21r, S21i] = import_real_imag_hvs(file_name);
S11 = complex(S11r, S21i);
S21 = complex(S21r, S21i);
eps_guess = input('Initial guess for relative epsilon: ');

%---------------SMOOTHING OF MEASURED DATA----------------------%

PFC=5;
S22_real_fit = polyfit(F,real(S22),PFC);
S22_real_val = polyval(S22_real_fit, F);
S22_imag_fit = polyfit(F,imag(S22),PFC);
S22_imag_val = polyval(S22_imag_fit, F);
S22_smooth = S22_real_val + i.*S22_imag_val;

S22new = S22_smooth(1:(length(S22_smooth)));



S12_real_fit = polyfit(F,real(S12),PFC);
S12_real_val = polyval(S12_real_fit, F);
S12_imag_fit = polyfit(F,imag(S12),PFC);
S12_imag_val = polyval(S12_imag_fit, F);
S12_smooth = S12_real_val + i.*S12_imag_val;

S12new = S12_smooth(1:(length(S12_smooth)));
```

```
%-----------------------PLOT SMOOTH VS ORIGINAL -------------------%

figure
plot(F,mag2db(abs(S22)),F,mag2db(abs(S12)));
hold on
plot(F,mag2db(abs(S22_smooth)),F,mag2db(abs(S12_smooth)));
hold off
xlabel('Frequency(GHz)');
ylabel('dB');

%-----------------------DEFINE VARIABLES-------------------------%

th=1.75*10^(-3) ; %th material in m
Fmiddle=data(1,1)+((data(201,1)-data(1,1))/2);
c=299792458; % Speed of light in vacuum (m/s)
Fc=21.077; %cutoff frequency in GHz
lc=c/(Fc*10^9); % cutoff wavelength in m
lo=c./(F.*10^9); % wavelength free space in m
Fnew = F(1:(length(F)));
lonew=c./(Fnew.*10^9);% Wavelength free space calculated using
average frequency

%-------------DETERMINE GROUP DELAY------------------------------%

%Group delay = Negative rate of change of phase of S12 with respect
to frequency.

magS12 = abs(S12_smooth); % Magnitude of SPar2
phaseS12 = unwrap(angle(S12_smooth)); % Angle of SPar2 in radians;
Unwrap to avoid jumps in phase
gradient = diff(-phaseS12); % Difference in angle between every 2
successive f-points in degrees.
df = diff(F); % Difference between each 2 succesive frequency points
tg = (gradient./df)./(2*pi); % Group delay according to definition

%--------------------CALCULATE GAMMA Reflection coeff------------%

X=(S22new.^2-S12new.^2+1)./(2.*S22new);

tel = 1; % Define counter

while(tel <= length(S22new)) % Test if gamma <= 1
%If not the negative sign of root should be used
Gb(tel) = X(tel) + sqrt(X(tel)^2 - 1); % Reflection coefficient
if abs(Gb(tel)) > 1 % Test if biger than 1
disp('Nou in if stelling')
Gb(tel) = X(tel) - sqrt(X(tel)^2 - 1); %Use the negative sign if
gamma > 1
end
tel = tel + 1;
end

G=Gb.';

%----------------CALCULATE T transmission coeff------------------%

T = (S22new + S12new - G)./(1 - (S22new + S12new).*G); % tansmission
coeff

%-------------------------calculate n-------------------------%
```

```
phi = log(1./T); % Natural log of complex Propagation Factor
phi2 = real(phi) + 1i*unwrap(imag(phi));

n = (Fnew.*(tg) - unwrap(imag(phi))./(2*pi)); % n2 calculated from
formula & rounded to nearest integer.

z = 1; % Counter z
while(z < 201)
if n(z) > 0
n(z) = floor(n(z));
elseif n(z) < 0
n(z) = abs((ceil(n(z))));
else
n(z) = 0;
end;
z = z + 1;
end


while(z < 200)
if n(z) > 0; disp('N groter as 0'); end; % Show message when n2 > 0
if n(z) < 0; n(z) = 0; end;
z = z + 1;
end


%------------CALCULATE PARAMETER WITH CORRECT n-------------%

inv_lambda2 = -((((1/(2*pi*th)).*(phi2 + (2.*pi.*n).*1i))).^2); %
Calculated from definition
inv_lambda = sqrt(inv_lambda2);


%----------Calculate Permeability and Permittivity----------%

m=1;

l_og=1./(sqrt((1./lonew.^2)-(1/lc^2))); % wavelength in empty cell

u_eff = ((1 + G).*inv_lambda)./((1 - G).*sqrt((1./(lonew.^2)) -
(1/lc^2)));

% General Case perm_eff

e_eff1 = (((1-G)./(1+G))).*(l_og.*inv_lambda);

% Case when if u_r=u_eff = 1:

e_eff = (((1+G)./(1-G)).^(m-1)).*(l_og.*inv_lambda).^(m+1);

% General case

permittivity = e_eff1.*(1-((lonew.^2)./lc^2))+(u_eff.^(-
1)).*((lonew.^2)./lc^2);

% Case when if u_r=u_eff = 1 -- non magnetic material:

permittivity2 = e_eff.*(1-((lonew.^2)./lc^2))+(1^(-
1)).*((lonew.^2)./lc^2);
```

```
Real_perm=mean(real(permittivity)) % Average value real part of
permittivity
Im_perm=mean(abs(imag(permittivity))) % Average value im part of
permittivity
Lossfactor=Im_perm/Real_perm % Average value loss factor of
permittivity
```